



THE UNIVERSITY *of* EDINBURGH

This thesis has been submitted in fulfilment of the requirements for a postgraduate degree (e.g. PhD, MPhil, DClinPsychol) at the University of Edinburgh. Please note the following terms and conditions of use:

This work is protected by copyright and other intellectual property rights, which are retained by the thesis author, unless otherwise stated.

A copy can be downloaded for personal non-commercial research or study, without prior permission or charge.

This thesis cannot be reproduced or quoted extensively from without first obtaining permission in writing from the author.

The content must not be changed in any way or sold commercially in any format or medium without the formal permission of the author.

When referring to this work, full bibliographic details including the author, title, awarding institution and date of the thesis must be given.

Advancement of Direct Drive Generator Systems for Offshore Renewable Energy Production

Joseph William Burchell



Doctor of Philosophy

THE UNIVERSITY OF EDINBURGH

2017

To whom it may concern

Abstract

“What must be obvious to all is that our oil and gas reserves are not renewable and they are diminishing, and to protect the generations to come, we must engage in nothing short of a radical shift in the diversification of the economy.”

- Anthony Carmona

As machine topologies and technologies mature, the fundamental function of the device is honed. Direct drive machines have the potential to launch the renewable energy sector into a new era of large scale, reliable, offshore power generation. With advancements in new technologies, such as superconductivity, the reduction of generator mass due to incorporation of machine and device structures, the continued advancements in component and system reliability; direct drive generators have the ability to outsize geared wind systems and simplify submerged linear and rotary power generation.

The research held within this thesis will focus on improving direct drive power take off systems for offshore renewable energy power generation by splitting the area into four parts. The first part will discuss the various methods of energy extraction within the offshore and marine environment. The future of the sector will be discussed, and a forecast of technological advancement and existing reliability issues will be provided based on current data. The second part will focus on drive trains and direct drive generators, assessing the current topologies and suggesting alternatives that may thrive in a variety of large and small offshore renewable machines.

The third part investigates the application of novel linear bearings in direct drive systems for offshore and submerged operation. A brief study of the loads found in wave applications will be presented and the testing of several polymer bearing materials will be outlined. The final part will discuss the potential benefits of flooding the airgap of a direct drive generator with sea water for marine applications. Results will be presented from two linear test rigs and the marinisation of devices will conclude the report.

Declaration

I hereby declare that this thesis has been composed by myself and that except where stated, the work contained is my own. I also declare that the work contained in this thesis has not been submitted for any other degree or professional qualification except as specified.

Joseph William Burchell

July 2017

Acknowledgements

I would like to thank my principal supervisor, Professor Markus Mueller who provided me with the opportunity, support and freedom to carry out my research. Without his guidance, ideas and technical contributions, this work would not have been possible. I would also like to thank my second supervisor Dr John Chick, who provided support and well measured advice whenever I need it.

I am very grateful to all my friends that have supported me through this PhD, especially you poor fools that lived with me during this period of my life. I would also express my gratitude that I was able to meet so many kind, generous and interesting people throughout my studies, many of whom I would not only consider my colleagues but close friends. I would especially like to mention (in no particular order) the following people who helped me stay sane: Neil, Mark, Nacho, Monika, JenHao, Kaswar, Yukio, Ben, Hasty, Mattie, Knoxy, Billy, Gareth, Anna, Will, James, Alberto, Euan, Ashley, Kevin, Tom, Analys, Zeynep, Siraj, Maggie and Latha.

Additional special thanks must go to Mike Galbraith of Fountain Design, Dr Ozan Keysan and Dr David Forehand for all their continued support, advice and ideas.

I am eternally grateful to my parents for their unwavering love, understanding, advice and encouragement. Without their support I would not be where I am today, and I promise I will now have the time to help with lambing and fencing again!

Finally, but most importantly, I would like to thank that special person I met during my studies. You are the best outcome of my PhD, which makes everything else worthwhile. Her patience and love mean that even when we're apart I'm truly not alone.

Contents

Chapter 1.....	1
1.1. Introduction	1
1.2. Summary & Aim of Thesis.....	1
1.3. Outline of Thesis	2
1.4. Publications	4
Journal Papers	4
Conference Papers.....	4
1.5. Animation and video links.....	5
Chapter 2.....	6
2.1. Wind Energy: A brief History	6
2.2. Marine Energy: A brief History.....	9
2.3. Offshore Renewable Energy Resource.....	11
2.3.1. Offshore Wind.....	12
Horizontal Axis Wind Turbines	14
Vertical Axis Wind Turbines	16
2.3.2. Wave.....	22
Wave Devices.....	26
Attenuator.....	28
Point Absorber.....	29
Bulge Wave	29
Oscillating Water Column.....	29
Oscillating Wave Surge Converter.....	30
Overtopping/Terminator Device	30
Submerged Pressure Differential	31
Rotating Mass.....	31
2.3.3. Tidal Stream	32

Tidal Stream Devices	34
Horizontal Axis Turbines.....	35
Vertical Axis Turbine.....	36
Oscillating Hydrofoil	36
Ducted Devices	36
Archimedes Screw	37
Tidal Kite	37
2.4. PTO Systems for Renewable Power Generation.....	38
2.4.1. Geared	41
Conventional Gearing	41
2.4.2. Hydraulic and Pneumatic	44
2.4.3. Direct Drive.....	46
2.4.4. Bearings.....	48
Chapter 3.	52
3.1. Renewable Electrical Generation: An Overview	52
3.2. Direct Drive Electrical Generator Topologies.....	56
3.2.1. Operational Loads	62
Shear stress.....	64
Maxwell stress.....	65
Gravitational force	65
Thermal expansion and contraction	66
Centripetal force.....	66
Propagated Loads	67
Cogging Torque	67
3.3. Superconducting Direct Drive Technology.....	69
3.3.1. Superconducting 101.....	71
Infinite conductivity	71

Perfect diamagnetism and the Meissner effect.....	72
Critical Current and Quench	75
Superconducting materials	76
Cryo-coolers and cooling systems.....	79
3.3.2. Superconducting technology for energy	82
Superconducting Generators	83
Suprapower Project	85
HTS-GEN Project	88
INNWIND Project.....	89
Ecoswing	92
Alternative SC Machine topologies	93
Superconducting Structural Design.....	93
3.4. Case Studies.....	94
3.4.1. Transverse-flux HTS generator	94
3.4.2. C-GEN direct drive generator	97
3.5. Discussion.....	100
Chapter 4.....	101
4.1. Structural Analysis for Direct Drive Machines	101
4.2. Linear Claw Pole Prototype.....	101
4.2.1. Design and Assembly.....	102
Field winding and core	104
Claw pole translator	105
Armature coil and core	105
Assembled machine and support structure.....	107
4.2.2. Experimental Results.....	108
Structural Test	109
Flux Testing.....	112

4.2.3.	Design Alterations for HTS Testing	114
	Structural	114
	Initial HTS Cryogenic Design.....	116
	Vacuum Chamber Testing.....	118
4.3.	30kW HTS Claw Pole Prototype.....	120
4.3.1.	Electrical Topology	121
4.3.2.	Structural Topology	122
4.3.3.	Discussion	126
4.4.	Scaled Claw Pole HTS Design	127
4.4.1.	Proposed Electrical Design	128
4.4.2.	Structural Design.....	130
4.4.3.	Loading Simulations and Optimisation.....	131
4.4.4.	Discussion	134
Chapter 5.	136
5.1.	Offshore Renewables	136
5.2.	Loading.....	137
5.2.1.	Marine Wave Loading.....	138
5.2.2.	Wave Loading Results	140
5.3.	Polymer Journal Bearing Testing	140
5.3.1.	Linear Test Rig Design	143
5.3.2.	Testing Procedure.....	145
5.3.3.	Mechanical Faults	146
5.3.4.	Bearing C-support Alterations	148
5.3.5.	Loading Results.....	150
5.3.6.	Bearing sample results	152
	Dry Tests	154
	Wet Tests.....	156

5.3.7. Microscopy Imaging	158
5.4. Discussion.....	162
Chapter 6.....	165
6.1. Introduction	165
6.2. Miniature PM Linear Thermal Test Rig.....	166
6.2.1. Test Programme	167
6.2.2. Results Comparison.....	169
Stationary Test Results.....	169
Stationary to reciprocating testing.....	171
Resistive and Thermal Data Comparison.....	173
6.2.3. Discussion	174
6.3. 5 kW C-GEN Prototype Thermal Tests.....	175
6.3.1. Test Programme	178
No load and Load Testing	178
6.3.2. Thermal Data Comparison	181
6.3.3. Discussion	184
6.4. Marine Protection	186
Chapter 7.....	188
7.1. Approach	188
7.2. Discussion.....	190
7.3. Contribution to Knowledge	191
7.4. Recommendations for Future Work	192
Appendix A	195
Appendix B.....	197
Appendix C	200
Appendix D	207
Appendix E.....	219
References	222

List of Figures

Figure 2-1. Left. Professor James Blyth vertical axis wind turbine. Right Charles F. Bush 12kW horizontal axis wind turbine generator [7] [8]	6
Figure 2-2: Left Putnam-Smith 1 MW AC wind turbine. Right: Gedser wind turbine in 1956 at Vester Egesborg, Denmark [11] [8].....	7
Figure 2-3: Offshore wind turbine growth and future predicted developments. Created with data from [18] [19] [20] [21] [22] [23] [24] [25].....	8
Figure 2-4. Diagram of a tidal mill [33].....	9
Figure 2-5. Diagram of a modern tidal barrage. Source Encyclopedia Britannica 2008	10
Figure 2-6. Potential wind resource: Qualitative evaluation of global wind speeds at 100m above displacement height [43]	13
Figure 2-7. Horizontal and vertical axis wind turbine configurations [44].....	14
Figure 2-8. Example of a wind turbine power curve, indicating wind speeds required for rated operation	15
Figure 2-9. Three blade offshore HAWT installed wind farm, Sheringham Shoal Wind Farm, North sea [46]	15
Figure 2-10. Two blade Nenufar VAWT offshore concept [48].....	16
Figure 2-11. Global cumulative installed wind capacity 2001-2016 [17]	18
Figure 2-12. Global cumulative installed offshore wind capacity 2011-2016 [17] ...	18
Figure 2-13. Average size of offshore wind farm projects (MW) [26].....	19
Figure 2-14. Average installed offshore turbine rated capacity [26]	19
Figure 2-15. Estimated reduction in cost of energy as turbine ratings increase [50].	20
Figure 2-16. Global Cumulative Offshore Wind Capacity (MW) January 2017 [17] [26].....	20
Figure 2-17. Particle movement within waves and the definition of deep water, transitional water and shallow water waves. Adapted from [59].....	23
Figure 2-18. Estimate of global wave power levels [63]	25
Figure 2-19. Wave power resource off the coast of Scotland. Data averaged from a ~ 11 year period presented in kW/m [65].....	25

Figure 2-20. Water depth (m) of the northwest European shelf [66]	26
Figure 2-21. Distribution of wave developers in the world 2017 [69].....	27
Figure 2-22. Distribution of Wave Developers according to Wave Device Types, 2017 [69]	28
Figure 2-23. Pelamis wave attenuator device [57]	28
Figure 2-24. Seabased Point Absorber device [71].....	29
Figure 2-25. The Anaconda bulge wave WEC [72]	29
Figure 2-26. An example of an OWC device, Oceanlinx [73].....	30
Figure 2-27. Aquamarine’s Oyster OWSC device [74]	30
Figure 2-28. An example of an overtopping WEC device, Wavedragon [75].....	30
Figure 2-29. AWS submerged pressure differential device [76]	31
Figure 2-30. Example of a rotating mass device, Wello Penguin [72]	31
Figure 2-31. Internal topology of the Wello Penguin Rotating Mass device [77]	31
Figure 2-32. Tidal period and strength as given by the aliment of the sun and moon [70]	32
Figure 2-33. Global tidal Energy Estimates [78]	33
Figure 2-34. Distribution of tidal developers in the world, 2017 [79]	34
Figure 2-35. Distribution of Tidal Developers according to Tidal Device Type, 2017 [79]	35
Figure 2-36. Example of a horizontal axis tidal turbine installation [80]	35
Figure 2-37. Vertical axis tidal turbine topology [81]	36
Figure 2-38. Example of an Oscillating Hydrofoil topology [80].....	36
Figure 2-39. OpenHydro ducted device [82]	36
Figure 2-40. Jupiterhydro Archimedes screw device [83]	37
Figure 2-41. Tidal kite topology from Deep Green, Minesto [84].....	37
Figure 2-42. Various PTO methods for offshore renewable resources. Adapted from [61] [92].....	39
Figure 2-43. Identified rated power applicability ranges for various drive train options. Adapted from [93]	40
Figure 2-44. Drive train efficiencies of various drive train designs [94]	40
Figure 2-45. Damaged gear teeth on a wind turbine gearbox [96]	41

Figure 2-46. Left: Single stage planetary helical gearbox topology. Right: Multi stage planetary helical gearbox topology [99]	42
Figure 2-47. Two stage planetary gearbox, Adwin and Winenergy [100].....	42
Figure 2-48. Torque splitting between four electrical generators on the 2.5 MW Clipper Liberty Wind turbine [97]	43
Figure 2-49. Cascade gear, mechanical linear-rotary power take off [103].....	44
Figure 2-50. Cutaway of Pelamis 2 joint and power take off [105].....	45
Figure 2-51. Hydraulic Drive Train. Source Mitsubishi Heavy Industries, Ltd. [111]	46
Figure 2-52 Direct-Drive wind turbine, ENERCON E-82 [112].....	47
Figure 2-53. Survey of 800 failed wind turbine generators [118].....	49
Figure 2-54 Typical journal bearing abrasive rates [123].....	51
Figure 3-1. Fixed Speed Squirrel cage induction generator machine based electrical generation system [124]	52
Figure 3-2. Variable resistance control of the wound rotor induction generator [124]	53
Figure 3-3. Doubly fed induction machine based electrical generation system [124].....	53
Figure 3-4. Variable speed control with fully rated power converter [124]	54
Figure 3-5. Comparison of physical size between a 36.5 MW conventional induction motor and a 36.5 MW High Temperature Superconducting motor [127] [128].....	56
Figure 3-6. Layout of outer rotor iron-cored surface-mounted RFPM generator with NdFeB permanent magnets on outer rotor drum [130].....	58
Figure 3-7. An example of multi-pole buried magnet radial flux machine [131].....	58
Figure 3-8. Slotted surface-mounted AFPM machines. (a) one rotor and one stator [132], (b) one rotor and two stators [133], (c) two rotors and one stator [134]	59
Figure 3-9. A slot-less TORUS machine [135].....	59
Figure 3-10. Air-cored axial flux with double sided surface mounted permanent magnet rotor, Boulder Wind Power [136].....	60
Figure 3-11. Radial flux air-cored machine with surface mounted permanent magnets [137].....	60
Figure 3-12.(a) Surface mounted. (b) Buried magnet transverse flux machines [138]	61

Figure 3-13. A rotary claw pole machine, showing one phase.	62
Figure 3-14. Forces acting on a radial flux electrical machine	63
Figure 3-15. (a) Structural loading and moment due to applied gravitational forces on an asymmetric machine topology. (b) Shear stress & (c) normal component of Maxwell stress acting on a radial flux machine or linear machine	63
Figure 3-16. Heike Kamerlingh Onnes in his Leiden laboratory, circa 1911. [148] .	69
Figure 3-17. The critical temperature (T_c) of superconductors against their discovery. Adapted from [151] [152] [153] [154] [155]	70
Figure 3-18. Three dimensional boundary of the superconducting state. Created based on [160]	71
Figure 3-19. Temperature against electrical resistance for conductors and superconductors indicating the effect of critical temperature, T_c , for a superconductor. Created based on [160]	72
Figure 3-20. Phase diagram of a perfect non superconducting conductor, a Type I superconductor and a Type II superconductor when field B_a is applied during various external conditions. Created based on [156]	73
Figure 3-21. Simplified magnetic phase diagram of a Type I and Type II superconductor showing the Meissner region and mixed flux states. Altered from [163]	75
Figure 3-22. Current Superconducting elements and elements which form superconducting composite compounds [164]	76
Figure 3-23. a) A BSCCO tape architecture. b) Material and filament impurities causing an undulating current path [171]	77
Figure 3-24. Schematic of a YBCO tape architecture [172]	78
Figure 3-25. Left: Example of the cross-sectional architecture of a MgB_2 SC wire. Right: (a) Schematic illustration of a two strand cable indicating the twist pitch T_p and the half twist pitch, $1/2 T_p$. (b) Part of the one meter cable composed by a Cu core and 18 MgB_2 strands [175]	78
Figure 3-26. YBCO, BSCCO and copper wire price (€/kAm) projection from 2014 [164]	79
Figure 3-27. Schematics of five common cryo-cooler systems [177]	80

Figure 3-28. Efficiency of small cryo-coolers as a percentage of the Carnot cycle [177]	80
Figure 3-29. Map of cryo-cooler applications indicating the numerous applications for superconducting technology [177]	82
Figure 3-30. Mass comparison between current geared and direct drive wind turbine technology and proposed superconducting generator technology. Based on details provided in [164]	85
Figure 3-31. Left. External detail of Suprapower modular cryostat and cryo-cooler design [191]. Right. Internal detail of Suprapower modular cryostat and cryo-cooler design [192]	86
Figure 3-32. Schematic of cooling cycle for the Superpower project [193]	86
Figure 3-33. Suprapower's 10MW superconducting generator structure [195]	87
Figure 3-34. Left. Sectional machine in situ for testing. Right. A one quarter model of the section for 3D electromagnetic analysis [196]	88
Figure 3-35. Cross section Schematic of INNWIND 10 – 20 MW turbine generation system and nacelle King-Pin layout [198]	89
Figure 3-36. Potential superconducting generator topologies [199]	90
Figure 3-37. Variations of torque with superconducting tape area per pole for a 7m diameter SC generator [199]	90
Figure 3-38. Right foreground. Envision GC-1 Turbine, Thyborøn, Denmark. Courtesy of Ecoswing [53]	92
Figure 3-39. Illustration of a fully superconducting wind turbine generator [208]	93
Figure 3-40. Proposed transverse flux superconducting machine structure. a) Main magnetic flux direction through the claw-pole rotor (axial cross-section view). b) Main magnetic flux direction through the inner and outer stator (vertical cross-section view) [209]	95
Figure 3-41. Double sided claw pole machine topology, cut away [164]	95
Figure 3-42. Double sided claw pole machine topology, top view [164]	96
Figure 3-43. Left: C-Core topology with flux path indicated around neodymium iron boron (NdFeb) magnets [117]. Right: Adjacent stacked C-Core topology [210]	97
Figure 3-44. An explanation of C-Gens radial topology, assembly and modularity	98

Figure 3-45. Left: 1 MW C-GEN axial flux multi-stage rotary machine. Right: C-Gen air cored stator module installation [211]	99
Figure 3-46. Left: 20 kW C-GEN rotary machine and test rig. Centre. 15 kW C-GEN rotary machine. Right: Wind turbine installation of 15 kW C-GEN machine [117]	100
Figure 3-47. 50 kW C-GEN linear generator prototype and test rig [212]	100
Figure 4-1. Basic indicative topology of the linear claw pole machine prototype...	102
Figure 4-2. Left: a) ISO & b) Top view formed laminated field core. Right: c) ISO & b) Top view simplified laminated field core	103
Figure 4-3. Epoxy impregnated linear machine components.....	104
Figure 4-4. Cracked epoxy test sections. Left: Clear PC6159 epoxy resin. Right: Blue PC5308 epoxy resin. Details in Appendix B.....	104
Figure 4-5. Left. Laminated claw pole construction. Right. Armature and field cores prior to vacuum resin impregnation	105
Figure 4-6. Front view of linear claw pole prototype active topology including bearings	106
Figure 4-7. Isometric view of the linear claw pole prototype active topology including bearings	106
Figure 4-8. Side view of the linear claw pole prototype	106
Figure 4-9. Assembled linear prototype	107
Figure 4-10. Position of loads applied to field core (Top) and claw pole (bottom) for initial static investigation. Green shows supporting fixture, red indicates attraction forces and central large arrow indicates gravitational force	108
Figure 4-11. Structural deflection of the linear prototypes components over increasing field coil excitation.....	109
Figure 4-12. Structural deflection of the linear prototypes field core and mid-point of the translator structure	110
Figure 4-13. End profile of linear guide roller bearings. (a) Balanced load profile when installed at 0 degrees. (b) Unbalanced load profile creating moments and unsymmetrical bearing loads when installed at 90 degrees from vertical.....	111
Figure 4-14. Maximum linear force required to move the translator.....	111
Figure 4-15. Schematic of search coil locations on claw pole to investigate flux linkage	112

Figure 4-16. Airgap flux density plotted against field current for both top and bottom airgaps	113
Figure 4-17. Simulated FEA airgap flux densities as calculated for the linear prototype in [164].....	113
Figure 4-18. HTS coil topology as supplied by GE Power Conversion, Rugby.....	114
Figure 4-19. Altered field core topology for HTS field coil. (a) Front view showing lamination profile and stainless steel bolt configuration. (b) Isometric view showing reinforced solid stainless steel bar supports installed within the structure of the field core. (c) Top view showing support bars installed in parallel to the field core laminations	115
Figure 4-20. Altered claw pole topology. Left: Individual claw pole. Right: Claw pole translator assembly.....	116
Figure 4-21. Structural testing results for field core, maximum deflection is highlighted in red and is equal to 0.085 mm	116
Figure 4-22. Small vacuum chamber with liquid nitrogen circulation pipes connecting to the HTS coil cold head connections. Fiberglass (Green) and ceramic (Yellow) supports maintain rigidity for the cryogenic pipes and HTS coil while separating cold and warm areas.....	117
Figure 4-23. Liquid Nitrogen bath and coil support designed by MEng Student Patryk Radyjowski.....	117
Figure 4-24. Vacuum chamber and associated cryogenics and vacuum pumps describing the indicative experiment set up required.....	118
Figure 4-25. Linear HTS claw pole prototype placed within vacuum chamber	119
Figure 4-26. Left: position of a vacuum proof actuator motor for testing. Right: Incorporation of coil and supporting structure into machine design.....	119
Figure 4-27. Assembled linear HTS claw pole prototype machine	120
Figure 4-28, Proposed 30 KW claw pole HTS generator structure, including cryostat and stationary HTS field coil	121
Figure 4-29. Left: Proposed 5 – 10 MW electrical topology. Right: Altered topology for 30 kW prototype	122
Figure 4-30. The variation of Maxwell stress with flux density	123
Figure 4-31. Example of compression strut design [213].....	124

Figure 4-32. Left: Rotor structure with armature core highlighted in red. Right: Claw pole structure with claw poles highlighted in red	124
Figure 4-33. Claw pole structure indicating loads and total deflection	125
Figure 4-34. Rotor structure indicating loads and axial deflection	125
Figure 4-35. Complete 30 kW prototype machine including cryostat, HTS field winding, armature coils and support structure	126
Figure 4-36. Left: Potential structure for an axial flux configuration. Right: Proposed structure for a radial flux configuration [143] [164]	127
Figure 4-37. Proposed design of a 10 MW radial flux claw pole HTS connected to an indicative wind turbine drive train, hub and rotor blades	128
Figure 4-38. The active electromagnetic topology with indicated flux path	129
Figure 4-39. Left: 3D representation of the claw poles, red arrows indicate the direction of magnetic attraction. Right: 3D representation of active electrical components ..	130
Figure 4-40. Left: Cross section of stator structure. Right: Cross section of rotor section. Forces and fixtures are indicated	132
Figure 4-41. Stator structure simulation, cooler colours indicate areas of low stress	133
Figure 4-42. Stator structure simulation, sections removed and simulation re run..	133
Figure 4-43. Stator simulation, further sections removed. Simulation re run and yield stress observed to insure structural cohesion	134
Figure 4-44. Projections for offshore generator size including trend lines. Blue trend line for HTS trends and grey dotted trend line based on Bang et al [143] mass estimations for DDPG. Red circle indicates the placement of the 10 MW machine presented in this study	134
Figure 5-1. An example of a high speed radial bearing test rig for the rail industry [217]	137
Figure 5-2. Submerged 3x2m point absorber, indicating a full generation stroke of in shallow water.....	139
Figure 5-3. Stribeck curve illustrating the build-up of the hydrodynamic film on a journal bearing. Zn/P is the hydrodynamic parameter of the material [123]	141
Figure 5-4. Bearing material samples with corresponding reference.....	141

Figure 5-5. Linear bearing test rig c shaped supporting clamp with installed bearing samples. Arrows indicate order and placement of bearing sample pads.....	142
Figure 5-6. Bearing pad dimensions	143
Figure 5-7. Simplified linear bearing test rig	143
Figure 5-8: Constructed linear bearing test rig. Left: Completed rig including actuators connected to the piston carriage. Right: The fabricated c-support with Type III test samples.....	144
Figure 5-9. Critical bearing test rig components. Left: External. Right: Internal....	144
Figure 5-10. Damage to L bracket connecting piston to load carriage	147
Figure 5-11. Proposed improved piston load carriage topology, including ball joint and load cell with reinforce L bracket connection.....	147
Figure 5-12. Installed improved piston load carriage topology, including ball joint and load cell with reinforce L bracket connection.....	148
Figure 5-13. Improved linear bearing test rig c-support topology with sprung bearing pads. Spring locations shown in green	149
Figure 5-14. Left: Abrasion to bearing surface caused by metal shards from damaged guide rail. Right: Two damaged bearing guide rails	149
Figure 5-15. Spring coefficient vs experimental data	150
Figure 5-16. Friction force during 0.5 ms^{-1} operation.....	151
Figure 5-17. Friction force during 0.6 ms^{-1} operation.....	151
Figure 5-18. Bearing pad surface wear from initial tests before sprung bearing pads were employed. (A) Type I (B) Type II (C) Type III, (1) New pad; (2) Pad B surface wear; (3) Side view of pad B wear.....	154
Figure 5-19. Distance vs mass lost for dry bearing operation.....	155
Figure 5-20. Extrapolated bearing data for dry tests indicating high wear rates with increased line gradient.....	155
Figure 5-21. Type II. (A1) New Pad (A2) Pad B Surface Wear after 350km (A3) Side View of Pad B Surface Wear	156
Figure 5-22. Distance vs mass lost for wet bearing operation	156
Figure 5-23. Extrapolated bearing data for wet tests indicating high wear rates with increased line gradient.....	157

Figure 5-24. Wear rates over the samples during testing, solid for dry testing, and shaded for wet testing.....	157
Figure 5-25. Sample I before testing. Top: Machined bearing pad. Bottom Left and Right: Irregular surface produced during machining	158
Figure 5-26. Sample II before testing. Top: Machined bearing pad. Bottom Left and Right: Surface images	159
Figure 5-27. Sample III before testing. Top: machined bearing pad. Bottom Left and Right: Surface images	159
Figure 5-28. Sample IV after 50 km salt water testing. Top: Bearing pad showing wear. Bottom Left and Right. Break in wear from guide rail	160
Figure 5-29. Microscopy of sample I after 150km dry testing. Top: Bearing pad showing wear. Bottom Left and Right: Imaging taken from scorched area	160
Figure 5-30. Microscopy of sample II after 150km. Bottom Left and Right: Indicating embedded particles.....	161
Figure 5-31. Microscopy of sample III after 150km. Bottom Left and Right: Indicating a scored surface	161
Figure 6-1. Small linear machine stator topology	166
Figure 6-2. Left: Construction of small linear machine within a stainless steel tank. Right: Small linear machine flooded with artificial sea water	167
Figure 6-3. Three coil epoxy potted translator blade sample, CAD assembly.....	167
Figure 6-4. Test rig samples. Left to right: Epoxied coils with gaps, fully epoxied coils, enamelled coils.....	168
Figure 6-5. Testing equipment and samples. Left to right: Power source, variable resistor, sample coils and ammeter	169
Figure 6-6. Enamelled coils, 3 A/coil. The final temperatures of the potted surfaces are highlighted.....	170
Figure 6-7. Epoxied coils with gaps, 3 A/coil. The final temperatures of the potted surfaces are highlighted.....	170
Figure 6-8. Epoxied coils, 3 A/coil. The final temperatures of the potted surfaces are highlighted.....	170
Figure 6-9. Movement with 4 Amps excitation per coil	171
Figure 6-10. Movement with 6 Amps excitation per coil	172

Figure 6-11. Movement with 8 Amps excitation per coil	172
Figure 6-12. Enamelled coils submerged in water, 8 Amps per coil	173
Figure 6-13. Epoxied coils with gaps submerged in water, 8 Amps per coil	174
Figure 6-14. Epoxied coils submerged in water, 8 Amps per coil.....	174
Figure 6-15. Left: 5 kW linear C-GEN prototype topology. Right: Linear test rig with C-GEN linear prototype installed within a water tank.....	176
Figure 6-16. Cut through view from top indicating (1) linear actuators, (2) surrounding tank, (3) translator, (4) permanent magnets (black) and support structure (silver) and (5) linear journal bearing arrangement.....	177
Figure 6-17. Translator velocity profile. Acceleration 0.4 ms^{-2} , max velocity 0.4 ms^{-1}	178
Figure 6-18. Dry no load voltage test results, maximum velocity 0.4 ms^{-1}	178
Figure 6-19. Flooded no load voltage test results, maximum velocity 0.4 ms^{-1}	179
Figure 6-20. Three phase current output with related velocity profile with a 20 Amp load per phase and a maximum velocity of 0.4 ms^{-1}	179
Figure 6-21. Peak power per phase and total peak power output of the machine, indicating the difference in wet to dry operation	180
Figure 6-22. 5 kW linear C-GEN prototype installed and operating with a flooded airgap.....	181
Figure 6-23. Coil temperature varying over time at a maximum velocity of 0.3 ms^{-1} and a peak current of 12 Amps per phase. Dotted lines indicate trend of graph	182
Figure 6-24. Coil temperature varying over time at a maximum velocity of 0.3 ms^{-1} and a peak current of 13.5 Amps per phase. Dotted lines indicate trend of graph ..	182
Figure 6-25. Coil temperature varying over time at a maximum velocity of 0.3 ms^{-1} and a peak current of 15 Amps per phase. Dotted lines indicate trend of graph	183
Figure 6-26. Coil temperature varying over time at a maximum velocity of 0.5 ms^{-1} and a peak current of 18 Amps per phase. Dotted lines indicate trend of graph	183
Figure 6-27. Coil temperature varying over time at a maximum velocity of 0.5 ms^{-1} and a peak current of 22 Amps per phase. Dotted lines indicate trend of graph	184
Figure 6-28. Coil temperature varying over time at a maximum velocity of 0.5 ms^{-1} and a peak current of 24.5 Amps per phase. Dotted lines indicate trend of graph ..	184

Figure 7-1. The alteration of the bearing test rig to include a second compressed air actuator in order to improve bearing testing and machine performance.....	193
Figure 7-2. Addition of a stepper motor to the 5 kW test rig in order to simulate wave loads as calculated in chapter 5	194
Figure A-1. Normalised failure rates and downtimes for geared generators ≥ 1 MW wind turbines [88]	195
Figure A-2. Normalised Failure Rates and Downtimes for Direct Drive Wind Turbines [88]	196
Figure D-1. Horizontal forces at bottom of stroke, wave loading case 1	207
Figure D-2. Momentum about z_m at bottom of stroke, wave loading stroke case 1	207
Figure D-3. Horizontal forces at top of stroke, wave loading data case 1	208
Figure D-4. Momentum about z_m at top of stroke, wave loading data case 1	208
Figure D-5. Horizontal forces at bottom of stroke, wave loading data case 2	209
Figure D-6. Momentum about z_m at bottom of stroke, wave loading data case 2....	209
Figure D-7. Horizontal forces at top of stroke, wave loading data case 2	210
Figure D-8. Momentum about z_m at top of stroke, wave loading data case 2.....	210
Figure D-9. Horizontal forces at bottom of stroke, wave loading data case 3	211
Figure D-10. Momentum about z_m at bottom of stroke, wave loading data case 3..	211
Figure D-11. Horizontal force at top of stroke, wave loading data case 3	212
Figure D-12. Momentum about z_m at top of stroke, wave loading data case 3	212
Figure D-13. Horizontal forces at bottom of stroke, wave loading data case 4	213
Figure D-14. Momentum about z_m at bottom of stroke, wave loading data case 4..	213
Figure D-15. Horizontal force at top of stroke, wave loading data case 4	214
Figure D-16. Momentum about z_m at bottom of stroke, wave loading data case 4..	214
Figure D-17. Horizontal forces at bottom of stroke, wave loading data case 5	215
Figure D-18. Momentum about z_m at bottom of stroke, wave loading data case 5..	215
Figure D-19. Horizontal force at top of stroke, wave loading data case 5	216
Figure D-20. Momentum about z_m at top of stroke, wave loading data case 5	216
Figure D-21. Horizontal forces at bottom of stroke, wave loading data case 6	217
Figure D-22. Momentum about z_m at bottom of stroke, wave loading data case 6..	217
Figure D-23. Horizontal force at top of stroke, wave loading data case 6	218
Figure D-24. Momentum about z_m at top of stroke, wave loading data case 6	218

Figure E-1. Enamelled coil translator, submerged in water, 4A per coil.....	219
Figure E-2. Epoxy potted coil translator with gaps, submerged in water, 4A per coil	219
Figure E-3. Epoxy potted coil translator, submerged in water, 4A per coil	220
Figure E-4. Enamelled coil translator, submerged in water, 6A per coil.....	220
Figure E-5. Epoxy potted coil translator with gaps, submerged in water, 6A per coil	220
Figure E-6. Epoxy potted coil translator, submerged in water, 6A per coil	221

List of Tables

Table 2-1. Largest wind turbines currently installed for testing/commercial operation [55]	21
Table 2-2. Power available from various wind speeds [56]	22
Table 2-3. Total failures and downtimes per turbine per year for various wind turbine drive train topologies [88]	39
Table 3-1. Typical parameters and cost for commercially available superconductors [176]	79
Table 3-2. Illustration of the amount of power required to remove 1W at specific operating temperatures [166]	81
Table 3-3. Suprapower's 10 MW and scaled demonstrator specifications [191]	87
Table 3-4. Specifications for a 7m diameter 10 MW, a 7m diameter 20 MW (20MW-I) and an 11m diameter 20 MW (20MW-II) SC generators [199]	91
Table 3-5. Comparison of an air cored SC machine and a homopolar synchronous machine for a 5 MW, 230 rpm motor design [164]	94
Table 4-1 Linear claw pole prototype specifications, full electrical design provided in Keysan [164]	107
Table 4-2. Induced voltage and flux measurements from an applied AC field current, maximum 2.42 A at 50 Hz [164]	112
Table 4-3. Operational data for copper field winding and HTS field winding	114
Table 4-4. Specification of 30 kW HTC claw pole transverse flux prototype	122
Table 4-5. 10 MW HTS claw pole generator specifications	129
Table 5-1. Sea states values and occurrences provided by a WES device developer with the calculated applied forces/moments	140
Table 5-2. Test samples physical properties	142
Table 5-3. Details of test rig design components	145
Table 5-4. S Summary of Type I and II experimental results	152
Table 5-5. Summary of Type III and IV experimental results	153
Table 6-1. Specifications of smaller linear machine windings per translator sample	166

Table 6-2. Linear generator specifications.....	176
Table 6-3. Peak load data collected from the load cells during prototype testing ...	180

Abbreviations

AC	Alternating Current
DC	Direct Current
AD	Anno Domini
R&D	Research and Development
HAWT	Horizontal Axis Wind Turbines
VAWT	Vertical Axis Wind Turbines
LCoE	Levelized Cost of Energy
CAPEX	Capital Expenditure
O&M	Operation and Maintenance
RPM	Rotations per Minute
WEC	Wave Energy Convertor
PTO	Power Take Off
OWC	Oscillating Water Column
OWSC	Oscillating Wave Surge Converter
TEC	Tidal Stream Energy Convertor
HPTO	Hydraulic Power Take Off
DD	Direct Drive
DDPMG	Direct Drive Permeant Magnet Generator
SCIG	Squirrel Cage Induction Generator
DFIG	Doubly Fed Induction Generator
PMG	Permeant Magnet Generator
IG	Induction Generator
HTS	High Temperature Superconductor
LTS	Low Temperature Superconductor
SC	Superconductor

RMS	Root Mean Square
RFPMG	Radial Flux Permeant Magnet Generator
AFPMG	Axial Flux Permeant Magnet Generator
TFM	Transverse Flux Machine
TF	Transverse Flux
MMF	Magnetomotive Force
DOF	Degree of Freedom
YBCO	Yttrium Barium Copper Oxide
BSCCO	Bismuth Strontium Calcium Copper Oxide
MgB ₂	Magnesium Diboride
COP	Coefficient of Performance
TRL	Technology Readiness Levels
SMC	Soft Magnetic Composite
FEA	Finite Element Analysis
GE	General Electric Ltd
MLI	Multi Layer Insulation
UMP	Unbalanced Magnetic Pull
NdFeB	Neodymium-Iron-Boron
EESG	Electrically Excited Synchronous Generator

Nomenclature

Symbol	Unit	Description
P	W	Power
P_w	W	Power available from wind
P_T	W	Power in turbine shaft
P_{mech}	W	Mechanical power
P_{Elec}	W	Electrical power
ρ_{air}	kg/m ³	Density of air
ρ_{water}	kg/m ³	Density of water
A	m ²	Area
v	ms ⁻¹	Velocity
ω_{rpm}	rpm	Rotational velocity
a	ms ⁻²	Acceleration
g	ms ⁻²	Acceleration due to gravity
r	m	Radius
D	m	Diameter
C_p	-	Turbine power coefficient
v_{tip}	ms ⁻¹	Turbine blade tip velocity
λ	-	Turbine blade tip speed ratio
E	Wm ⁻²	Wave energy density
A	m	Wave amplitude
H	m	Wave height
H_s	m	Significant wave height
T	s ⁻¹	Wave period
T_e	s ⁻¹	Energy period
ω	rads ⁻¹	Wave angular frequency

c_g	-	Group velocity of waves
λ	m	Wavelength
η	-	Drive train efficiency
\mathcal{C}	W	Constant electrical losses
L	W	Linear electrical losses
Q	W	Quadratic electrical losses
T	Nm	Torque
F	N	Force
I	A	Electrical current
V	V	Electrical voltage
R	ohm	Electrical resistance
$\cos\phi$	-	Power factor
σ	Nm ⁻²	Shear stress
B	T	Magnetic flux density
K	W	Electric load
l	m	Machine core length
μ_0	H/m	Magnetic permeability of free space
q	Nm ⁻²	Maxwell stress tensor
F _g	N	Force due to gravity
m	kg	Mass
P _w	W	Copper losses
t	s	Time
J	J	Joule
F _{bmp}	N	Balanced magnetic pull
F _{ump}	N	Unbalanced magnetic pull
e	m	Rotor eccentricity
g	m	Airgap Length
A _g	m ²	Airgap area
B _g	T	Airgap flux density

L	m	Axial length
B_{rem}	T	Remnant flux density
h_m	m	Magnet height
l_g	m	Concentric airgap length
P	-	Number of pole pairs
θ	deg	Angular coordinate
T_{cog}	Nm	Cogging torque
W_{fld}	H	Energy stored within a magnetic field
Z_{allow}	$^{\circ}$	Torsional deflection
H_c	Am^{-1}	Permanent magnet field intensity
Φ	Wb	Magnetic flux
T_c	K	Critical temperature
B_c	T	Critical magnetic field strength
J_c	Amm^{-2}	Critical current density
T_m	$^{\circ}C$	Melting temperature
V	m^3	Volume
P	Atm	Pressure
Q	-	Number of stator slots
J_s	Amm^{-2}	Stator current density
C_m	-	Inertia coefficient
C_d	-	Drag coefficient
F_{Tot}	N	Total force on buoy
M_{Tot}	Nm	Total moment acting at point
K	Nm^{-1}	Spring coefficient
P	Pa	Pressure

Chapter 1.

Motivation

1.1. Introduction

Since the advent of the industrial revolution, global energy requirements have increased exponentially, with the global energy consumption in 2016 estimated to be more than 152000 TWh [1]. As the global population has more than quadrupled in size since the beginning of the twentieth century [2], from 1.6 billion in 1900 to more than 7.4 billion people in 2017, the requirement for energy is estimated to increase by up to 48% by 2040 [3]. Fossil fuels have provided a compact, transportable, chemical store of solar energy. However, increasing concerns over high CO₂ production, increasing global temperatures, resource availability and energy security, have forced countries to look elsewhere for their energy demands. Over the last 20 years the focus on renewable energy has gripped the world like never before. Technological, environmental, socioeconomic and political changes have led to high investment and growth within the renewable sector [4]. Technologies such as hydro power, solar and onshore wind are now well established, however for sustained growth to continue in other sectors to produce a diverse global renewable energy portfolio, newer technologies must become competitive against more “traditional” sources of energy production. For renewable sources such as offshore wind, wave and tidal, this means increased efficiencies and technological development.

1.2. Summary & Aim of Thesis

This thesis focuses on direct drive power generation from offshore renewable sources. The nature of the offshore environment is notably inhospitable and difficult to access, therefore high reliability, modularity and survivability are key to providing an effective power extraction system.

Geared power take-off systems suffer from low reliability for high torque offshore shore installations and require regular maintenance in order to operate efficiently.

Direct drive systems offer a reliable alternative to geared systems. With higher power transfer efficiencies (up to rated speeds), fewer complex components required for energy transfer and the ability to operate at low velocities, direct drive machines seem well suited to offshore energy extraction. However, for offshore installation, their large size means that transportation and installation costs are high, especially for wind turbine installations, while for wave and tidal energy extraction bearing failures and survivability are major concerns.

The aim of this thesis is to provide solutions to these three main issues in order to facilitate the use of direct drive generator technology in the offshore energy industry. Further details of the contents of this thesis are presented in the next section.

1.3. Outline of Thesis

This thesis has been divided into 7 chapters, the contents of which are described as follows:

Chapter 2 presents the history of offshore renewable generation techniques including offshore wind, wave and tidal devices. Current devices are discussed and a selection of suitable power take off topologies presented with the aim of understanding the current requirements for the offshore renewable energy. Finally, systems and components required for reliable energy extraction are proposed.

Chapter 3 presents electrical generation systems suitable for renewable energy extraction. The chapter focuses on direct drive machines, including the operational loads that are associated with this type of generation system. Superconducting machines are introduced and the technology explained as an alternative to traditional direct drive topologies. A high temperature superconducting machine topology and a permanent magnet machine topology is explained for use in later chapters.

Chapter 4 details the progress made on the construction of a linear and rotary high temperature superconducting machine and proposes a structure for a 10 MW rotary superconducting machine topology. The main focus of this chapter is the construction of structures suitable for direct drive superconducting machines, with the ultimate aim of producing a low mass direct drive system for offshore wind.

Chapter 5 proposes the use of polymer journal bearings in offshore devices, especially for tidal and wave power take off systems. The design and construction of a linear bearing test rig is presented and a simple wave study detailed for the purposes of defining machine loading data. Data gathered from the testing of a selection of polymer bearing samples is discussed and the testing process is compared to the theoretical wave loadings.

Chapter 6 examines the premise of running a permanent magnet machine with a flooded airgap in order to increase the thermal performance of the machines windings for both wave and tidal power take off systems. The design and build of a small linear test rig is detailed and the results from dry and flooded tests for various coil samples is presented. The experimental process is then be detailed for coil testing within a 5 kW permanent magnet linear generator and test rig topology. The results from both test rigs are compared and a short description of marinisation is provided.

Chapter 7 concludes the thesis and provides information on the knowledge gained as well as proposals for future work.

1.4. Publications

Journal Papers

M. A. Mueller, J. W. Burchell, Y. C. Chong, O. Keysan, A. McDonald, M. Galbraith, “Improving the Thermal Performance of Rotary and Linear Air-Cored Permanent Magnet Machines for Direct Drive Wind and Wave Energy Applications”, IEEE Transactions on Energy Conversion, TEC-00122-2018.R1, Jul. 2018.

N. J. Baker, M. A.H. Raihan, A. A. Almoraya, J. W. Burchell, M. A. Mueller, “Evaluating Alternative Linear Vernier Hybrid Machine Topologies for Integration into Wave Energy Converters”, IEEE Transactions on Energy Conversion, TEC-00013-2018, Jul. 2018.

P. Radyjowski, O. Keysan, J. Burchell, and M. Mueller, “Development of a superconducting claw-pole linear test-rig”, Supercond. Sci. Technol., vol. 29, no. 4, p. 44002, Apr. 2016.

Conference Papers

J. Burchell, N. Ahmed, J. I. Barajas-Solano, M. Mueller, M. Galbraith, “Project Neptune: Critical Component Tests for a Fully Flooded Direct-Drive Linear Generator for Wave Energy Convertors”, AWTEC, Taipei, Sept. 2018.

J. Burchell, M. Mueller, “Marinised Bearings for Offshore Generators”, The 9th International Conference on Power Electronics, Machines and Drives, PEMD, Liverpool, Apr. 2018.

J. Burchell, O. Keysan, M. Mueller, “Proposed Structure for a HTS Generator for Direct Drive Offshore Wind Turbines”, EWEA, Barcelona, Mar. 2014.

J. Burchell, O. Keysan, M. Mueller, “The Advantages of a High Temperature Superconducting Direct Drive Transverse Flux Generator Design”, Superconducting4Energy, Paestum, May 2014.

J. Burchell, O. Keysan, P. Radyjowski, M. Mueller, “Proposed Electrical and Mechanical Topology for a 30kw HTS Prototype Transverse Flux Generator”, Grand Renewable Energy, Toyko, Jul. 2014.

O. Keysan, J. Burchell, M. Mueller, “Magnetic and Structural Analysis of a Transverse Flux Claw Pole Linear Machine”, IEEE ICIT, Cape Town, Feb 2013.

O. Keysan, J. Burchell, M. Mueller, “Towards More Reliable and Cost Effective Superconducting Generators for Wind Turbines”, PEMD, Manchester, 2014.

O. Keysan, J. Burchell, M. Mueller, “A Novel Superconducting Generator Concept for a Successful Entry to the Offshore Renewable Energy Market”, Superconducting4Energy, Paestum, May. 2014.

1.5. Animation and video links

Due to the large amount of testing and simulation contained within this thesis, a selection of animations and video links have been made available in order to provide an indication of scale of the project.

1. Animation detailing the structure critical parts of a 10MW direct drive superconducting claw pole generator within a wind turbine topology - <https://drive.google.com/open?id=122cD8L1WtfqDAa2J6MdSdEiUUfEh5g5f>
2. Animation providing an example of the structural optimisation carried out in Solidworks Finite Element Analysis software for a 10MW direct drive superconducting claw pole generator structure - <https://drive.google.com/open?id=1J7kpjzt3HX9YhIKTTvKsbIMGzBr1HMQY>
3. Video of large linear machine test rig during operation and linear bearing test rig during operation – https://drive.google.com/open?id=1r1laaAXUJRa8X_E7HDMPP1Py_GWRKG_D6
4. Video of large linear machine test rig during operation - https://drive.google.com/open?id=1r1laaAXUJRa8X_E7HDMPP1Py_GWRKG_D6

Chapter 2.

Offshore Renewable Energy Technology

2.1. Wind Energy: A brief History

Wind energy has been harnessed by humans for thousands of years, from applications in food production, to recreation such as kites, to intercontinental travel. In the last few centuries the concept of wind turbines as recognised today took shape, utilising the kinetic energy of the wind to provide mechanical power for industrial and farming practices. With the invention of electric generation technology in the 19th century, the first wind powered electric generators were installed in Scotland and the United States of America within a year of each other. Scottish Professor James Blyth installed a vertical axis wind turbine generator by July 1887, to charge early batteries for lighting purposes [5]. While in the winter of 1887, Charles F. Bush installed a 12kW horizontal axis wind turbine generator for the supply of electricity in Cleveland Ohio [6].

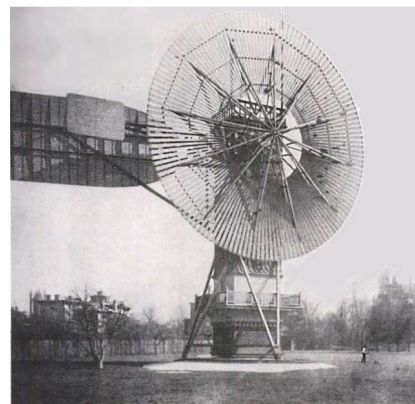
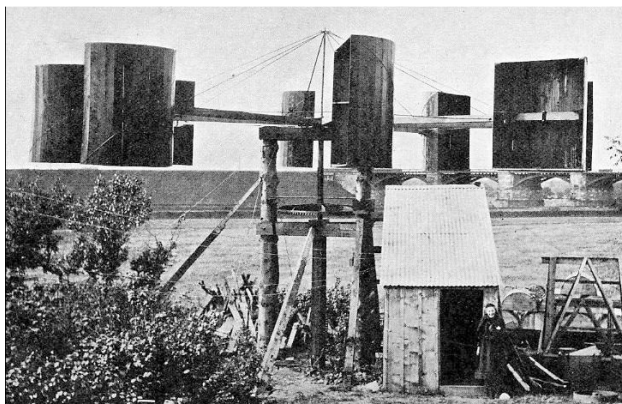


Figure 2-1. Left. Professor James Blyth vertical axis wind turbine. Right Charles F. Bush 12kW horizontal axis wind turbine generator [7] [8]

In the following decades many more small turbines were produced for rural and remote areas, with outputs ranging from 5-25 kW. The first turbine capable of electrical generation over 1 MW was developed in the 1940's by P. Putnam on Grandpa's Knob, Vermont, and supplied the local grid with AC power. The turbine only operated for 4 years, however it was decades before another MW turbine was developed [9].

In addition various European countries started to develop turbines in the early 20th century, advancing from 25 kW turbines to the Danish 200 kW Gedser mill turbine by the 1960s [10] . These early wind turbine developments are shown in Figure 2-1 and Figure 2-2.

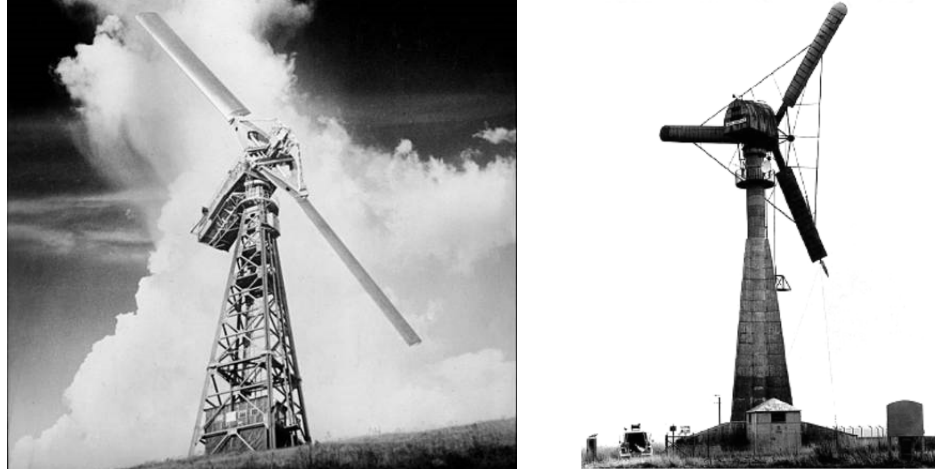


Figure 2-2: Left Putnam-Smith 1 MW AC wind turbine. Right: Gedser wind turbine in 1956 at Vester Egesborg, Denmark [11] [8]

With an increase in cheap hydrocarbon energy production and the connection of rural areas to a reliable centralised electricity supply, turbine development was slow and it wasn't until the early 1970s oil crisis that wind turbine technology benefitted from a leap in global research and development [12]. Over the next decade technological advancements were made in the US and Europe driven by tax breaks and high oil costs however when the price of oil dropped in the 1980's, wind technology became too expensive and development slowed [13].

The second leap for the wind turbine industry came in the late 1990's when global action was called for to reduce harmful fossil fuel emissions and address climate change, to create sustainable energy sources for an increasing global energy demand and to curtail foreign energy dependencies [14], [15]. The incremental steps that had improved wind turbine technology since the 1970's meant that wind was the most mature and globally available renewable technology by the end of the twentieth century. In the last two decades wind power generation has been growing by an average 23.5% per year, [16], with a global installed capacity estimated at almost 487 GW by the end of 2016 [17].

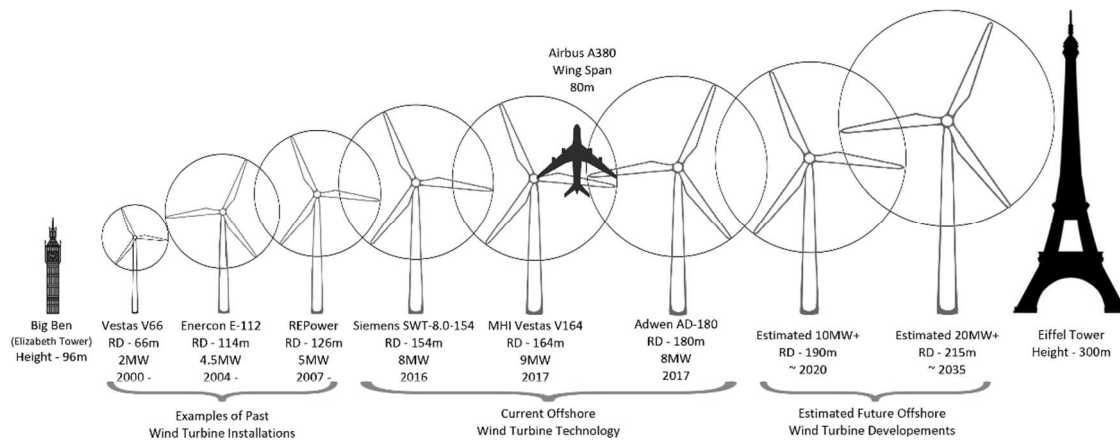


Figure 2-3: Offshore wind turbine growth and future predicted developments. Created with data from [18] [19] [20] [21] [22] [23] [24] [25]

The maturity of the onshore wind energy market stimulated the next leap for the technological development of wind turbines, the offshore market. The average offshore wind turbine size by the end of 2016 was 4.8 MW [26] and within the next few years the offshore wind market is due to install multiple 8 MW and test 10 MW wind turbines in European waters [21], [22], [27], as indicated in Figure 2-3. Onshore turbines are limited in size due to resource and structural constraints resulting from friction coefficients creating turbulent and limited wind resources. Maximum estimates of 3 – 4 MW turbines are suitable for onshore arrays [24]. Offshore wind has been growing globally over the last decade especially within northern European countries which have a well-established onshore wind presence and access to offshore sites. The major driving factors include a higher and more reliable offshore wind resource, a lack of viable onshore sites and an increased difficulty of passing planning applications [27]. The offshore wind environment has the potential to increase the capacity factor of a wind farm to almost 50%, in line with the average for small scale conventional power plants, and which is a 10-15% increase compared to onshore wind farm capacity factors. With a more constant and reliable wind resource, offshore wind could reach up to 84% of the Betz's limit, the maximum efficiency available from wind energy extract. With the ability to realise average energy extraction rates of more than 3000 hours at full load per year compared with less than 2000 hours per year for onshore, the offshore wind industry can afford the increase in costs that the offshore environment requires [28].

The first offshore wind farm was deployed by Denmark in the early 1990's utilising 11 turbines with a total array rating of 4.95 MW [29], within 25 years the installation of individual offshore wind turbines capable of producing almost double the rating of the original array have been realised [21]. Future advancements in wind turbine technology aim to produce bigger and more efficient offshore arrays. The EU funded Upwind and INNWIND projects are focusing on turbines up to 20 MW utilising Superconducting generation and novel materials, while the University of Virginia, backed by the U.S Department of Energy, are investigating turbine blades with the capability of producing 50 MW offshore machines [24]. The next stage of research and development will push materials and generation techniques further than before, and although such research projects may not fully fulfil the original goals, the advancements in scientific knowledge will undoubtedly make their way into commercial use, [30] [14] [31] [32].

2.2. Marine Energy: A brief History

Wave and Tidal energy have, in some form, been exploited by humans for hundreds of years. The history of tidal energy extraction dates back to tide mills in Europe developed around 8th century AD. Energy was harnessed by creating an enclosed basin or tidal pond which would fill as the tide rose. The water was then trapped creating a head of water which could be released through water mill technology as the tide waned [33], Figure 2-4 .

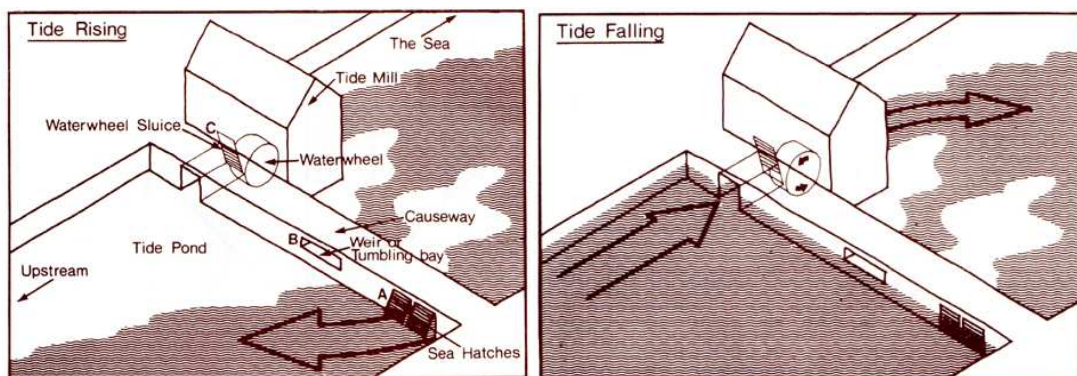


Figure 2-4. Diagram of a tidal mill [33]

This concept lasted hundreds of years, with small scale mills installed around the world until the 19th century, when the idea was picked up for electrical generation. However

large scale tidal basin schemes require high infrastructure costs, therefore it wasn't until the 1960's that the first tidal power plant was successfully funded and constructed in La Rance Estuary, France. The La Rance station has been active for over 40 years with an installed generation capacity of 240 MW generating an estimated 540 GWh/y [34], [35] . Although basins and barriers such as La Rance use the tidal resource, they are more akin to pumped hydro storage, a general topology for these installations is provided in Figure 2-5. In addition, the environmental concerns over large construction projects near shore have enthused developers to consider placing devices in the tidal current. The notion to utilise tidal current by placing energy convertors within the stream has only become a reality since the end of the 20th century.

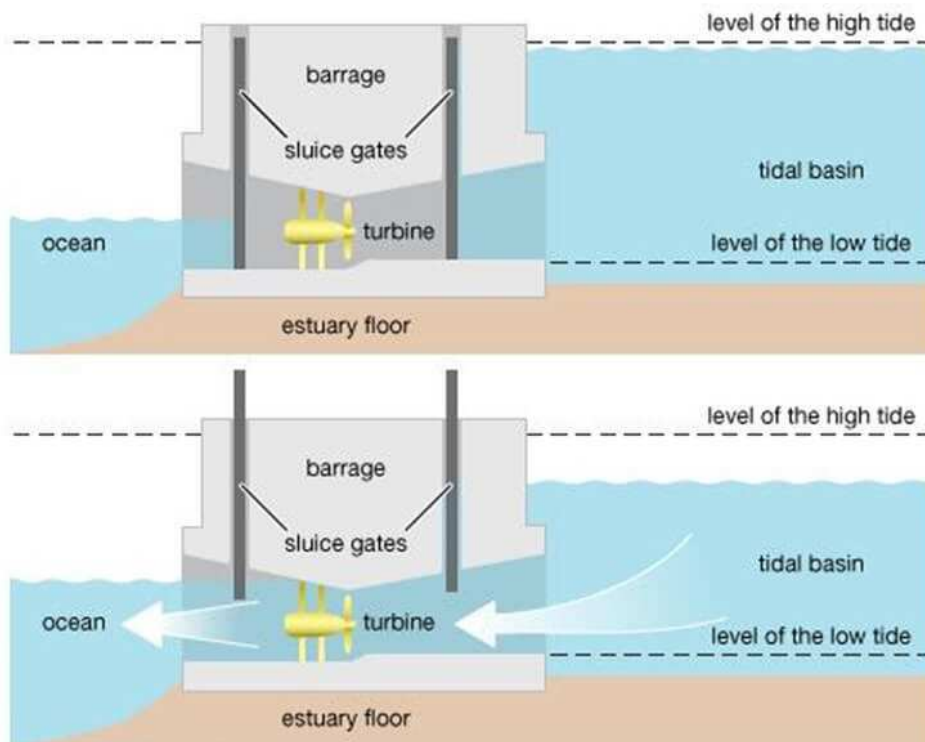


Figure 2-5. Diagram of a modern tidal barrage. Source Encyclopedia Britannica 2008

In the early 1990's the most documented attempt to extract tidal stream energy was conducted in the Scottish West Highlands. The project used a moored turbine suspended by cables in the tidal flow, but it wasn't until the turn of the 21st century that other topologies were ready for field tests [35]. In contrast over 1000 patents have been filed for wave energy devices since 1799 [36], when the first patent was filed by French Engineer, Pierre-Simon Girard.

Girard noted that “the enormous mass of an ocean liner... responds to the slightest wave motion. If... one imagines this ship suspended from the end of a lever, one will conceive the idea of the most powerful machine which has ever existed” [37]. Based on this observation Girard patented a device consisted of a lever with one end connected to the shore and the other connected to a float resting on the sea. As the float moved with the waves, pumps on land transferred the motion into usable energy. In 1909, wave power converters were harnessed to provide harbour lighting, providing the first installed electrical power generation from waves. However in the following centuries since Girard’s patent, there have been a handful of wave devices that have successfully captured energy from waves during sea trials’, these are detailed by Konstantinidis et al [36], Hammons [38], Bryden et al [39] and Pelc et al [40].

Although interest spiked during the 1970’s oil crisis, similar to wind, wave technology stagnated between the end of the 1980’s and beginning of the 20th century with a lack of funding and an unwillingness to share data in order to avoid repeating research [38]. Similar to wind, wave and tidal were both considered as alternative sources of energy after the 1970’s oil crisis [41], however unlike on shore wind, the extremely hostile offshore environment has curtailed the advancement of technologies [42]. Additionally, the R&D that secured the most efficient energy extraction topologies has been completed for wind whereas it is ongoing in relation to offshore tidal and wave devices. In order to improve the standing of marine energy, trusted and robust devices must be produced and therefore further investigations into effective, durable power take offs would allow the industry to plug in to tried and tested marinised technology.

2.3. Offshore Renewable Energy Resource

There are three distinct environments for marine renewable power generation devices.

- Shoreline devices which are based on land and generate power captured from offshore based resources.
- Near to shore, deployed in shallow water. 10 -20 meters depth.
- Offshore, deployed in deep water, 60+ meters depth, far from shore.

Offshore wind and wave power generation both promise high outputs when deployed in open waters since both wind and wave resources contain substantially greater energy

further from the coast. Tidal power generation requires installation relatively near shore to take advantage of the interaction of the tidal cycles with land masses. However, the real challenges to offshore power generation are the development of reliable near shore to far offshore devices. Therefore, this thesis will focus on offshore power generation as onshore generation techniques are not as hindered in construction or reliability.

2.3.1. Offshore Wind

Wind is created by the transfer of solar energy to the earth's atmosphere by direct radiation or by the indirect radiation absorbed via heat sinks such as bodies of water or the earth's surface. By warming the atmosphere, the sun causes the air to expand and rise as it become more buoyant. As warm air rises it causes low pressure which pulls cooler air to replace it. The flow of air pockets from one region to another produces winds with speeds that vary due to the pressure differentials between the warm and cool regions of air.

Global air currents are created by large scale solar warming and cooling, where warm air flows to the poles and mixes, cooling, becoming denser and sinking to produce pockets of high pressure. The global currents create weather and seasonal variations, the wind available for energy extraction is a mixture of local topology, friction variables, seasonal effects and these global currents. The strength and availability of wind offshore is greater and less turbulent than that found onshore since no landmass topologies block access or reduce net power due to friction. Figure 2-6 indicates the global mean wind speeds, highlighting the effect of land masses have on wind speeds. The overarching message suggested by the figure is the high potential wind resource available for offshore devices compared to onshore devices, with many coastal and onshore regions half the mean speed of offshore environments.

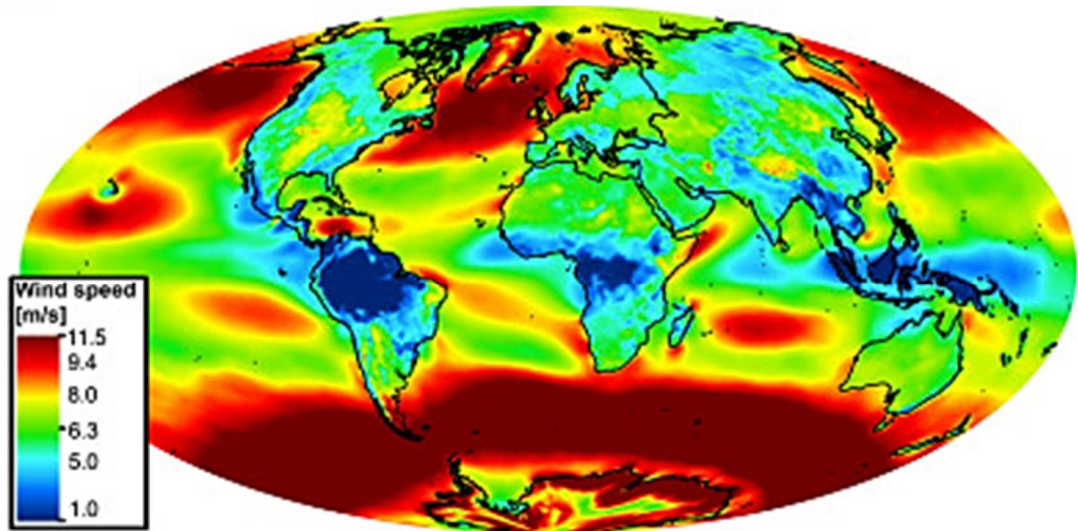


Figure 2-6. Potential wind resource: Qualitative evaluation of global wind speeds at 100m above displacement height [43]

Wind turbines utilise rotor blades to harness the kinetic energy present in wind. As the air moves over the surface of the blade, a pressure differential is formed creating lift. The lift forces the blade to move, creating torque as it rotates around the central drive shaft of the turbine. The rotation of the drive shaft transfers the mechanical energy through a gearbox or directly to the generator where it is converted into electrical energy. Large wind turbines generally produce low rotational velocities with high torque, which often require a gearbox to convert to high-speed rotation and low torque for power generation. The energy available from the wind, P_w , is proportional to the cube of its velocity, v , the density of air, ρ_{air} , and the turbines swept area, A , as described in Equation 2-1.

$$P_w = \frac{1}{2} \rho_{air} A v^3 \quad 2-1$$

In 1919 a physicist called Albert Betz calculated that no wind turbine can convert more than 59.3% of the available kinetic energy from the wind into mechanical energy. This theoretical maximum power efficiency is known as the Betz limit however most onshore turbines sit at efficiencies between 35-45%, with only 10-30% of the wind energy going to produce electricity once subsystem efficiencies are taken into account.

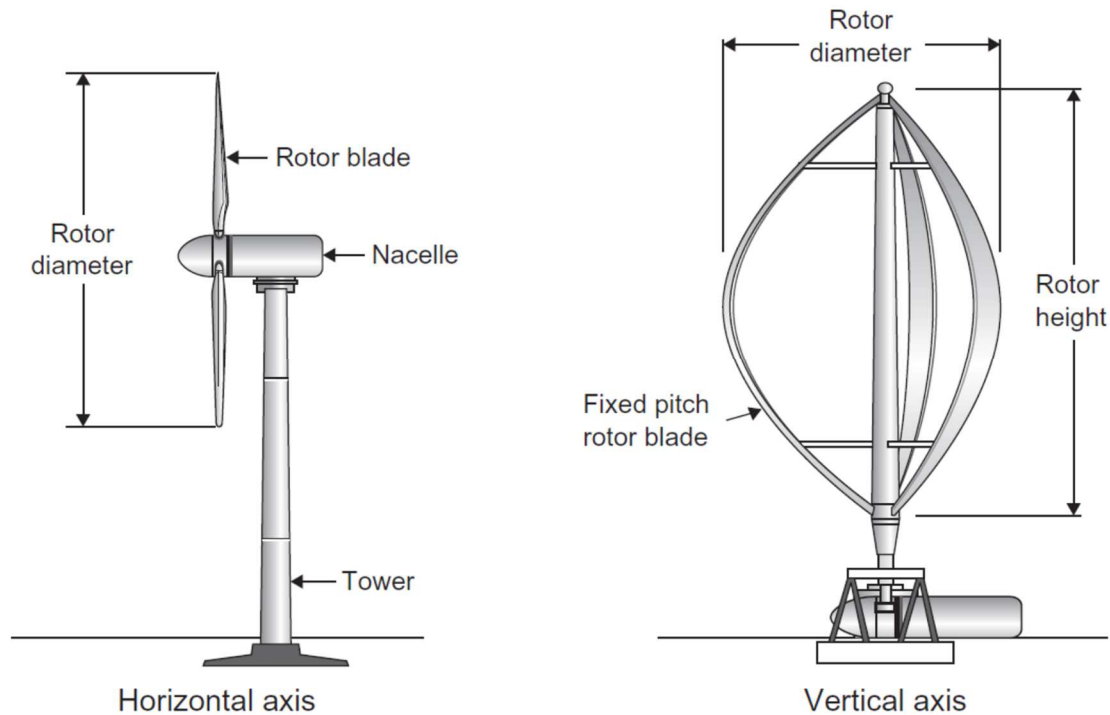


Figure 2-7. Horizontal and vertical axis wind turbine configurations [44]

Figure 2-7 provides topologies for the two main sub divisions of modern wind turbines proposed for offshore wind energy harvesting, i.e. horizontal axis and vertical axis turbines. Both types of turbines conform to specific power curves, indicating over which range of wind speeds they are capable of capturing and converting energy from the wind. An example of a wind turbine power curve is provided in Figure 2-8.

Horizontal Axis Wind Turbines

Horizontal axis wind turbines (HAWT) consists of a tower supporting a nacelle, containing a horizontal rotor shaft, power take off system, electrical generation equipment and most of the electrical and control sub systems. Attached to the nacelle is the hub and rotor blades including a pitch system to ensure efficient energy extraction at various wind speeds and protect the blades from unfavourable wind conditions. In order to position the rotor blades into the direction of the oncoming wind, a yaw system is employed to orientate the nacelle correctly [32], [45]. The yaw system is located between the tower and nacelle forming a rotatable connection enabling a full 360 degree rotation of the active elements of the HAWT.

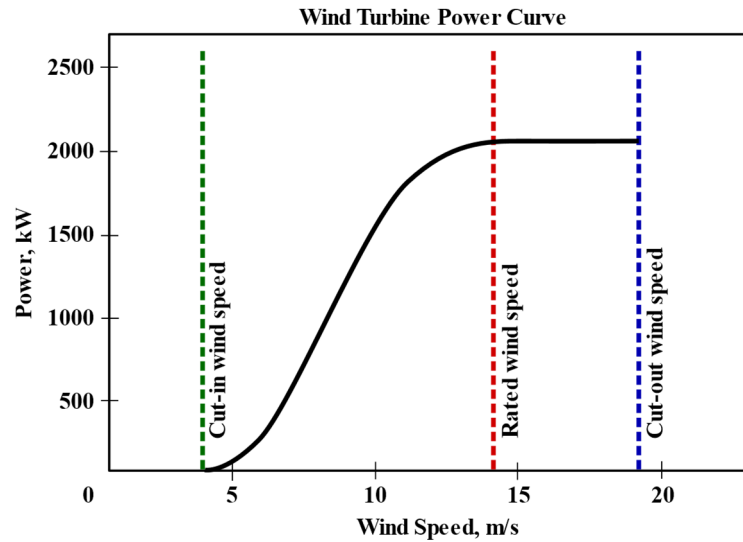


Figure 2-8. Example of a wind turbine power curve, indicating wind speeds required for rated operation



Figure 2-9. Three blade offshore HAWT installed wind farm, Sheringham Shoal Wind Farm, North sea [46]

Upwind HAWTs are the most commonly installed turbine of the two, usually utilising three rotor blades to capture energy from the wind as this has been found to be the optimum number of blades to reduce noise while maintaining energy extraction and low material usage [47].

Vertical Axis Wind Turbines

Vertical axis wind turbines (VAWT) generally comprise of a rotor shaft transverse to the direction of the wind, normally vertical, rising through a tower to a hub with blades rotating around the central hub point. The power take off, generator and electrical sundries can therefore be located at the base of the tower. The main advantages of a VAWT are the lack of a mechanical yaw system - since it harvests wind energy from any direction - a lower distribution of mass and the ability to harness lower wind speeds. However, VAWTs require more material and larger sizes to capture the same energy as HAWTs, they are generally less reliable since the distance from the bottom to the top of the rotor blades means a highly varied wind loading profile over the blade length. This leads to higher instances of material fatigue.



Figure 2-10. Two blade Nenuphar VAWT offshore concept [48]

Since the mid-nineties, HAWT have been the most successful wind turbine topology, however due to the more uniform offshore wind profile and lower friction coefficients on the ocean surface, VAWT may push the offshore advantage especially as material costs reduce with time. For both instances a combination geared power or direct power take-off can be utilised.

Since HAWT's have been developed, refined and installed offshore since before the turn of the 21st century, this report will focus on the conventional upwind three bladed horizontal axis topologies for the purposes of expanding the offshore marine energy industry. The energy extracted by a HAWT is dependent on the turbines swept area, given in Equation 2-2.

$$A = \pi r^2 \quad 2-2$$

Where r is the radius of the rotor blades from the centre of the nacelle. The usable power from the wind is based on the turbines power coefficient C_p , described as:

$$C_p = \frac{P_T}{P_w} \quad 2-3$$

Where P_T is the turbines shaft power and P_w is the power available in the wind. Thus, Equation 2-3 can be altered to Equation 2-4 for a HAWT.

$$P_T = \frac{1}{2} \pi r^2 \rho_{air} v^3 C_p \quad 2-4$$

The maximum rotational speed of a wind turbine is limited by the turbine's maximum tip speed. In order to minimise noise and curtail excessive centrifugal forces which could potentially damage the blade structures, the maximum tip speed is limited and taken into consideration when designing the turbine's operational criteria.

For large wind turbines the tip speed, v_{tip} , is set $\sim 75 \text{ ms}^{-1}$ in order that the tangential tip speed is maintained at a suitable ratio to the incoming wind speed, v , thus ensuring reasonable energy harvesting efficiencies. The blade tip speed can be calculated using equation.

$$v_{tip} = \frac{\omega_{rpm} \pi D}{60_{sec/min}} \quad 2-5$$

Where D is the diameter of the rotor and ω_{rpm} is the rotational speed of the turbine blade. To optimise turbine blade designs, a ratio of the tangential blade tip speed and wind speed is used as provided in equation.

$$\lambda = \frac{v_{tip}}{v} \quad 2-6$$

Where λ is the tip speed ratio, which varies with the power coefficient of the turbine.

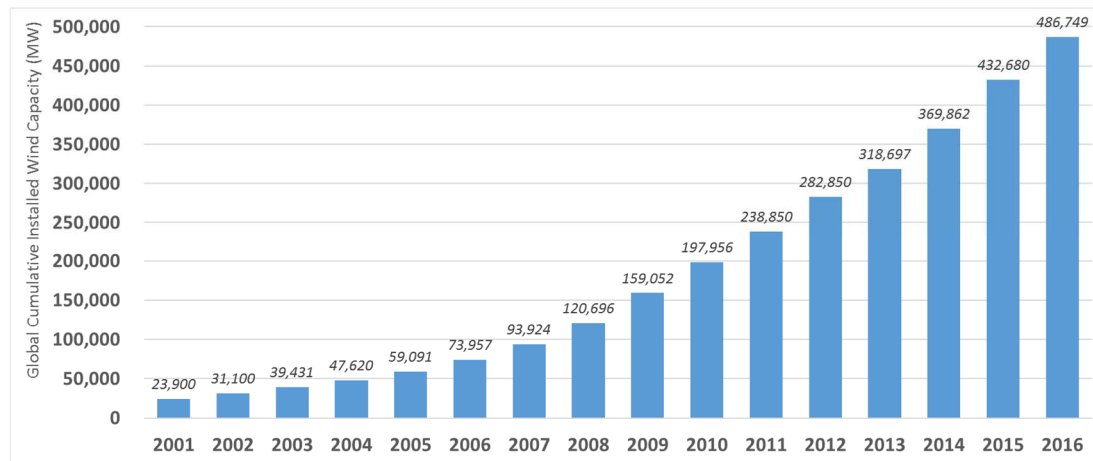


Figure 2-11. Global cumulative installed wind capacity 2001-2016 [17]

Figure 2-11 indicates the rapid growth of installed wind turbine generation capacity, almost all of which are HAWT. It is therefore no surprise that HAWT are favoured for offshore installations, being the most understood wind turbine technology available to be tailored for one of the most challenging environments on earth.

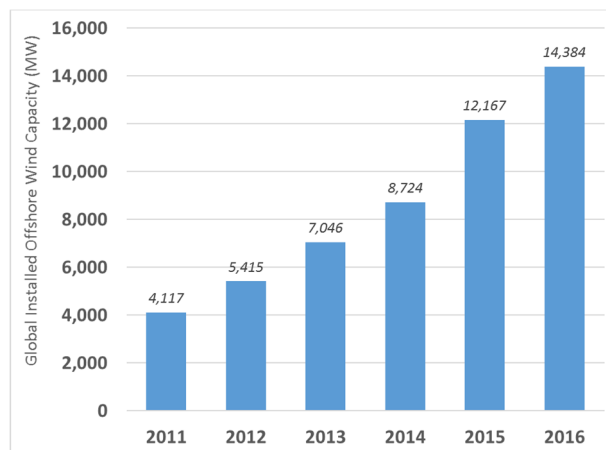


Figure 2-12. Global cumulative installed offshore wind capacity 2011-2016 [17]

Figure 2-12 indicates the increasing trend in offshore turbine installed capacity, increasing on average by 22% per annum while individual turbine capacity has increased by 62% in the last decade [26]. By 2020 it is estimated that the European offshore installed capacity will be in the region of 24.6 GW [26].

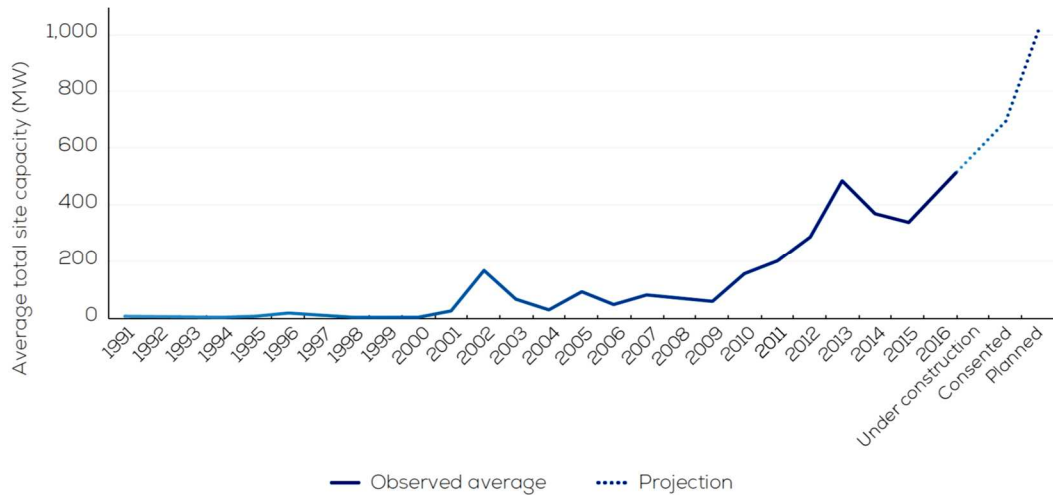


Figure 2-13. Average size of offshore wind farm projects (MW) [26]

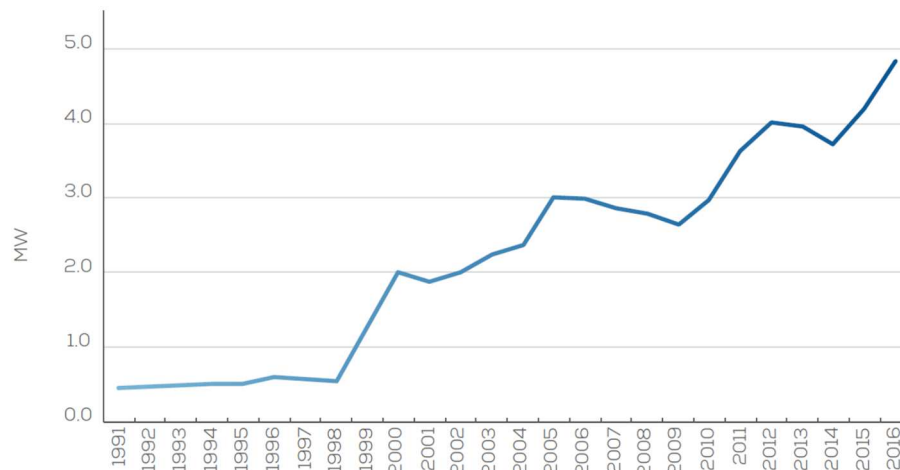


Figure 2-14. Average installed offshore turbine rated capacity [26]

Figure 2-13 indicates the trend for increasing offshore site capacity, while Figure 2-14 indicates the continuous growth in offshore turbine rated size. The main driver behind the rapid upscaling of onshore and offshore turbine technology is the reduced cost of energy that results from increasing turbine capacity [49], indicated in Figure 2-15. The growth in turbine size onshore has been curtailed for various efficiency, transportation and installation issues. The offshore landscape has fewer restrictions, with no limit currently found for maximum size restraints and the only decisive factor being the harsh marine environment, which in turn leads to the requirement for fewer turbines of larger capacity to be installed [44]. As can be seen from Figure 2-15, economies of scale mean the cost of energy decreases as turbines increase in size.

Wind turbines – Size and LCoE

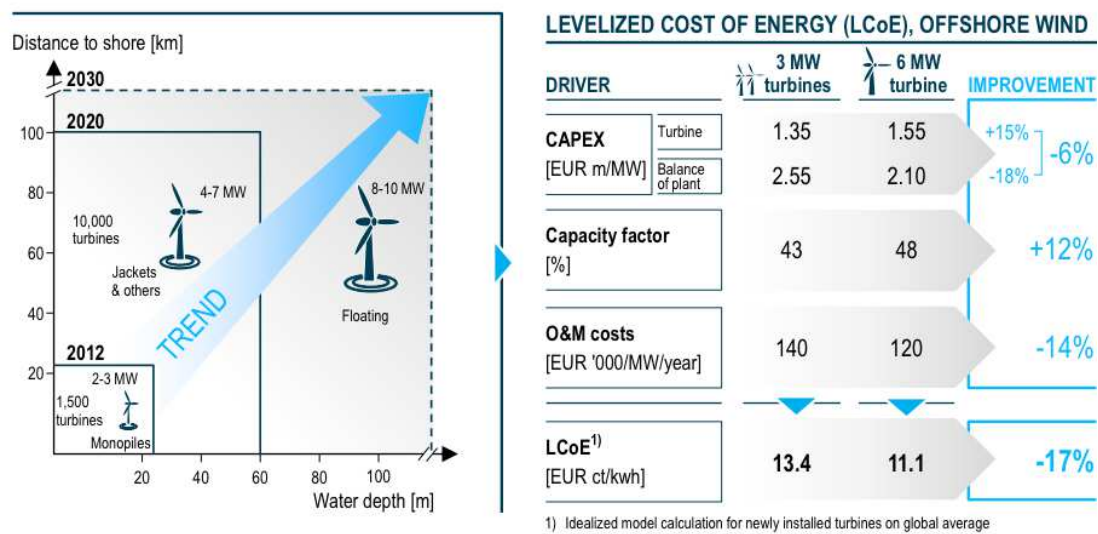


Figure 2-15. Estimated reduction in cost of energy as turbine ratings increase [50]

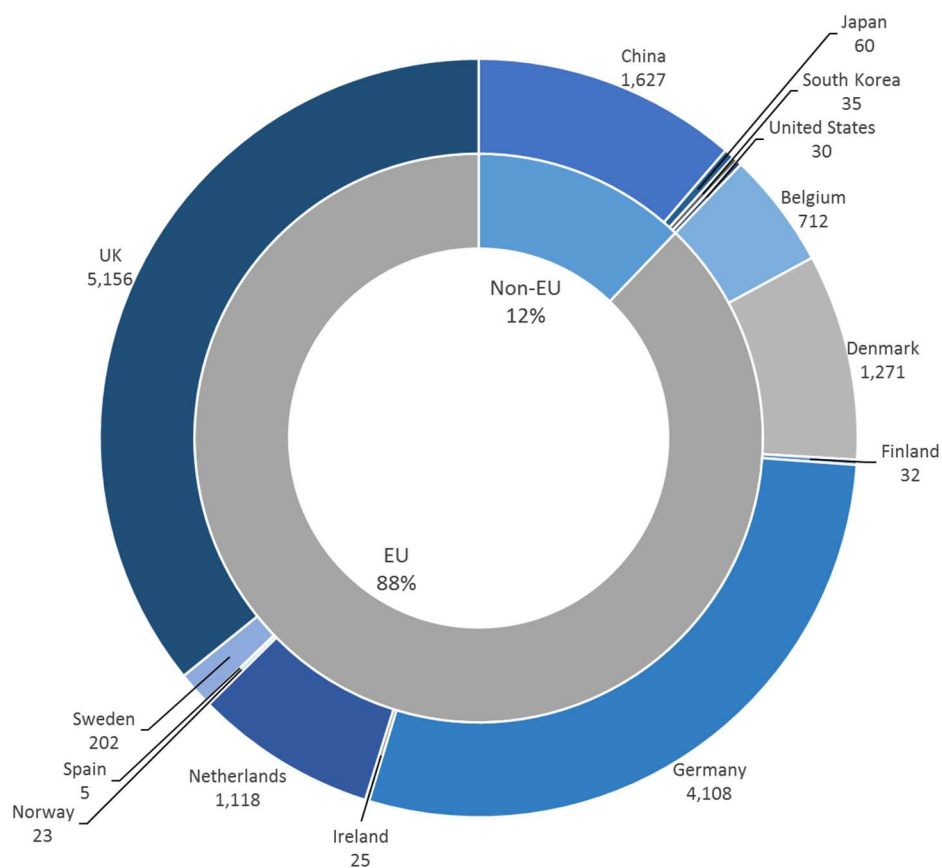


Figure 2-16. Global Cumulative Offshore Wind Capacity (MW) January 2017 [17] [26]

The largest wind turbines installed for testing and commercial use are provided in Table 2-1. Ongoing research from projects such as Suprapower [51], HTS-GEN [52], Ecoswing [53] and Sandia labs, with their 200 m wind turbine blade for a 50 MW turbine [54], and continued support from agencies such as the European Wind Energy Association, International Energy Agency and Horizon 2020, turbines are expected to continue to grow, with outputs of 10 – 20 MW for the offshore energy market not far away.

Manufacturer	Name	Size (MW)	Drive Train	Operational Location
MHI Vestas	V164	9.5	Medium Speed	Offshore
Enercon	E126	7.5	Direct Drive	Onshore
Samsung	S7.0	7	Medium Speed	Offshore
MHI	SeaAngel	7	Hydraulic	Offshore
Repower	6M Series	6	Geared	Onshore/ Offshore
Siemens	SWT-7.0	7	Direct Drive	Offshore

Table 2-1. Largest wind turbines currently installed for testing/commercial operation [55]

The installation of wind turbines in the offshore environment increases installation and O&M costs in comparison to onshore technology. The offshore environment sets the wind industry several challenges. The advent of offshore turbine installations is a recent development and supporting technologies such as barges and installation platforms are currently borrowed from the oil industry at high cost. As turbines and arrays are set to increase in size, a dedicated infrastructure of support and installation vessels must be produced to help drive down offshore costs. In addition, weather and sea conditions can add significant delays to installation, maintenance and repair times. Increasing the output of individual turbines can help reduce the cost of energy, as larger turbines should maintain higher power outputs for similar repair and maintenance down time. Additionally, as will be discussed in later chapters, increasing the modularity of turbines can also decrease down time and in recent years this has been highlighted by increased modularity in power electronics [31]. As the offshore environment offers higher wind resources, energy available to a wind turbine is proportional to the swept area of the rotor blades, therefore increasing the size of offshore turbines increases the torque acting on the drive shaft, gearbox and generator [45].

Wind Speed and Power Density at 50m		
Wind Speed (ms ⁻¹)	Wind Power Density (Wm ⁻²)	US Wind Class
0 – 5.6	0 - 200	1
5.6 – 6.4	200 – 300	2
6.4 – 7.0	300 – 400	3
7.0 – 7.5	400 – 500	4
7.5 – 8.0	500 – 600	5
8.0 – 8.8	600 – 800	6
8.8 – 11.9	800 - 2000	7

Table 2-2. Power available from various wind speeds [56]

2.3.2. Wave

Solar energy is ‘stored’ and magnified in waves via the transfer of energy from the wind. Original solar heat transfer levels of typically 100 Wm⁻² can be converted into waves with power levels of over 1000 kW per metre of wave crest [35]. Waves propagate from their origin as a transport of energy with the water particles moving in orbital motions but with very little net mass transport, drift. The fluctuating resonance between the kinetic and potential energies within the water give rise to the undulating shape of waves. The superposition of waves with different frequencies and directions results in the formation of more complex wave forms (irregular seas) with the different frequency components travelling at different speeds across the surface of the water. Waves are generally created and supported by the interaction of the wind with the surface friction of the water and these waves can travel vast distances with very little energy loss, depending on their interaction with other mediums such as shorelines or wave energy converters. Wave height is determined by wind speed, water depth and the distance (fetch) over which energy is passed from the wind to the sea surface. Although larger waves are more powerful, energy density is also determined by wave speed, wavelength and density [57].

Although wave energy has the potential to transfer vast quantities of energy, the nature of the offshore marine environment means that harnessing and predicting the potential power is extremely challenging [58]. Firstly, deep water waves are defined as occurring when the depth is larger than half of the wavelength of the travelling wave, whereas shallow water waves are defined to occur when the depth is less than 1/20th of the wavelength. Intermediate waves exist between these two defining

characteristics. Explanations of particle movement within deep and shallow water waves are provided in Figure 2-17.

From linear wave theory, the average energy density per unit surface area of deep water waves in a sinusoidal sea state can be described as proportional to the square of the wave amplitude, A , as presented in Equation 2-7.

$$E = \frac{\rho_{\text{water}} g A^2}{2} \quad 2-7$$

Where ρ is the mass density of water and g is the acceleration due to gravity.

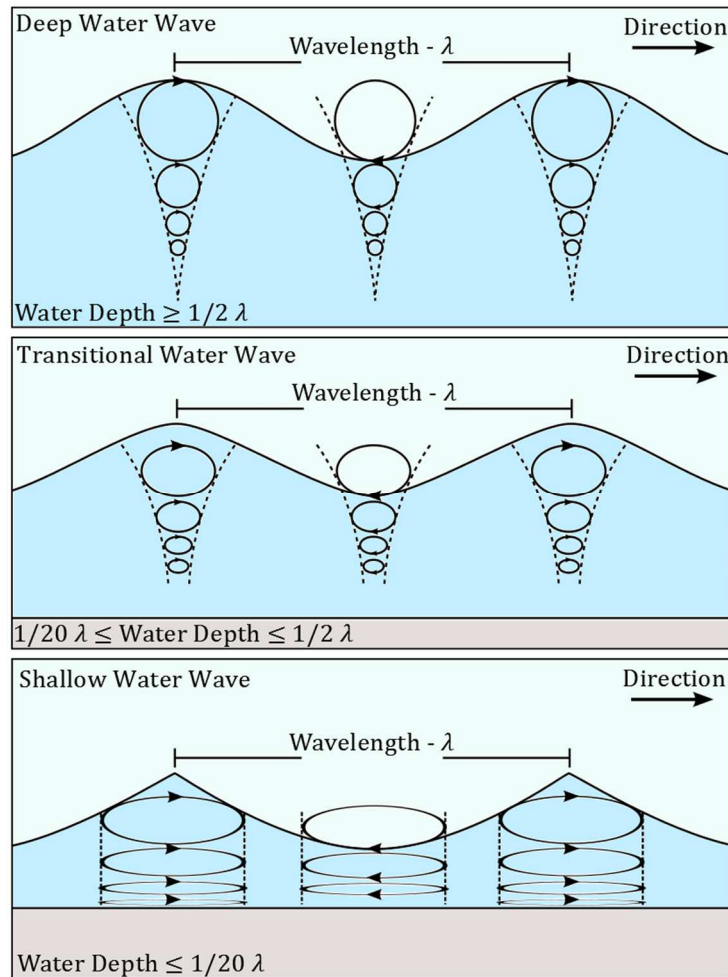


Figure 2-17. Particle movement within waves and the definition of deep water, transitional water and shallow water waves. Adapted from [59]

The energy flux, power transported per metre crest length, of deep-water waves is proportional to the wave period and the square of the wave height, H , and can be derived from the energy density of the waves as shown below.

$$P = E c_g \quad 2-8$$

$$c_g = \frac{g}{2\omega} \quad 2-9$$

Where c_g is the group velocity of the waves transporting the energy and ω is the wave's angular frequency.

$$P = \frac{\rho_{water} g^2 A^2}{4\omega} = \frac{\rho_{water} g^2 H^2 T}{32\pi} \quad 2-10$$

Where T is the wave period equal to $2\pi/\omega$, and H is the wave height, equal to two times the wave amplitude, A .

A similar expression holds for the energy flux in unidirectional irregular seas [60].

$$P = \frac{\rho_{water} g^2 H_s^2 T_e}{64\pi} \quad 2-11$$

Where H_s is the significant wave height and T_e is the energy period.

Estimates for the global wave resource power vary wildly between 1 - 30+ TW. Examples of the potential global and Scottish wave resource are presented in Figure 2-18 and Figure 2-20. Drew et al [61] cite a global power potential of 2 TW, while Gunn et al [62] estimate 2.11 TW, the World Energy Council [4] cite an energy resource of 29,500 TWh/yr (~12 TW) and Bryden et al [35] estimates that the deep water resource is between 3 – 32 TW, with potential realistic energy extraction at roughly 800 GW.

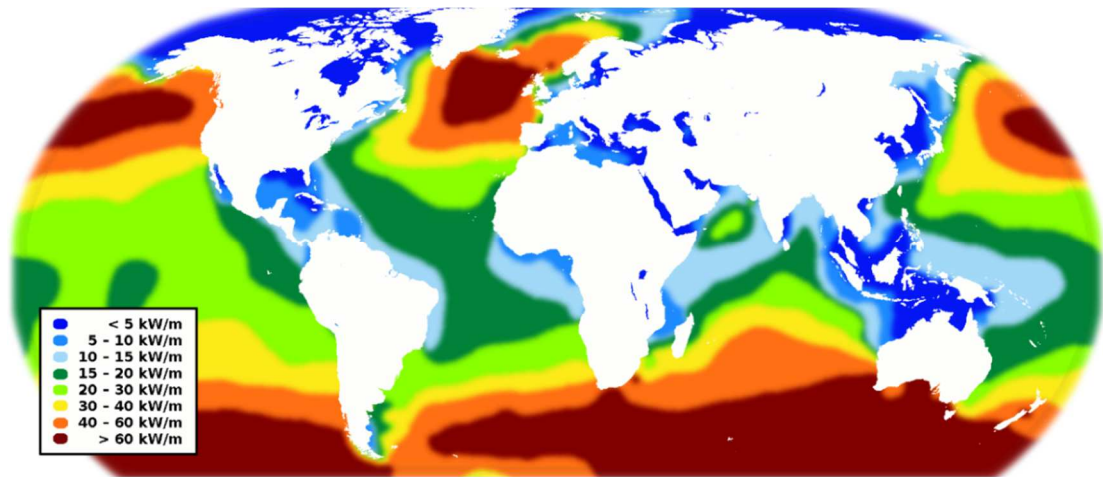


Figure 2-18. Estimate of global wave power levels [63]

However, the ability to extract the available energy depends on the efficiency and type of device installed, therefore due to the low maturity of the wave industry compared to wind, efficiencies and energy extraction limits are not so widely known compared to that of the wind and tidal industries. Although an example of the theoretical extraction limit for a heaving buoy device is provided below. In a sinusoidal sea-state, the maximum power that can be extracted by a point absorber moving in heave is that available across a wave front of length $\lambda/2\pi$, where λ is the wavelength. This is the so called Newman-Evans limit [64].

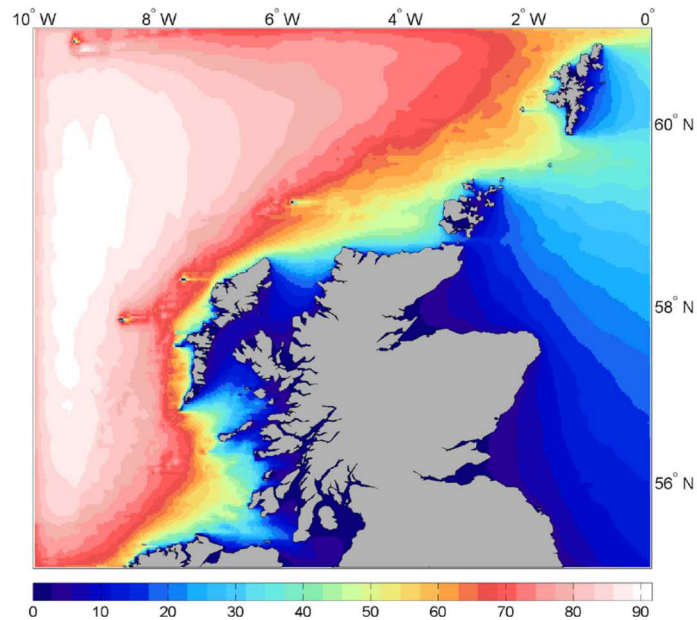


Figure 2-19. Wave power resource off the coast of Scotland. Data averaged from a ~ 11 year period presented in kW/m [65]

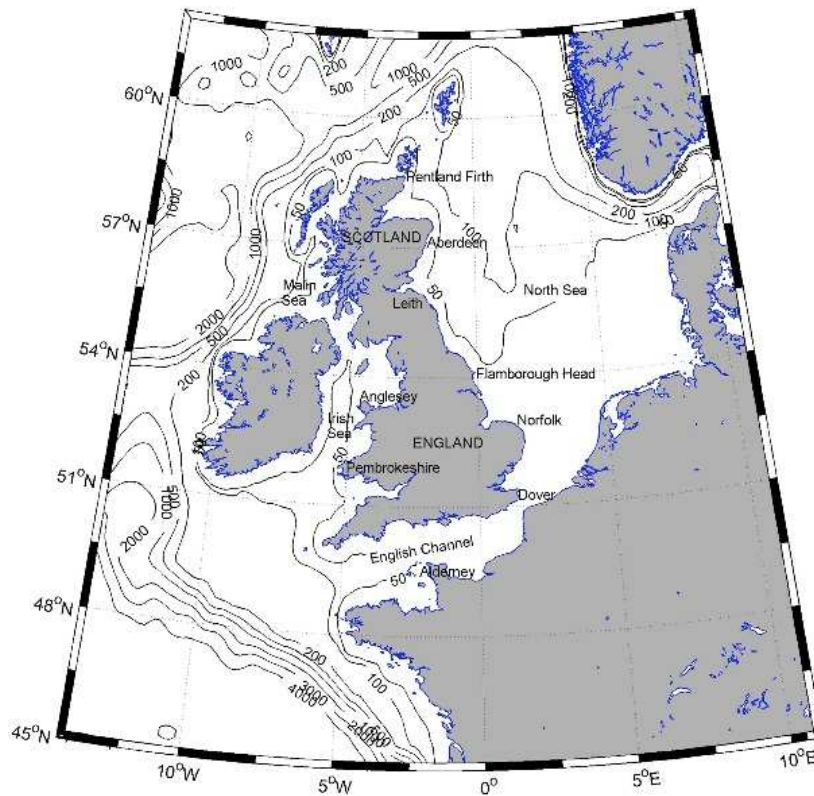


Figure 2-20. Water depth (m) of the northwest European shelf [66]

Wave Devices

A significant challenge for wave energy converter designers and manufacturers is the efficient conversion of differing wave types into useful motion to produce electricity. The height, period and orientation of waves vary greatly as do their respective power levels [61]. European waves have power levels in the region of 30-70 kW/m, however extreme waves can contain power levels of more than 2000 kW/m [67] [61].

Although rare, the structure of the device must be designed to survive these events, thus causing a balancing act whereby the day to day operation of the device must be considered in tandem with infrequent freak wave states. Survivability is the crucial design consideration for wave energy devices. Additional explanations of the factors that have provided challenges to the wave industry is provided here [68], and summarised below.

- Irregular wave amplitudes, frequencies and directions mean creating efficient power take off systems is a challenge

- Deep water waves provide the most power, however isolated far shore installations cost most and require expensive grid connections.
- The variety of wave energy devices suggested for energy harvesting has made investment and selection difficult.
- Large scalable installations are prioritised therefore the learning curve for smaller installations is damaged

The global distribution of WEC developers is provided in Figure 2-21. The figure indicates the two countries with the most wave developers are the UK and the USA, while the EU accounts for almost half of all wave developers in the world.

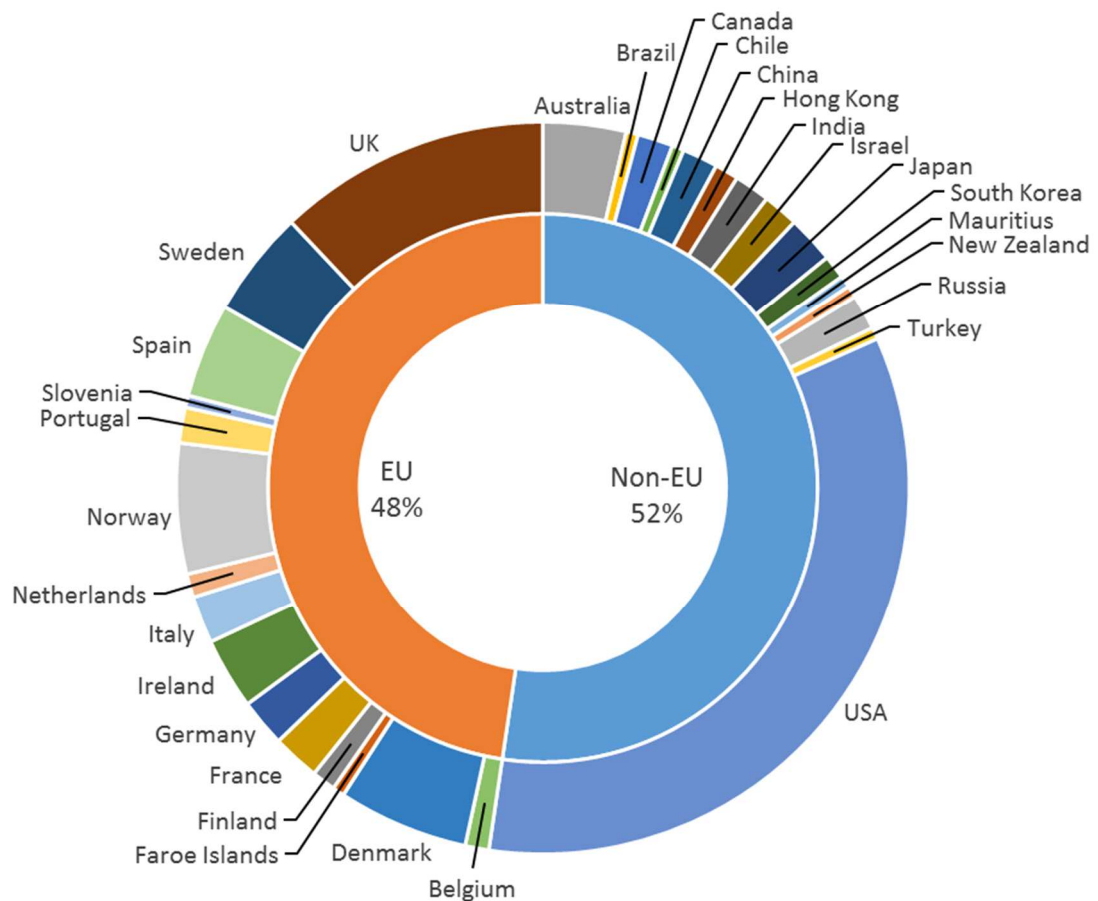


Figure 2-21. Distribution of wave developers in the world 2017 [69]

There are various WEC reviews which are continuously updated as technologies are introduced, revised or retired, a selection of these reviews includes Drew et al [61], Uihlein et al [42], Amir et al [39], Khan et al [70] and Wolfram [41]. Most of the technologies mentioned within these papers fit into the following WEC types.

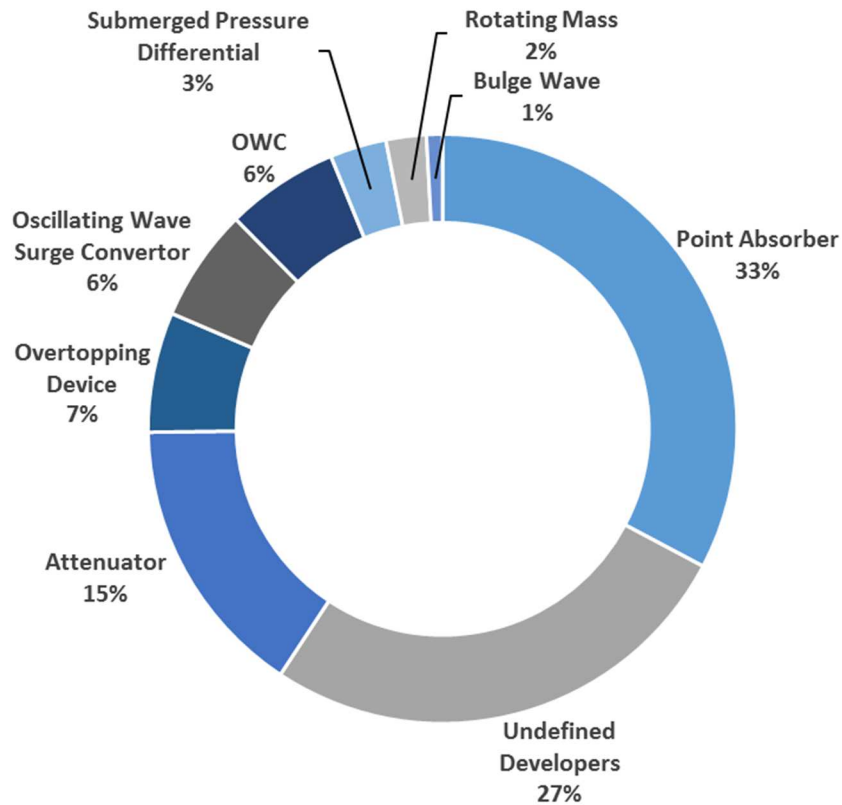


Figure 2-22. Distribution of Wave Developers according to Wave Device Types, 2017 [69]

Attenuator

Attenuator devices are commonly linked buoyed units which float on the water surface, operating parallel to the incoming wave direction. As individual units follow the movement of incoming waves, energy is captured from the unit's oscillating motion, relative to its neighbour, via a hydraulic motor or direct drive generator.



Figure 2-23. Pelamis wave attenuator device [57]

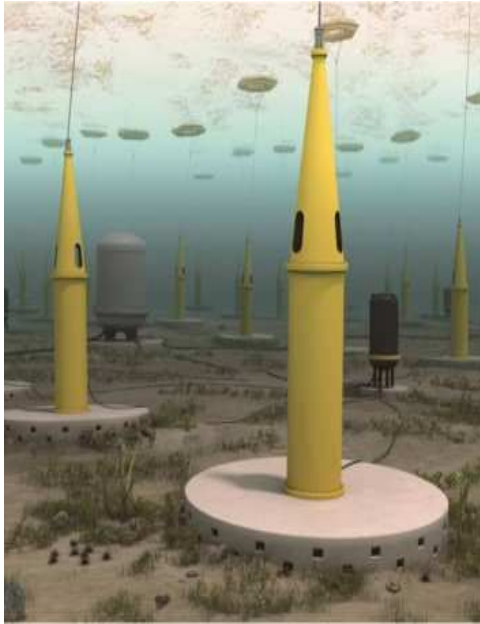


Figure 2-24. Seabased Point Absorber device [71]

Point Absorber

Point absorbers are non-directional dependant devices, extracting energy from all wave directions without requiring repositioning. The device consists of a floating unit, located at or near the sea surface, connected to a relatively static power take off (PTO) system moored to or installed on the seabed. The buoyant unit heaves and pitches with the motion of the waves creating electrical power from its relative movement to the power take off.

Bulge Wave

Bulge wave devices consist of a buoyant flexible tube, filled with water and tethered to the seabed. As a wave moves parallel to the device, water enters the tube causing a pressure differential or “bulge” which increases in energy as the wave move s it along the device. Water exits the device through a low head turbine connect to a power take off device.



Figure 2-25. The Anaconda bulge wave WEC [72]

Oscillating Water Column

Oscillating water column, OWC, devices can either be shoreline or offshore devices. The OWC is a semi submerged, hollow structure with a subsurface opening to the sea. The column of water inside the structure acts as a piston, rising and falling with the motion of the incoming waves producing an oscillating air current. Energy is then extracted from the air flow via a Wells turbine, which rotates continuously in one direction regardless of the direction of the airflow.

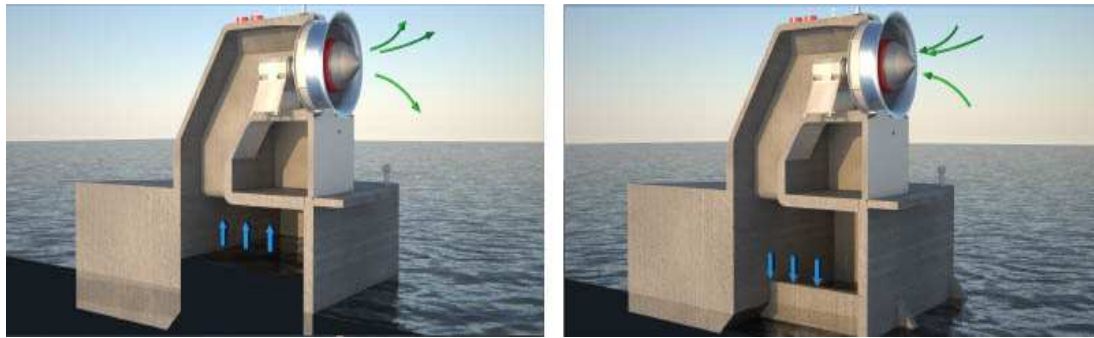
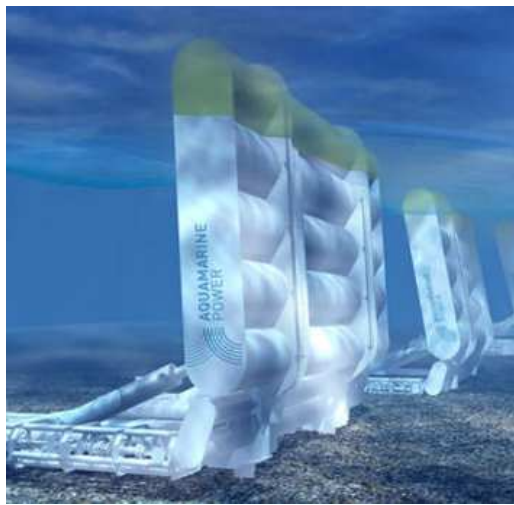


Figure 2-26. An example of an OWC device, Oceanlinx [73]



Oscillating Wave Surge Converter

Oscillating wave surge converters, OWSC, are near shore submerged devices that rely on a flap oscillating with the circular motion of subsurface water particles produced by surging waves. The flap is mounted on a pivoting arm and produces electricity via a hydraulic power take off or directly coupled generator.

Figure 2-27. Aquamarine's Oyster OWSC device [74]

Overtopping/Terminator Device

Overtopping or terminator devices consist of a stationary or floating storage reservoir behind a ramp. Waves wash over the ramp filling the reservoir and creating a head of water within the structure. The potential energy within the stored water is extracted by low head turbines as the water is released through the bottom of the reservoir into the sea. Multiple storage reservoirs can be utilised to concentrate a head of water.



Figure 2-28. An example of an overtopping WEC device, Wavedragon [75]



Submerged Pressure Differential

Submerged pressure differential devices convert hydrodynamic pressure changes into vertical motion. A submerged unit is forced to oscillate as passing waves increase and decrease water pressure above the device. As a wave passes over the device, the trough induces a reduction in water pressure, forcing the device upwards, while the increased pressure caused by the wave peak returns the device to its original position. This oscillating motion produces electricity via a hydraulic power take off.

Figure 2-29. AWS submerged pressure differential device [76]

Rotating Mass

Rotating mass convertors are floating units tethered to the seabed, which pitch and roll with the motion of the waves. This movement induces an unbalanced mass or gyroscope to rotate on a vertical shaft within the device, which in turn drives a generator as indicated in Figure 2-31. The topology of rotating mass convertors allows for operation via all wave directions.



Figure 2-30. Example of a rotating mass device, Wello Penguin [72]



Figure 2-31. Internal topology of the Wello Penguin Rotating Mass device [77]

2.3.3. Tidal Stream

Tidal streams or tidal waves are periodic and are caused by the gravitational pull acting on large bodies of water resulting in opposite wave like swellings of water which circle the globe following the passage of the moon and sun. The resulting forces created by the passage of the moon and sun are presented in Figure 2-32.

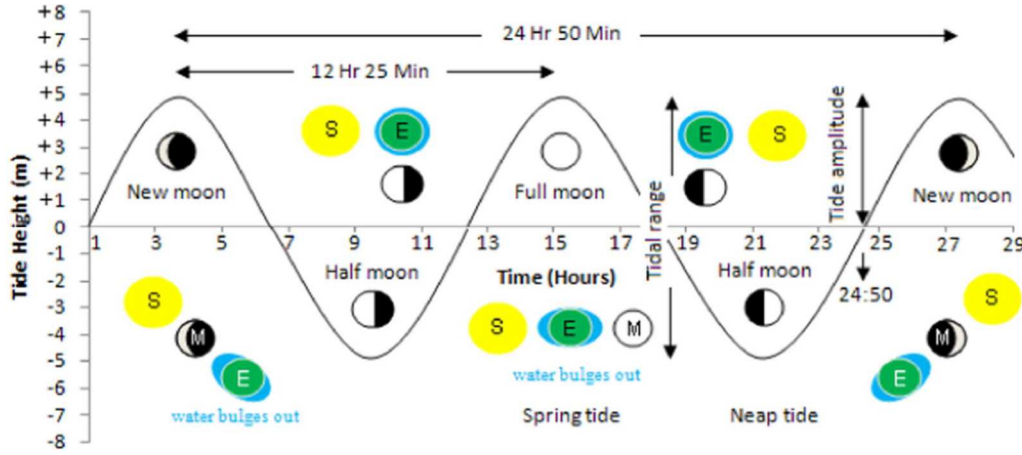


Figure 2-32. Tidal period and strength as given by the alignment of the sun and moon [70]

Combined with the centrifugal force of the Earth's rotation, the Coriolis Effect, these swells introduce a potential energy to the water as it flows through a contained site producing tidal currents as water fill and empty from coastal regions. Tidal energy can be harnessed by introducing a device into this flow and extracting the energy from the water as it moves from one site to another. Although similar in theory to the extraction of energy from wind, the energy present in tidal flows is much harder to quantify. The density of sea water is around 840 times that of the air, meaning that water waves and currents can transfer significantly higher energy at low speeds compared to wind. The total energy available must be calculated from the potential energy present and the kinetic energy contained within the flow, minus the energy dissipated from the friction between the flow and the natural boundaries as well as any interaction of the device with flow close to the surface or boundaries of the area.

The power density of a tidal current, with power P per unit area A , is described in the following equation.

$$\frac{P}{A} = \frac{1}{2} \rho_{water} v^3 \quad 2-12$$

Where ρ is the mass density of water and v is the incoming velocity of the tidal stream. However, this equation cannot be spatially aggregated to estimate the available resource over a large region due to the effects turbulent flow.

The potential power output for a tidal turbine is similar to that for wind and is described in equation 2-13.

$$P = \frac{1}{2} \pi r^2 \rho_{water} C_p v^3 \quad 2-13$$

Where r is the swept radius of the tidal stream and C_p power coefficient of the turbine. Friction coefficients vary greatly depending on the submerged topology and flora and fauna of the sea bed, thus site-specific investigations are required in order to install devices in the best possible configurations. With the lack of high quality hydraulic data and accurate estimates of frictional losses it is currently impossible to produce an accurate picture of the global resource available to tidal technologies [35]. However recent research has allowed some tentative estimates of the resource to be made. It has been stated by Khan et al [70] and Atlantis Resources [78], that the global potential of tidal stream energy could exceed 120 GW, with specific global estimates indicated in Figure 2-33.



Figure 2-33. Global tidal Energy Estimates [78]

There are two types of tidal device, tidal range and tidal stream. Tidal range devices rely on a head of water created between high and low tide, such as the previously mentioned tidal lagoons and bays. These energy converters are located close to shore or within man made dams. Tidal stream devices convert the kinetic energy from tidal currents and are located within the water column often as stand-alone devices. The installation of direct drive generators and drive trains will be proposed for tidal stream devices only since tidal range devices are further advanced and often simpler to install. Figure 2-33 shows the regions of the world where tidal stream energy contains the best potential.

Tidal Stream Devices

Tidal Stream Energy Convertors, TEC, as indicated from the power take off equations, often extract energy from the sea in similar ways to wind energy. The distribution of tidal developers throughout the world are provided in Figure 2-34. Similar to the distribution of wave developers, the UK and the USA contain the most tidal developers compared to any other country. While Europe accounts for almost two thirds of the global tidal developers.

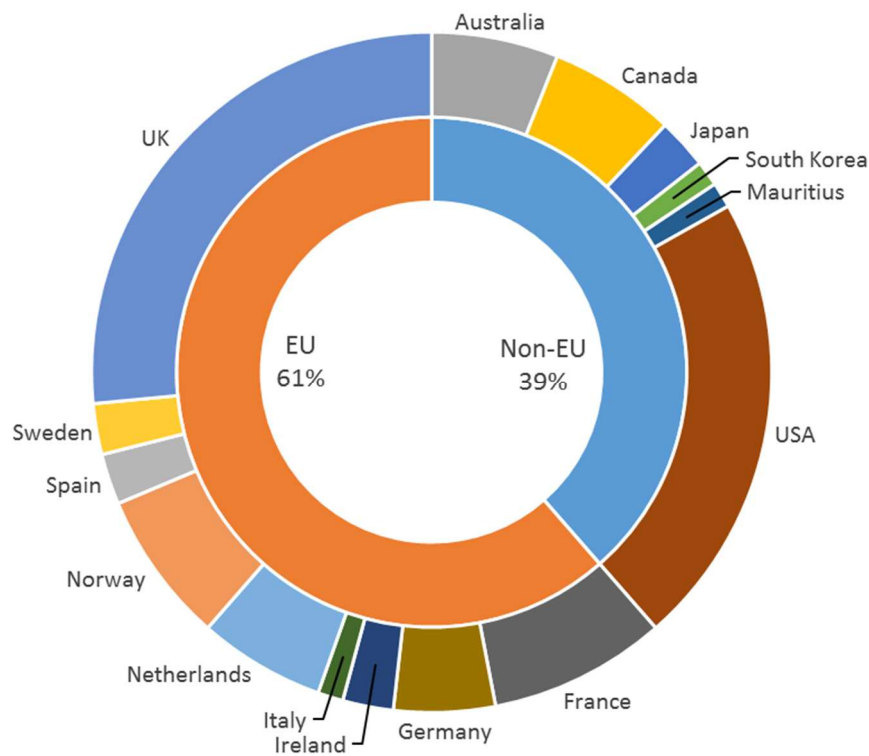


Figure 2-34. Distribution of tidal developers in the world, 2017 [79]

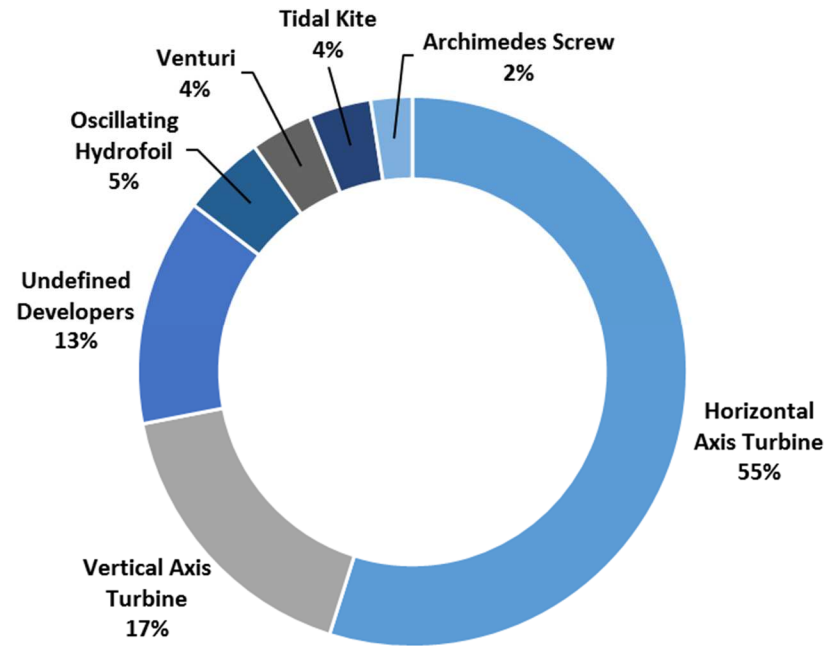


Figure 2-35. Distribution of Tidal Developers according to Tidal Device Type, 2017 [79]

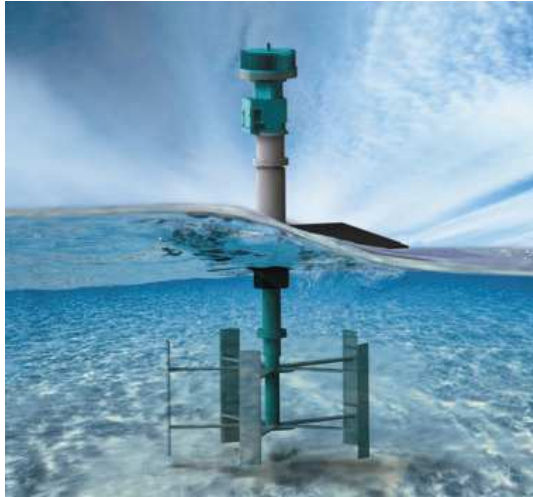
The variety of devices that are currently installed or under development is provided in Figure 2-35 and explanations of their operation are supplied below.

Horizontal Axis Turbines

Horizontal axis turbines extract energy from tidal streams by exploiting the lift. As water passes over the turbine blades, lift causes them to rotate about a central horizontal axis generating electricity. Often these TEC's are designed to yaw with the tidal flow or utilise a bidirectional turbine to maintain electrical energy production with the ebb and flow of the tide.



Figure 2-36. Example of a horizontal axis tidal turbine installation [80]



Vertical Axis Turbine

Vertical axis turbines extract energy from tidal streams by exploiting the same principle as horizontal axis turbines but in the vertical axis. The lift generated by the tidal flow causes the rotor to revolve around a vertical axis generating electricity. The turbine topology allows operation via all flow directions.

Figure 2-37. Vertical axis tidal turbine topology [81]

Oscillating Hydrofoil

Oscillating hydrofoils, or reciprocating devices, utilise hydrofoils at the end of arm. The tidal flow enables upwards and downwards vectors of force, moving the arm in an oscillating motion. At the bottom of the stroke the foil pivots to provide uplift, while at the top of the stroke the foil pivots to produce a downwards thrust. The motion of the arm drives fluid in a hydraulic system to be used to produce electricity.

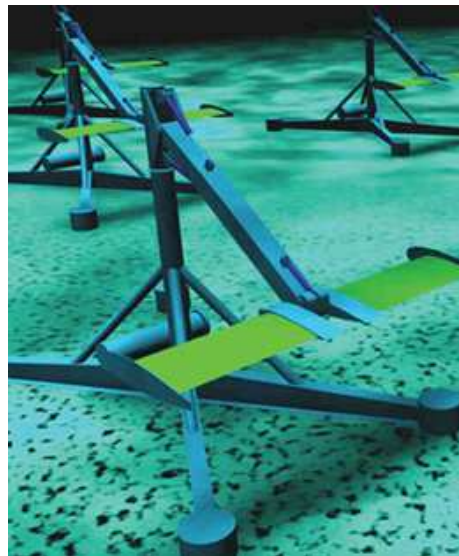


Figure 2-38. Example of an Oscillating Hydrofoil topology [80]



Ducted Devices

Ducted devices, or enclosed tip devices, are submerged devices that concentrates tidal flow through a duct. The funnel topology accelerates and concentrates the tidal flow which can be used to drive a turbine directly, or which can be used to drive an air turbine via the pressure differential in the flow of water.

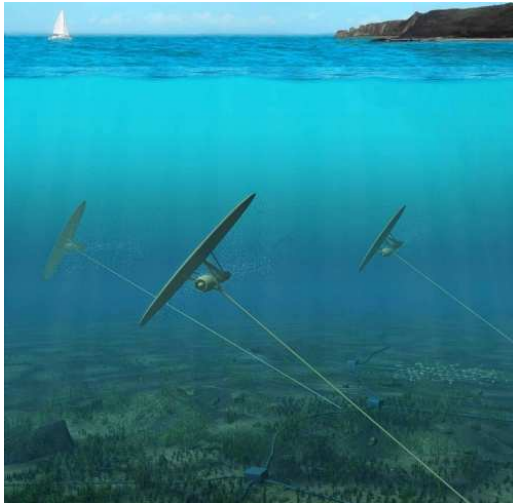
Figure 2-39. OpenHydro ducted device [82]

Archimedes Screw

The Archimedes screw is an ancient design which utilises a helical surface wrapped around a central shaft. The device produces rotational movement as water moves over the spiralling blades, this movement rotates the shaft which is connected to a generator. The Archimedes screw can be described as a variation of the vertical axis turbine.



Figure 2-40. Jupiterhydro Archimedes screw device [83]



Tidal Kite

A tidal kite moves through the tidal flow in a looping figure of eight. The device consists of a wing and a turbine at the end of a tether connected to the sea bed. The wing produces lift and a control system enables the device to move in a looping motion, during which turbine experiences higher flow velocities compared to the surrounding tidal flow.

Figure 2-41. Tidal kite topology from Deep Green, Minesto [84]

2.4. PTO Systems for Renewable Power Generation

As described by Kurniawan et al [85], renewable energy convertors can generally be split into the following sub-assemblies:

- A prime mover such as a blade or buoy, capturing kinetic energy from its interaction with the surrounding fluid creating a relative motion.
- A power take off system, PTO, to convert the prime mover energy into electrical energy, this sub system can be a standalone or combination of mechanical gearing, hydraulics, pneumatics, direct drive rotary or linear electrical drive systems.
- Power electronic converter to convert the variable voltage and frequency output to fixed voltage and frequency for connection to the grid.
- Control system to optimise energy capture, and to provide supervisory control for condition monitoring.
- Grid interface, consisting of switchgear and transformers to step up the voltage to the required grid level according to the network voltage at the point of connection.

Figure 2-42 summarises the different options for PTO in offshore renewables, while gearing and hydraulics enable low torque high speed power take offs for high speed generation systems. The PTO required within offshore renewable energy devices must be capable of withstanding the offshore marine environment and the varying loads that are subsequently produced, while performing efficiently for a long life span [86]. The drive train is such a crucial subsystem within the generating system, it is vital to know and improve upon the existing technology. Although Takoutsing et al [87], Reder et al [88], Pinar Perez et al [89], Carroll et al [90] and Igba et al [91] note that publicly available failure and condition monitoring data is scarce in the wind industry there is more information than in the marine energy sector. Therefore, using the limited wind data available and estimating the torque generated by wave and tidal devices, it is expected that the marine energy sector may experience similar difficulties. As shown in Table 2-3 and Appendix A, drive trains are one of the most common sub systems

which fail, leading to significant down time. Figure 2-43 shows the range of power ratings generally suitable for different PTO systems.

WT Technology	Failures/Turbine/Year	Downtime/Turbine/Year	Downtime/Failure
$G < 1$ MW	0.46	78.46 h	151.46 h
$G \geq 1$ MW	0.52	44.51 h	112.67 h
DD	0.190	20.50 h	34.98 h

Table 2-3. Total failures and downtimes per turbine per year for various wind turbine drive train topologies [88]

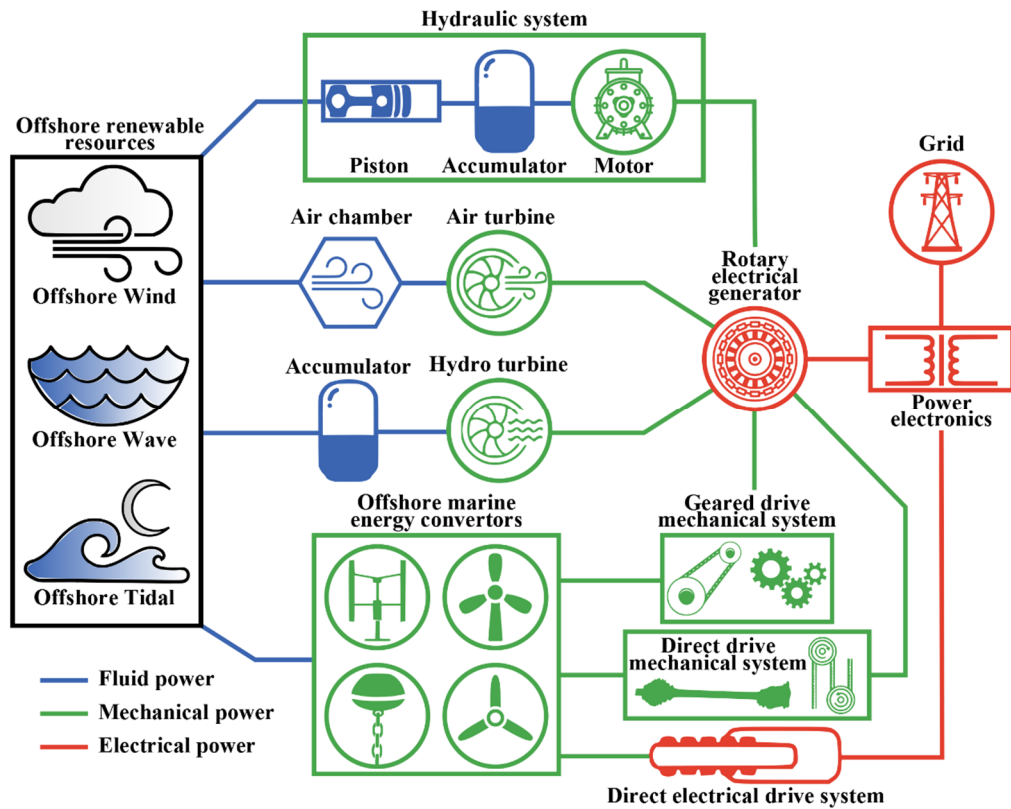


Figure 2-42. Various PTO methods for offshore renewable resources. Adapted from [61]
[92]

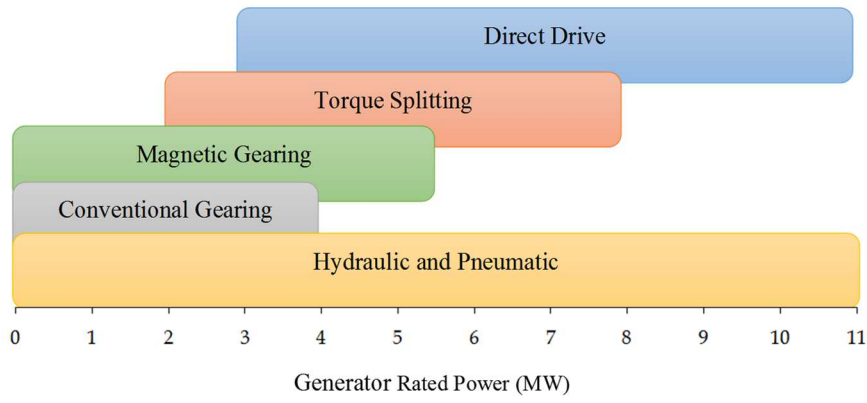


Figure 2-43. Identified rated power applicability ranges for various drive train options.

Adapted from [93]

Maples et al [94] provide efficiency curves for various drive train designs, Figure 2-44, based on an efficiency calculation in Equation 2-14.

$$\eta = \frac{P - (C + L \times P + Q \times P^2)}{P} \quad 2-14$$

Where C is constant losses, L is linear losses, Q is quadratic losses and P is the power divided by the rated power of the machine.

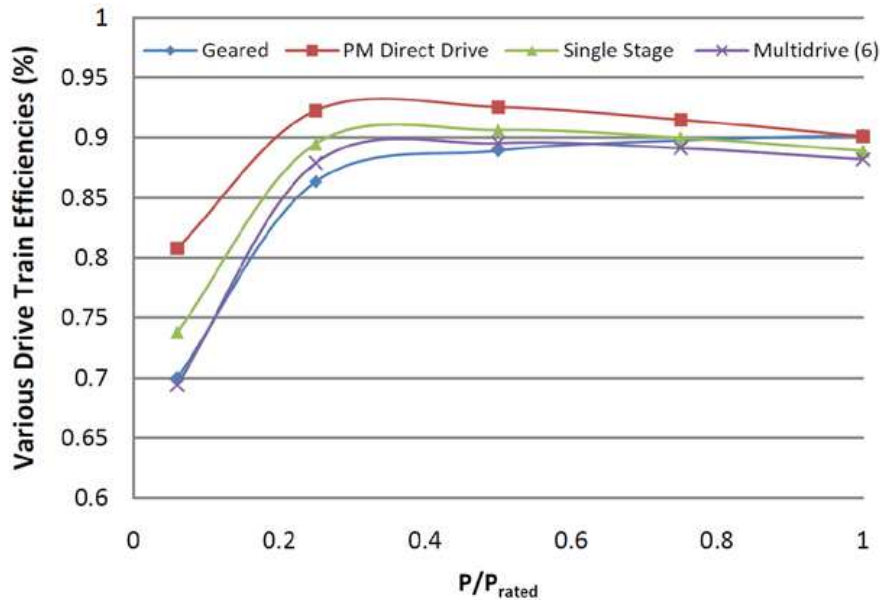


Figure 2-44. Drive train efficiencies of various drive train designs [94]

For the remainder of this section the main power take off systems will be discussed in more detail.

2.4.1. Geared

A gearbox increases low rotational or linear velocity to a higher velocity with a lower relative torque, for efficient power production from high speed generators. The type of gearbox influences the size, type and efficiency of generator as well as the reliability of the drive train as a whole. Conventional gearboxes have been installed in wind turbines and offshore devices for decades, but they have proved difficult to increase in size for high torque applications, hard to maintain with environmentally harmful consequences, due to lubrication leaks, and unreliable, with breakdowns accounting for over 20% of a typical wind turbine downtime [95]. An example of gear teeth failure in a wind turbine gearbox is shown in Figure 2-45. Therefore, alternative gearing systems such as magnetic gearing and medium speed geared installations are currently under development.



Figure 2-45. Damaged gear teeth on a wind turbine gearbox [96]

Conventional Gearing

Traditional gearing utilises surface contact between toothed mechanical components which transfer speed and torque, increasing or decreasing their magnitude based on the gear ratio. Single stage gearboxes consist of one stepped gear stage, often consisting of a planetary gear system as they exhibit higher power densities than parallel gearing topologies [97]. The basic system consists of multiple outer planetary gears revolving around a central gear called the sun. All the gears are contained within a ring or annulus gear, see Figure 2-46 - left panel. The annulus gear connects to the

rotor shaft while the sun gear connects to the generator shaft. Multi stage gearboxes consist of two or more stages of gearing and are the most common type for wind turbines. A typical three stage gearbox topology is presented in Figure 2-46 - right panel, comprising of two planetary stages and one parallel gearing shaft. For each gearbox stage approximately 1% of the input energy is lost, therefore gearbox stages must be limited in order to maintain efficiencies [98].

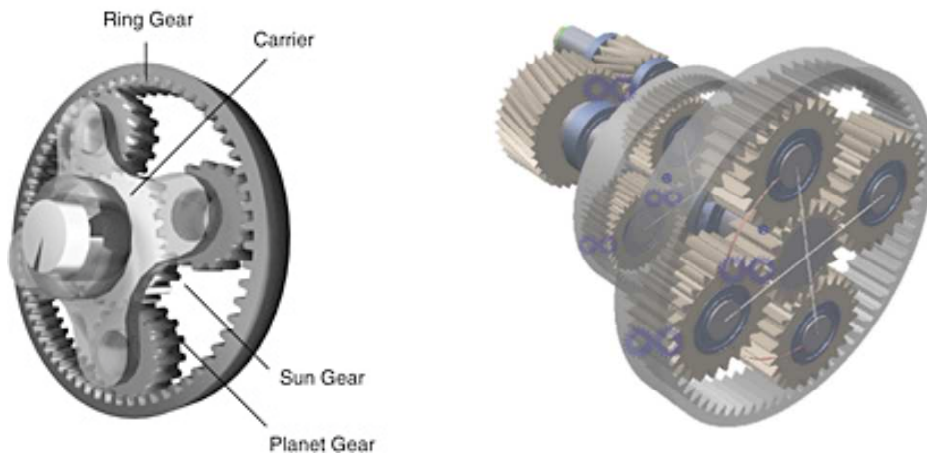


Figure 2-46. Left: Single stage planetary helical gearbox topology. Right: Multi stage planetary helical gearbox topology [99]



Figure 2-47. Two stage planetary gearbox, Adwin and Winenergy [100]

The largest wind turbine gearbox currently in existence is a two-stage planetary gearbox, designed for Adwen's AD 8-180 by Winergy as shown in Figure 2-47. With a turbine rating of 8 MW and a medium speed drive train concept, the gearbox boasts the highest torque input of any gearbox, at 10 MNm. However the gearbox adds an additional 86 tonnes to the mass of the turbine nacelle [101].

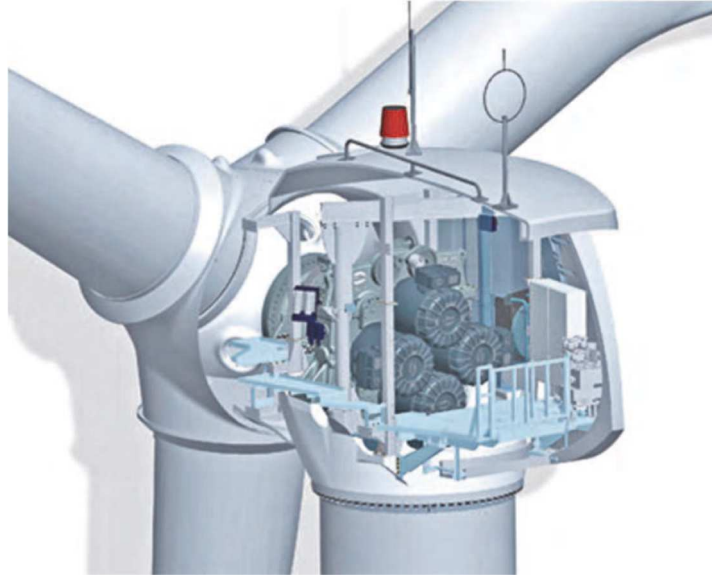


Figure 2-48. Torque splitting between four electrical generators on the 2.5 MW Clipper Liberty Wind turbine [97]

Torque splitting or distributed gearing splits the incoming torque between multiple generators [97]. Not only does this reduce the overall torque acting on the generator but it allows for redundancy should a generator suffer a breakdown or require maintenance. In addition, the construction of a distributed gearing system requires less manufacturing tolerances than planetary gearing. An example of a torque splitting drive train topology is presented in Figure 2-48. For linear wave power converters various gearing technologies have been proposed. CorPower Ocean, [102] have produced Cascade gearing, a method of converting linear motion to rotatory via multiple small gears splitting the incoming linear motion into high load power transmission [103], Figure 2-49.



Figure 2-49. Cascade gear, mechanical linear-rotary power take off [103]

Geared systems for wave and tidal tend to be smaller in size compared with wind turbine gearing, but issues about reliability, efficiencies, seals and marine protection all make simpler drive trains more appealing. For large torque applications gearbox manufactures that are offering solutions for the renewable energy market include Bosch-Rexroth, with current gearboxes for systems up to 3 MW and future designs on a 10 MW medium speed gearbox. David Brown and Samsung Heavy Industries partnered to construct a medium speed gearbox for a 7 MW prototype turbine. Meanwhile companies such as Eicogear and Ishibashi currently produce gearboxes for ratings up to 3.8 MW and 5 MW respectively [49].

The main benefit of geared systems is the conversion of low speed high torque to high speed low torque for conventional electrical generators, but disadvantages include: multiple bearings; long down time periods; multiple seals and operation in the marine environment; including environmental concerns over lubrication leakages.

2.4.2. Hydraulic and Pneumatic

A hydraulic power take off (HPTO) is generally applied to a system which extracts high loads at low frequencies. It converts linear or rotary motion into a fluid pressure to be used for generation alongside the energy extraction device. In most cases a hydraulic power take off utilises a linear actuator which acts as a pump to displace a hydraulic liquid through a hydraulic motor to provide energy to an electric generator [92].

HPTO's are applied to devices which are unable to be coupled with rotary or linear generators for topology reasons or energy efficiency. In order to reduce losses, devices can be connected to hydraulic systems which feed into accumulators in order that cumulative hydraulic power can be fed through a generator.

Advantages of hydraulic power take off systems include:

- Slow energy dissipation in order to smooth energy harvesting fluctuations
- Increased generation efficiency when combined with multiple devices
- Transfer of energy with minimal losses to a convenient electrical generation site

Disadvantages include:

- Multiple moving parts
- Low part load efficiency
- Multiple seals and operation in marine environment
- Environmental concerns over hydraulic fluid leakages

Hydraulic power take off systems for wave energy devices were utilised in devices such as Salter's Duck, Pelamis and the Oyster [39], [104], [105], while new developments are proposed by Gaspar et al [104] and a general review of various WEC devices combined with HPTO systems is provided by Lin et al [106].

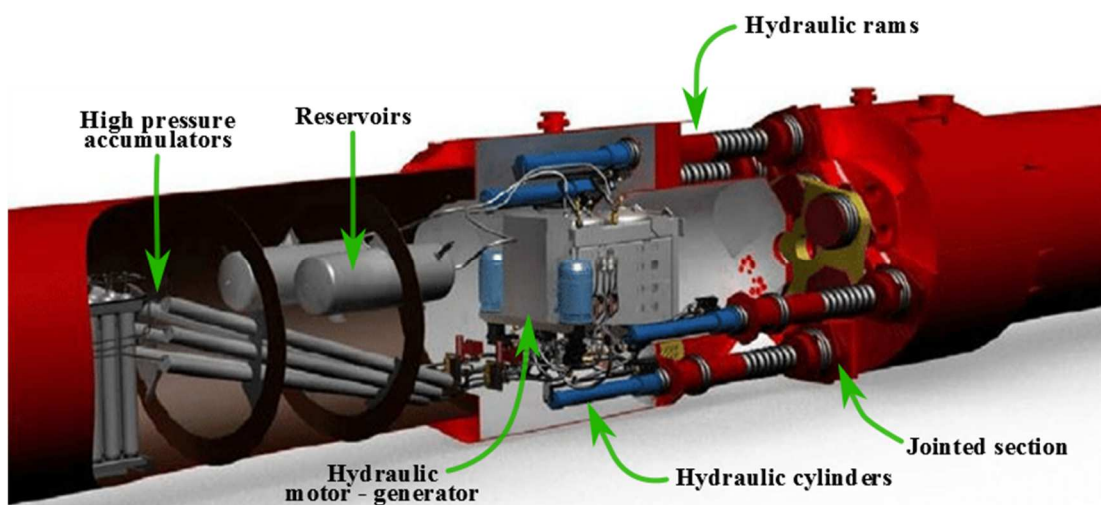


Figure 2-50. Cutaway of Pelamis 2 joint and power take off [105]

Although HPTO systems are unusual for wind turbines, since the advent of an offshore wind turbine industry various HPTO have been suggested. For example a salt water hydraulic power take off was proposed for a two bladed offshore wind turbine to focus hydraulic power from numerous wind turbines on a centralised generation platform [107]. While Zaing et al [108], Skaare et al [109] and Silva et al [110] suggest that HPTO is a method of maintaining the speed and frequency of the generation system as well as improving reliability, energy transfer and reducing maintenance costs. An example of a nacelle based hydraulic drive train system for a wind turbine with dual synchronous generators is presented in Figure 2-51.

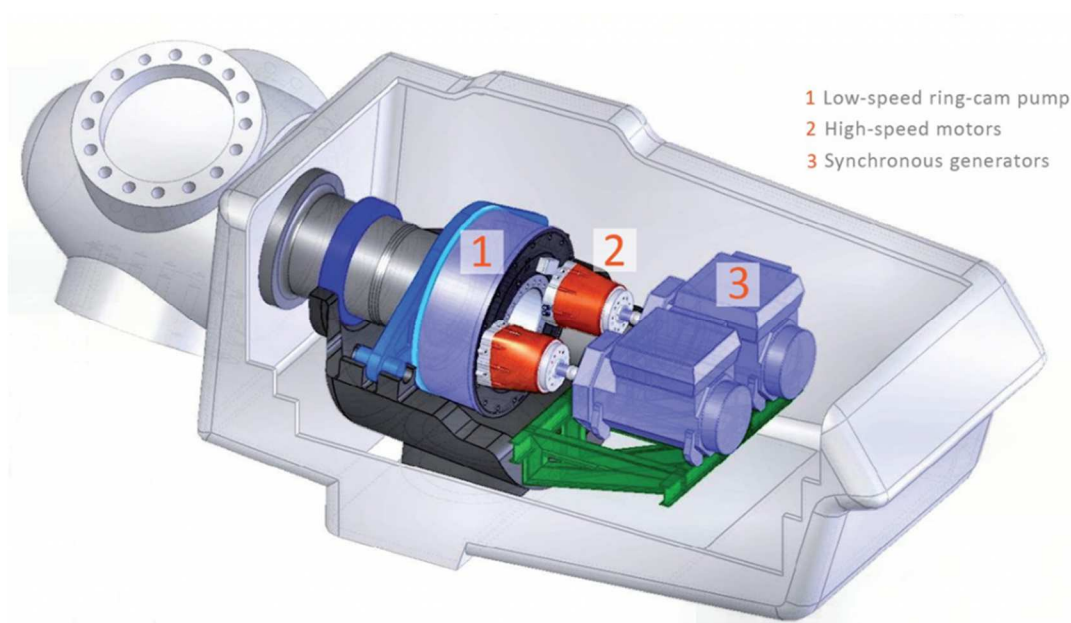


Figure 2-51. Hydraulic Drive Train. Source Mitsubishi Heavy Industries, Ltd. [111]

2.4.3. Direct Drive

Direct drive drive-trains are the simplest method of transferring mechanical power from a renewable energy prime mover to a power take off system, coupling directly from the prime mover to the generator. Figure 2-52 shows a direct drive generator coupled to the hub where the wind turbines are mounted. An indication of physical size for such machines is clear in Figure 2-52 with the diameter of the generator being similar to that of hub supporting the turbine blades. Direct drive generators tend to be synchronous machines, electrically excited or permanent magnet (PM) excited. Direct drive systems mostly operate at low rotational or linear velocity, therefore the

generator must be able to create electricity efficiently at low speeds and high torque or forces. Figure 2-44 shows that a PM direct drive generator is able to meet this criteria, and in fact exhibits higher efficiency than any other form of PTO over the entire load range. Since direct drive systems contain minimal mechanical components, the transfer of energy is more efficient and the overall system should be more reliable.



Figure 2-52 Direct-Drive wind turbine, ENERCON E-82 [112]

Simplifying geared and complex drive train systems to a direct drive system generally results in the following:

- Reduced mass – Depending upon the topology and the design optimisation, large direct drive machines can reduced the overall mass of the generator subassembly compared to a geared system.
- Higher reliability - Gearboxes account for long down times within drive trains. Removing the gear box and associated bearings and seals from the drive train increases operational life and improves reliability.
- Higher power transfer efficiencies - As shown in Figure 2-44, direct drive systems are more efficient than geared drive trains, unless the machine is also running at its rated output which is generally not the case for renewable energy devices.
- Reduced maintenance - Generally geared systems must be regularly maintained in order to ensure lubrication and efficient operation, by reducing friction forces between teeth.

- Reduced noise and vibration - Bearings, whether in physical contact with active components or separated via a fluid, such as with hydrodynamic/static bearings or magnetic bearings, are required in any system which relies on moving components. Therefore, although a direct drive train is the simplest method of transferring energy from the energy harvesting device to the generation system, the improvement of the bearing system should be continuously investigated.

There are engineering challenges with direct drive systems, with regards to structural design and bearings, which will be addressed in more detail in the following chapters.

Current offshore renewable energy converters where direct drive systems have or are being utilised include OpenHydro's tidal device [82], Tocardo's 100kW tidal generator [113], GE Alstom's 6 MW offshore wind turbine [114], Siemens 6MW and 8MW offshore wind turbines, [25] [21], the 2MW AWS wave device installed in 2004, [115], and SeaBased in Sweden, [71]. Whilst Nova Innovation is developing a direct drive power train for their tidal device as part of the H2020 funded TIPA project [116].

2.4.4. Bearings

Bearings are a critical component in a power take off and drive train system. Mechanical bearings are a method of allowing the radial or linear movement of two surfaces in respect to each other while curtailing unwanted motion or displacement caused by force loading and thus reducing friction between moving bodies enabling a more efficient transfer of energy. For both offshore wind and marine generation, the operational and maintenance environment is more extreme than onshore power generation techniques, thus requiring sturdier bearing installations while demanding higher reliability and longer life spans [117]. Figure 2-53 indicates the failure rate of bearings as the generation system increase in size. Similarly, marine applications face uncertainties in bearing operation and life span due to the severe offshore environment.

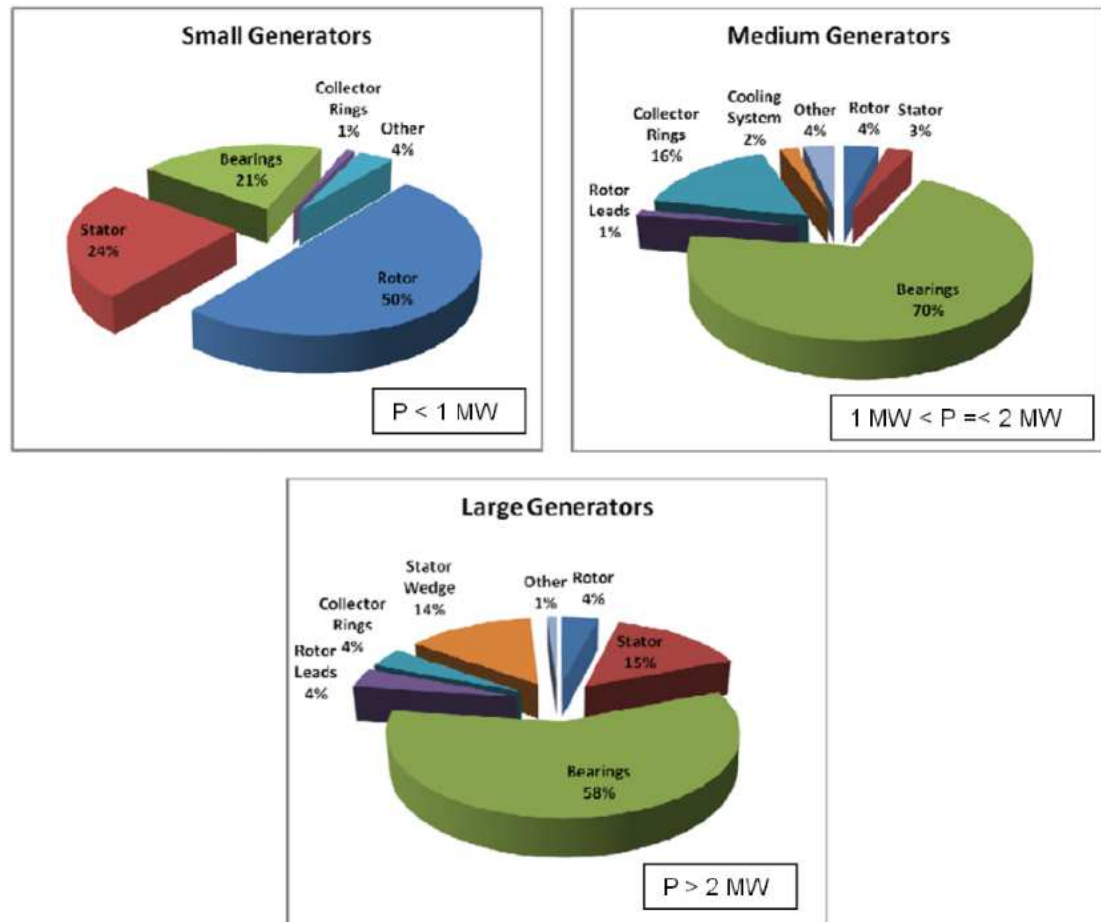


Figure 2-53. Survey of 800 failed wind turbine generators [118]

A full bearing study has been completed by Caraher in [119], however a brief overview of bearing types will be provided here for completeness.

Depending on the application there, are a variety of different bearings that can be used to mitigate the application of thrust, radial or point loads.

- Roller bearings or roller element bearings utilise moving balls or rollers placed between two surfaces, reducing friction and bearing sliding. Unforeseen knocking or vibration loading combined with high radial loads can cause these bearings to fail prematurely, a major concern for multiple MW wind turbines. In addition, corrosion and pitting drastically reduce the life and function of these bearings. Further causes of failure for roller bearings are supplied in [120].

- Hydrostatic and fluid dynamic bearings exploit a layer of fluid, usually oil, water or air, between two surfaces to produce low friction, high speed, high load capable bearings. Hydrostatic bearings rely on an external pump to create a pressurised fluid film, while fluid dynamic bearings generally utilise rotation to form a lubricating liquid wedge against the inner wall of the bearing.
- Magnetic bearings employ a magnetic field to support loads and moving parts without physical contact. Although they have very low to no friction values, they require continuous power, control systems and a surface bearing backup in case of failure [121] [122]. Magnetic bearings have yet to be proven for renewable energy devices, they are a relatively new development and are not considered a conventional PTO bearing system.

The bearings described above require one or more of the following:

- Complex multi component assembly
- The inclusion of seals and lubrication in order to operate
- A non-corrosive environment in which to operate
- Active control or constant monitoring

In recent years surface plain bearings or journal bearings have been suggested as an alternative to conventional bearing topologies. Surface plain bearings have no moving parts and consist of a surface which enables low friction movement but high load carrying capacity. Bearings of this type are the simplest, least expensive and generally the longest lived of all bearing types. Wear rates can be calculated into the life expectancy of the bearing material more fully than other bearing types, thus drastically reducing the possibility of bearing failure. Surface plain bearings come in various forms depending on the application. External lubrication can be applied so that a low friction surface can travel freely on a guide surface, however often polymer bearings can be manufactured to be self-lubricating, creating a hydrodynamic layer between their contact surface and guide surface. For centuries plain bearings have been used in marine environments where the risk of wear and corrosion of moving parts is high. For most applications, plain bearings are utilised to withstand axial and thrust loads as a sleeve or radial topology. However, with the advent of advanced polymer materials

with low static and dynamic coefficients of friction, smooth operation can be achieved under high pressures and at low speeds in both dry and wet environments, ideal for marine direct drive machine PTO. In addition, life times can be predicted based on wear rates, as shown in Figure 2-54, a method that can be more accurate than conventional bearing systems. A more detailed polymer bearing study will be presented in Chapter 5.

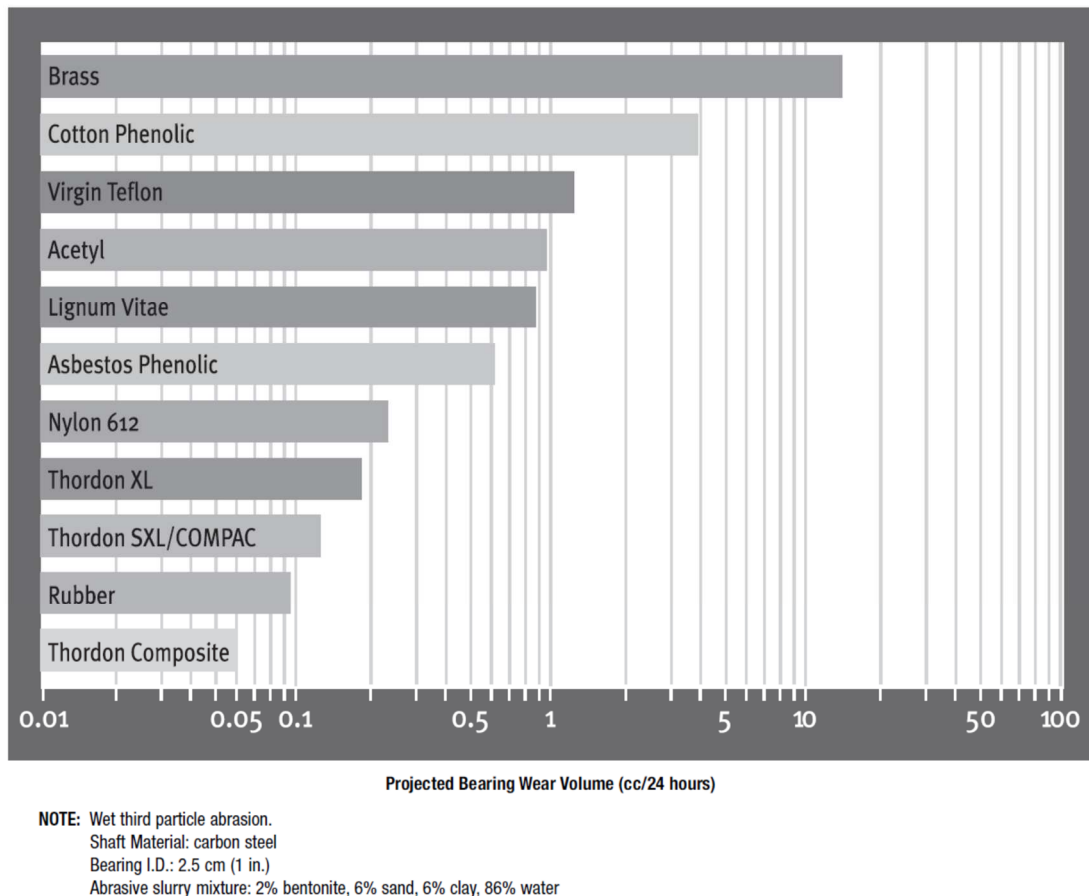


Figure 2-54 Typical journal bearing abrasive rates [123]

Chapter 3.

Electrical Generators for Renewable Energy Converters

3.1. Renewable Electrical Generation: An Overview

In renewable energy converters the focus of development has been in the mechanical design of the prime mover in order to optimise conversion efficiency. The electrical generation system tended to be an off-the-shelf solution using conventional high speed rotary generators, such as the squirrel cage or doubly fed induction machine (SCIG and DFIG respectively). As of 2017, the DFIG accounts for more than 90% of the installed onshore and offshore wind generator topologies.

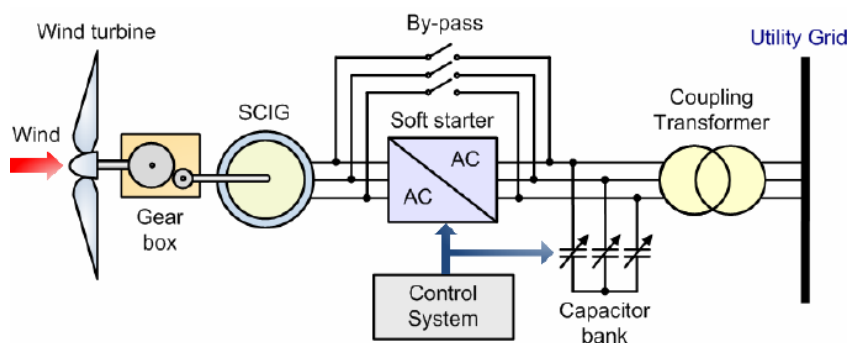


Figure 3-1. Fixed Speed Squirrel cage induction generator machine based electrical generation system [124]

Early wind turbines using the SCIG operated at fixed speed, and thus required no power conversion system. Figure 3-1 shows the system outline for a fixed-speed based system with a SCIG. The soft-starter is required to limit starting currents, and once the machine was up to the nominal speed the bypass switches connected the generator output directly to the grid. Although very simple and robust such systems were not very efficient, as the turbine did not always operate at its optimum power conversion efficiency. In addition, any fluctuations in the wind turbine power due to for example turbulence would be seen directly at the output to the grid. Fixed speed systems tended

to be at low power ratings, 100 kW or less. As the power rating increased there was a move to some limited speed control, resulting in the need to use a wire wound rotor induction generator as shown in Figure 3-2. By controlling the rotor resistance through external resistors the induction machine slip can be modified providing some limited speed variation.

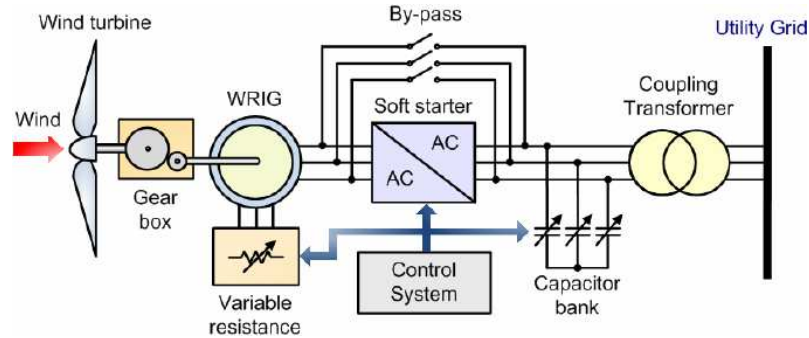


Figure 3-2. Variable resistance control of the wound rotor induction generator [124]

The use of external resistors resulted in losses, and thus was not very efficient. An alternative to the fixed speed SCIG was to use a fully rated power converter providing full speed control, however in the early stages of development of wind turbines, power electronic converters were very expensive, and hence this was not an economic option, even though in terms of overall system performance it is a very good option. Hence, the widespread use of the DFIG according the system shown in Figure 3-3, in which a partially rated power converter is connected between the rotor winding and the grid.

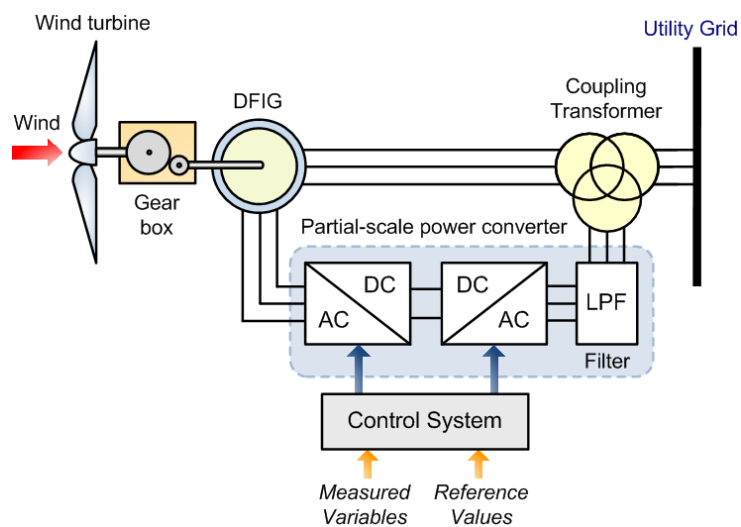


Figure 3-3. Doubly fed induction machine based electrical generation system [124]

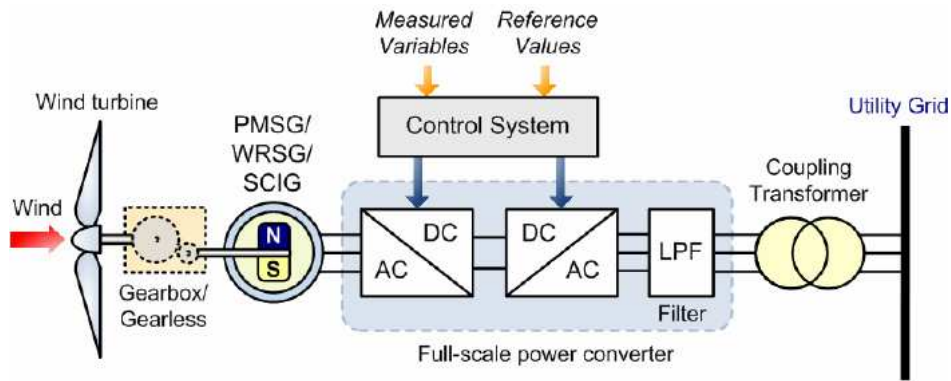


Figure 3-4. Variable speed control with fully rated power converter [124]

Power flow in this path is used to control the rotational speed, providing about a 30% variation in speed, but only requiring a power converter rated at 1/3 the rating of the generator. The generated power is passed to the grid via the stator winding. The main disadvantage of this option is the requirement for brushes on the rotor, which require maintenance. Onshore, this is manageable, but a burden in the offshore environment. Early offshore developments in wind adopted the standard onshore technology of the DFIG system, and more recently the SCIG with a fully rated converter has been adopted as the price of power converters has reduced, as shown in Figure 3-4. Clearly the SCIG has the advantage of no brushes on the rotating parts.

Another option is to replace the SCIG with a permanent magnet, PM, synchronous machine or electrically excited synchronous machine, but with a fully rated converter in both cases. The overall system is similar to that of a SCIG. The PM option provides a more power dense generator and exhibits higher efficiency across a wider speed range, but the cost is dominated by the use of rare earth materials in the magnets. Electrically excited synchronous machines are well known technology used in all power stations and hydro plants around the world. However, the power density is not as good as the PM generators, and again brushes are required to excite the rotating field winding, although brushless systems are available.

All these options involve a high speed rotating machine operating in the region of 1000 to 1500 rpm. As stated earlier a gearbox is used to match the low speed prime mover to such high speed generators. Work on reliability by Tavner, showed that although the gearbox although it does not exhibit the highest failure rate, it has a long down-

time. Gearbox failures have been a major issue in some of the early UK offshore wind farms, for example at the Scroby Sands wind farm all gearboxes failed within the first 18 months of operation [125], and since the cost of replacing a gearbox offshore approaches €0.5m, this is a major problem. Hence the move towards direct drive systems in which the gearbox has been eliminated, and the generator is coupled directly to the prime mover operating at the same slow speed as the prime mover. Although simpler in terms of the number of mechanical components in the drivetrain, the design of direct drive generators opens up other challenges to be discussed in the next section.

Marine renewables, wave and tidal, have adopted a similar approach to wind in the choice of electrical generation systems, namely the use of conventional off-the-shelf high-speed electrical generators, principally the SCIG and the field wound synchronous machine. For tidal energy extraction the SeaGen, built by Marine Current Turbines, use a SCIG with fully rated converter. For the wave energy sector, the Oyster wave energy convertor, built by Aquamarine Power, utilised high pressure pumped water to drive a conventional hydro turbine with field wound synchronous machine. Pelamis Wave Power used a SCIG running at fixed speed from a hydraulic system, but also considered the field wound synchronous machine. The rationale for doing so is to simplify the system, but gearboxes and hydraulic systems are then required to match a reciprocating prime mover to a high speed rotating electrical generator, which introduces more complexity to the system. There have been some examples of direct drive systems in wave and tidal, but the challenges are even greater than in wind, due to the low speeds, greater forces and sub-sea operation. O&M has to be minimised in the offshore environment, and is particularly challenging for wave and tidal, as access is more difficult than in offshore wind. As wind turbines increase in rating to 10MW and beyond, conventional generator technology for direct drive systems will become too large and heavy. The use of high temperature superconducting machines to reduce the physical size of the machine has been demonstrated for marine propulsion by American Superconductor [126], in which the HTS machine was a third the physical volume of an equivalent copper motor, Figure 3-5. High temperature superconducting, HTS, technology is, therefore, considered an option for direct drive machines with ratings of tens of MW.

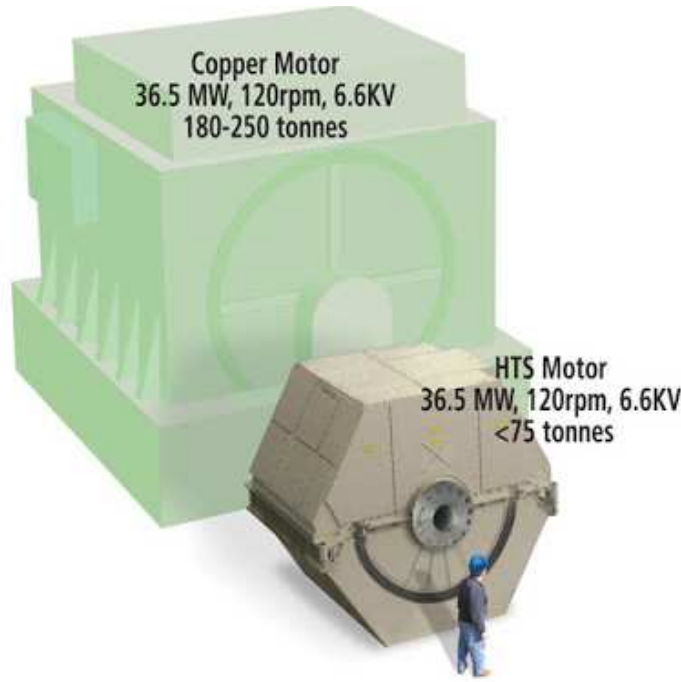


Figure 3-5. Comparison of physical size between a 36.5 MW conventional induction motor and a 36.5 MW High Temperature Superconducting motor [127] [128]

The remainder of this chapter will therefore focus on direct drive systems, using both conventional and HTS technology, addressing the design challenges that need to be overcome.

3.2. Direct Drive Electrical Generator Topologies

An electric generator converts mechanical energy into electrical energy by moving a conductor through a magnetic field or vice versa. As the conductor is acted upon by the changing magnetic field, a potential difference or voltage is created between the two ends of the conductor. If the conductor is connected to a closed circuit with a resistance, a flow of electrons or current is observed with a magnitude based on the strength and rate of change of the magnetic flux or excitation field. Thereby mechanical power, P_{mech} , as described in Equations 3-1 and 3-2 is converted into electrical power, P_{elec} , Equation 3-3.

Linear mechanical power, where F is force and v is linear velocity, is given by:

$$P_{\text{mech}} = Fv \quad 3-1$$

Rotational mechanical power is provided in equation 3-2.

$$P_{mech} = T\omega_{rpm} \quad 3-2$$

Where T is torsional force, torque, and ω_{rpm} is rotational velocity. 3-phase electrical power in the generator is given by:

$$P_{elec} = 3IV\cos\phi \quad 3-3$$

Where I and V are the rms phase current and voltage respectively, $\cos\phi$ is the power factor.

In converting the mechanical power into electrical power in a generator at typically fixed rms voltage, V , the electrical force or torque is directly proportional to the rms current flowing in the generator windings, I , and inversely proportional to the linear velocity or rotational speed, v or ω respectively. A machine of high rotational speed will require high currents in order to achieve a certain torque or force. At the same torque or force output a reduction in speed, as observed in direct drive, can be accompanied by a reduction in current, leading to a more efficient machine. However, physical size is a major issue when comparing high speed and low speed machines, and therefore reducing the mass of direct drive generator systems while increasing their power densities is crucial when offering alternatives for high speed machines.

Direct drive generators can be classified into two groups, permanent magnet machines or electrically excited machines, and depending upon the orientation of the flux flow these machines can be classified as radial flux, axial flux or transverse flux, in both rotary and linear configurations. A detailed description of these different topologies is provided by Mostafa, [129], with a focus on permanent magnet direct drive generators. For completeness a summary is provided below.

Figure 3-6 shows the topology of a radial flux machine, with surface mounted permanent magnets on an external rotor. Flux crosses the gap radially from the magnets to the stator windings, which in this case are embedded in slots as part of an iron core.

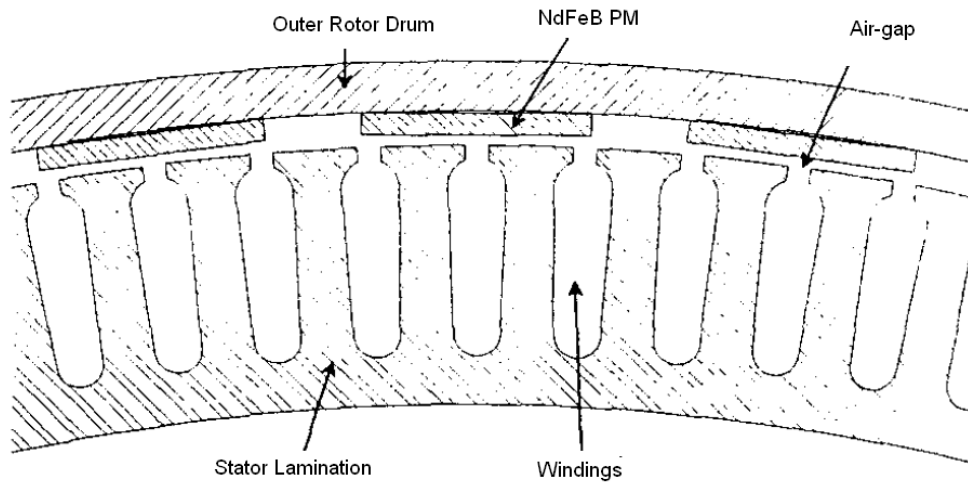


Figure 3-6. Layout of outer rotor iron-cored surface-mounted RFPM generator with NdFeB permanent magnets on outer rotor drum [130]

Although Figure 3-6 shows surface mounted permanent magnets, a radial flux machine can also utilise buried or internal magnets, with an example shown in Figure 3-7. The active length of the machine acts along the z-axis of the machine.

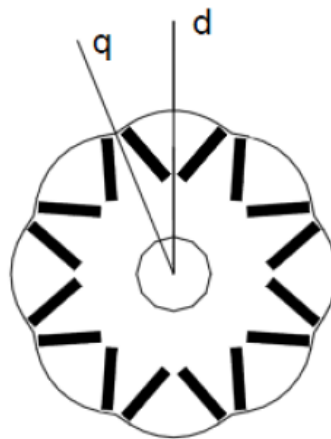


Figure 3-7. An example of multi-pole buried magnet radial flux machine [131]

Figure 3-8 shows examples of slotted axial flux topologies with surface mounted airgaps. The flux now crosses the gap in the axial or z-axis, and the active length of the machine is now in the radial direction. The principle of operation in both radial and axial flux machines is the same.

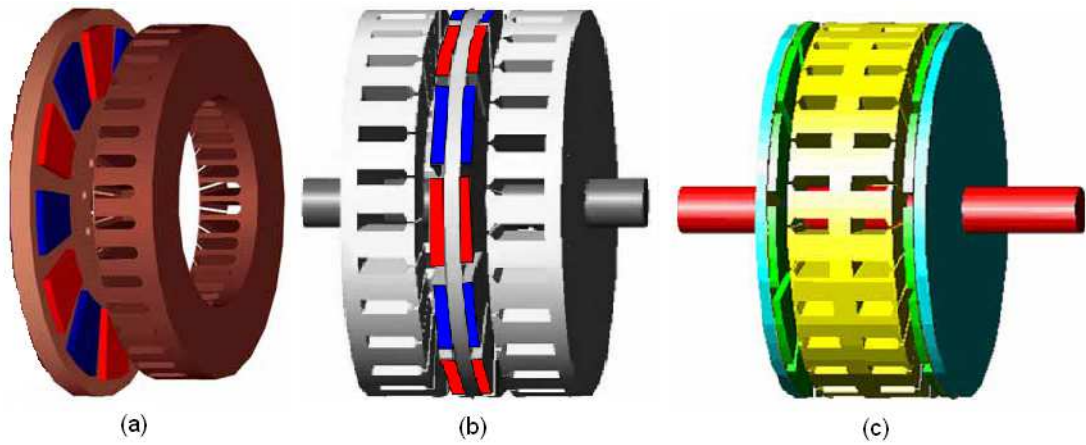


Figure 3-8. Slotted surface-mounted AFPM machines. (a) one rotor and one stator [132], (b) one rotor and two stators [133], (c) two rotors and one stator [134]

Rather than use a slotted structure, airgap windings can be used in both radial flux and axial flux machines, in which the windings are and physically located in the airgap attached to a smooth iron surface. Figure 3-9 shows the TORUS machine with an airgap winding.

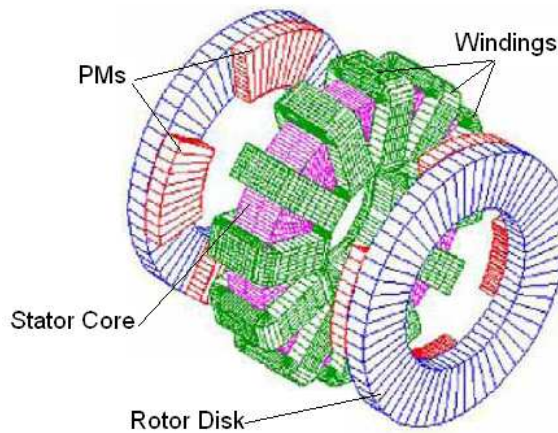


Figure 3-9. A slot-less TORUS machine [135]

Fully aircored permanent magnet machines have also been developed, in which the winding is supported in non-magnetic material within the airgap of the machine. Figure 3-10 shows a machine developed by Boulder Wind Power, in which the winding is sandwiched between two permanent magnet discs separated by an airgap on either side. A radial flux air-cored machine is shown in Figure 3-11 developed at University of Durham, by Professor Ed Spooner.



Figure 3-10. Air-cored axial flux with double sided surface mounted permanent magnet rotor, Boulder Wind Power [136]

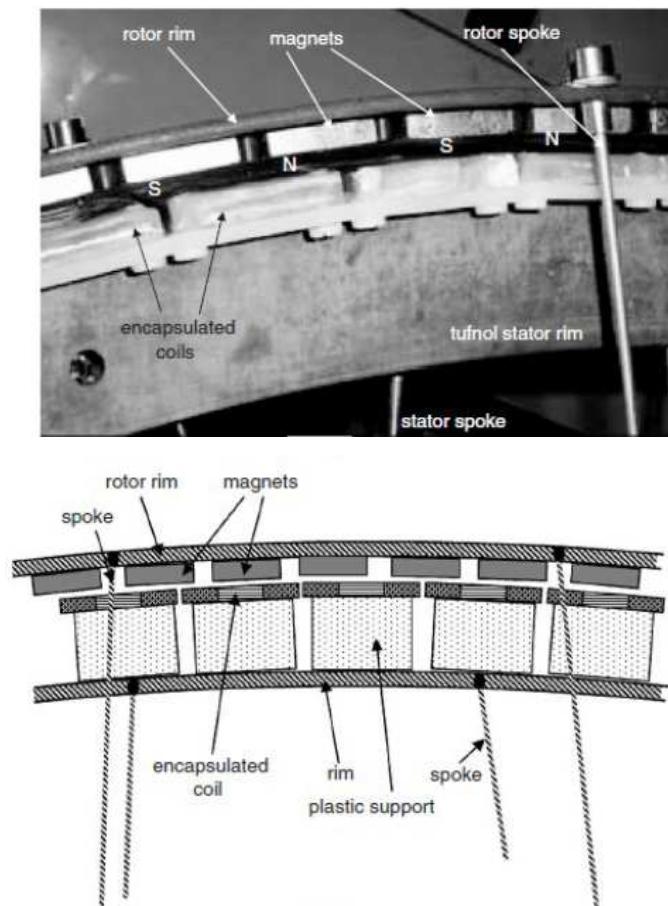


Figure 3-11. Radial flux air-cored machine with surface mounted permanent magnets [137]

The C-GEN technology is another example of an air-cored permanent magnet machine, more detail of which is provided at the end of this chapter.

Synchronous machine based generator topologies exhibit modest shear stresses in the airgap – typically 50kN/m^2 for a naturally cooled machine. For direct drive systems, being able to react to more force per square metre of airgap would assist in reducing the size of the machine. An innovative machine topology developed in the 1980s known as the transverse flux machine (TFM) boasted very high shear stress, with a peak of 200 kNm^{-2} quoted in [138].

Figure 3-12 shows a section of a TFM with surface mounted magnets (a) and buried magnets (b) designed and built by HWeh et al [138]. There is one stator coil per side, which lies transverse to the axial length, whereas, in a conventional machine the coils lie in the longitudinal plane. With reference to

Figure 3-12(a), two rows of surface mounted PMs forming the translator move parallel to the stator coil, with magnets of opposite polarity facing each other in each row. C-cores are used to channel the flux between opposing magnets in each row and a return path is provided by a triangular section opposite each C-core. Flux therefore flows in the radial direction across the airgap and in the axial direction between the two rows of magnets. The raw structure of the machine is very simple, but it is expected that significant supporting structure will be required to hold the C-cores in place, overcoming the immense radial forces produced by the magnets.

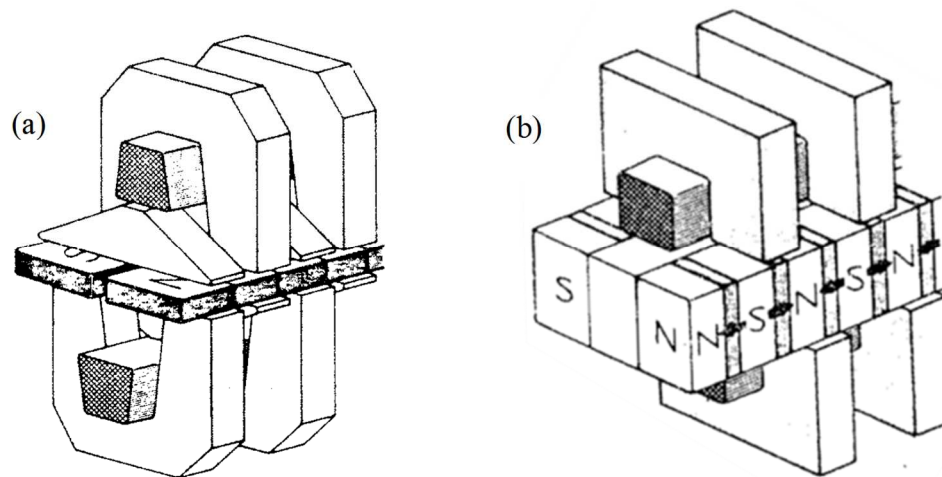


Figure 3-12.(a) Surface mounted. (b) Buried magnet transverse flux machines [138]

A variant of the TFM is the claw-pole machine, a rotary version is supplied in Figure 3-13.

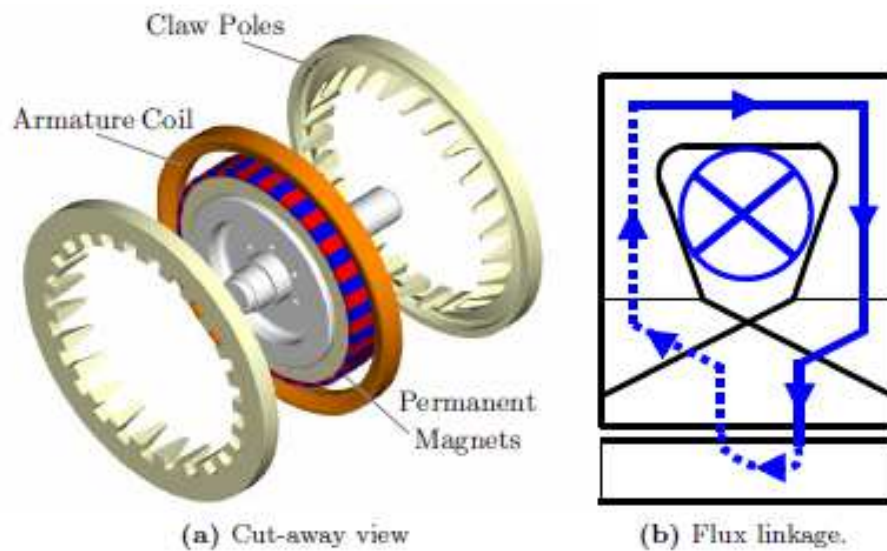


Figure 3-13. A rotary claw pole machine, showing one phase.

The claw poles provide a similar function to the c-cores in Figure 3-12 providing a path for the flux to be carried round. Bang et al [139] and Polinder et al [140] compare radial and TFM machines for direct drive wind turbines, concluding the TFM is more suitable depending upon the topology used. In the TFM the mmf is produced by a single coil per phase, which allows a higher number of poles to be used than in a conventional machine, resulting in a higher rate of change of energy transfer, and thus higher torque/force density. Assembling and building such machines is, however, very challenging because the airgap has to be very small because of the small pole pitch. The general TFM claw-pole topology was favoured by Keysan for a novel HTS generator, which will be discussed in more detail in Section 3.4.

3.2.1. Operational Loads

Previous structural studies of renewable energy direct drive machines have been presented by Dubois et al [141], McDonald [142], Bang [143] and Zavvos [95], while Sethuraman [144] presented structural considerations of direct drive trains for floating offshore wind turbine installations including propagated wave loads. The type of structural forces sustained by direct drive generators under operational conditions are the same as those borne by smaller geared generators, the difference being the

magnitude of the applied loads. Due to the size of direct drive generators, many of the applied loads require additional support structures to withstand operating conditions.

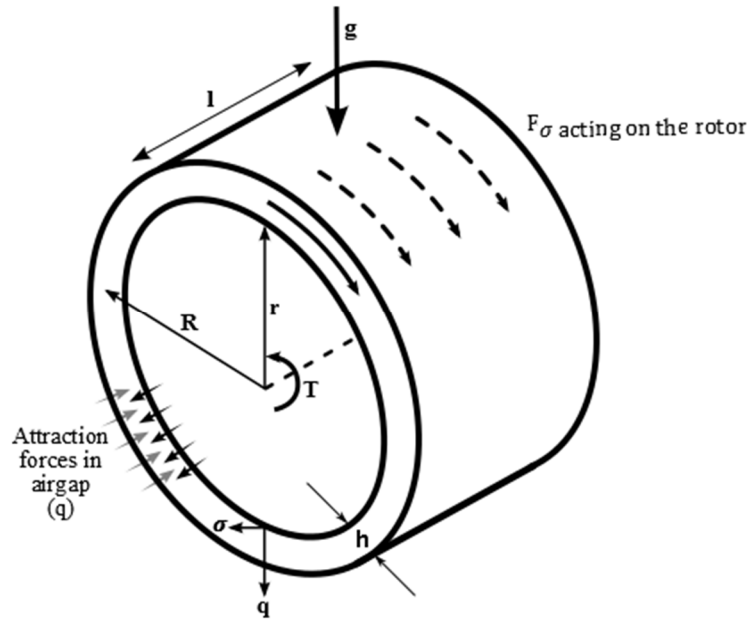


Figure 3-14. Forces acting on a radial flux electrical machine

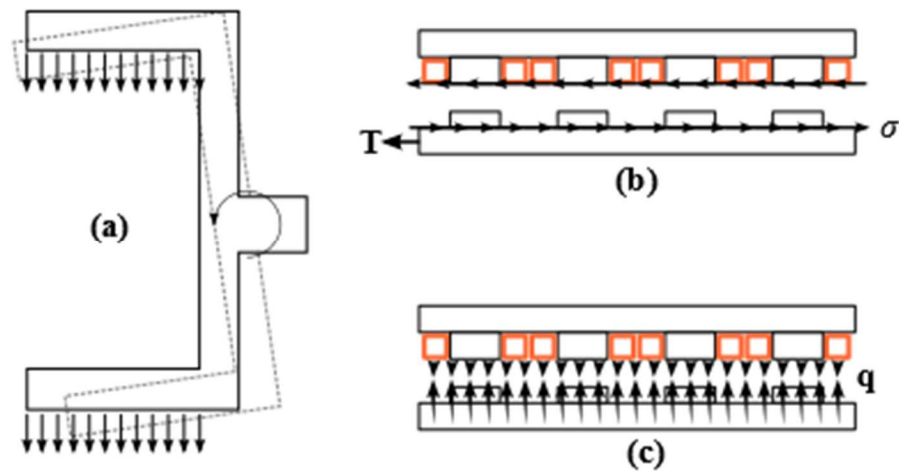


Figure 3-15. (a) Structural loading and moment due to applied gravitational forces on an asymmetric machine topology. (b) Shear stress & (c) normal component of Maxwell stress acting on a radial flux machine or linear machine

The main forces present within an electrical machine, as described by the authors above are listed here:

Shear stress

During operation, electrical machines generate shear stress in the airgap, Figure 3-14 and Figure 3-15. This is the useful force, acting perpendicular to the airgap and creating torque, based on the machines physical dimensions. The shear stress is given as the product of the magnetic and electric loading:

$$\sigma = F/A = BK \quad 3-4$$

Where σ is shear stress, F is perpendicular force on the rotor, A is the rotor surface area, B is the magnetic loading and K is the electric loading.

The magnetic loading is a measure of the maximum magnetic field possible in a machine and is constrained by the properties of electrical steels. In a typical iron-cored generator the magnetic loading could lie between 0.8 and 1.0 T. The electric loading is a measure of the maximum current that can flow in the machine, and is limited by the ability of the cooling system to limit temperature rises. For a naturally air-cooled machine, K is typically 40-50 kAm⁻¹, but for a water cooled machine this could rise to in excess of 100kAm⁻¹. Depending upon the magnetic material properties and the cooling system, the shear stress is a constant, and can then be used as follows to investigate the basic geometry of the machine.

$$A = 2\pi r l \quad 3-5$$

$$T = rF = 2\pi r^2 l \sigma \quad 3-6$$

$$P = \omega T = 2\pi r^2 l \sigma \omega \quad 3-7$$

Where r is the rotor radius, l is the rotor length, T is torque, P is power and ω is angular velocity.

$$\sigma = T/2\pi r^2 l \quad 3-8$$

For a fixed shear stress the power is a function of the radius squared, r^2 , the core length, l , and the angular velocity, ω , and thus depending upon the rotational speed the geometrical space of the machine can be identified. For high speed rotational machines of the order of 1000s rpm, the radius tends to be low with a long core, but with low rotational speed machines, 10s rpm in the case of direct drive, the designer takes advantage of the square relationship for radius resulting in large diameter machines with a short core, resulting in the typical pancake machines as designed for the wind industry.

Maxwell stress

The largest force which acts within an electrical machine, the Maxwell stress, q , is a magnetic attraction force produced by a magnetic field flowing between two iron surfaces as shown in Figure 1-5(c). It is proportional to the square of the flux density B and acts to close the air gap in an electrical machine, given by:

$$q = B^2 / 2\mu_0 \quad 3-9$$

Where μ_0 is the permeability of free space, equal to $4\pi \times 10^{-7}$ H/m. The bigger the airgap in an electrical machine the lower the flux density and hence the lower the Maxwell Stress force. Air cored permanent magnet machines exhibit a larger magnetic gap than in an iron cored machine, resulting in lower magnetic attraction forces. Therefore, iron core machines generally have higher structural mass in order to maintain the required airgap.

Gravitational force

Acceleration due to gravity acts vertically on the machine placing a constant load on the support structure. The force applied due to gravity F_g is provided in equation 3-10.

$$F_g = mg \quad 3-10$$

Where m is the mass of the generator and g is the gravitational acceleration equal to 9.81 ms^{-2} . The structure of a machine can experience high gravitational loading if its topology is asymmetric, leading to tipping and bending moments as shown in Figure 3-15(a).

Thermal expansion and contraction

Thermal expansion of the rotor and stator can lead to the closing of the airgap and thus higher Maxwell stresses on the machines structure. Thermal expansion can occur through friction and heating due to electrical losses. An example of electrical resistance generated heat are copper losses.

$$P_w \propto I^2 R \quad 3-11$$

Where P_w is the copper loss which are proportional to the square of the current, I , times resistance of the coil, R . Copper losses can therefore be described as releasing heat energy as shown by:

$$P_w t = I^2 R t = J \quad 3-12$$

Where t is time and J is heat energy, thus one watt of loss is equal to 1 joule of heat energy. As the temperature increases with in the machine or coils, the resistance of the coils increases leading to higher copper losses therefore adequate cooling must be supplied to stop further losses or structural stresses. Superconducting machines must be able to separate cold components from warm components not only to maintain a superconductive state but to avoid thermal aging of components, localised stresses and unwanted thermal contraction. Many materials become brittle at the temperatures required for superconductivity, therefore special consideration must be made in the selection and separation of superconducting machine components.

Centripetal force

The angular acceleration of a machine rotor can cause torsional deflection of the machine rotor support structure. Centripetal force is proportional to the rotational velocity and the diameter of the machine, it can therefore be equated to the total torque of the machine acting at the airgap radius r , described in equation 3-13. Centripetal force acts radially with the highest force applied to the structure at the airgap.

$$T = P/\omega \quad 3-13$$

Propagated Loads

Harmonic and moment loading due to the interaction of the renewable energy harvesting device and the renewable fluid can apply unforeseen transferred forces to drive train components and the generator structure. Examples of transferred loadings include horizontal and vertical wind shear, yaw error, extreme or irregular waves and inertial vibrations. Vibration and unbalanced loading can drastically decrease the life span of components and supporting structures. In some cases, unbalanced magnetic pull can arise from eccentric rotor positions leading to an increase in radial loads.

$$F_{bmp} = A_g B_g^2 / 2\mu_0 \quad 3-14$$

$$F_{ump} = A_g B_g^2 / 2\mu_0 \times e/g \quad 3-15$$

Where F_{bmp} and F_{ump} represent the balanced and unbalanced radial loads due to eccentric rotor position respectively, A_g is the airgap area, e is the eccentricity of the rotor and g magnetically effective airgap width. While in [129], Mostafa describes unbalanced magnetic pull as:

$$F_{ump} = \frac{L}{2\mu_0} \int_0^{2\pi} \left(\left[\left(\frac{B_{rem} \cdot h_m \cdot e}{(l_g + h_m)^2 - 2e \cdot (l_g + h_m)} \right) \cos((P \pm 1) \cdot \theta) \right]^2 + \left[\frac{B_{rem} \cdot h_m}{l_g + h_m} \cos(P \cdot \theta) \right]^2 \right) d\theta \quad 3-16$$

Where L is the axial length of the machine, B_{rem} is the remnant flux density for permanent magnets, h_m is the magnet height, e is the eccentricity of the rotor, l_g is the concentric airgap length and P is the number of pole pairs. Mostafa's equation provides a simple analytical model for direct radial force calculation generated by static rotor eccentricity, e .

Cogging Torque

Cogging torque is created by the attraction of ferromagnetic materials to the magnetic field created by permanent magnets or field windings in the absence of currents in the armature. The effects of cogging torque can be marginalised for high speed generators,

however within low speed direct drive generators, cogging torque can produce vibrations, speed ripples, noise, position error and reduced generator efficiency. Within claw pole machines cogging torque is especially prevalent due to the increased volume of magnetic material within the claw pole elements. Skewed claw poles, armature stacks and field cores can help reduce cogging torque, as well as optimizing magnet pole width. As suggested by Guo et al [145] and Zarko et al [146], estimation of clogging torque, T_{cog} , can be calculated using the Maxwell stress tensor method or the virtual work method, indicated by equation 3-17.

$$T_{cog} \approx \frac{\Delta W_{fld}'}{\Delta \theta} = \frac{W_{fld2}' - W_{fld1}'}{\theta_2 - \theta_1} \quad 3-17$$

Where W_{fld} is the total energy stored within the magnetic field and θ the rotor position.

Although torque is one of the primary design criteria for electrical machines, it can be deduced from the equations above that a fine line must be tread in order to balance mechanical and structural stresses, electrical losses and power output. Zavvos [95] and Macdonald [142] posit that for direct drive permanent machines the structural deflection criteria must be adhered to:

- A radial deflection restricted to 5-10% of the airgap length, which is assumed to equal 1% of the airgap diameter.
- An axial deflection restricted to 1-2% of the axial length.
- A torsional deflection is restricted to a relative twist of $0.01^0 - 0.5^0$, described by the equation.

$$Z_{allow} \cong \frac{1}{720} 2\pi R \quad 3-18$$

For the purposes of this study these criteria will be compared to the results provided in later chapters.

3.3. Superconducting Direct Drive Technology

“The phenomenon, exhibited by various metals, alloys, and compounds, of conducting electrical current without resistance when cooled to low temperatures”

The serendipitous discovery of superconductivity occurred in 1911. A Dutch Physicist by the name of Heike Kamerlingh Onnes, Figure 3-16, studied the properties and behaviour of materials when cooled to extremely low temperatures. During this research Onnes used various cryogenic techniques to cool elements to super low temperatures, including utilising the Kelvin-Joule effect via the Hampson-Linde cycle [147]. It was with this method that on the 10th of July 1908, two years after liquefying hydrogen, Onnes succeeded in liquefying helium, cooling the gas to below 4 Kelvin.

One of the leading theories about resistance at the time stated that a conductor would reach a lower limit of resistance which would remain constant until absolute zero at which point the resistance would become infinite within the material. However, through various experiments Onnes was able to contradict this theory and on the 8th of April 1911, using the newly created liquid helium and a newly designed cryostat, he cooled mercury to near absolute zero and observed that the resistance decreased continuously until at 4.2 K the resistance of the material jumped to “practically zero” and remained at zero as low as 1.5 K [148]. The temperature at which the material gained its unique properties was named the Critical Temperature (T_c) and Onnes described this concept of virtually zero resistance as superconductivity (SC), receiving a Nobel prize in 1913 for his work on the low temperature properties of materials and his production of liquid helium [149] [150].

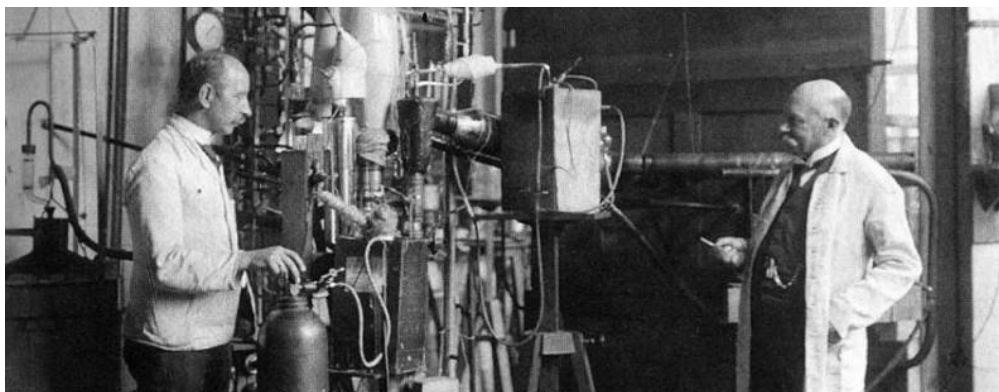


Figure 3-16. Heike Kamerlingh Onnes in his Leiden laboratory, circa 1911 [148]

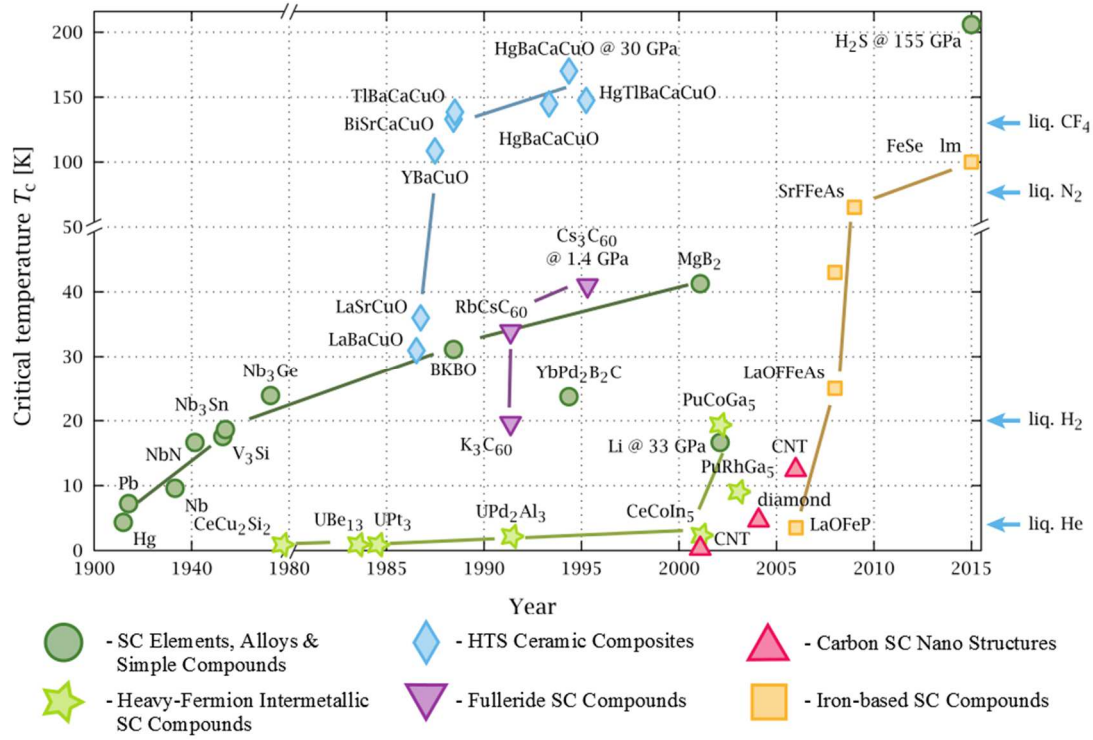


Figure 3-17. The critical temperature (T_c) of superconductors against their discovery.

Adapted from [151] [152] [153] [154] [155]

In the century following its discovery there were limited advancements in the field of superconductivity. However, in 1986 a major discovery was made. While studying copper oxide compounds, Bednorz and Muller discovered that a ceramic compound produced from Lanthanum, Barium, Copper and Oxygen could also become superconducting, and at much higher T_c than previously achieved, up to 138 K [156] [157]. This led to the discovery of many more high temperature superconducting (HTS) composites over the following decades and research into ceramic materials has thrust SC composites into the realms of real world applications with the elusive room temperature superconducting potentially no longer a pipe dream [158] [159]. This section will outline the nature and advantages of the superconducting phenomena and propose its application to renewable energy electrical generation, outlining topologies and reviewing the most promising proposed superconducting machines.

3.3.1. Superconducting 101.

The most important feature leading to the release of a superconductor's superconducting properties is its critical temperature, T_c . Above the T_c a superconductor acts as a normal conductor, when brought below the T_c , a superconducting material displays several properties that make them unique and valuable conductors. As well as T_c , there are two other defining features to the superconducting state, critical magnetic field strength B_c , and critical current J_c . The three-dimensional boundary based on these factors is highlighted in Figure 3-18. For each SC material these three limiting properties may vary, however once outside this boundary superconductors revert back to their non-superconductive state.

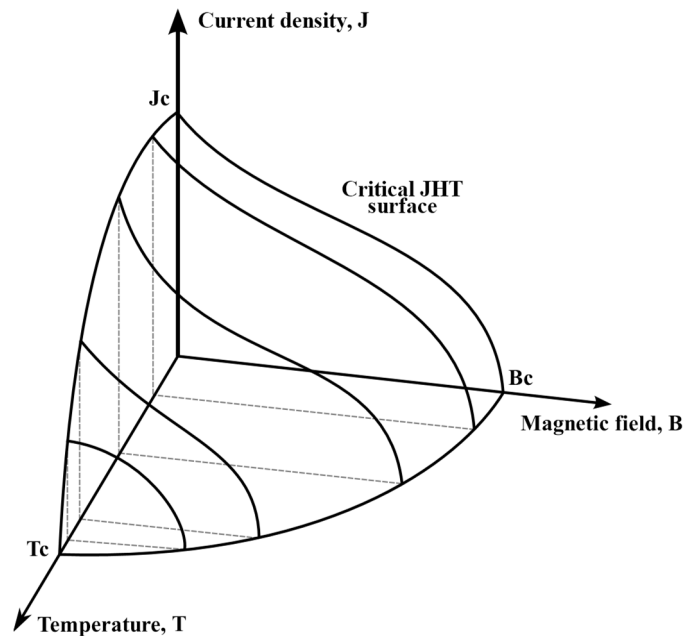


Figure 3-18. Three dimensional boundary of the superconducting state. Created based on [160]

Infinite conductivity

Infinite conductivity or zero resistance allows the persistence of current within the conductor with no decay in energy. Electrical resistance within a conductor occurs due to the interaction of ions and phonons, present within the crystalline structure, with free moving electrons. As the conductor increases in temperature more electrons are able to move within the material resulting in a further scattering effect, increasing the materials resistance. However, as a superconducting material is cooled, electrons act

more as a quantum wave, able to bypass the normal electron path. When super cooled below the conductors T_c , electrons pair and locking into a crystalline structure merging into one quantum wave or condensate, which interacts less with the sub atomic dynamics of the material, thus eradicating the materials internal resistance as shown in Figure 3-19. Until the temperature of the conductor reaches absolute zero, not all electrons are part of the condensate. Electrons that are termed as superconducting electrons while electrons that have not yet reached that phase are called normal electrons. Direct current is able to flow through the conductor without interfering with the normal electron path, however alternating current requires the acceleration and deceleration of electrons which, unless kept at low frequency, generate internal voltages and interact with normal electron paths and disrupt the infinite conductivity properties of the conductor [161] [162].

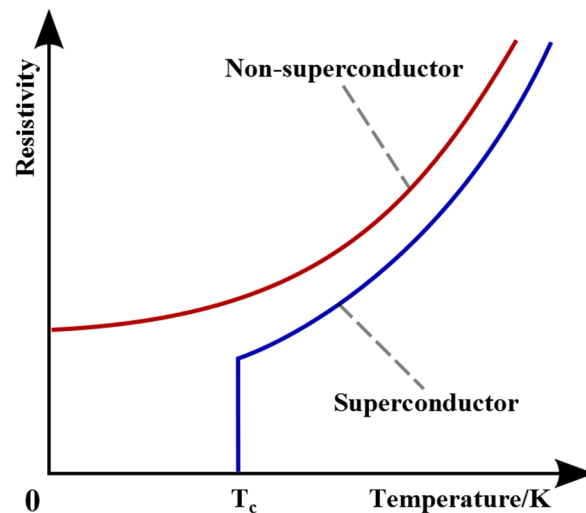


Figure 3-19. Temperature against electrical resistance for conductors and superconductors indicating the effect of critical temperature, T_c , for a superconductor. Created based on [160]

Perfect diamagnetism and the Meissner effect

Perfect diamagnetism is the state in which a conductor will exclude and repel an external magnetic field. When placed near a magnetic field, induced currents inside the conductor will produce a magnetic field which matches exactly that of the external field, the addition of the induced field and the external field causes the total internal field to equal zero. In a normal conductor, perfect diamagnetism is a state that is

temporary and cannot be maintained. This is because induced currents inside the material are dissipated by internal resistance. This property can be maintained within a superconductor due to the lack of internal resistance. When a superconductor is placed within a magnetic field and cooled, currents induced by the magnetic field continue indefinitely with the same magnitude, thus cancelling and excluding any external field change. In addition superconductors exhibit the Meissner effect, which was discovered by Walther Meissner in 1933 [149]. The Meissner effect is the expulsion of any internal magnetic field from a superconducting material during transition to its superconducting state. As a superconductor is cooled, non-decaying electrical currents are formed close to the materials surface, producing magnetic fields which expel its internal magnetic field [17].

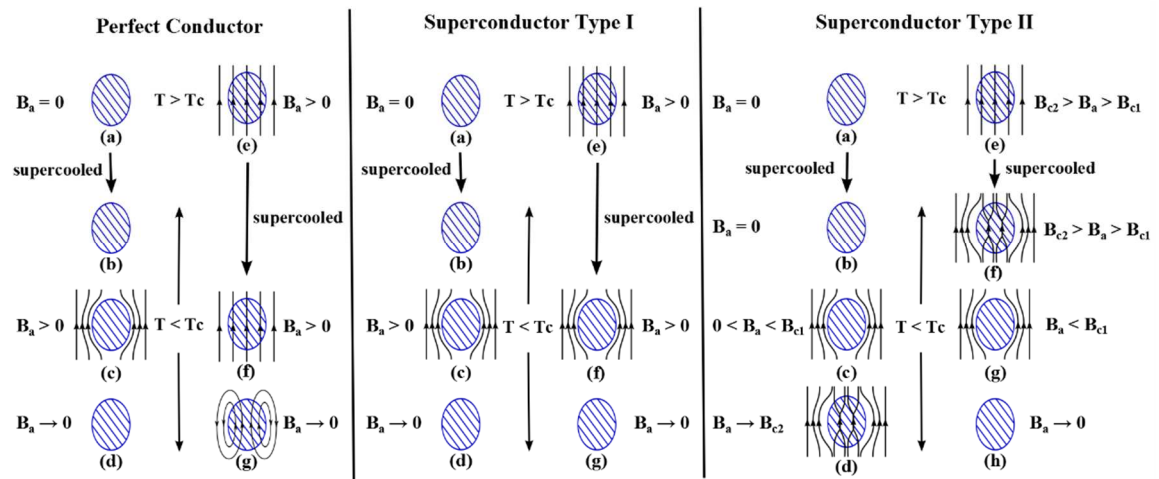


Figure 3-20. Phase diagram of a perfect non superconducting conductor, a Type I superconductor and a Type II superconductor when field B_a is applied during various external conditions. Created based on [156]

Superconducting materials can be split into two types, Type I and Type II. Type I superconductors are generally made from one pure metal element, Figure 3-22, and display both zero internal resistance and the Meissner effect when cooled below T_c . Type II superconductors are alloys or compounds, Figure 3-21, which also display zero DC resistance but exhibit more complex magnetic properties than Type I [163]. Type I Superconductors are susceptible to losing superconducting capabilities when an external magnetic field greater than the materials critical field B_c is reached. However, Type II superconductors adhere to two critical fields, B_{c1} and B_{c2} . Below an external

field of B_{c1} , a Type II compound exhibits the same properties as a Type I, however between B_{c1} and B_{c2} the external magnetic field is not completely excluded, this is called the vortex state. The interior of the superconducting compound starts to arrange itself into normal conducting filaments or flux tubes surrounded by supercurrents, this leads to an effect called a vortex state. External magnetic flux is therefore able to penetrate the flux tubes while the surrounding superconducting material continues to exclude the external flux until its magnitude raises above B_{c2} at which point the compound loses its superconducting abilities. The differences between Type I and Type II phases are shown in Figure 3-21.

The mixed state Meissner property is specific to Type II superconductors since this effect expels magnetic fields regardless of presence of a magnetic field before or after cooling, whereas a normal conductor with perfect diamagnetism would keep the magnitude of the magnetic field in place if cooled within an external magnetic field, as shown in Figure 3-20. This state leads to properties such as flux pinning, based on the propagation of flux in internal flux tubes. Flux pinning or quantum locking allows a superconductor to be pinned in space within a magnetic field. This property becomes important for electrical generation as it curtails the effect of critical current densities and critical field as discussed later.

T_c for Type I superconductors generally have lower T_c than Type II superconductors and Type II superconductors are able to maintain superconductivity in external magnetic fields >10 T, as high as 38 T (Nb_3Ge) [153], whereas Type I are susceptible to fields > 0.2 T. Not all Low Temperature Superconductors, LTSC, are Type I SC while generally most High Temperature Superconductors, HTSC, are Type II. LTSC and HTSC help define the cross over point at roughly 30 K, those above are termed HTSC while those below are termed LTSC and require liquid helium as their cryogen.

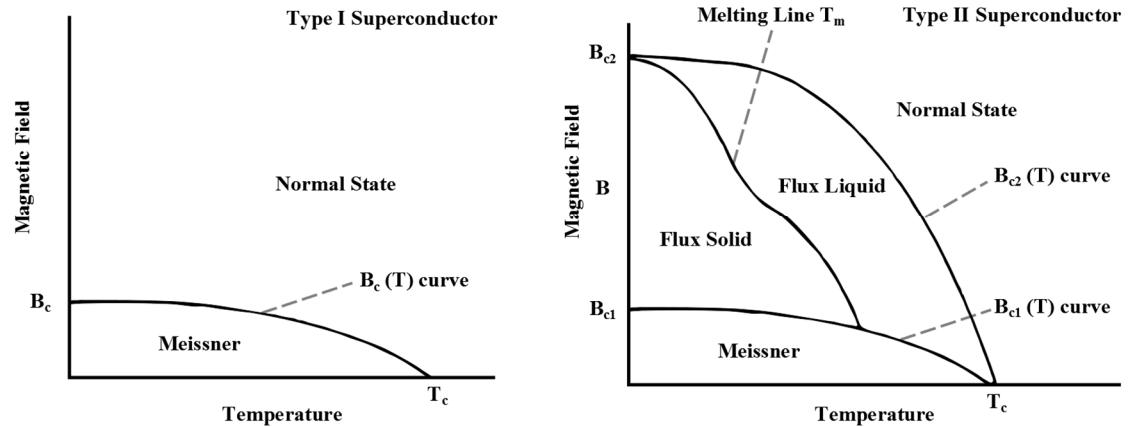


Figure 3-21. Simplified magnetic phase diagram of a Type I and Type II superconductor showing the Meissner region and mixed flux states. Altered from [163]

Critical Current and Quench

While in the superconducting state, SC are able to carry many times the electric current of conventional conductors due to their zero resistivity. However, there is a limit to the amount of current that a SC can maintain. The critical current, J_c , within a SC material is the limit at which above the superconductor will no longer be superconducting, reverting back to a normal conductor. When this occurs the SC material can be badly damaged and the process can be accelerated through the instant introduction of resistive heating effects. This rapid process is called quench. Quench can also be triggered when the T_c or B_c are exceeded.

Within Type I SC J_c is relatively low making them unsuitable for power generation [156]. However, in Type II SC J_c is curtailed by vortex pinning therefore the J_c is generally higher than that found in Type I. The focus for Type II materials is based more on the material and structural purity since these can drastically alter the limit of J_c leading to unexpected quenching.

1 IIA

1
H
Hydrogen

2 IIA

3
Li
Lithium

3 IIIA

19
K
Potassium

4 IVB

20
Ca
Calcium

5 VB

21
Sc
Scandium

6 VIB

22
Ti
Titanium

7 VIIB

23
V
Vanadium

8 VIIIB

24
Cr
Chromium

9 VIIIB

25
Mn
Manganese

10 VIIIB

26
Fe
Iron

11 IB

27
Co
Cobalt

12 IIB

28
Ni
Nickel

13 IIIA

29
Cu
Copper

14 IVA

30
Zn
Zinc

15 VA

31
Ga
Gallium

16 VIA

32
Ge
Germanium

17 VIIA

33
As
Arsenic

18 VIIA

34
Se
Selenium

19 VIIA

35
Br
Bromine

20 VIIA

36
Kr
Krypton

2
He
Helium

10
Ne
Neon

18
Ar
Argon

36
Kr
Krypton

54
Xe
Xenon

86
Rn
Radon

118
Og
Oganesson

1
H
Hydrogen

3
Li
Lithium

11
Na
Sodium

19
K
Potassium

37
Rb
Rubidium

55
Cs
Cesium

87
Fr
Francium

2
He
Helium

10
Ne
Neon

18
Ar
Argon

36
Kr
Krypton

54
Xe
Xenon

86
Rn
Radon

118
Og
Oganesson

3
Li
Lithium

11
Na
Sodium

19
K
Potassium

37
Rb
Rubidium

55
Cs
Cesium

87
Fr
Francium

4
Be
Beryllium

12
Mg
Magnesium

20
Ca
Calcium

38
Sr
Strontium

56
Ba
Barium

88
Ra
Radium

5
B
Boron

13
Al
Aluminum

21
Sc
Scandium

39
Y
Yttrium

57-71
La-Lu
Lanthanide

89-103
Ac-Lr
Actinide

6
C
Carbon

14
Si
Silicon

22
Ti
Titanium

40
Zr
Zirconium

72
Hf
Hafnium

104
Rf
Rutherfordium

7
N
Nitrogen

15
P
Phosphorus

23
V
Vanadium

41
Nb
Niobium

73
Ta
Tantalum

105
Db
Dubnium

8
O
Oxygen

16
S
Sulphur

24
Cr
Chromium

42
Mo
Molybdenum

74
W
Tungsten

106
Sg
Seaborgium

9
F
Fluorine

17
Cl
Chlorine

25
Mn
Manganese

43
Tc
Technetium

75
Re
Rhenium

107
Bh
Bohrium

10
Ne
Neon

18
Ar
Argon

26
Fe
Iron

44
Ru
Ruthenium

76
Os
Osmium

108
Hs
Hassium

11
Na
Sodium

19
K
Potassium

27
Co
Cobalt

45
Rh
Rhodium

77
Ir
Iridium

109
Mt
Meitnerium

12
Mg
Magnesium

20
Ca
Calcium

28
Ni
Nickel

46
Pd
Palladium

78
Pt
Platinum

110
Ds
Darmstadtium

13
Al
Aluminum

21
Sc
Scandium

29
Cu
Copper

47
Ag
Silver

79
Au
Gold

111
Rg
Roentgenium

14
Si
Silicon

22
Ti
Titanium

30
Zn
Zinc

48
Cd
Cadmium

80
Hg
Mercury

112
Uub
Ununbium

15
P
Phosphorus

23
V
Vanadium

31
Ga
Gallium

49
In
Indium

81
Tl
Thallium

113
Uut
Ununtrium

16
S
Sulphur

24
Cr
Chromium

32
Ge
Germanium

50
Sn
Tin

82
Pb
Lead

114
Uuq
Ununquadium

17
Cl
Chlorine

25
Mn
Manganese

33
As
Arsenic

51
Sb
Antimony

83
Bi
Bismuth

115
Uup
Ununpentium

18
Ar
Argon

26
Fe
Iron

34
Se
Selenium

52
Te
Tellurium

84
Po
Polonium

116
Uuh
Ununhexium

19
K
Potassium

27
Co
Cobalt

35
Br
Bromine

53
I
Iodine

85
At
Astatine

117
Uus
Ununseptium

20
Ca
Calcium

28
Ni
Nickel

36
Kr
Krypton

54
Xe
Xenon

86
Rn
Radon

118
Uuo
Ununoctium

21
Sc
Scandium

29
Cu
Copper

37
Rb
Rubidium

55
Cs
Cesium

87
Fr
Francium

22
Ti
Titanium

30
Zn
Zinc

38
Sr
Strontium

56
Ba
Barium

88
Ra
Radium

23
V
Vanadium

31
Ga
Gallium

39
Y
Yttrium

57-71
La-Lu
Lanthanide

89-103
Ac-Lr
Actinide

24
Cr
Chromium

32
Ge
Germanium

40
Zr
Zirconium

72
Hf
Hafnium

104
Rf
Rutherfordium

25
Mn
Manganese

33
As
Arsenic

41
Nb
Niobium

73
Ta
Tantalum

105
Db
Dubnium

26
Fe
Iron

34
Se
Selenium

42
Mo
Molybdenum

74
W
Tungsten

106
Sg
Seaborgium

27
Co
Cobalt

35
Br
Bromine

43
Tc
Technetium

75
Re
Rhenium

107
Bh
Bohrium

28
Ni
Nickel

36
Kr
Krypton

44
Ru
Ruthenium

76
Os
Osmium

108
Hs
Hassium

29
Cu
Copper

37
Rb
Rubidium

45
Rh
Rhodium

77
Ir
Iridium

109
Mt
Meitnerium

30
Zn
Zinc

38
Sr
Strontium

46
Pd
Palladium

78
Pt
Platinum

110
Ds
Darmstadtium

31
Ga
Gallium

39
Y
Yttrium

47
Ag
Silver

79
Au
Gold

111
Rg
Roentgenium

32
Ge
Germanium

40
Zr
Zirconium

48
Cd
Cadmium

80
Hg
Mercury

112
Uub
Ununbium

33
As
Arsenic

41
Nb
Niobium

49
In
Indium

81
Tl
Thallium

113
Uut
Ununtrium

34
Se
Selenium

42
Mo
Molybdenum

50
Sn
Tin

82
Pb
Lead

114
Uuq
Ununquadium

35
Br
Bromine

43
Tc
Technetium

51
Sb
Antimony

83
Bi
Bismuth

115
Uup
Ununpentium

36
Kr
Krypton

44
Ru
Ruthenium

52
Te
Tellurium

84
Po
Polonium

116
Uuh
Ununhexium

37
Rb
Rubidium

45
Rh
Rhodium

53
I
Iodine

85
At
Astatine

117
Uus
Ununseptium

38
Sr
Strontium

46
Pd
Palladium

54
Xe
Xenon

86
Rn
Radon

118
Uuo
Ununoctium

39
Y
Yttrium

47
Ag
Silver

55
Cs
Cesium

87
Fr
Francium

40
Zr
Zirconium

48
Cd
Cadmium

56
Ba
Barium

88
Ra
Radium

41
Nb
Niobium

49
In
Indium

57-71
La-Lu
Lanthanide

89-103
Ac-Lr
Actinide

42
Mo
Molybdenum

50
Sn
Tin

72
Hf
Hafnium

104
Rf
Rutherfordium

43
Tc
Technetium

51
Sb
Antimony

73
Ta
Tantalum

105
Db
Dubnium

44
Ru
Ruthenium

52
Te
Tellurium

74
W
Tungsten

106
Sg
Seaborgium

45
Rh
Rhodium

53
I
Iodine

75
Re
Rhenium

107
Bh
Bohrium

46
Pd
Palladium

54
Xe
Xenon

76
Os
Osmium

108
Hs
Hassium

47
Ag
Silver

55
Cs
Cesium

77
Ir
Iridium

109
Mt
Meitnerium

48
Cd
Cadmium

56
Ba
Barium

78
Pt
Platinum

110
Ds
Darmstadtium

49
In
Indium

57-71
La-Lu
Lanthanide

79
Au
Gold

111
Rg
Roentgenium

50
Sn
Tin

72
Hf
Hafnium

80
Hg
Mercury

112
Uub
Ununbium

51
Sb
Antimony

73
Ta
Tantalum

81
Tl
Thallium

113
Uut
Ununtrium

52
Te
Tellurium

74
W
Tungsten

82
Pb
Lead

114
Uuq
Ununquadium

53
I
Iodine

75
Re
Rhenium

83
Bi
Bismuth

115
Uup
Ununpentium

54
Xe
Xenon

76
Os
Osmium

84
Po
Polonium

116
Uuh
Ununhexium

55
Cs
Cesium

77
Ir
Iridium

85
At
Astatine

117
Uus
Ununseptium

56
Ba
Barium

78
Pt
Platinum

86
Rn
Radon

118
Uuo
Ununoctium

57-71
La-Lu
Lanthanide

79
Au
Gold

87
Fr
Francium

72
Hf
Hafnium

80
Hg
Mercury

88
Ra
Radium

73
Ta
Tantalum

81
Tl
Thallium

89-103
Ac-Lr
Actinide

74
W
Tungsten

82
Pb
Lead

90
Th
Thorium

75
Re
Rhenium

83
Bi
Bismuth

91
Pa
Protactinium

76
Os
Osmium

84
Po
Polonium

92
U
Uranium

77
Ir
Iridium

85
At
Astatine

93
Np
Neptunium

78
Pt
Platinum

86
Rn
Radon

94
Pu
Plutonium

79
Au
Gold

87
Fr
Francium

95
Am
Americium

80
Hg
Mercury

88
Ra
Radium

96
Cm
Curium

81
Tl
Thallium

89-103
Ac-Lr
Actinide

97
Bk
Berkelium

82
Pb
Lead

90
Th
Thorium

98
Cf
Californium

83
Bi
Bismuth

91
Pa
Protactinium

99
Es
Einsteinium

84
Po
Polonium

92
U
Uranium

100
Fm
Fermium

85
At
Astatine

93
Np
Neptunium

101
Md
Mendelevium

86
Rn
Radon

94
Pu
Plutonium

102
No
Nobelium

87
Fr
Francium

95
Am
Americium

103
Lr
Lawrencium

88
Ra
Radium

96
Cm
Curium

89-103
Ac-Lr
Actinide

97
Bk
Berkelium

90
Th
Thorium

98
Cf
Californium

91
Pa
Protactinium

99
Es
Einsteinium

92
U
Uranium

100
Fm
Fermium

93
Np
Neptunium

101
Md
Mendelevium

94
Pu
Plutonium

102
No
Nobelium

95
Am
Americium

103
Lr
Lawrencium

96
Cm
Curium

97
Bk
Berkelium

98
Cf
Californium

99
Es
Einsteinium

100
Fm
Fermium

101
Md
Mendelevium

102
No
Nobelium

103
Lr
Lawrencium

Figure 3-22. Current Superconducting elements and elements which form superconducting composite compounds [164]

Superconducting materials

The properties of superconductors are vitally important for SC utilisation and the creation of reliable tapes, wires and bulk materials for active SC applications. The SC material properties must be understood in order for the correct material to be used within an electrical motor or generator, ideally utilising materials with high critical temperatures, high current densities, high critical field tolerance and low susceptibility to quench due to material flaws and operational constraints. The installation and commercial availability of SC materials has been difficult to achieve due to the requirement for pure structures and repeatable production techniques [165]. The fabrication of HTS ceramic materials has proved highly problematic, which has slowed the development of SC applications, however as the commercial use of SC continues to rise in turn this should drive the investment for refined fabrication techniques resulting in lower production costs [166] [167].

The first practical superconducting wires were produced in the 1960's, constructed from NbTi and Nb₃Sn [168]. For applications such as NMR machines or plasma reactors, these materials are critical in providing high powered magnets however with very low T_c, cooling and cryogenic systems are expensive. During the late 1990's

commercially ready HTS tapes could be practically manufactured, thus boosting the development of HTS materials. Currently the three commercially available materials proposed for superconducting machines are first generation BSCCO tapes, second generation YBCO tapes and MgB_2 wire. First generation (1G) BSCCO HTS tapes contain SC material as filaments surrounded by a silver support. The tapes are sensitive to material imperfections created during manufacture thereby suffering performance limitations. Therefore due to expensive material and labour costs curtailing commercial production, first generation (1G) BSCCO tapes have limited active industrial use [169] [170].

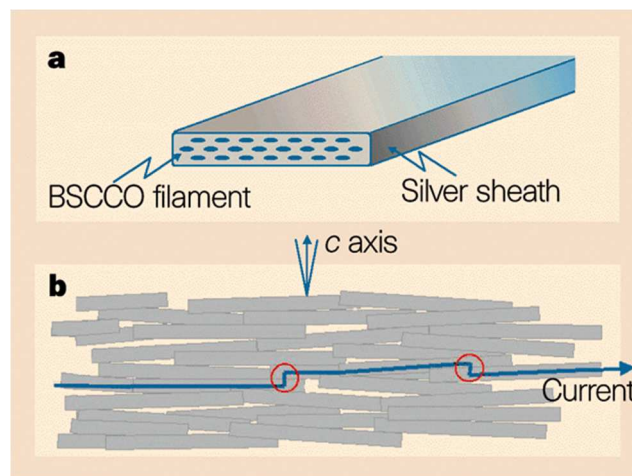


Figure 3-23. a) A BSCCO tape architecture. b) Material and filament impurities causing an undulating current path [171]

Second generation HTS (2G) tape is generally more mechanically, thermally and electrically stable than first generation (1G) tape architecture. This has led to the ability to produce more complex winding designs, higher manufacturing reliability and thus lower production costs [169]. Material costs are lower due to the inexpensive nickel alloy substrate which makes up to 97% of the tapes material and production is made simpler by automated production [170]. Second generation (2G) YBCO tape has a T_c of 92K.

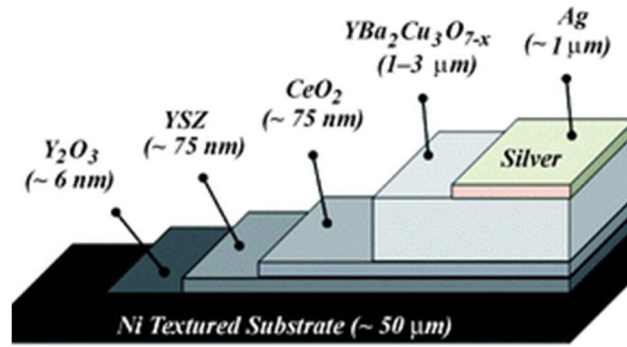


Figure 3-24. Schematic of a YBCO tape architecture [172]

MgB₂ is a low temperature superconducting (LTS) compound with a T_c of ~ 39 K. An unusual material on the cusp of being termed a HTS, MgB₂ was not investigated as a superconducting material until 2001, 51 years after its discovery as a compound. Although potentially costly in cryogenic cooling, MgB₂ is a fairly cheap and relatively easy material to manufacture into bulk, tape, films and wire. It also boasts an estimated J_c up to 130000 kA/cm² approaching 0 K [173] [174].

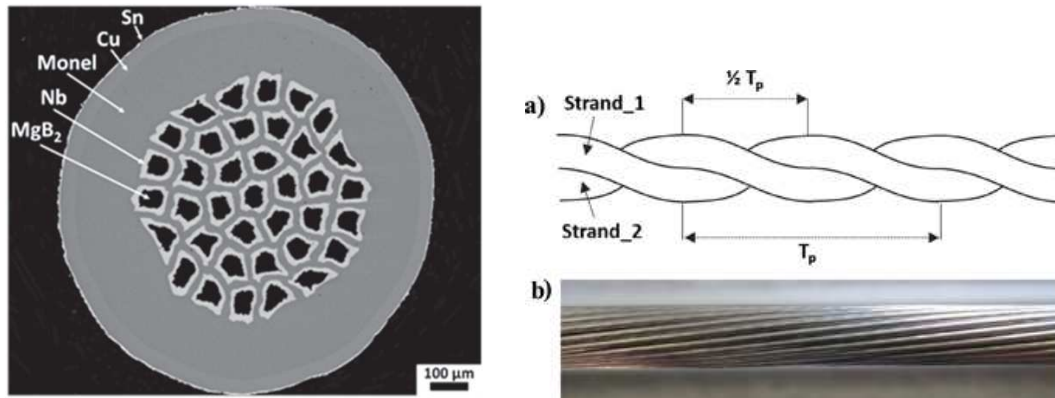


Figure 3-25. Left: Example of the cross-sectional architecture of a MgB₂ SC wire. Right: (a) Schematic illustration of a two strand cable indicating the twist pitch T_p and the half twist pitch, $1/2 T_p$. (b) Part of the one meter cable composed by a Cu core and 18 MgB₂ strands [175]

The common properties of the superconducting composite materials mentioned above are provided in Table 3-1. The projected price of BSCCO and YBCO wires is plotted against an extrapolated copper price in Figure 3-26. In addition, companies continue to investigate other superconducting tape and substrates, with the intention of easier to manufacturing techniques or superior material properties.

Parameter	MgB ₂	YBCO	Bi-2223
T _c (K)	39	92	110
J _c at 4.2 K (A/cm ²)	~10 ⁶	~10 ⁶	~10 ⁷
B _{c2} at 4.2 K	15 - 20	>100	>100
B _{c1} at 4.2 K	6 ~12	5 ~7 (77K)	0.2 (77K)
Resistivity ρ(T _c) (μΩcm)	0.4	150 ~800	40 ~60
Cost	1 €/m	20-30 €/m	10 €/m

Table 3-1. Typical parameters and cost for commercially available superconductors [176]

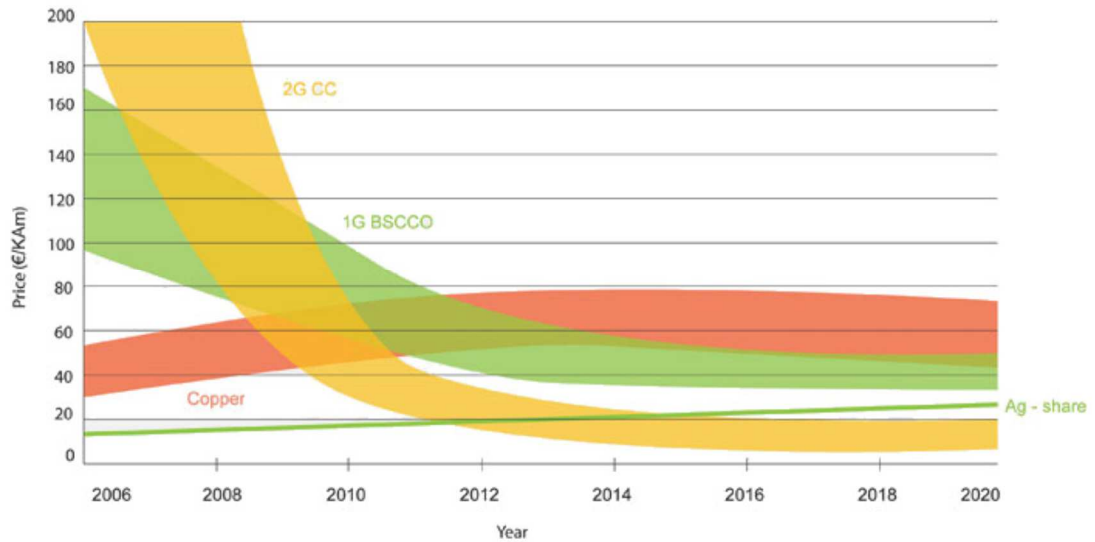


Figure 3-26. YBCO, BSCCO and copper wire price (€/kAm) projection from 2014 [164]

Cryo-coolers and cooling systems

Cryo-coolers or alternative low temperature cooling systems are required to maintain a SC material in its preferred superconducting state and will continue to go hand in hand with superconducting machines until a SC composite can operate near to atmospheric temperatures. Cryogenic systems have made great technological strides within the last 25 year, pushed on by such advancements as MRI machine refinement, scientific research requirements and aerospace programs [177] [178]. A cryogenic system typically removes heat energy from a material via a cryogen which is cooled in a cryo-cooler via heat exchange at various compression and expansion pressures. Heat exchange must typically occur at an efficiency of 95% in order to provide net refrigeration, however the efficiency of the cooling system is usually between 1-20% depending on the cryogenic medium [177]. The five most common cryo-cooler systems are given in Figure 3-27, while the system efficiency for small cryo-coolers is provided in Figure 3-28.

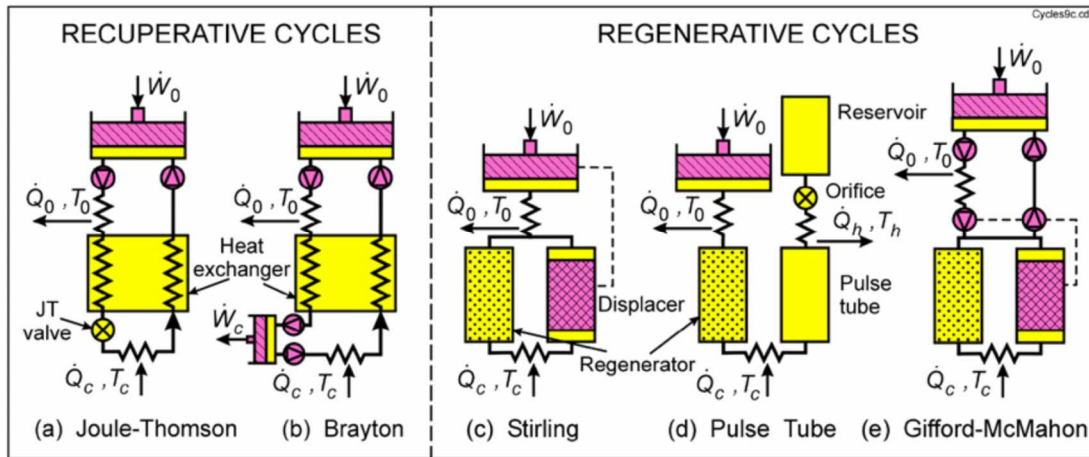


Figure 3-27. Schematics of five common cryo-cooler systems [177]

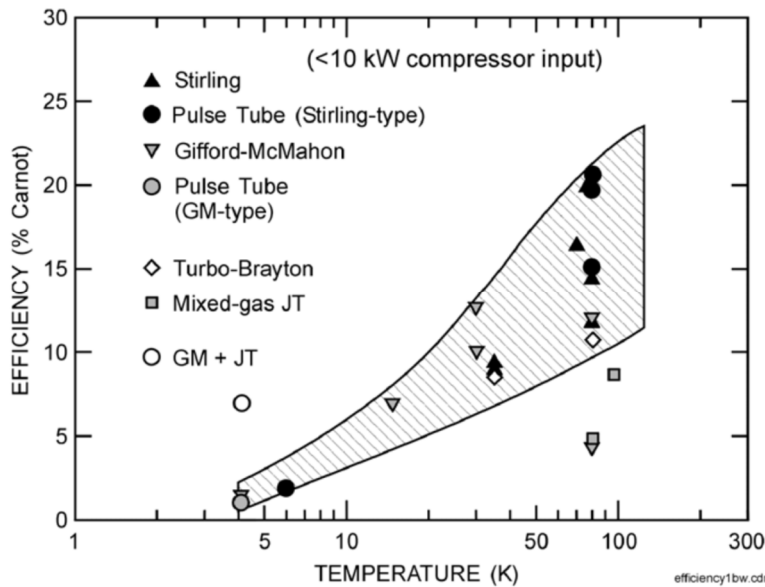


Figure 3-28. Efficiency of small cryo-coolers as a percentage of the Carnot cycle [177]

The efficiency of cryo-coolers decrease dramatically as the cryogen's temperature approaches absolute zero. It has been summarised by O. Keysan [164] and J. W. Bray [166] that the removal of 1W of heat at ~70K, 15-20 W of power is required by the cryo-cooler, as the required cryogen temperature reduces the cooling power increases, so that at 30 K it most cryo-coolers will require 50-75 W, as shown in Table 3-2.

Operating Temperature (K)	Watt Input per Watt Lifted
273	~0.4
200	~2
150	~4
100	~8-10
77	~12-20
50	~25-35
40	~35-50
30	~50-75

Table 3-2. Illustration of the amount of power required to remove 1W at specific operating temperatures [166]

Cryogenic cooling power can therefore vary from 0.16% for a machine operating at 30 K to 1.2% for a machine operating at 4 K, which can drastically effect overall power generation efficiency [164].

There are currently a handful of cryogens able to be utilised for SC machines. Many cryogenic systems require the relatively rare and expensive helium gas as the cooling medium with low vacuum levels to maintain a superconductive state. Helium gas has a boiling point of 4.2 K, hydrogen can be cooled to 15 K useful for cooling MgB₂ wires and although readily available and inexpensive it is not preferred due to its chemical volatile state. Neon has a boiling point of 27 K and boasts cryo-coolers cheaper than helium coolers, however the gas itself is expensive and its chemical properties do not lend themselves to efficient cooling. With the advent of HTS conductors it became possible to use liquid nitrogen with an operating temperature of 63 K and cryo-coolers which are much cheaper and more available than helium.

In order to reduce cost, increase reliability and limit machine complexity, direct conduction cooling has been employed on SC machines [179], [180], [181], [182], [51] and [53]. Direct conduction still requires a cryogen however the cryogen does not come into contact with the machine or coils directly. Instead a cold head is used as a medium to transfer heat away from the coil via separation of the cryogen. The cold head re-condenses the cryogen for reuse, instead of allowing the cryogen direct contact with the coil which could lead to cryogenic boil off. In this manner a less complicated cryogen circulatory system is required thus enabling a more compact and reliable method of cooling.

Currently cryogenic systems are an unfortunate efficiency and cost burden that superconductors must carry, however continued advancements in cryo-cooler systems, superconducting compound properties and cryo free cooling systems may open the door for improved system costs, size, efficiency and reliability.

3.3.2. Superconducting technology for energy

Replacing all copper windings and permanent magnets within an electrical machine with superconducting wire or tape would lead to a revolution in motors and electrical energy production. Although SC technology has yet to reach its full potential, far from being a new concept, SC machines have been researched and improved for many decades. Figure 3-29 indicates the breadth of cryogenics and superconducting applications within the modern world.

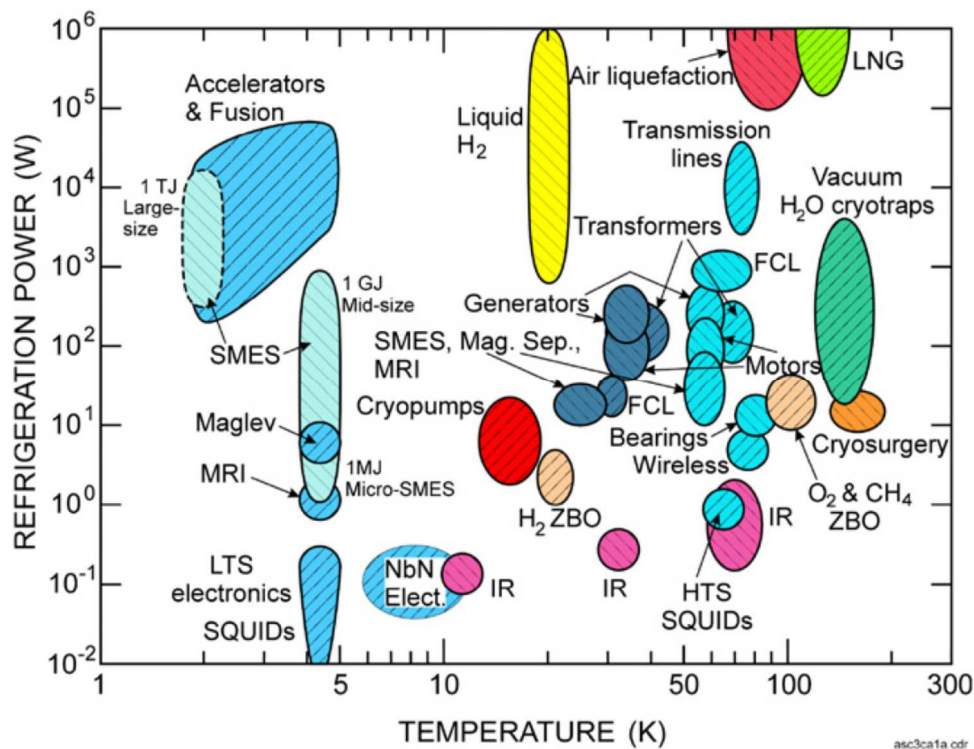


Figure 3-29. Map of cryo-cooler applications indicating the numerous applications for superconducting technology [177]

There are a variety of studies which proves the feasibility of SC within ship motors, aircraft propulsion, electric vehicles as well as numerous electrical generation applications as detailed by Ainslie et al [183], Snitchler et al [65], and Qu [66].

Superconducting elements used for power generation or motors have shown increasing promise in the last few decades. From bulk superconducting magnets to high temperature superconducting tape, there has been wide and varied topologies aimed at harnessing the benefits of superconductivity.

For over a century the benefits of superconductors for motors and generators have been well documented. High flux fields can lead to highly compact machines with high torque, high power densities and close to 100% efficiency when utilising DC. Realising the potential of this technology depends on the advancement and cost reduction of SC composite materials as well as new structural designs, new motor and generator design. Many papers have been written on the theoretical potential of different SC machine designs. To gain industrial respect, SC technology must prove to be as effective as current the industrial standard. The superconducting motor and generator industry does not yet have a working record, especially in the renewables sector. To compound the issue, the harsh offshore marine environment adds additional hurdles for the technology to overcome especially when considering a cryogenic cooling system.

Superconducting Generators

While there have been few moves to apply superconducting technology to wave or tidal installations, many studies and conceptual designs have been produced for superconducting generators suitable for wind turbine and hydro electric energy extraction. Figure 3-30 depicts current geared and PM direct drive systems against the theoretical benefits HTS technology could bring to the wind industry. Superconducting machines can offer the following overall benefits to the energy industry:

- Reduced mass
 - Ironless active parts
 - Higher magnetic fields
- Lower rotational speeds
 - High torque, direct drive power take off
- Higher efficiencies
 - Lower generational losses

- Higher current densities
- Higher magnetic field
- Reduction or absence of rare earth materials
- Low inductance

Maples et al [94] and Lesser et al [186] compared HTS machines against conventional DDPM generators, with the conclusion that although SC systems introduces new untested technology to the sector, the economics of HTS improve with increasing turbine size and the application of HTSC generators have an advantage in weight, efficiency and scalability. However, Lesser et al also comments on the availability, manufacturability and reliability of BSCCO and YBCO tapes and the direct cost implications on this relatively new technology.

Jensen et al [187] discuss the commercial activities in the field of SC generation for wind turbines. They agree that until a market has been created for SC tape and wire, manufacturers will be unwilling to place the investment required to expand production. However, they conclude that since SC machines have retained industrial interest for decades and turbines are expected to increase in size and electrical output, SC generators may outcompete existing technologies. Lloberas et al [188] and Qu et al [189] produce extensive reviews of direct drive SC generators for wind power generation. Lloberas et al conclude that SC rotor technology require greater research investment to understand the thermal, mechanical and fabrication implications for a rotor SC design. Qu et al agrees that further design considerations must be undertaken for the technology to advance, while stating that the best topology will be created from a combination of maximised output, minimum expense and highest reliability.

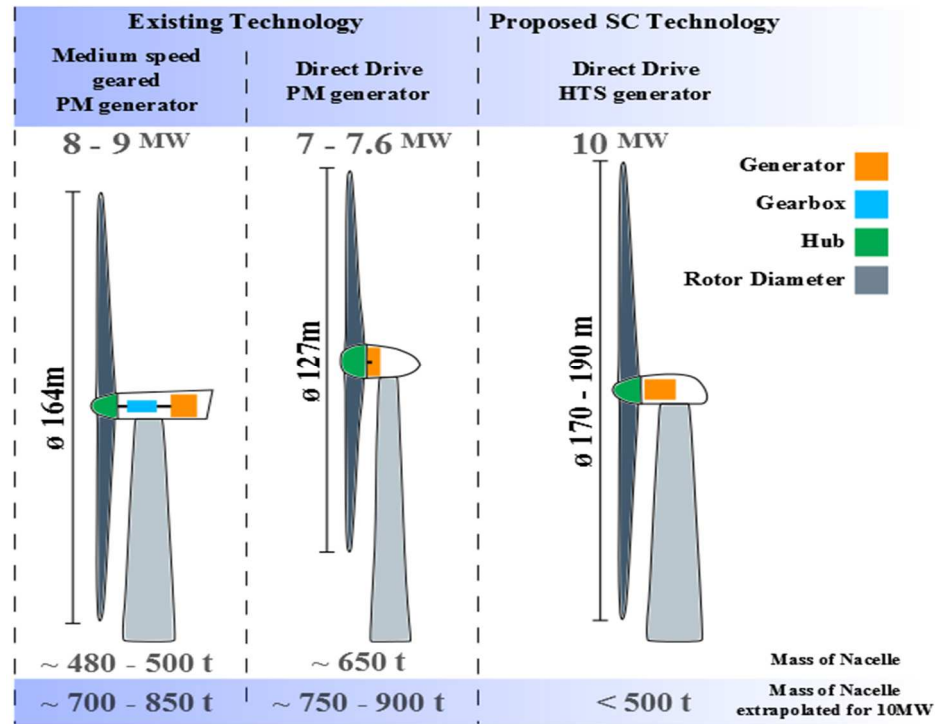


Figure 3-30. Mass comparison between current geared and direct drive wind turbine technology and proposed superconducting generator technology. Based on details provided in [164]

In [164] Keysan outlines proposed superconducting machine topologies and discusses applications for superconductors in electric power. Common superconducting machine topologies are discussed providing details about conventional stators with superconducting rotors, homopolar superconducting machines and axial flux superconducting machines. Finally, a transverse flux superconducting machine is presented which will later be used as the basis of a superconducting generator study. The following section will highlight some of the new generation topologies while mentioning some of the most promising historical superconducting generator concepts.

Suprapower Project

The Suprapower project is an EU FP7 research project. Since its commencement in December 2012, the project aimed to develop a lightweight, reliable, compact, direct drive partially superconducting generator for offshore wind turbines, as patented by TecNALIA [190]. The generating system comprises of a salient pole synchronous

machine utilising MgB_2 wire in 9 modular race track wound field coils [51]. Copper windings at ambient temperature are used for the stator coils. The project proposes a crogen-free cold head cooling system, with modular two stage Gifford-McMahon cryo-coolers and modular cryostats in order to improve reliability and simplify the system for the offshore environment, these are presented in Figure 3-31.

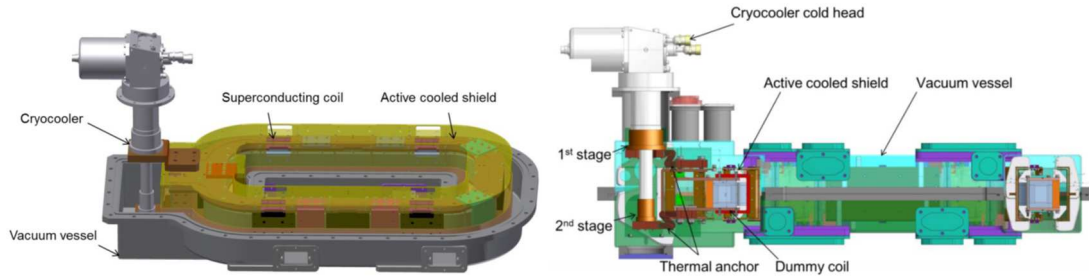


Figure 3-31. Left. External detail of Suprapower modular cryostat and cryo-cooler design [191]. Right. Internal detail of Suprapower modular cryostat and cryo-cooler design [192]

The MgB_2 field coils operate at a temperature of 20 K with a heat load per coil of 2.17 W per coil during secondary stage cooling [191]. The cooling system, from stationary compressor to cryo-coolers on the rotor is given in Figure 3-32.

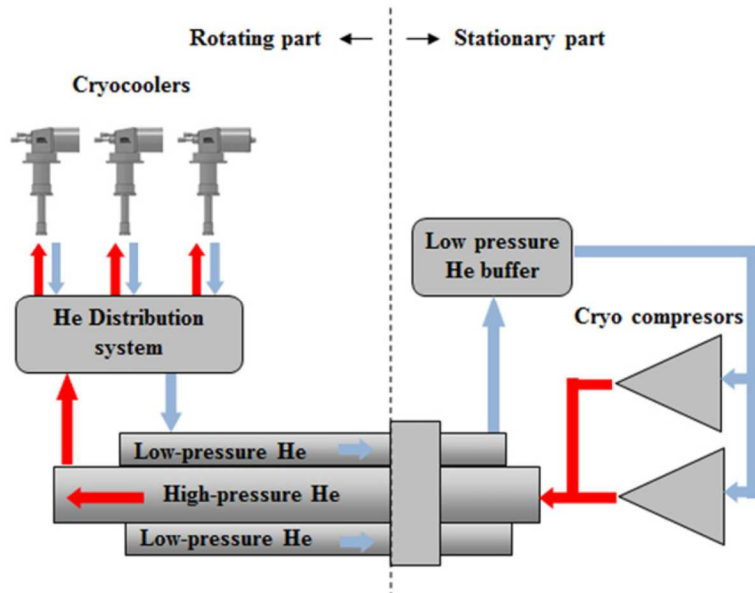


Figure 3-32. Schematic of cooling cycle for the Superpower project [193]

During the project testing was successfully completed on a full size MgB_2 field coil and a modular cryostats that would be used on in a proposed 550 kW demonstrator

[51], [194]. Suprapower's 10 MW, 8.1 rpm generator structure and cooling system are presented in Figure 3-33, while the specifications of both the 10 MW machine and proposed scale demonstrator are provided in Table 3-3.

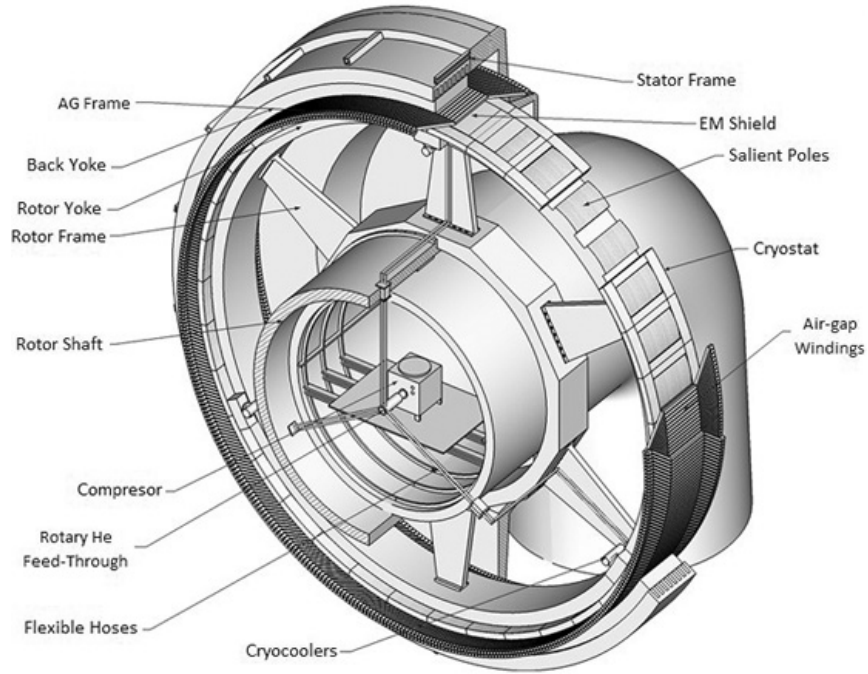


Figure 3-33. Suprapower's 10MW superconducting generator structure [195]

Parameters	10 MW generator	Scale generator
Number of poles	60	4
Rated power (kW)	10000	550
Rated speed (rpm)	8.10	121.5
Rated torque	11.8 MN·m	45.502 kN·m
Air gap diameter	15 m	750 mm
Stack length (m)	0.52	0.52

Table 3-3. Suprapower's 10 MW and scaled demonstrator specifications [191]

The generator is expected to reduce head mass by up to 30% compared to conventional generation systems, resulting in an overall structural mass of ~200 tons and an estimated drive train cost of ~300,000 €/MW. Generator efficiency at full load is expected to be over 95% [195]. However, rotating superconducting connections have often proved unreliable and the rotors rotational stresses and vibrations have yet to be proven on the MgB₂ coils and modular cryostats.

HTS-GEN Project

The Danish based HTS-GEN project, started in October 2013, aims to develop the first direct drive HTS generator for wind turbines [52]. In order to achieve this aim the group designed and built a test segment of a generator in order to study the thermal, mechanical and electromagnetic properties of the proposed machine. Seng et al [196] provide a description of testing a full sized HTS coil and pole pair segment for a 2 MW generator is presented. Figure 3-34 presents the test apparatus and sectional generator geometry.

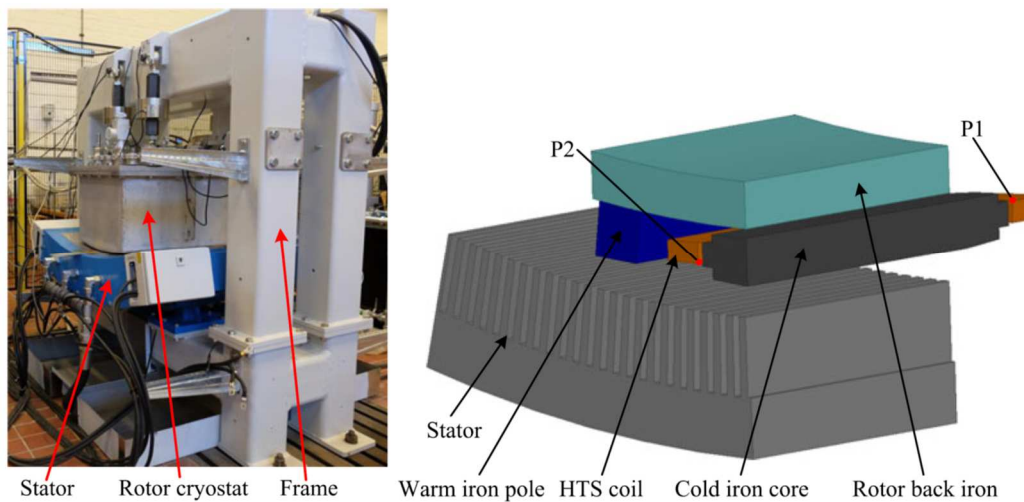


Figure 3-34. Left. Sectional machine in situ for testing. Right. A one quarter model of the section for 3D electromagnetic analysis [196]

The proposed 2 MW machine utilises YBCO HTS tape on the rotor with operating temperatures during testing of 77 K and 40 K, using first liquid nitrogen and then an enclosed vacuum cryostat. Full test results are currently unavailable and the generators final design will be based on continued research. However, the step by step approach to the design and build of a large scale superconducting generator with detailed reporting will no doubt benefit and improve the knowledge within the sector. As with the Suprapower project, Seng et al expect that confirmed full scale performance data means coil design, cooling and installation will be honed for industrial production instead of scaling from prototype topologies.

INNWIND Project

The INNWIND project is a beyond state of the art successor of the Upwind project (2006 - 2011) which aimed to develop and verify vital wind turbine components in order for the wind industry to mature and continue to grow [197]. The INNWIND project continues the premise of researching the entire turbine system, from resource to grid connection, however with the additional aspiration of moving well beyond current technology possibilities and focusing offshore wind turbine designs of 10 – 20 MW. Figure 3-35 indicates the INNWIND's SC DD generator topology connected to a rotor and nacelle. The novel placement of the generator in front of the rotor, the King-Pin drive, allows the generator to be directly coupled with the rotor hub creating a simplified drive train.

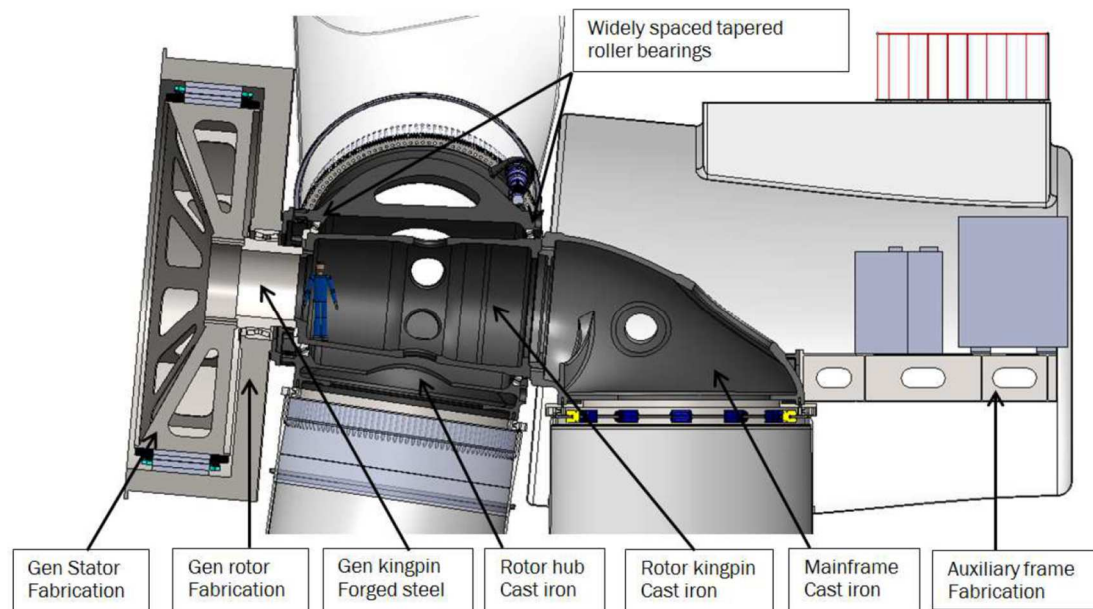


Figure 3-35. Cross section Schematic of INNWIND 10 – 20 MW turbine generation system and nacelle King-Pin layout [198]

The INNWIND project has compared both MgB_2 and HTS YBCO rotor field windings, whilst also investigating the optimized cost and construction for the rotor and stator topology, from fully iron-cored to air-cored as shown in Figure 3-36 and Figure 3-37.

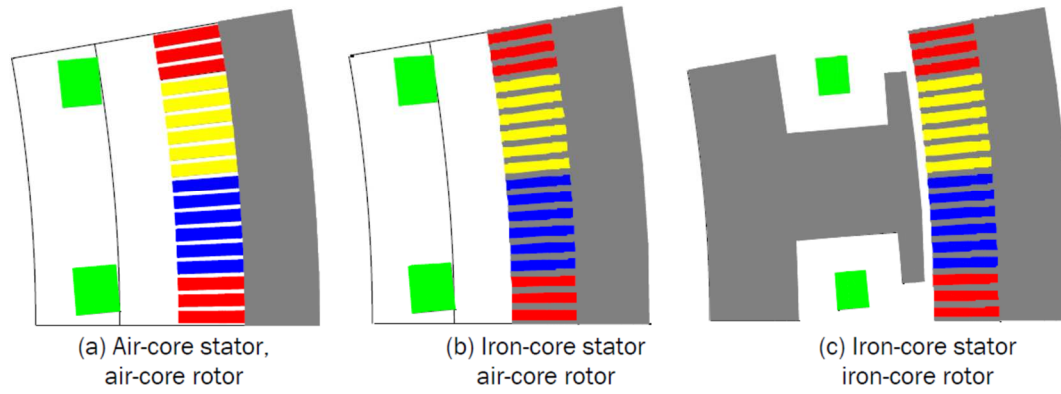


Figure 3-36. Potential superconducting generator topologies [199]

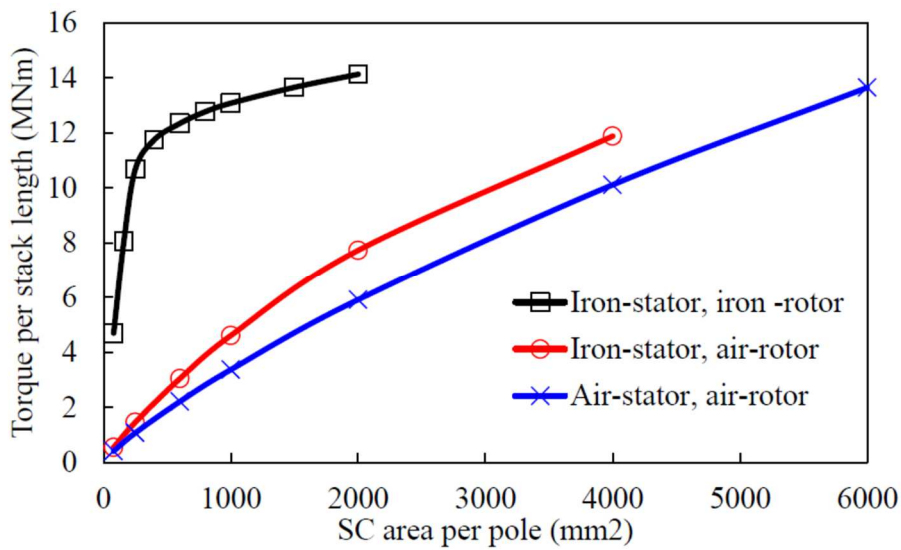


Figure 3-37. Variations of torque with superconducting tape area per pole for a 7m diameter SC generator [199]

While the application of HTS materials is easier for SC machines, due to cryo-cooler efficiencies and cryogenic costs, INNWIND is currently focused on MgB₂ superconductor performance. Therefore for a 10 MW SC generator using MgB₂ windings at 20 K, INNWIND has estimated a generator diameter of 6 m and a turbine rotor diameter of 178 m with a nominal rotor speed of 9.7 rpm and torque capacity of 10.5 MNm [200]. Specifications for a scaled up 20 MW 7 m diameter and 11 m diameter generator are provided in Table 3-4, with a comparative 10 MW 7 m diameter generator provided alongside.

	10 MW	20 MW-I	20 MW-II
Stator outer diameter D (m)	7	7	11
Stack length (m)	1.2	1.95	1.16
Speed n (rpm)	9.6	6.8	6.8
Torque T_{em} (MNm)	10.5	30	30
Stator current density J_s (A/mm ²)	3.5	3.5	3.5
Stator slot packing factor	0.6	0.6	0.6
Number of poles 2p	32	32	64
Number of stator slots Q	384	384	768
Air gap length g (mm)	9	9	13
SC current density J_{sc} (A/mm ²)	340	273	340
SC area per pole (mm ²)	200	1000	200
Length of SC wire (km)	5.35	39.2	10.54
Ampere turns of SC per pole (AT)	34,000	136,500	34,000
Type of stator core	Iron-core	Iron-core	Iron-core
Type of rotor core	Iron-core	Iron-core	Iron-core
Volume of generator (m ³)	42.3	68.7	100.5
Mass of Iron (ton)	141	271.9	208
Cost of SC (million €)	0.543	3.92	1.054
Cost of copper (million €)	0.117	0.215	0.192
Cost of Iron (million €)	0.112	0.217	0.166
Cost of total (million €)	0.764	4.35	1.412

Table 3-4. Specifications for a 7m diameter 10 MW, a 7m diameter 20 MW (20MW-I) and an 11m diameter 20 MW (20MW-II) SC generators [199]

Based on current superconducting prices, INNWIND suggest that increasing rotor and stator iron can lower the active material cost by up to 75%, increasing mass but creating a machine comparable in cost to a DDPM generator [201].

In addition to the superconducting generator design, INNWIND has engaged in and achieved results from improving rotor aerodynamics, blade structural designs, offshore support structures, wind profile data and magnetic gearing for a high power Pseudo Direct Drive 10 -20 MW generator. The scope of the project is vast with a wealth of information provided for the evolving wind industry.

Ecoswing

Ecoswing is part of the EU Horizon 2020 initiative, starting in 2015, and aims to provide the world's first HTS, low-cost, low-mass power take off for installation on a 3.6 MW, 2 bladed, 128 m rotor, turbine, Envision GC-1 [53], Figure 3-38.



Figure 3-38. Right foreground. Envision GC-1 Turbine, Thyborøn, Denmark. Courtesy of Ecoswing [53]

As of 2017 Ecoswing have completed the design and validation of the generator and supporting subsystems, with manufacturing ongoing. The superconducting generator will utilise THEVA TPL2100 Pro-Line HTS tape, constructed with the composite $\text{GdBa}_2\text{Cu}_3\text{O}_7$ as the superconducting layer, operating at ~ 30 K via cryogen free convection cooling. 30 coils with a total of 15 km of HTS tape are to be installed on the rotor, with conventional ambient temperature cooper armature windings. The cooling system will be similar to that of the Suprapower project, that is to say the compressor will be stationary while the cryo-coolers are to be attached to the rotor.

Ecoswing plan to produce a generator with 40 % less mass than a conventional DD PM machine [202]. Potentially this project could become the first installed HTS wind generation system in the world, pushing the technology further than before. However superconducting windings and cryo-coolers located on the rotor could cause significant problems if not thoroughly investigated.

Alternative SC Machine topologies

All four of the projects mentioned rely on a conventional stator and a superconducting rotor. Recent topologies have also been presented for HTS bulk magnet machines by authors Chen et al [203] and Liu et al [204] with Combs [205] providing a fully superconducting motor utilising HTS bulk magnets on the rotor. Recent researched topology for fully superconducting generator topologies are provided by Kalsi et al [173], Jia et al [206] and Kostopoulos et al [207], an example of a fully superconducting generator topology is provided in Figure 3-39.

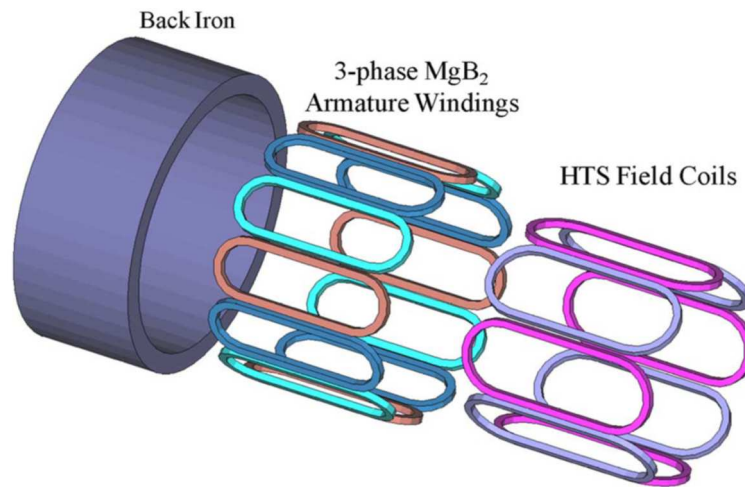


Figure 3-39. Illustration of a fully superconducting wind turbine generator [208]

Superconducting Structural Design

The attraction forces, or the normal component of Maxwell stress, created within the airgap of a superconducting generator can be many times that of a permanent magnet generator. Therefore, iron cored machines must be structurally durable to maintain the active airgap within the machine. Air cored SC generators suffer less from high attractive loads, however in most cases place higher torques onto the SC material which can potentially damage the sensitive SC composite winding. An air cored machine design can require up to double the SC material in order to produce the required magnetic flux within the airgap compared to an iron core machine. However due to the presence of magnetic materials on the rotor, Iron cored machines can be twice the mass of an air cored machine, a comparison of two 5 MW air cored and iron core machines is provided in Table 3-5. Both topologies must be wary of thermal stresses. Thermal stress can occur on the structural elements connecting cold and hot

sections of the generator. At cryogenic temperatures many materials become brittle, therefore the correct supports must be able to withstand the thermal differences within the machine, ideally utilising materials with low heat conduction constants. In addition, the unforgiving nature of the offshore environment and the precise nature of cryogenic systems may create problems which must be curtailed through built in system redundancy, modularity or the reduction of cryogenic rotor systems.

	Air-cored HTS	Homopolar
Outer Diameter (m)	1.75	2.5
Volume (m ³)	3.15	6.95
Weight (t)	18	44
SC wire length (km)	100	50

Table 3-5. Comparison of an air cored SC machine and a homopolar synchronous machine for a 5 MW, 230 rpm motor design [164]

3.4. Case Studies

Two direct drive topologies were considered for case studies. The case studies will be used to discuss generator structure, mass and drive train loading when applied to the three main offshore renewable energy resources, wind, wave and tidal. The following two sections will briefly outline the direct drive generator concepts, topologies and research history.

3.4.1. Transverse-flux HTS generator

In [38] Keysan presents a single sided Transverse flux (TF) high temperature superconducting (HTS) generator. The combination of a high flux superconducting field winding with a claw pole transverse flux machine topology leads to a machine suitable for direct drive, low speed, and high torque applications. The active electrical topology of the TF HTS is provided in Figure 3-40. It utilises a stationary superconducting DC winding with inner and outer stationary stator sections. A moving claw pole variable reluctance rotor creates a variable magnetic field around the armature winding supported by the outer stator.

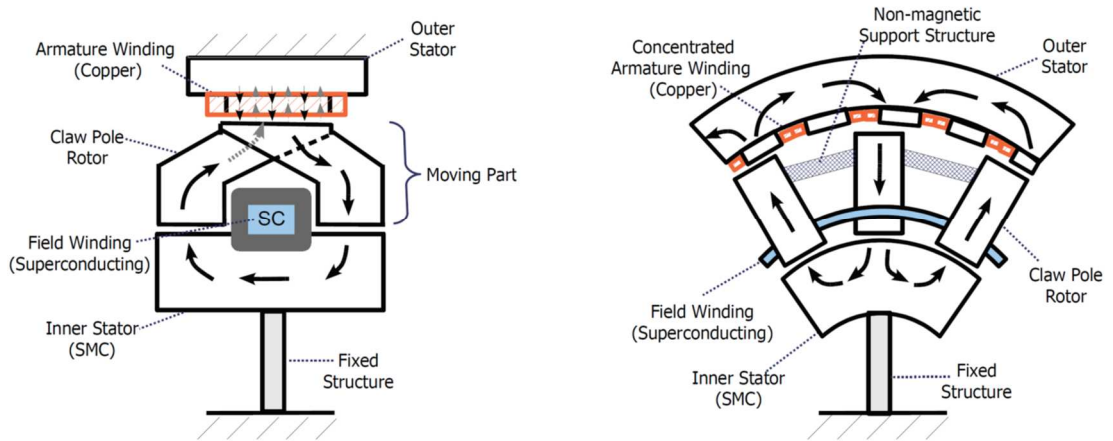


Figure 3-40. Proposed transverse flux superconducting machine structure. a) Main magnetic flux direction through the claw-pole rotor (axial cross-section view). b) Main magnetic flux direction through the inner and outer stator (vertical cross-section view) [209]

As the TF HTS topology was refined, adaptations led to the design given in Figure 3-42 and Figure 3-42. The claw poles and armature winding were rotated 90 degrees and mirrored about the superconducting winding. The inner stator is reduced leading to a double sided claw pole design suitable for radial or axial flux machine topologies.

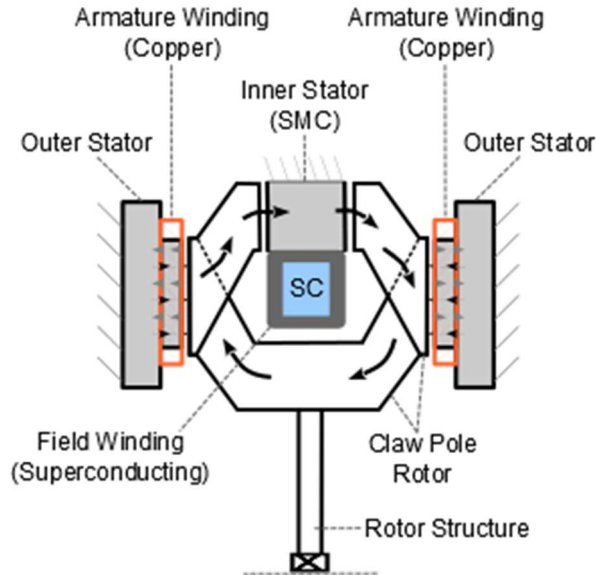


Figure 3-41. Double sided claw pole machine topology, cut away [164]

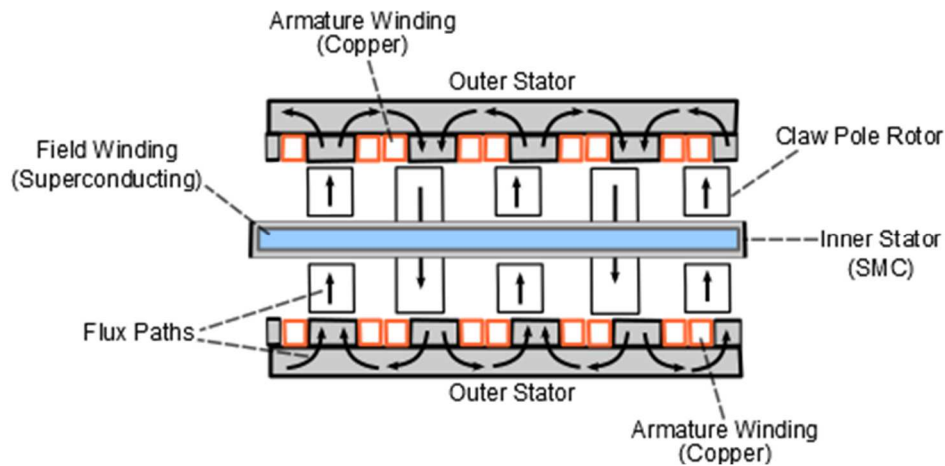


Figure 3-42. Double sided claw pole machine topology, top view [164]

Although the machine contains four airgaps, the Magnetomotive force (MMF) of the superconducting winding compensates for any leakage or losses. Keysan summarised the advantages of a double sided design as follows:

- A stationary superconducting field core negates the requirement for moving parts such as cryocouplers, brushes or additional rotational forces experienced by the coil, thus increasing reliability and easing fabrication.
- Magnetic attraction forces on the claw poles are symmetrical which sum to cancel each other.
- Double armature winding configuration increases modularity.
- It is presented by Keysan [164] that the topology requires notably less superconducting material than many superconducting, with only up to 15 km of MgB₂ wire required for a 10 MW machine.
- Compared to the topology presented in Figure 3-40, the double claw pole design reduces the superconducting field coil back-core mass producing a lighter machine.

However, Keysan also lays out the following drawbacks:

- Active mass is high in order for the superconducting and armature coils to remain stationary.
- Magnetic attraction forces are high.
- Lower power factor than conventional machines.

The single sided TF HTS machine topology will be studied as a linear test prototype in Chapter 5, while the double sided TF HTS machine structure will be considered for large offshore wind applications.

3.4.2. C-GEN direct drive generator

C-GEN is an innovative multi-stage air-cored PMG technology developed at the University of Edinburgh that is applicable to direct drive, slow or medium speed generator designs as described by Polinder et al [67], Figure 3-43. The differentiating design features of the patented C-GEN design include:

- An axial flux topology with C-shaped rotor core
- An air-cored stator arrangement
- Generator divided into several axial generator stages that are electrically independent
- Generator rotor and stator divided into low weight standardised modules around the circumference

C-GEN is made up of light weight stator and rotor modules, Figure 3-44. The low generator and module weight of the C-GEN technology reduces O&M costs compared to traditional iron-cored, radial flux PMG systems. The maintenance of drive train components, if necessary, can be carried out with lighter lifting equipment or an internal turbine crane.

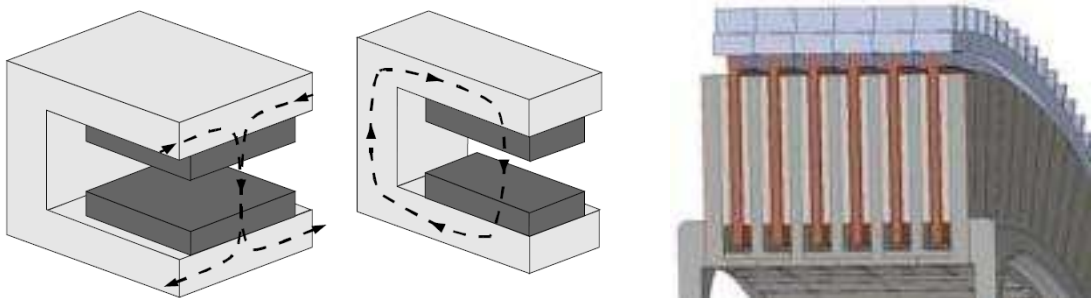


Figure 3-43. Left: C-Core topology with flux path indicated around neodymium iron boron (NdFeB) magnets [117]. Right: Adjacent stacked C-Core topology [210]

Multiple generators consisting of simple, lightweight modules can be “stacked” back-to-back along the shaft of a wind turbine to create a multi-MW rating without increasing the machine diameter. This means that for certain generating system line failures, one generator line can be isolated, enabling the wind turbine to continue generating revenue whilst maintenance is scheduled. This redundancy characteristic is even more relevant for remote areas with challenging conditions for access, e.g. offshore wind farms. In C-GEN the number of generators in operation can be adjusted based on wind conditions to optimise the power output, efficiency and increase longevity. In conventional PMGs magnets try to align themselves with steel teeth onto the stationary part of the generator and cogging torque will result in overcoming this alignment force. This characteristic increases the cut-in wind speed, the minimum wind speed at which the turbine produces power and creates vibrations in the generator. C-GEN does not have any cogging torque to overcome, there is zero cogging torque as there is no iron in the stator and can thus generate power at low wind speeds, whilst lowering the presence of vibrations within the generator, reducing noise and overall generator material costs.

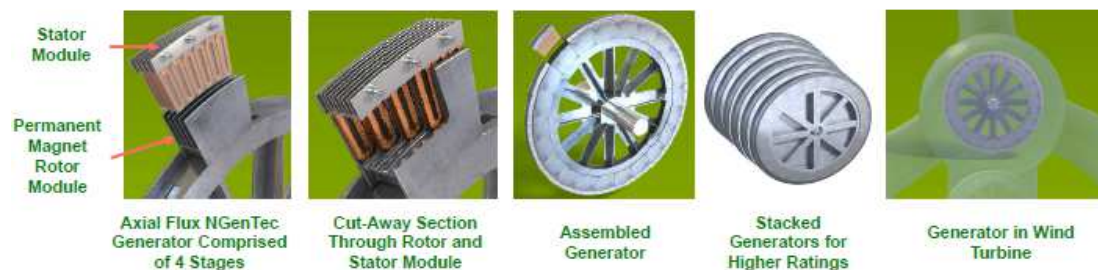


Figure 3-44. An explanation of C-Gens radial topology, assembly and modularity

The C-GEN generator technology therefore has the following unique selling points over existing generator technologies used for direct drive:

- No Magnetic Attraction Forces closing the airgap - this simplifies the support structure required, and makes assembly of the stator and rotor modules easier.
- No cogging torque - more of the input mechanical energy will be converted to electrical energy, and noise and vibration will be reduced.
- High Degree of Modularity - the use of air-cored coils allows a high degree of modularity in both the stator and rotor construction.

- Higher availability - Due to the high degree of modularity the C-GEN generator is a multi-stage machine, which means that it is built up of a number of machines, eg a 4 stage 1MW generator consists of 4 separate 250kW machines, all of which can be isolated. Hence if there is a fault in one stage, then it can be isolated and the remaining 3 stages can generate. In a conventional generator a fault in a machine will result in complete shut down, and hence no revenue is generated. By being able to operate with few stages the C-GEN generator will have more availability, increasing annual energy yield and hence reducing LCOE.
- Ease of O&M - the high degree of modularity enables replacement of single faulty modules rather than the complete machine. This reduces O&M costs and increases the turnaround of any O&M procedures. Depending upon the size of the device, the O&M procedure could be done on board a ship using an on-board crane. Modules can be designed to have a mass typical of standard ship craneage.



Figure 3-45. Left: 1 MW C-GEN axial flux multi-stage rotary machine. Right: C-Gen air cored stator module installation [211]

C-GEN technology has been demonstrated at various scales:

- 20 kW rotary machine proof of concept [117].
- 15 kW rotary machine successfully installed and operated on a wind turbine [117].

- 6 kW rotary machine successfully installed and operated on a wind turbine.
- 25 kW axial flux multi-stage rotary machine as proof of concept of multi-stage topology pre scale up to 1 MW.
- 1MW axial flux multi-stage rotary machine, demonstrator of a slice of a 6 MW direct drive generator.
- 50 kW linear machine for wave energy applications [212].



Figure 3-46. Left: 20 kW C-GEN rotary machine and test rig. Centre. 15 kW C-GEN rotary machine. Right: Wind turbine installation of 15 kW C-GEN machine [117]

Based on the European Commission's definition of Technology Readiness Levels, TRL, the C-Gen has been proven to the following levels. For small wind applications the technology is at TRL 5, as it has been demonstrated in the real environment, but at multi-MW scale it is at TRL 4 and for marine energy at TRL 3.

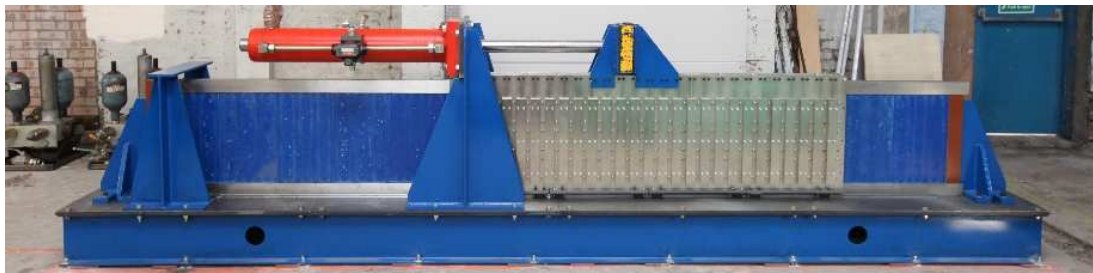


Figure 3-47. 50 kW C-GEN linear generator prototype and test rig [212]

3.5. Discussion

The information contained within this chapter will be used for simulated and physical testing later in the thesis, with chapter 4 continuing the discussion and design of the HTS claw pole machine and chapter 5 and 6 investigation methods to improve the performance and reliability of direct drive generators, utilising the C-GEN generator topology.

Chapter 4.

Direct Drive HTS Structures

4.1. Structural Analysis for Direct Drive Machines

In Chapter 3 permanent magnet direct drive machines and superconducting direct drive generators were discussed. In order to understand the electrical, mechanical and fabrication concerns of direct drive machines, a HTS claw pole transverse flux machine has been chosen as a case study. This chapter will be divided into three sections. The first will focus on the development and structural design of a transverse flux claw pole linear test rig, the second will propose a structure for a 30 kW rotary HTS claw pole machine and the third will discuss scaling the HTS concept up to 10 MW.

4.2. Linear Claw Pole Prototype

In Chapter 3 a transverse flux claw pole machine was described as proposed by Keysan in [164]. A linear prototype of the topology was designed and constructed replacing the SC field coil with a copper coil due to budget restrictions. The construction and testing of the prototype was to enable the mechanical and electrical properties of the machine to be understood while the overarching aim of the prototype construction was to better understand the introduction of superconductivity to the design and investigate structural concerns before the construction of a SC rotary prototype. The design enabled a modular section of a rotational machine to be constructed, replacing the claw pole rotor with a reciprocating translator in order to migrate flux to the armature coils.

The linear prototype topology is presented in Figure 4-1, and although numerous alterations occurred in the structural and electrical topology before construction, the core three elements remain, stationary field coil, moving claw pole sections and stationary armature windings.

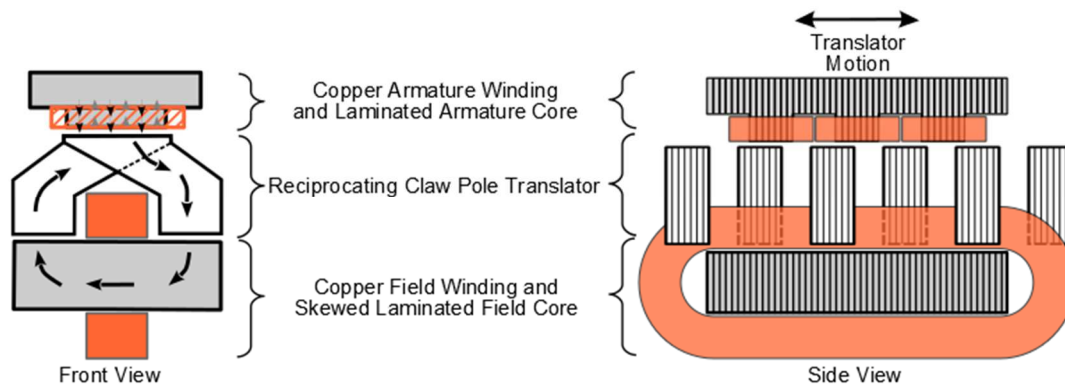


Figure 4-1. Basic indicative topology of the linear claw pole machine prototype

4.2.1. Design and Assembly

The main mechanical design concerns for electrical machines were described in Chapter 3 and can be summarised below:

- Maxwell stress
- Gravitational force
- Eccentricity
- Shear stress
- Cogging torque
- Thermal expansion

In order to mitigate the combined effect of gravitational and magnetic loading, it was decided that the field coil would be placed above the translator and the claw poles flipped around the horizontal plane. Magnetic forces are present between the armature and the claw poles as well as the field winding and the claw poles, however due to concentrated flux density, the forces are higher between the claw poles and field core. Therefore, by altering the layered topology of the prototype, the claw pole attractive load from the field coil is counteracted by the mass of the translator structure.

In order to achieve the required flux path within the linear prototype, electrical steel laminations were used to create the core, claw poles and armature core. In this manner magnetic flux is able to move from one claw pole to the next by following the skewed field core steel laminations, Figure 4-2. The original field core design contained a pressed bent laminated structure, however due to costs and manufacturing difficulties,

it was decided to use a purely skewed field core as shown in figure. Within a radial machine soft magnetic composite material, SMC, can be used to complete the three dimensional flux path.

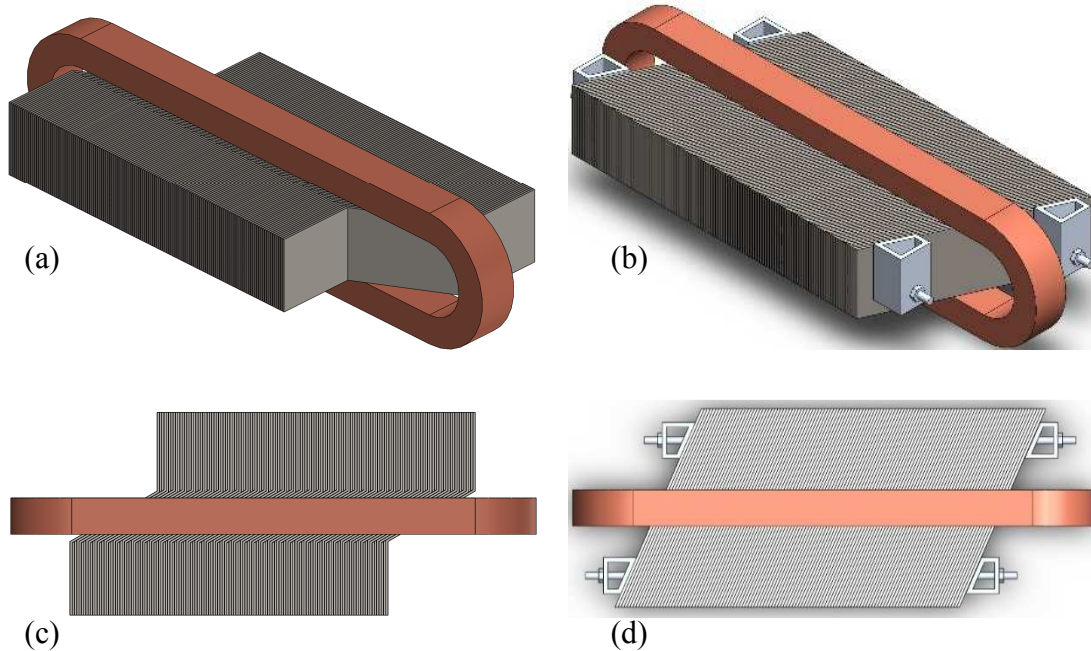


Figure 4-2. Left: a) ISO & b) Top view formed laminated field core. Right: c) ISO & b) Top view simplified laminated field core

Initially the construction of the machine included epoxy resin to provide the cores and coils as well as the translator fabrication additional structural support, Figure 4-3. The curing process for the epoxy requires warming of the epoxy and curing agent mix, the mould and laminations to be warmed to the same temperature, 60 degrees, and the mixture poured in around the translator. The mixture is degassed using a heat gun, a pre heated lid added the whole fabrication is allowed to cool to room temperature. The assembly is then placed in an oven for a period of 2 hours at 120 degrees. However due to the volume of epoxy and steel required in the machine, initial fabrication tests showed that even slowly cooling the whole assembly would result in cracking in the epoxy, Figure 4-4. The reason for this cracking can be explained by the difference in the heat transfer characteristics of the epoxy and steel, the steel cools quicker than the epoxy leading to a build up of stresses in the epoxy material. The thermal performance of the field and armature cores whilst suspended in epoxy were also queried, as it was assumed the low heat coefficient of the epoxy would lead to heat build-up in the copper

field and armature coils. It was therefore decided to support the translator section with an aluminium frame, whilst welding the cores with small seams in order to maintain structural integrity.

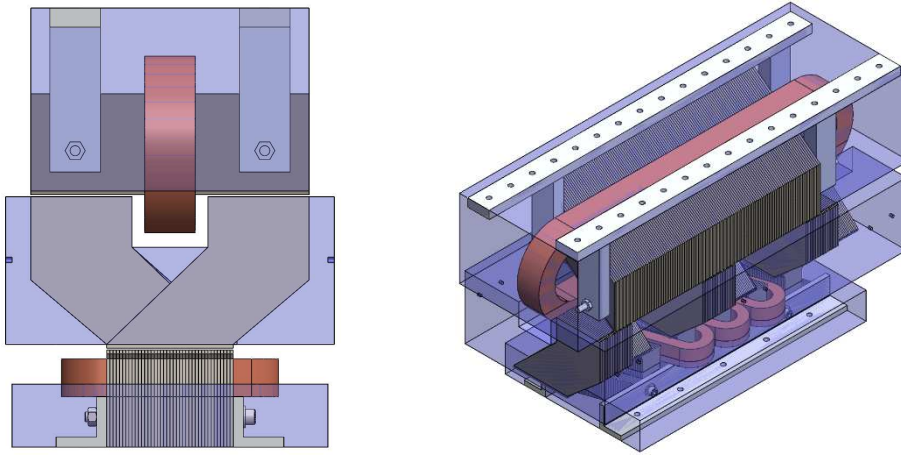


Figure 4-3. Epoxy impregnated linear machine components



Figure 4-4. Cracked epoxy test sections. Left: Clear PC6159 epoxy resin. Right: Blue PC5308 epoxy resin. Details in Appendix B

Field winding and core

One hundred and seventeen, 3 mm steel laminations were laser cut and drilled along the skew angle in order to create holes for the core to be held together along its length by two stainless steel bolts, maintaining a skew ratio of 0.55. The field winding was attached to the core using tufnol isolation plates and resin impregnated in situ to maintain rigidity. The fabricated field core and winding are shown in Figure 4-5. The assembly was then attached to the machine frame by two aluminium bars bolted to steel box section supports.

Claw pole translator

Each of the eight claw poles were manufactured using twenty 3mm laminated laser cut electric steel sections and held together by two stainless steel bolts, as indicated in Figure 4-5. The placing of the bolts ensured stiffness while minimising the loss of flux path. The claw poles were then mounted on a non-magnetic aluminium frame supported by four HIWIN HG25 linear roller bearings to help maintain air gaps of 1.5 mm between the field and armature cores and provide smooth low resistance reciprocation motion long the length of the machine.

Armature coil and core

The armature core was created using forty laser cut 3mm electrical steel laminations, skewed and bolted together with a skew ratio of 0.55 inverse to that of the field core. The silhouette of the laser cut laminations includes five teeth around which three concentrated armature coils are inserted. The coils were then resin impregnated for rigidity. The structure of the Armature winding before impregnation is provided in Figure 4-5. The finalised design topology of the machine are provided in Figure 4-6, Figure 4-7 and Figure 4-8.

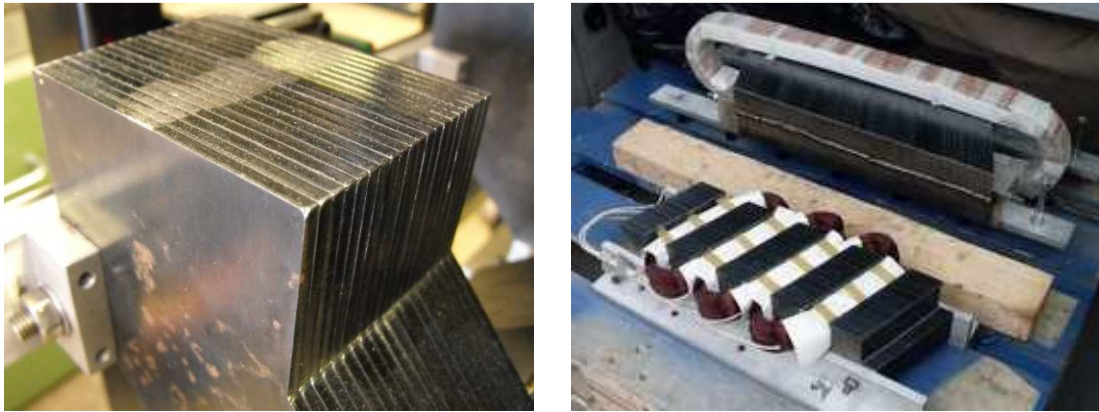


Figure 4-5. Left. Laminated claw pole construction. Right. Armature and field cores prior to vacuum resin impregnation

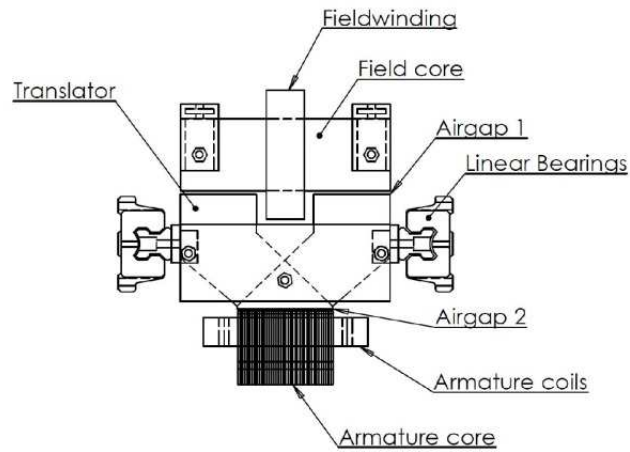


Figure 4-6. Front view of linear claw pole prototype active topology including bearings

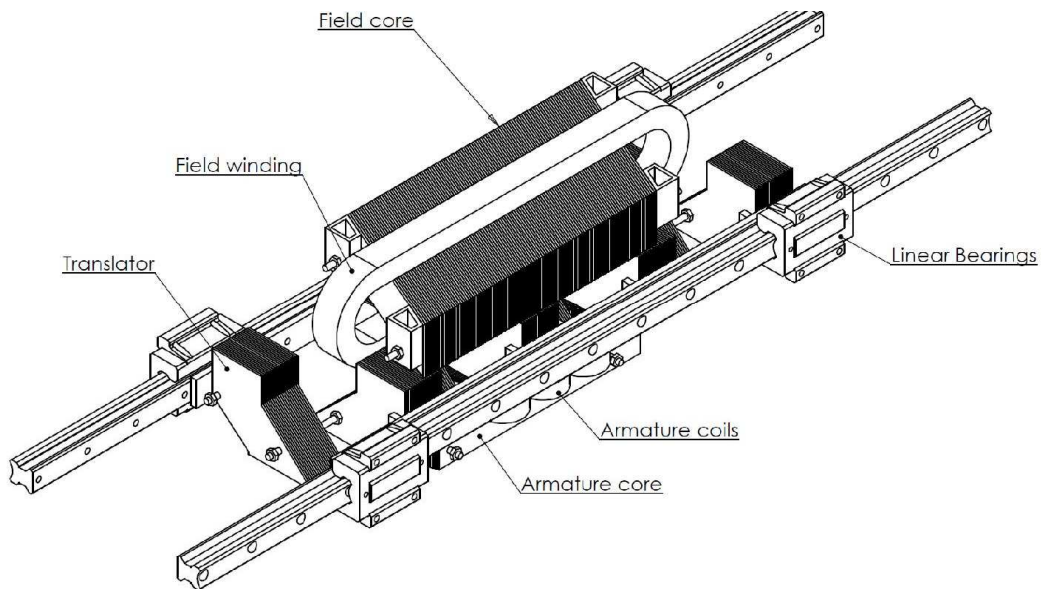


Figure 4-7. Isometric view of the linear claw pole prototype active topology including bearings

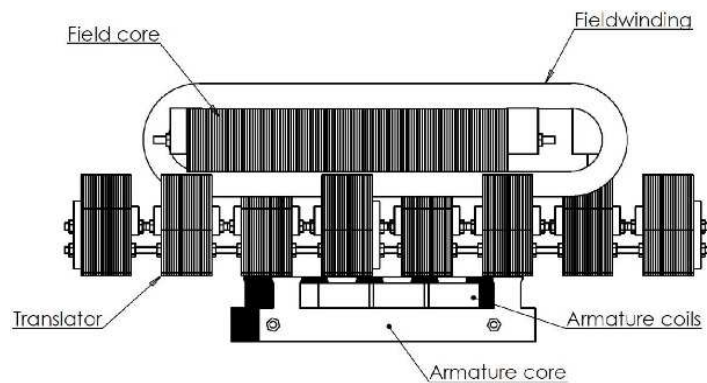


Figure 4-8. Side view of the linear claw pole prototype

Assembled machine and support structure

The final assembled machine is presented in Figure 4-9 while its main specifications are provided in Table 4-1. The translator was moved back and forth by hand, using a draw wire position sensor to record its position. The main support structure of the machine was constructed from 40x60 mm steel box section with a wall thickness of 5 mm.

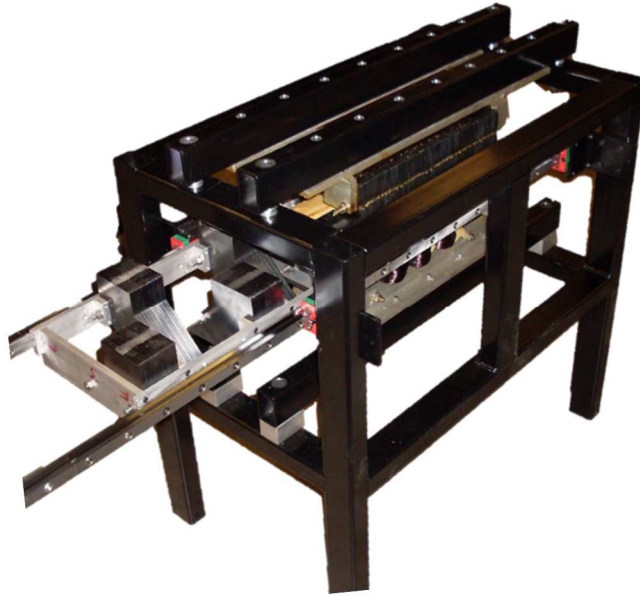


Figure 4-9. Assembled linear prototype

Parameter	Value
Mass (kg)	253
Stroke length (mm)	500
Number of claw pole pairs	4
Airgap clearance (mm)	1.5
Width of laminations (mm)	3
Number of field core laminations	107
Field coil wire diameter (mm)	1.6
Field coil number of turns	364
Number of armature core laminations	33
Armature coil wire diameter (mm)	1.25
Armature coil turns	190
Number of claw pole laminations	20 (each)

Table 4-1 Linear claw pole prototype specifications, full electrical design provided in Keysan [164]

Initial static structural analysis of the supporting structure indicated that the structure would experience a maximum deflection of 0.2 mm into the airgap between field core and adjacent clawpoles, based on flux values provided by Finite Element Analysis, FEA, analysis completed by Keysan in [164]. The initial topologies and the location of the loads are indicated in Figure 4-10.

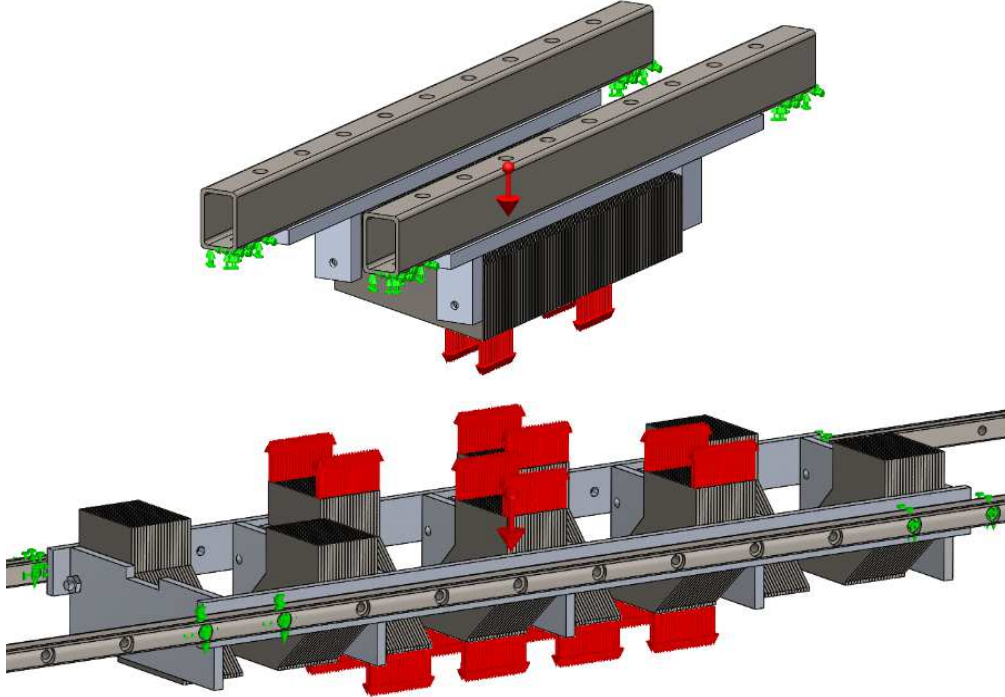


Figure 4-10. Position of loads applied to field core (Top) and claw pole (bottom) for initial static investigation. Green shows supporting fixture, red indicates attraction forces and central large arrow indicates gravitational force

4.2.2. Experimental Results

Since the extent of the magnetic attraction forces was constant for static testing of the machine, the supporting structure as a whole experienced large net forces. During structural and electrical testing of the machine, the field winding was excited with DC current. For static deflection testing, the excitation current was increased by a factor of 1A while the deflection of the armature core, field core and translator were measured using a mechanical displacement gauge. The gauge was placed in the middle of supporting structure each component, while the translator also had the deflection at the bearing measured. Point A was the measurement taken at the bearing support, while point B was the mid-point of the translator bearing guide rail support.

For the dynamic cogging torque testing, the excitation field was increased by 1 Amp for each test period, the experiment stopped when the translator could no longer be pulled back and forth. The force required to overcome the cogging torque was measured using a digital mass scale.

For flux linkage testing it was decided that a static test would be most suitable due to the overall observed deflection of the machines structure. Therefore, in order to create a changing magnetic field the field coil was excited with AC current, thereby inducing current in the armature windings. In order to measure the flux leakage from the claw pole, search coils were wound around the claw pole and connected to a voltmeter. For the flux density experiments, a Gaussmeter with a hall probe was used.

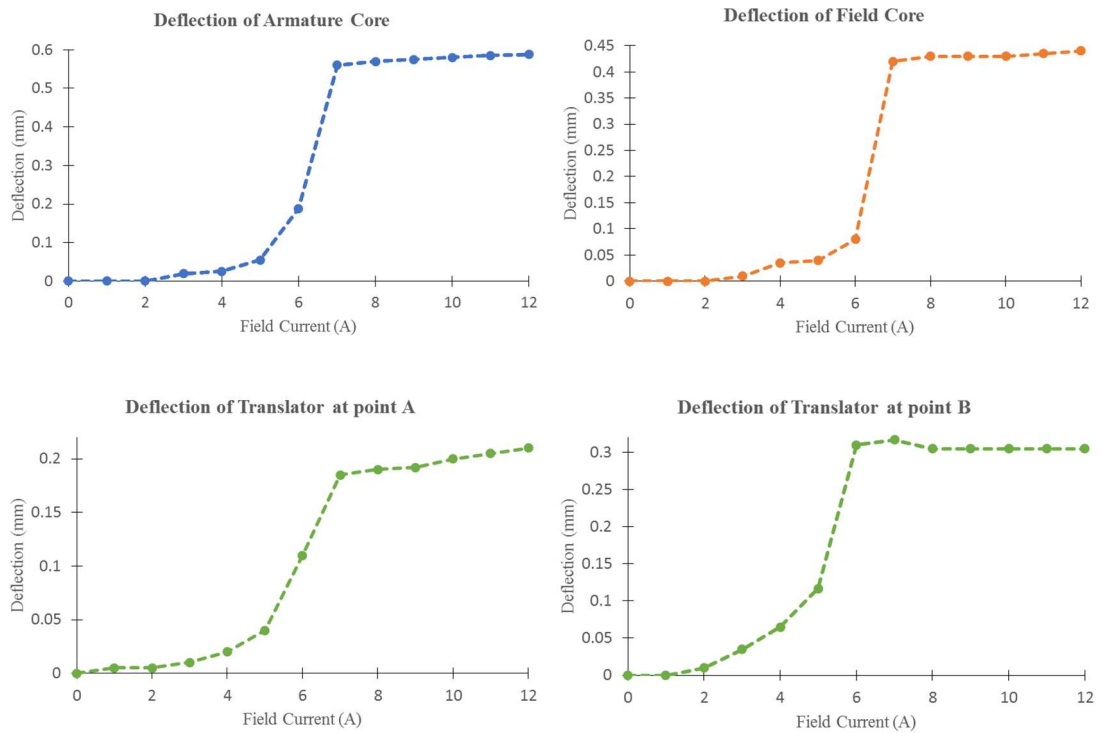


Figure 4-11. Structural deflection of the linear prototypes components over increasing field coil excitation

Structural Test

Due to underestimated magnetic forces present in the air gap, the original structure could not maintain its structural integrity and all elements experienced deflection, resulting in the closure of the top airgap, between the field core and adjacent claw poles. The measurement of the deflection indicates that the movement in the air gap is

proportional to the square of the field current up to 6 A. However, as the field current increased past 7 A, the deflection of the air gap caused a rapid increase in the forces acting on the structure of the machine resulting in a feed-forward mechanism that closed the air gap, as provided in Figure 4-11.

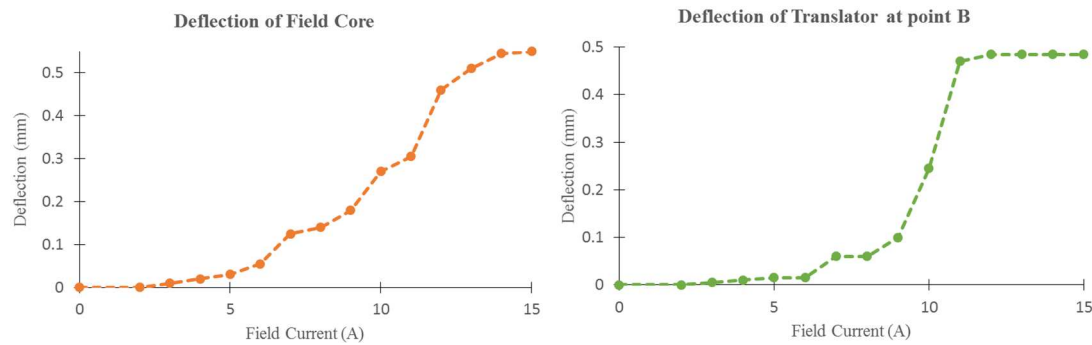


Figure 4-12. Structural deflection of the linear prototypes field core and mid-point of the translator structure

Improving the structure of the linear machine meant installing two additional bearings located at the centre of the translator bearing rail to further restrict movement of the clawpoles, and additional supports added to the box section structure supporting the field core. Deflection tests were carried out a second time on the field core and translator structure, these results are provided in Figure 4-12. The additional structural supports aided in maintaining the airgap up to 10 Amps, however as the current was increased past this point deflection rapidly increased leading to the closure of the airgap for currents larger than 12 Amps.

The machine was therefore unable to operate at its rated field current of 15 Amps due to structural deformation. However, it was deduced that the following factors aided in the deformation and these were factors that structural modelling did not necessarily take into account. The vertical displacement allowed within the linear roller bearings and their connection to the prototypes support structure allowed more movement than previously envisaged. Additionally, the movement of the field core was assisted by inadequate support of the laminations with bolts, joints and the mass of the core contributing to the movement.

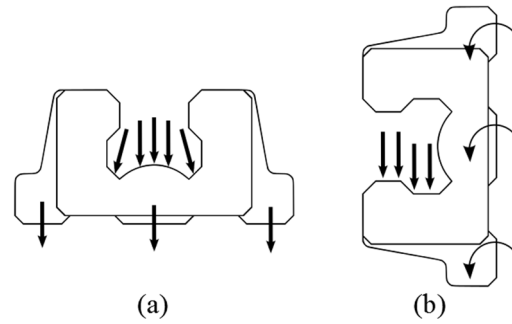


Figure 4-13. End profile of linear guide roller bearings. (a) Balanced load profile when installed at 0 degrees. (b) Unbalanced load profile creating moments and unsymmetrical bearing loads when installed at 90 degrees from vertical

The cogging force test was completed once the structural strengthening had been applied. For various field excitations the maximum force required to move the translator are provided in Figure 4-14. The linear resistance of the bearings should be below 5 N for the 50 kg mass of the translator, however the experimental results show that under only gravitational loading the maximum force required is to overcome friction is 50 N. This discrepancy is most likely due to the orientation of the linear bearings, as indicated in Figure 4-13. Instead of the bearings installed as in (a), distributing the load across all roller bearings, the bearings were installed according to (b), creating unbalanced loading. As testing continued the forces increased slightly until 8 Amps, at which point the force increases significantly and the translator cannot be moved once 12 Amps is reached.

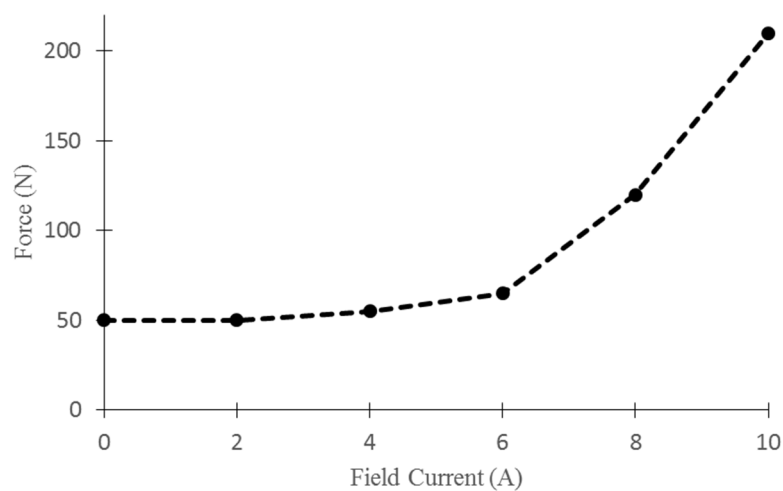


Figure 4-14. Maximum linear force required to move the translator

Flux Testing

In order to provide verification of the attractive forces contained within the airgap and the transfer of flux through the clawpoles, the following flux linkage and flux density investigations were performed.

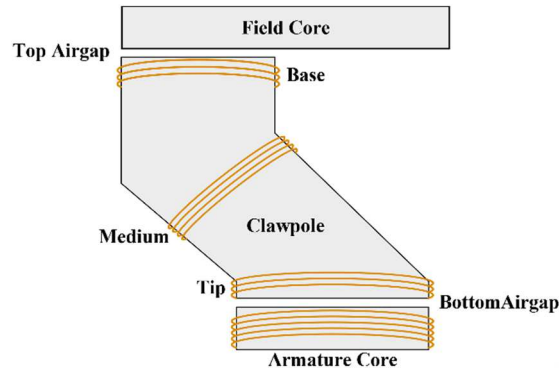


Figure 4-15. Schematic of search coil locations on claw pole to investigate flux linkage

Search coils were wound onto the base, middle and tip of a claw pole as indicated in Figure 4-15, the search coils consisted of 10 turns of copper wire wound around the claw pole. An AC current was applied to the field coil with a maximum excitation of 2.42 Amps at 50 Hz. The induced voltage for each search coil and adjacent armature coil was recorded and a calculation for the dissipation in flux completed with the results provided in Table 4-2.

	Induced voltage (V_{rms})	Number of turns	Flux (Wb_{rms})	% of flux transfer
Claw pole (base)	2.31	10	0.732	100
Claw pole (middle)	2.22	10	0.707	96.6
Claw pole (tip)	1.87	10	0.594	81.1
Armature coil	32.7	190	0.548	74.9

Table 4-2. Induced voltage and flux measurements from an applied AC field current, maximum 2.42 A at 50 Hz [164]

The results indicate that there is a degradation up to 25.1% of flux between the top of the claw pole and the tooth of the armature core. The flux density for the top and bottom airgap was then assessed from 6 – 14 Amps. The airgap was maintained using 1.5 mm aluminium L sections along the length of both top and bottom airgaps. The transverse flux probe was placed within the airgap and the Gaussmeter recorded the flux for a series of excitation currents.

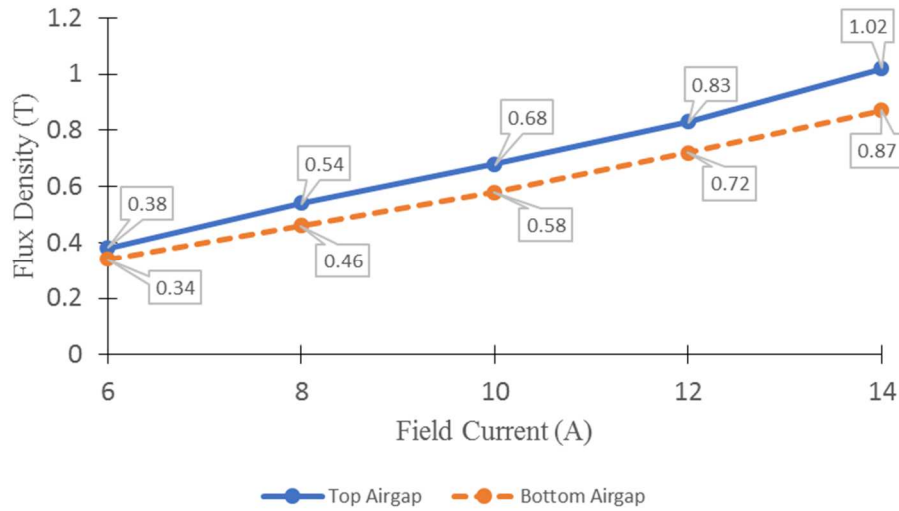


Figure 4-16. Airgap flux density plotted against field current for both top and bottom airgaps

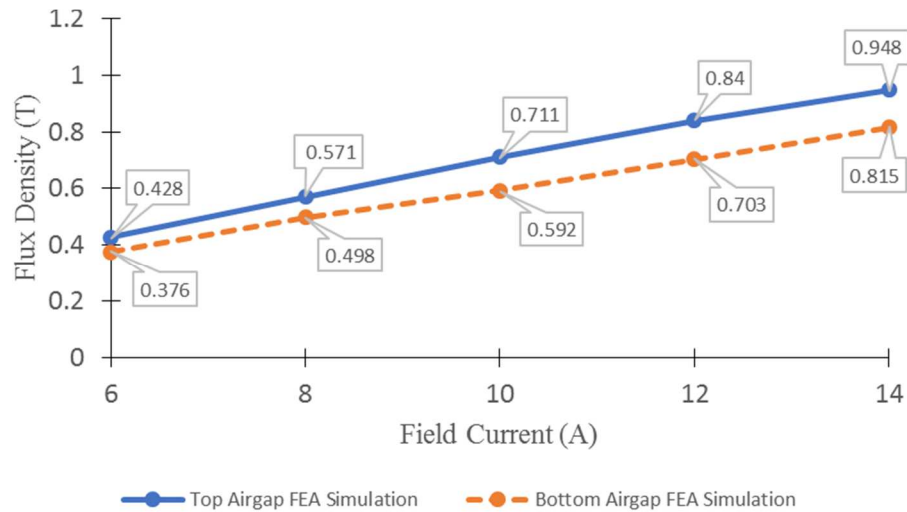


Figure 4-17. Simulated FEA airgap flux densities as calculated for the linear prototype in [164]

The experimental results are contained within Figure 4-16, while Keysan's FEA simulated airgap flux densities are provided in Figure 4-17. The results show good correlation with the maximum error calculated to be 12%. Therefore, the calculated flux density is suitable for use when calculating the structural loading of the airgap. It can also be said that the unsymmetrical flux densities of the top and bottom airgaps leads to an imbalance of attraction forces that increases as the top airgap closes and the bottom airgap opens, a characteristic that should be included when simulating structural performance.

4.2.3. Design Alterations for HTS Testing

The second stage of testing involved altering the linear test rig for the installation of a HTS field coil. As described previously, the airgap closed for field currents larger than 10 A (3640 At) whilst the HTS coil capacity is at around 12000 At. Thus, it is necessary to modify the structure. In order to improve the rigidity of the prototype a number of components had to be redesigned. In addition, the topology had to incorporate a coil of specific dimensions and potentially include a cooling system and vacuum chamber. This section will discuss the alterations made to the linear claw pole prototype design for future testing with a HTS field coil concept supplied by GE Energy and Power Conversion in Rugby, as presented in Figure 4-18.

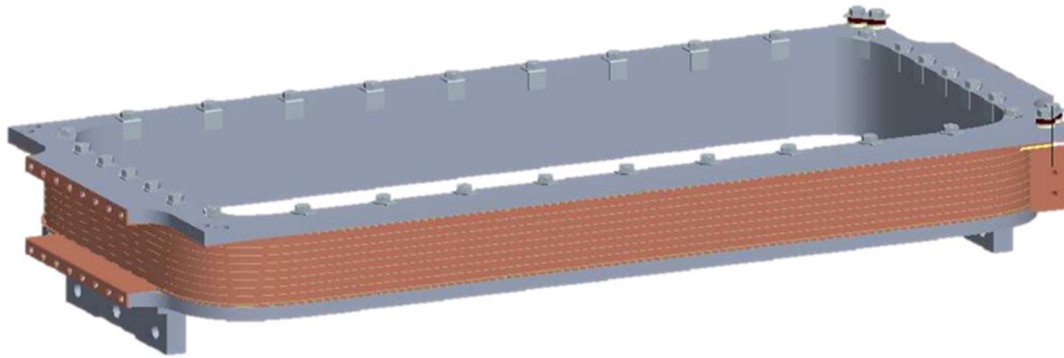


Figure 4-18. HTS coil topology as supplied by GE Power Conversion, Rugby

A comparison of the operational data for the HTS and copper field coils is provided in Table 4-3.

	Copper Field Winding	HTS Field Winding
Number of turns	364	200
Rated current (A)	15	145
MMF (At)	5460	12000
Operating temp (K)	< 343	< 40

Table 4-3. Operational data for copper field winding and HTS field winding

Structural

To improve the structural performance of the field core, a more complex laminated profile, Figure 4-19(a), was designed, manufactured and assembled. The bottom of the profile includes a stepped section in order to adequately house the HTS coil. Three

supporting bars were installed parallel with the stacked assembly of the laminations, Figure 4-19(c). The supports connected to the structure of the prototype on the side supports rather than along the length of the machine. The bars were produced from stainless steel solid bar and incorporated into the field core, as shown in Figure 4-19(b), to maintain rigidity of the laminations. Finally, the laminations and the solid support bars were bolted together using aluminium bolts along the length of the core.

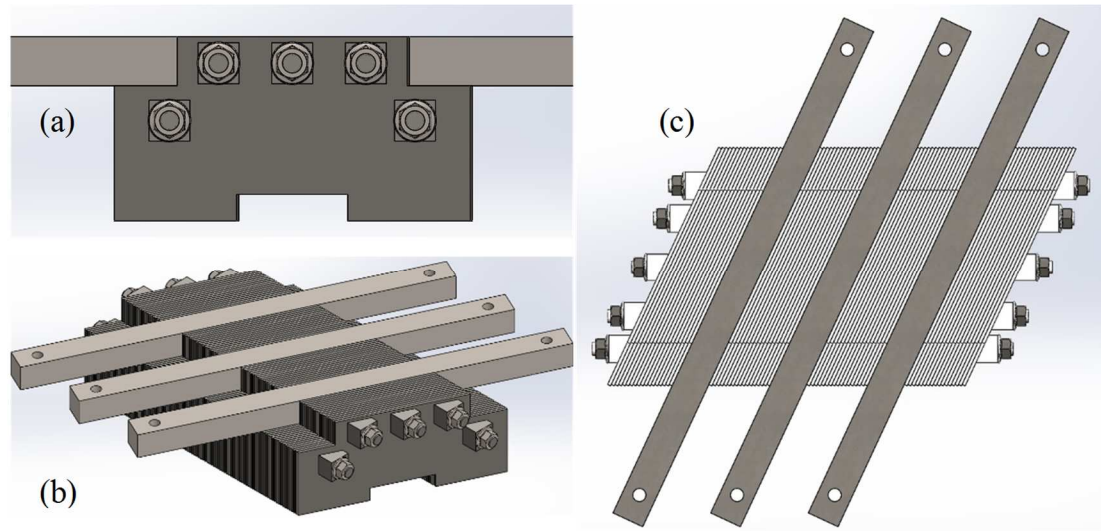


Figure 4-19. Altered field core topology for HTS field coil. (a) Front view showing lamination profile and stainless steel bolt configuration. (b) Isometric view showing reinforced solid stainless steel bar supports installed within the structure of the field core. (c) Top view showing support bars installed in parallel to the field core laminations

While a new field core was produced for the HTS assembly, the claw pole translator was adjusted to suit future testing requirements, Figure 4-19. In order to move the translator in a more controlled manner, a connection for a linear screw actuator was added to the front support. In addition, sections of the claw poles were removed in order to fit a pre-fabricated HTS coil and an associated cryogenic system into the machine. Although the area removed was small it was estimated that it could help reduce peak attraction forces by up to 12.5%, the new claw pole topology is presented in Figure 4-20. Structural deformation of the altered components has indicated that deflection into the airgap will be maintained under 5 – 7 % of the air gap length for both the field core and claw pole translator for attraction forces up to 1.2 MNm^{-2} . An example of the simulated loading to the field core is presented in Figure 4-21.

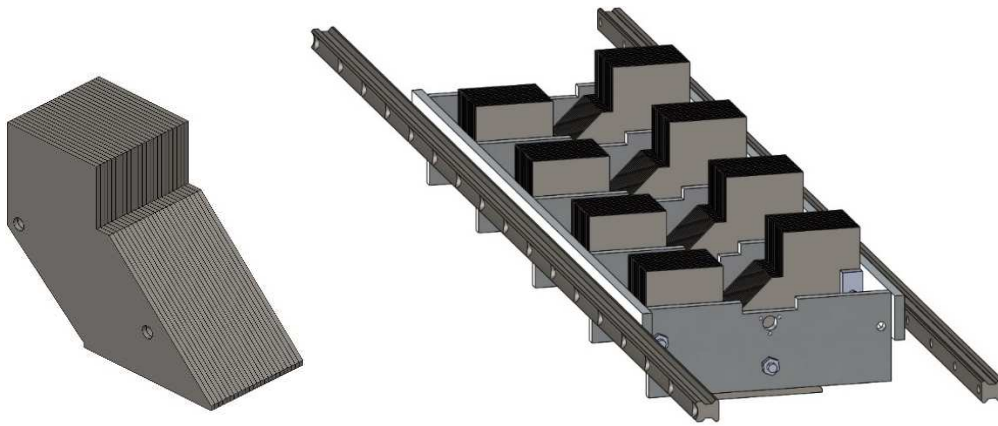


Figure 4-20. Altered claw pole topology. Left: Individual claw pole. Right: Claw pole translator assembly

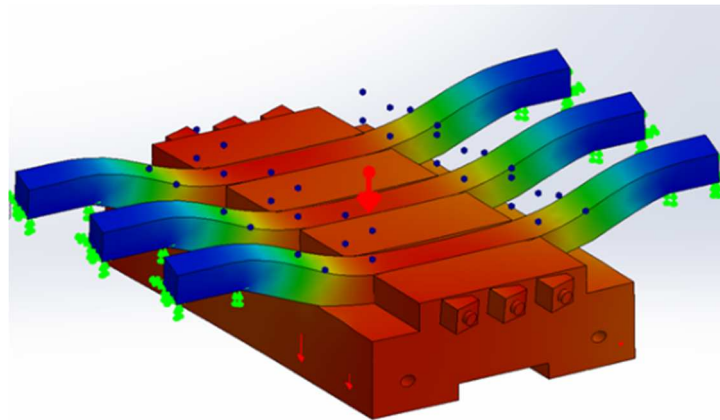


Figure 4-21. Structural testing results for field core, maximum deflection is highlighted in red and is equal to 0.085 mm

Initial HTS Cryogenic Design

The construction of a cryogenic circulatory system and a liquid nitrogen bath was investigated in order to provide a cooling medium to the HTS field winding. Initially a cry-cooler and cryogenic pump system was considered. A stainless steel vacuum chamber was designed to fit around the HTS coil with space in the centre for the field core. The cryogenic liquid would be pumped through insulated piping which would connect to two cold head parts on the coil. The coil and the piping would be supported within the vacuum with fiberglass supports mounted on thermally resistant ceramic pads, which would be bolted to the chamber. Sensors and a current supply would require air tight seals or connectors to exit the chamber. The original design is provided in Figure 4-23.

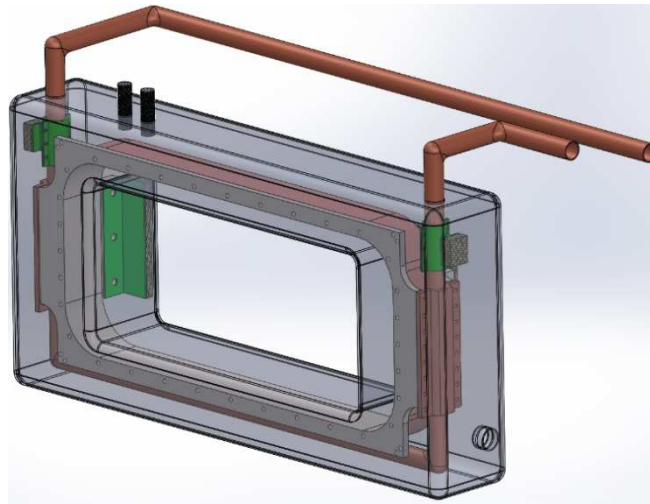


Figure 4-22. Small vacuum chamber with liquid nitrogen circulation pipes connecting to the HTS coil cold head connections. Fiberglass (Green) and ceramic (Yellow) supports maintain rigidity for the cryogenic pipes and HTS coil while separating cold and warm areas

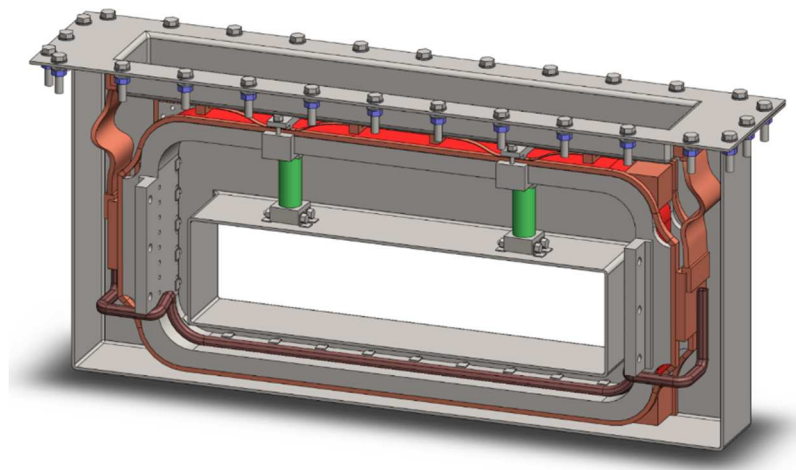


Figure 4-23. Liquid Nitrogen bath and coil support designed by MEng Student Patryk Radyjowski

During discussions with manufacturers, the construction of a thin walled chamber with vacuum proof welding and the purchase of a cryogenic pump was considered too difficult and costly, therefore an external hydrogen bath was considered. A more complete design was produced by Patryk Radyjowski, a Master Student within Edinburgh University. However, costs still proved too high, and concerns over the insertion, connection and future removal of the fragile coil meant testing was postponed until the installation of a large vacuum chamber and cryostat within the University of Edinburgh, Figure 4-24.

Vacuum Chamber Testing

Vacuum chamber testing will be carried out in the University of Edinburgh's School of Engineering cryogenic lab, due for completion December 2017. The linear HTS prototype will be placed inside a vacuum chamber as shown in Figure 4-25. Heat convection from the HTS coil will be curtailed by the vacuum and Multi Layer Insulation, MLI, which will be wrapped around the coil. Fiberglass supports will limit heat transfer to the structure of the prototype and current supply and cryogenic cold head connections will be inserted into the chamber through vacuum safe seals. The current bearings will be removed, and vacuum rated bearings are to be installed. The addition of these bearings will allow not only static, but dynamic testing. Movement of the clawpole translator was controlled by human input while external to the vacuum chamber, whereas in order to control the translator's movement in a vacuum a leadscrew assembly containing a vacuum rated stepper motor controlled remotely has been installed. The stepper motor, lead screw and related supporting structure can be seen in Figure 4-26.



Figure 4-24. Vacuum chamber and associated cryogenics and vacuum pumps describing the indicative experiment set up required



Figure 4-25. Linear HTS claw pole prototype placed within vacuum chamber

The complete insertion of the machine within the vacuum chamber allows for relatively easy access to the HTS coil and active structure in order that it can be maintained or require the installation of new sensors or supporting structure. The final machine topology is described in Figure 4-26 and Figure 4-27.

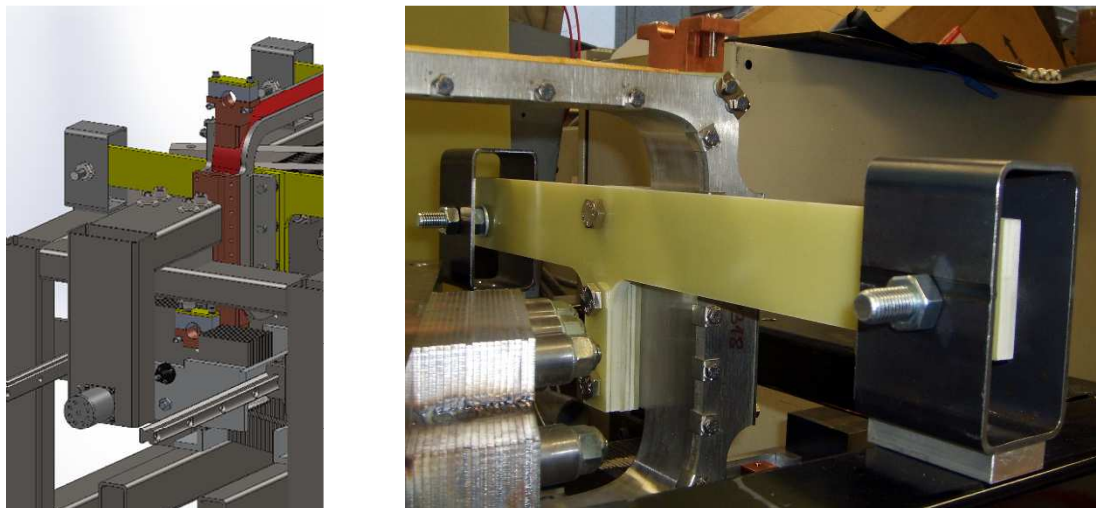


Figure 4-26. Left: position of a vacuum proof actuator motor for testing. Right: Incorporation of coil and supporting structure into machine design

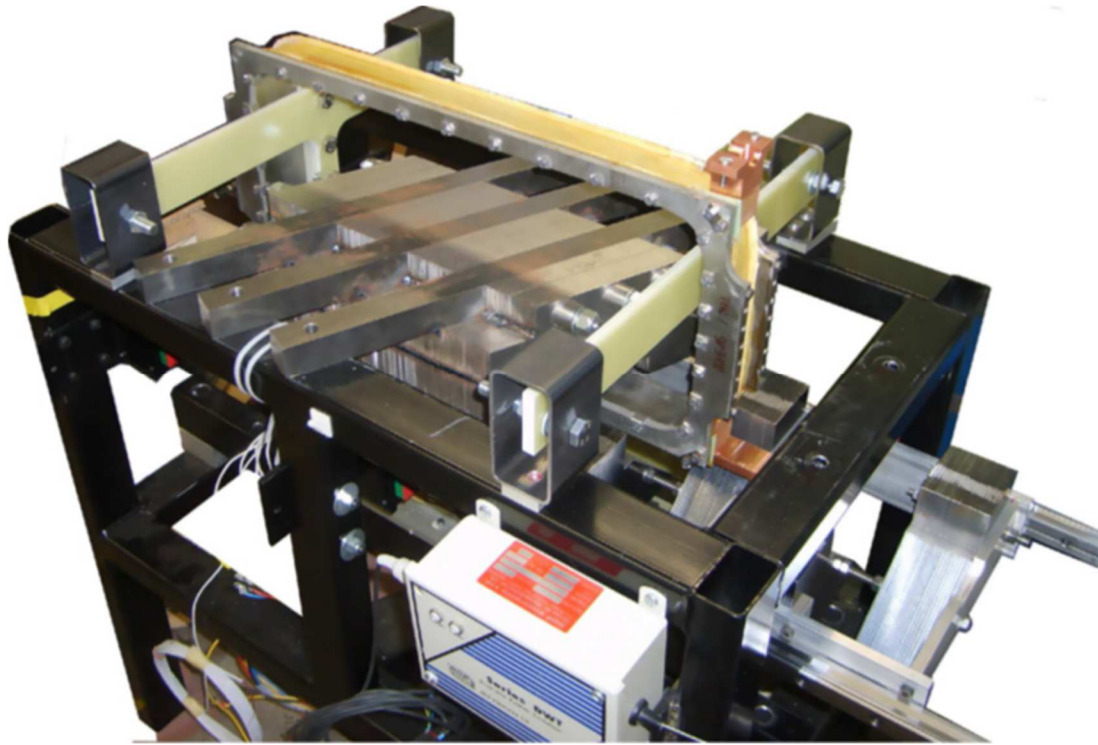


Figure 4-27. Assembled linear HTS claw pole prototype machine

4.3. 30kW HTS Claw Pole Prototype

In order to move closer to the production of 5 – 10 MW claw pole machine further information must be gathered by the design and build of a rotary machine. In this section the design and structural analysis of a 30 kW rotary claw pole machine prototype will be provided. Scaling up from the linear prototype design resulted in operational changes in order to create a practical and cost effective machine design. The initial operational results of the linear machine, provided in section 4.2.2 indicated that the claw pole translator was suitable for the installation of a superconducting coil, while the structure of the machine had to be tailored in order to maintain integrity under high magnetic attraction forces. The structure of the rotary machine must therefore be created to maintain the operational airgap and integrate a superconducting coil and cryogenic system.

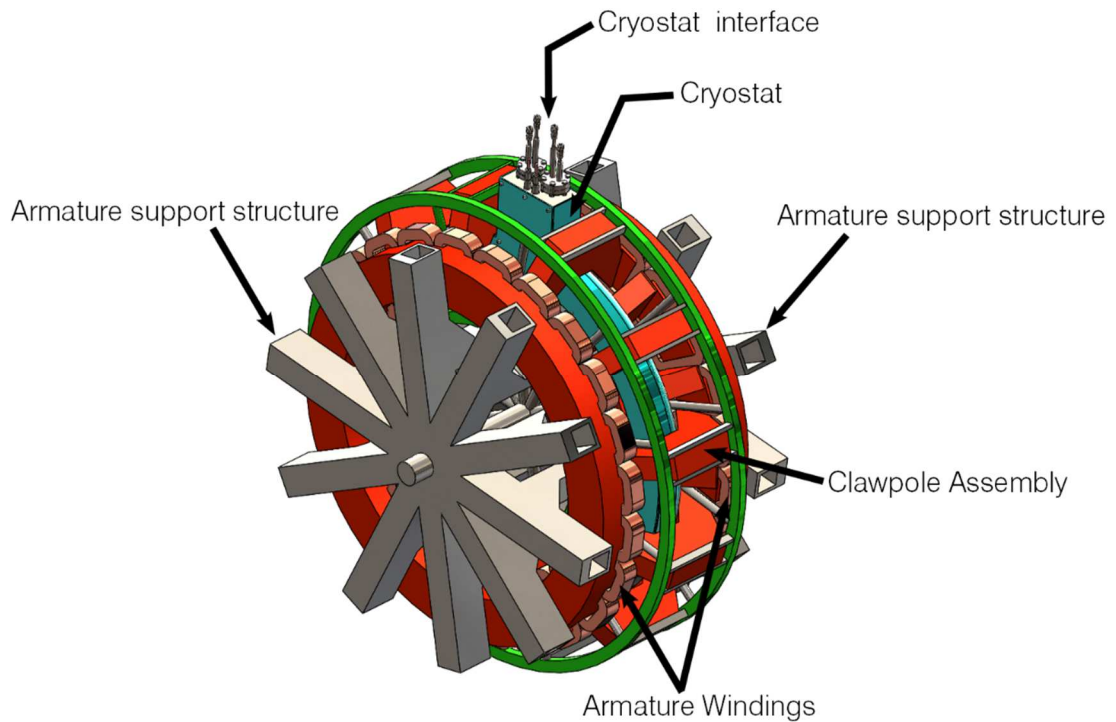


Figure 4-28, Proposed 30 KW claw pole HTS generator structure, including cryostat and stationary HTS field coil

4.3.1. Electrical Topology

The requirement to maintain an isolated cryogenic system and SC core is paramount, as these are the main benefits of this design. Due to size restraints, cryogenic access to the HTS core must pass through the claw pole's path of rotation. To alleviate this issue it was decided that rotating the armature windings would allow the claw poles to remain stationary and become part of the support for the HTS core and associated cryogenics. Rotating the armature sections of the prototype also allows for symmetrical claw pole topology, balanced structural loading. The electrical topographies are compared in Figure 4-29 while the specification of the prototype is supplied in Table 4-4.

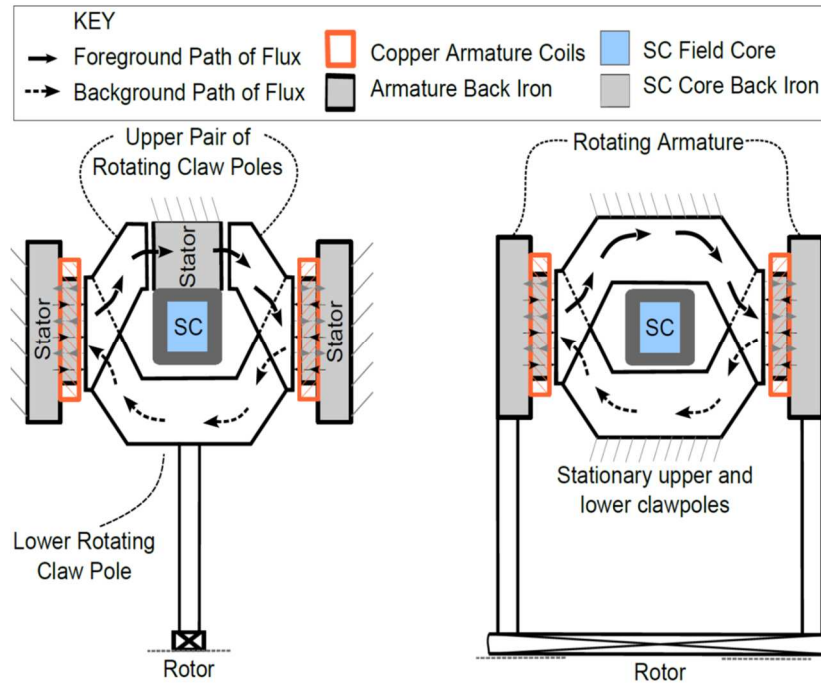


Figure 4-29. Left: Proposed 5 – 10 MW electrical topology. Right: Altered topology for 30 kW prototype

Quantity	Value
Rated Power	30 kW
Rated speed	100 rpm
Inner air gap radius	380 mm
Outer air gap radius	500 mm
Length	600 mm
Individual air gap length	2.5 mm
Cryostat diameter	800 mm
Number of poles	24
Number of armature coils	18
SC coil current density	91 A/mm ²
SC coil dimensions	12x16.5 mm
Total SC MMR	18000 A-turns

Table 4-4. Specification of 30 kW HTC claw pole transverse flux prototype

4.3.2. Structural Topology

High magnetic field strength is one of the benefits that enable SC technologies to achieve higher power densities. As Figure 4-30 indicates, the normal force per area is proportional to the square of the flux density, therefore a small increase in flux density can drastically increase the structural loading on the air gap, and this was provided to be the case during the testing of the linear claw pole machine. Therefore, for the

purposes of this design the flux density will be curtailed to roughly 1.5 T within the airgap, but for the purposes of this study the maximum attraction forces were said to be 1.2 MN/m^2 , which takes into account movement within the airgap. Although one of the benefits of this design is the symmetrical nature of the forces acting within the elements, the structure of this machine must still be designed to effectively manage these high attraction forces, as well as the torque present and the rotating mass of the armature windings and back iron. The operational torque of this prototype was calculated to be 3 kNm while the short circuit torque was calculated to be in the region of 18 kNm.

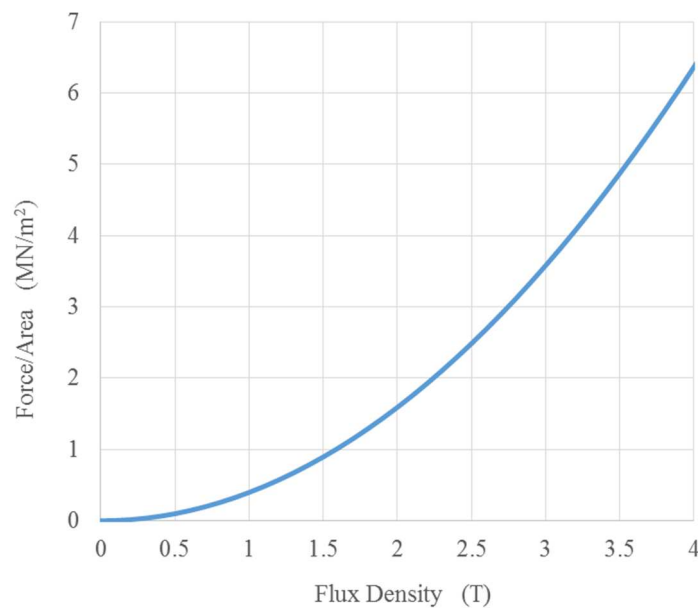


Figure 4-30. The variation of Maxwell stress with flux density

The structure of this prototype must also be cost effective. The structure provided in Figure 4-28 is to be constructed with box steel, steel rebar and compression struts. The high strength carbon chrome steel bar compression struts proposed within this design can be individually tailored at each spoke to counteract forces which may affect the air gap, Figure 4-31. A PM structure is under load at all times whereas utilizing SC technology means that the structure will only experience loading when the SC core is excited. Variations within the air gap could be monitored with extreme displacements triggering a shut off of the magnetic field, thus adding a safety feature to the design. For structural simulations the Young's modulus for box section structural steel is

assumed to be 200 GPa with a shear modulus of 77 GPa, while the ultimate yield strength of the compression strut is 1030 N/mm². The proposed rotor and claw pole structures are presented in Figure 4-32.



Figure 4-31. Example of compression strut design [213]

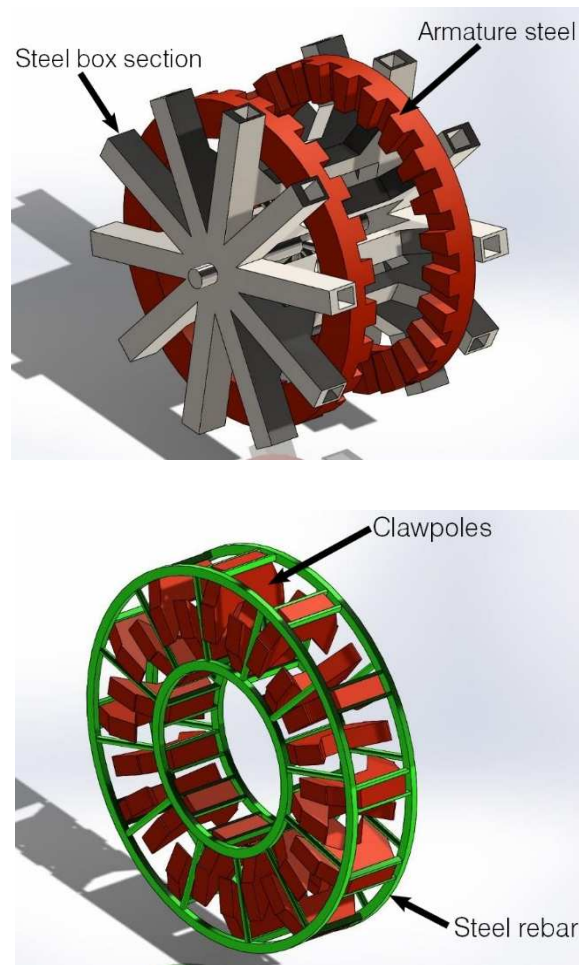


Figure 4-32. Top: Rotor structure with armature core highlighted in red. Bottom: Claw pole structure with claw poles highlighted in red

The forces modelled on this structure included gravitational loading, centrifugal loading, magnetic attraction forces, torque and short circuit torque. Examples of the simulated loading and deflections can be found in Figure 4-33 and Figure 4-34.

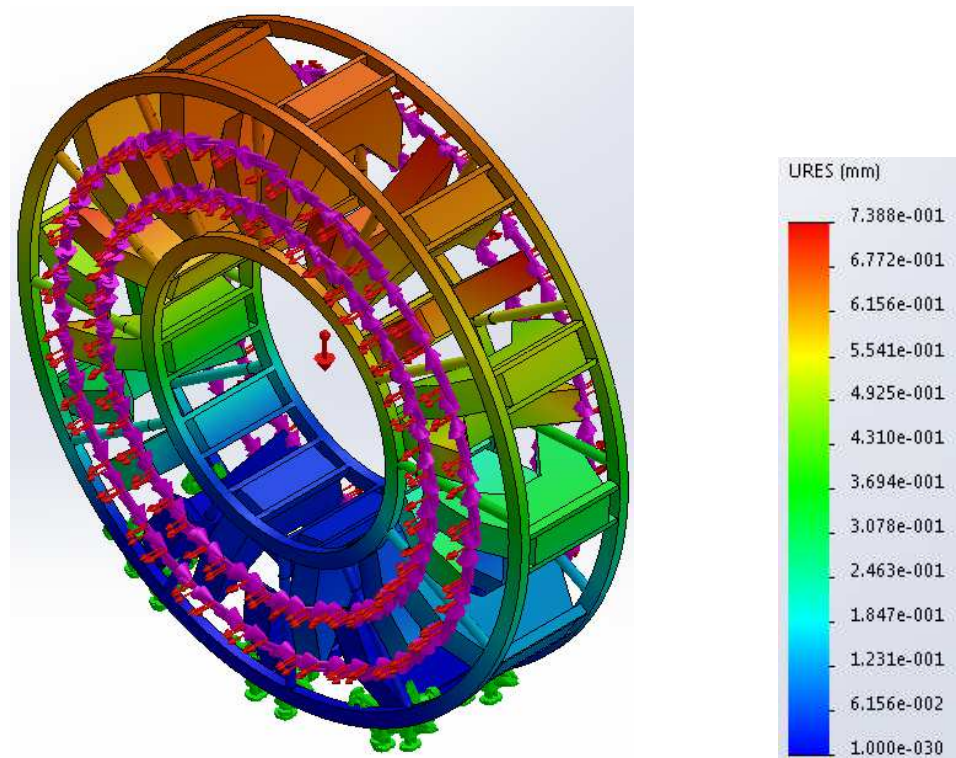


Figure 4-33. Claw pole structure indicating loads and total deflection

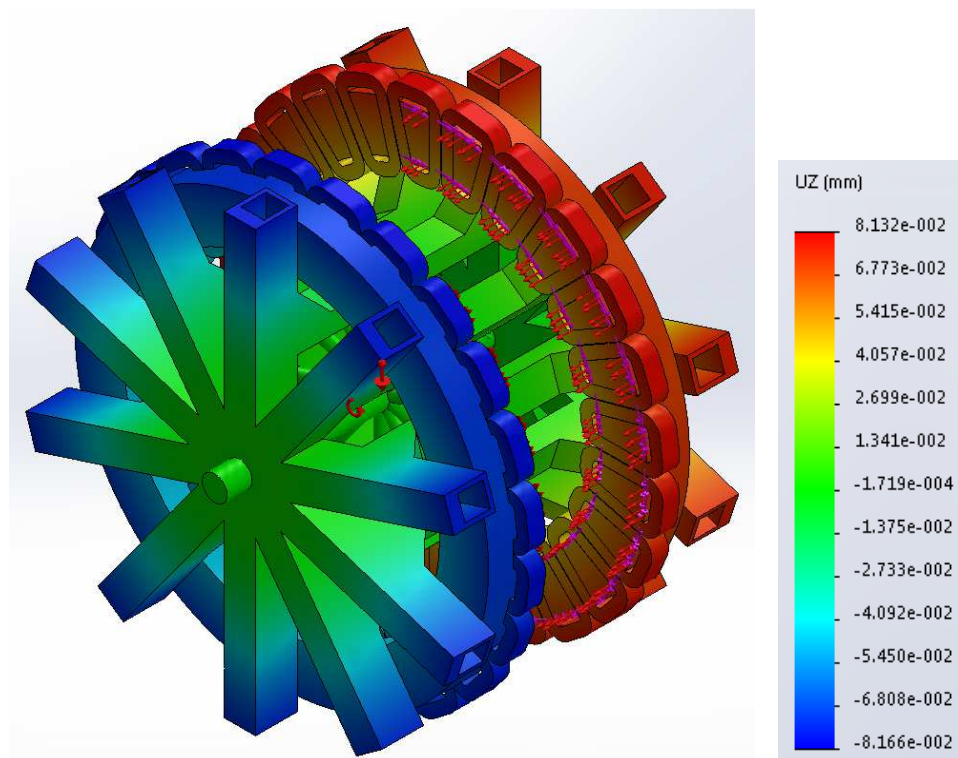


Figure 4-34. Rotor structure indicating loads and axial deflection

4.3.3. Discussion

The design is therefore not an optimised structure in the pure sense of the term; instead it is a structure which will be used as a test bed to provide further data on the structural forces present under loading and vibration testing. The results indicated that the rotors maximum radial deformation would be 4% of the airgap length at a maximum stress value in the region of 48 MNm^{-2} , while the stator's maximum radial deformation would be under 1% of the airgap length with a maximum stress value of 58 MNm^{-2} .

The addition of compression struts to the centre of the machine will enable adjustable tension to be applied to the armature rotor arms. In this manner the air gap can be maintained over various loads. The installation of the HTS field winding and the design of a potential cryostat is outlined in [214], an indication of the final structure is provided in Figure 4-35. Validating this topology will occur once the structure has been manufactured.

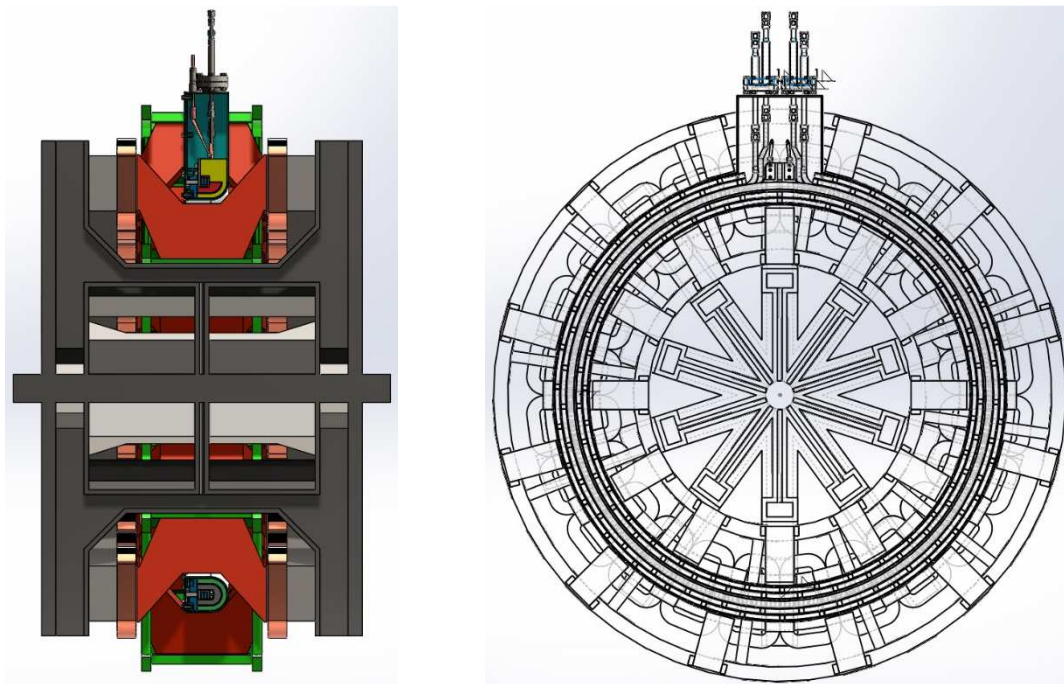


Figure 4-35. Complete 30 kW prototype machine including cryostat, HTS field winding, armature coils and support structure

4.4. Scaled Claw Pole HTS Design

The main objective of this section is to describe and provide data on the design and simulated testing of a 10 MW scaled claw pole HTS machine. In order to produce a design that can be considered optimised and competitive with existing and proposed SC machine designs the following constraints have been applied to the design.

- Produce a design which separates the electrical, mechanical and cryogenic elements
- Enable an electrical design which utilizes the high magnetic flux created in the SC field core, whilst maintaining stationary field and armature windings
- Construct a mechanical structure which is light-weight and strong
- Utilize sufficiently less SC tape in the field winding than most SC machines and maintain modularity
- Endeavour to produce a design which would be competitive and efficient compared with current offshore wind power generation options

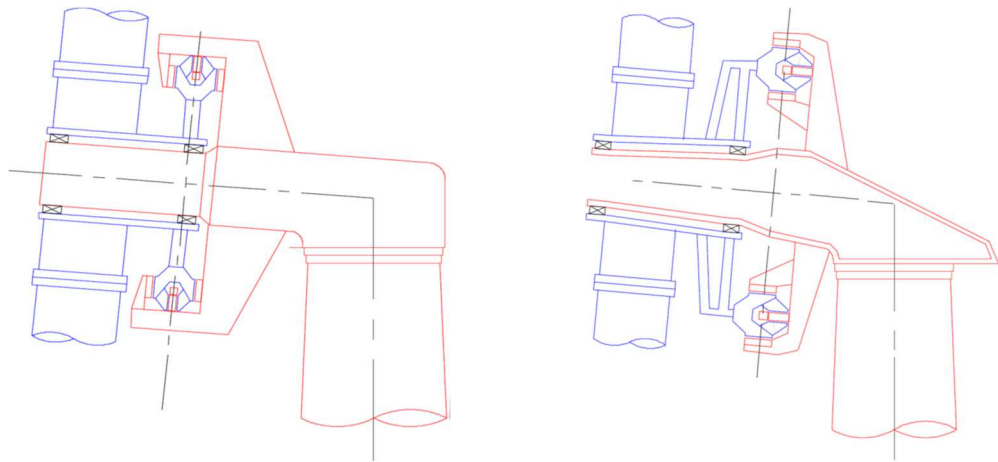


Figure 4-36. Left: Potential structure for an axial flux configuration. Right: Proposed structure for a radial flux configuration [143] [164]

The transverse flux claw pole machine design can be applied to both radial and axial generator topographies, as indicated by Figure 4-36. The radial flux topology was chosen for this study since it was considered easier to structurally support the active components compared to the axial flux topology. Therefore, the following sections will present a radial flux claw pole HTS generator design as proposed in Figure 4-37 and detailed in Video 1.

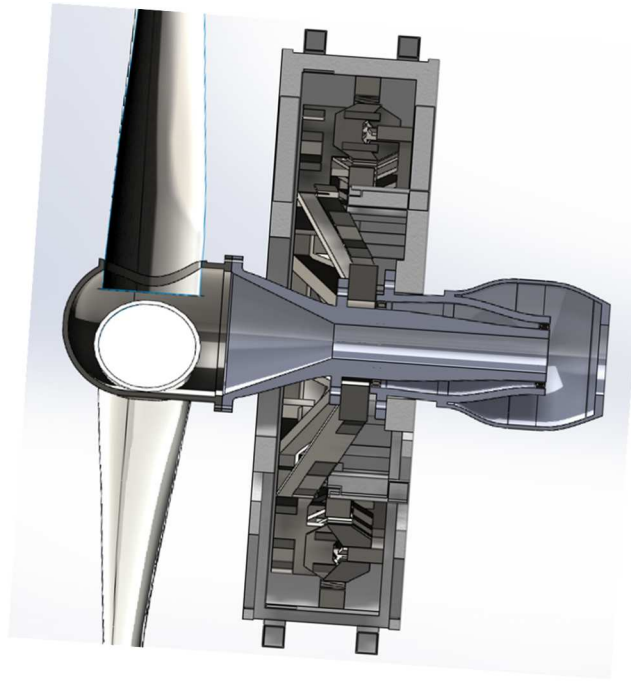


Figure 4-37. Proposed design of a 10 MW radial flux claw pole HTS connected to an indicative wind turbine drive train, hub and rotor blades.

4.4.1. Proposed Electrical Design

The proposed HTS generator has been scaled from the linear and 30 kW designs presented previously. The machine has a theoretical output of 10 MW using a homopolar claw pole transverse flux design suitable for low speed, high torque applications as described by Keysan in [164]. The active design of the machine is presented in Figure 4-38, and incorporates four stationary superconducting field coils, stationary copper armature windings and a rotating core of claw poles to guide the flux from the SC coil around the armature coils. The modularity of the design means that if a fault occurs in the HTS cooling system, HTS winding or armature windings, the remaining sections can continue to generate power at partial load until the next maintenance window is available.

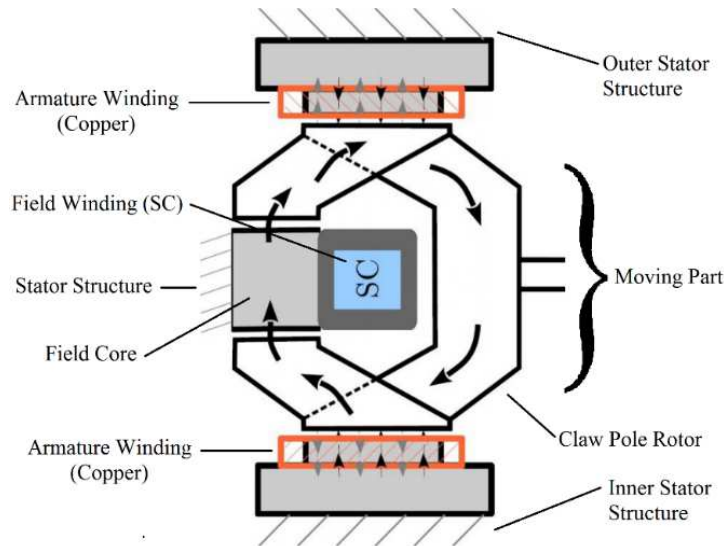


Figure 4-38. The active electromagnetic topology with indicated flux path

The design of the clawpoles and the skewed design of the armature back iron means that loadings would tend to be symmetrical and balanced. The stationary superconducting coil reduces the complexity of the cooling and excitation couplings. However due to the use of iron, soft magnetic composites (SMC) or other ferromagnetic materials within the design, very high magnetic attraction forces are present within the air gaps. Therefore, the rigidity of the support structure is of upmost importance in maintaining a constant air gap. The specifications for the proposed machine are provided in Table 4-5.

Quantity	Value
Rated Power (MW)	10
Rated Speed (rpm)	10
Air gap diameter (m)	6.5
Number of Poles	88
Phase Voltage	3.3
Copper Loss (kW)	510
Core Loss (kW)	7
Cry cooler (kW)	24
Efficiency	94.5%
Length (m)	1.6
Air gap (mm)	6
Active component (ton)	55
Construction mass (ton)	110
Total weight (ton)	165

Table 4-5. 10 MW HTS claw pole generator specifications

4.4.2. Structural Design

Results from the construction and testing of the 30 kW machine proposed in section 4.3 will be fed back into this scaled topology. However, for the purposes of this section the proposed structure will be based purely on the optimised electrical design, which requires the following physical factors had to be incorporated into the supporting structural design.

- The number of claw poles
- The length of air gap
- Dimension of armature back iron
- Dimension of HTS field core back iron
- HTS field flux

These active electromagnetic components are modelled and presented in Figure 4-39. For simulation purposes a claw pole rotor structure and a stationary support structure for the field and armature cores were produced. Forces were applied to the appropriate faces of the structural design emulating magnetic attraction and torsional loading forces. Stress and deformation analysis showed areas which required reinforcement or removal; through this method an optimized structure was created.

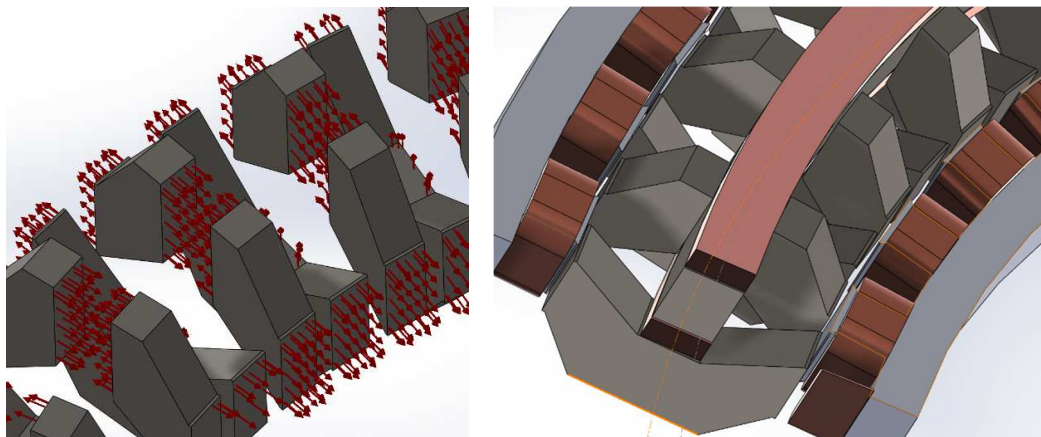


Figure 4-39. Left: 3D representation of the claw poles, red arrows indicate the direction of magnetic attraction. Right: 3D representation of active electrical components

The highest magnitude force that had to be considered was the magnetic attraction force between ferromagnetic materials. As previously stated, high magnetic field

strength is one of the benefits that enable SC technology to achieve higher power outputs; however topologies relying on ferromagnetic materials to direct flux tend to experience high forces acting on the structure. The maximum value of the air gap flux density is limited by natural permeability of the material. The proposed HTS topology incorporates Vacoflux50 into its design. This material has a high saturation point of roughly 2.2 T [215]. The flux present within the air gap for this topology will be in the region of 1.8 T – 1.9 T. Although forces are curtailed by the saturation level and flux leakage, resulting forces in the air gap can be as high as 1.5 MNm^{-2} . For this structure the maximum loading based on magnetic attraction was calculated to be 1.7 MNm^{-2} ; this was in order to compensate for increases in magnetic attraction due to deflection.

The stationary HTS field core and winding will not be required to withstand any large centrifugal forces unlike SC systems contained within the rotor. Additionally, there is no cryogenic coupler and transient torque on the SC coil, thus allowing the cooling and supporting insulation to be simplified. The machine design with a stationary SC core removes the complication of producing a cryogenic coupler able to withstand high torques and super low temperatures, separating the structural design from cryogenic concerns. The electric torsional force can be said to be acting at both the outer and inner faces of the armature and similarly on both the outer and inner faces of the clawpoles on the rotor. The force was calculated based on the power rating of the generator and its rotational speed. Therefore, the total torsional force used in the simulations was 9.6 MNm.

4.4.3. Loading Simulations and Optimisation

The design has been split into a loaded armature structure and a stationary loaded rotor structure. Stress and deformation analysis showed areas which required reinforcement or removal; through this method an optimized novel structure was created. The simulated bodies were fixed at the connection to the drive train or surrounding nacelle structure. For the purposes of this study these connections were treated as rigid. Figure 4-40 contains a cross sectional view of the structure of the stator and rotor. Highlighted in red are the positions of the inner and outer armatures, highlighted in blue is the position of the field core and the rotating claw poles are highlighted in green. The

loadings shown are noted with arrows indicating the direction in which they act. Red arrows denote the direction of the magnetic attraction forces; the pink arrows denote the application of torsional loadings, while the large red arrow in the centre indicates the direction of gravitational loading.

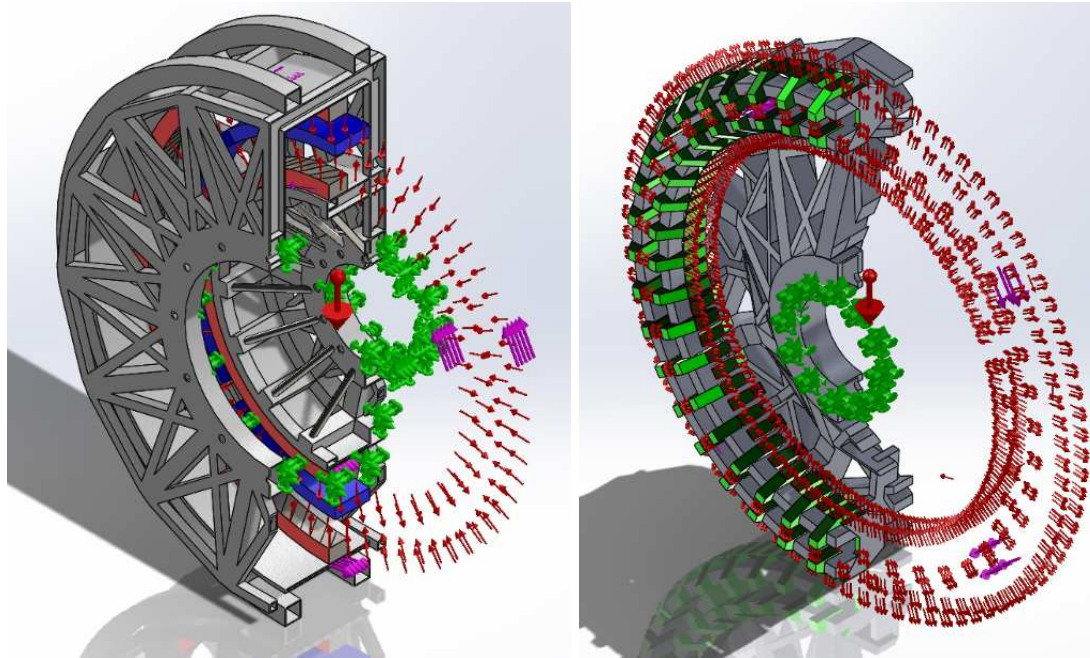


*Figure 4-40. Left: Cross section of stator structure. Right: Cross section of rotor section.
Forces and fixtures are indicated*

A basic cylindrical structure was produced which supported both the inner and outer windings and back iron. The structure was then loaded and structural analysis was carried out using Solidworks structural Finite Element Analysis, FEA, simulation package. To refine and analyse the results of the FEA studies, several precautions were undertaken. Firstly, the mesh applied to the bodies was refined from rough to fine over several simulation runs. This allowed for a convergence study to be completed, indicating when the resulting stress became most accurate. Secondly, the aspect ratio of the mesh investigated to ensure that the percentage of mesh elements with an aspect ratio greater than 1 is kept as low as possible, ideally lower than 5%. Thirdly, the chosen materials stress level was checked. If the FEA produced stress levels that approached 90% of the yield stress of the material, then the body was redesigned to strengthen the area in question. Although this was a time-consuming manual analysis of the design, it allowed all aspects of the generators structural design to be thoroughly

understood. In areas of low stress material was removed and the analysis repeated until an optimized balanced bespoke structure was produced. This structure was then assessed and common structural steel elements inserted to replace undesirable bespoke sections. The whole structure was structurally analysed and elements added or removed depending on stress markers. Finally, structural compression and tension rods replaced heavier box section in the relevant areas. An example of this process is supplied in Figure 4-41, Figure 4-42, Figure 4-43 and Video 2.

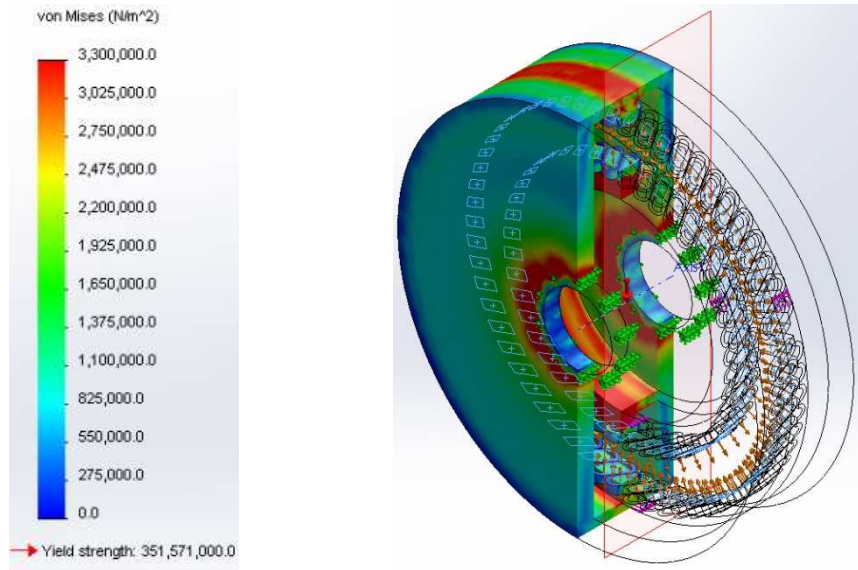


Figure 4-41. Stator structure simulation, cooler colours indicate areas of low stress

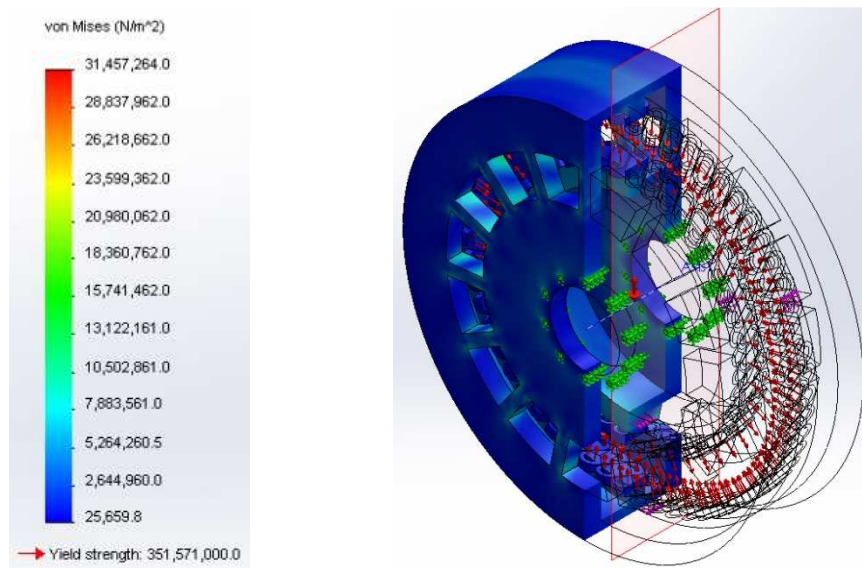


Figure 4-42. Stator structure simulation, sections removed and simulation re run

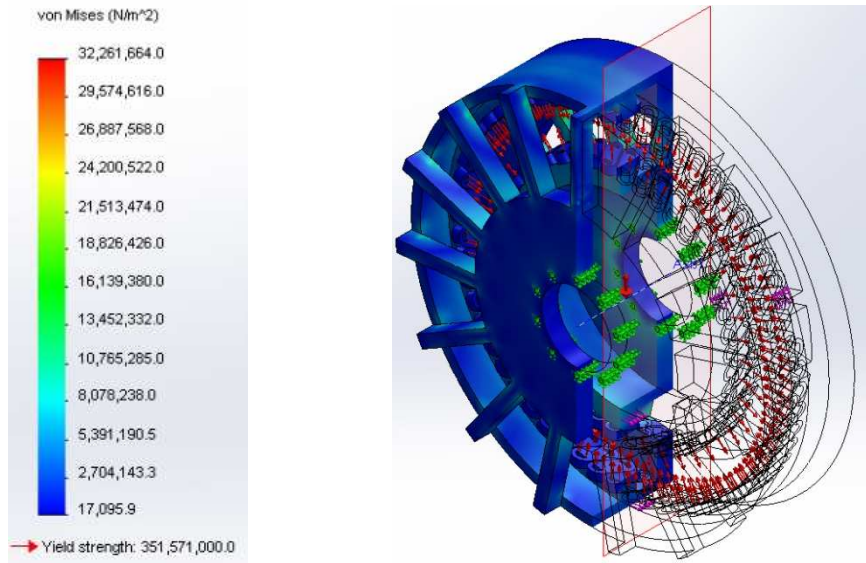


Figure 4-43. Stator simulation, further sections removed. Simulation re run and yield stress observed to insure structural cohesion

4.4.4. Discussion

The maximum radial deflection was proved to be below 5% of the air gap, the axial deflection was shown to be below 1% axial length and the circumferential deflection was calculated to be less than 0.5 degrees. The mass of the armature structure was shown to be in the region of 60 metric tons while the mass of the rotor structure calculated to be 50 tons, therefore the mass of machine over torque density was calculated to be 16.4 kg/kNm.

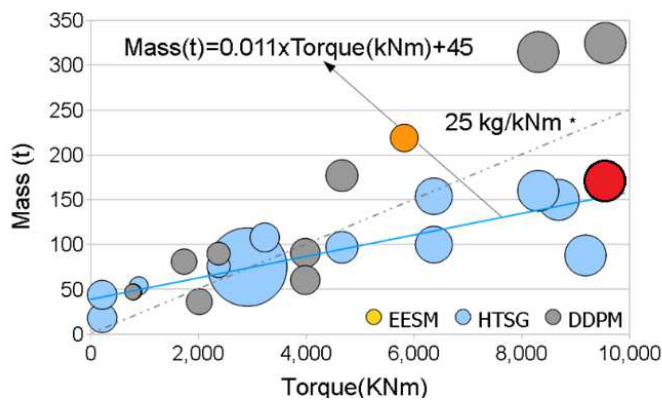


Figure 4-44. Projections for offshore generator size including trend lines. Blue trend line for HTS trends and grey dotted trend line based on Bang et al [143] mass estimations for DDPM. Red circle indicates the placement of the 10 MW machine presented in this study

Figure 4-44 indicates the relationship between the torque of DDPM and HTS generators with their corresponding mass. It can be seen that with a mass of around 165 tons, the machine outlined in this section is roughly half of the mass of a conventional DD machine for the same output and torque. It can also be seen that the machine proposed in this chapter roughly adheres to predictions of HTS generator mass. However, the machine was not subjected to full short circuit torques which implies further study is required to make the machine operational. Other future considerations will include the addition of drive train dynamics including harmonic loading, vibrations and displacements as well as unbalanced magnetic forces to determine the ability of this design to withstand the offshore turbine environment. The ability to alter the compression within tension struts to aid with fluctuation within the air gap will also be reviewed. In addition, a more accurate model of the dynamic nature of the magnetic attraction forces due to the rotation of the claw poles will be produced. Analysis of the connection of the SC core and field winding will be studied and loadings from harmonic vibrations and stall will be assessed to add to the machines structural integrity.

Chapter 5.

Linear Bearing Tests

5.1. Offshore Renewables

The installation of power generation devices in the harsh marine environments places increasing pressure on the reliability and longevity of mechanical components such as bearings. In addition, the forecasted size and rating of these machines is pushing bearing technology to the limits of their capacity. As professed in previous chapters, minimum O&M costs, and maximised running times are vital to wind, wave and tidal stream devices to maintain economic viability. Often failures in offshore machine components prove expensive and difficult to replace, especially if located below the seas surface or far from shore. Weather factors can also disrupt maintenance and repairs, increasing down times indefinitely. Improving the reliability of these energy harvesting systems is crucial to the development of an economically viable, clean, sustainable, energy infrastructure.

As mentioned in Chapter 2, the reliability of bearings has proven problematic for renewable energy devices. The majority of offshore devices come into contact with the corrosive nature of the marine environment. Salt water corrosion, bio-fouling, salt spray and humidity can degrade traditional bearing solutions designed for onshore applications. However shipping and other offshore industries have been utilising materials to suit the offshore environment for centuries. Bearings for ship propulsion systems were traditionally water lubricated and although synthetic lubrication systems were introduced in the 20th century, water lubricated journal bearings are now being utilised again [216]. Therefore, marine polymer journal bearings are a potential solution for marine renewable devices and in order to understand and improve the reliability and durability of incorporating these materials into offshore energy devices, mechanical testing is required.

The testing of rotary bearings is fairly common, an example of which is supplied in Figure 5-1. In a similar manner, wind turbine bearing testing is often aimed at

replicating the loads transmitted from the turbine's hub and blades, including off balanced loads. The loads are applied via finely controlled actuators or motor inputs. Results focus on material performance, durability deflection and stiffness measurements. However, results from linear bearing testing are scarce, especially when it comes to linear polymer surface bearings since their large scale application is predominantly in the shipping industry for rotary prop shaft applications. Therefore, this chapter will discuss the testing of polymer bearing material samples, including the calculation of loads, the design and build of a test rig and a comparison of wet and dry testing data.

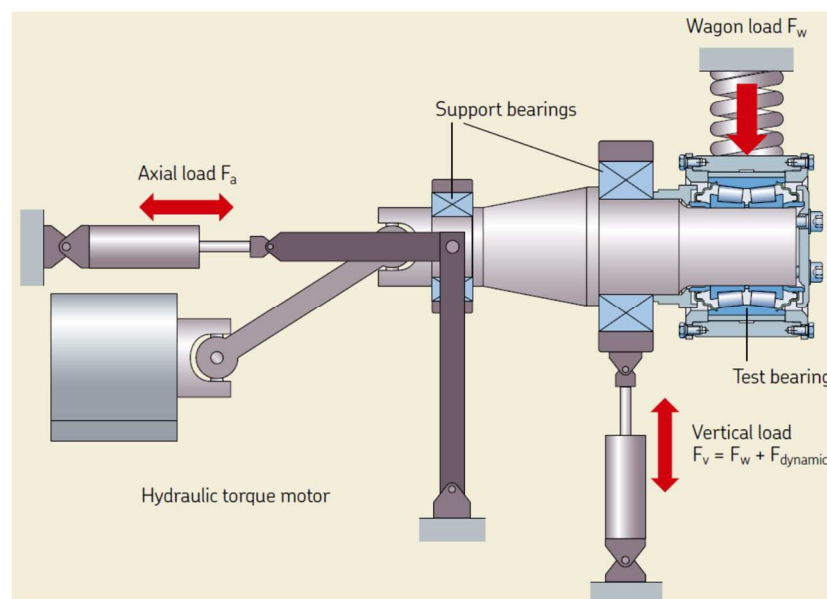


Figure 5-1. An example of a high speed radial bearing test rig for the rail industry [217]

5.2. Loading

The choice of machine and device topology indicates the size and design of bearings required, as well as the direction and magnitude of loads acting on the machines structure. Although real world wave loading data was not available during the period of this study, an analytical loading study was performed in order to gauge the validity of testing the performance of bearing samples under specific surface pressures. For purposes of the loading study a small 5 kW linear C-GEN machine topology is incorporated into a theoretical point absorber device. The resulting data from the loading study will then be utilized as applied loads on the bearing samples during testing.

5.2.1. Marine Wave Loading

A cylindrical heaving buoy of height 2 m and diameter 3 m was connected to the 5 kW C-GEN machine. The buoy will be submerged in water with a depth of 25 m, similar to installation provided in [218]. The 5 kW C-GEN generator topology used for this study is described with more detail within Chapter 6, however for this study consists of an external generator structure of 1.8 m in height, 0.65 m wide and 0.15 m deep.

In this study, Morison's equation [219], was used to calculate the horizontal force and moment on the buoy due to an incident sinusoidal wave of period T and wave amplitude a in a water depth h . For the purposes of this calculation, the buoy is split in to horizontal strips. The Morrison's equation can be used to provide the horizontal force, dF , across each strip of the frontal area, A_{front} , of a cylindrical buoy with volume V .

$$A_{front} = dD \quad 5-1$$

$$V = \frac{\pi D^2}{4} d \quad 5-2$$

Where d is the height of the buoy and D is the diameter of the buoy. The Morrison equation relies on the horizontal fluid velocity and acceleration at the midpoint of each strip, u and \dot{u} respectively, as described by Equation 5-3 and Equation 5-4.

$$u = a\omega \frac{\cosh(k(z+H))}{\sinh(kH)} \cos(\omega T - kx + \varphi) \quad 5-3$$

$$\dot{u} = -a\omega^2 \frac{\cosh(k(z+H))}{\sinh(kH)} \sin(\omega T - kx + \varphi) \quad 5-4$$

Where ω is the vertical fluid velocity at the midpoint of the strip, φ is the wave phase, k is the wave number, H is the total water depth and z is the depth of the midpoint of the specific strip. The horizontal forces acting on each strip can then be calculated and summed, as indicted by Equation 5-5.

$$\Delta F = \rho C_m \Delta V \dot{u} + \rho_{water} C_d \frac{1}{2} \Delta A_{front} u^2 \quad 5-5$$

Where ρ is the density of water, C_m is the coefficient of inertia and C_d is the drag coefficient. However, the Morison equation has certain limitations. For example, it can only be used when the diameter of the cylinder is much less than the wavelength. Furthermore, the two empirical hydrodynamic coefficients: C_m and C_d , depend on a number of parameters such as the Reynolds number, roughness and flow parameters. Achieving correct values of these coefficients is difficult, in this study, representative values of 1.3 and 0.6 were used for C_m and C_d , respectively. The assumption used within this decision is that the buoy as a smooth surface creating a laminar flow over its surface rather than turbulent.

Figure 5-2 indicates a graphic version of a loading case for a submerged point absorbing buoy. Horizontal forces and moments are calculated for normal wave operating conditions and an extreme wave loading in various water depths. The calculation of loads within the analytical code took place at the extreme values of the point z_m , i.e. the top and bottom of the generation stroke.

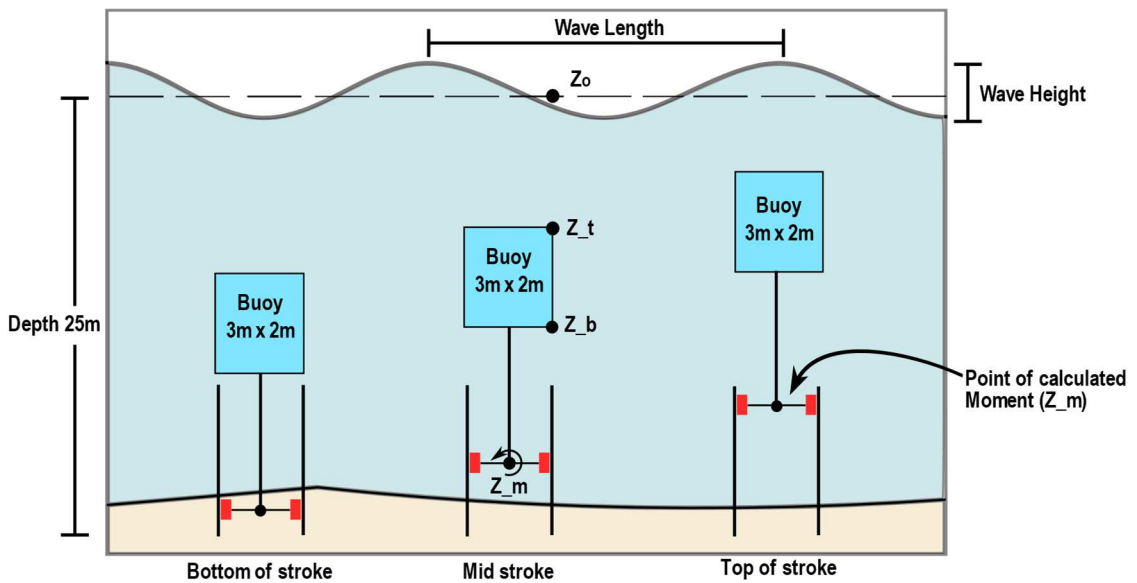


Figure 5-2. Submerged 3x2m point absorber, indicating a full generation stroke of in shallow water

5.2.2. Wave Loading Results

To calculate the loads produced from various sea states, statistical wave data has been obtained from a WEC developer. The amplitudes and periods of various wave states verses the percentage of time they are active have been supplied in Table 5-1. It can be said that waves which operate for a higher percentage of the year would be considered this device “normal” operating state, whilst waves which occur less frequently are towards the extreme wave size for a power take-off of this size and design. The resulting forces are included in Table 5-1 and indicate the force values that would be exerted on the buoy and point z_m for the top and bottom of the generators stroke. These results will be used in tandem with the results from the bearing test rig in order to validate the loading method. The source code has been provided in Appendix C with the resulting moment and force graphs for the wave conditions provided below.

A (m)	T (s)	% Time	Top of Stroke		Bottom of Stroke	
			F _{Tot} Buoy (kN)	M _{Tot} z_m (kNm)	F _{Tot} Buoy (kN)	M _{Tot} z_m (kNm)
0.76	5.20	51%	11.6	163	10	140.6
0.86	6.80	16%	9.8	138	9	126.6
1.55	6.40	16%	19	268.5	17.3	243.4
1.83	7.70	12%	17.7	248.9	16.6	232.7
2.59	8.30	4%	22.6	317.7	21.4	299.9
2.85	9.60	1%	22.8	319.9	21.9	307.5

Table 5-1. Sea states values and occurrences provided by a WES device developer with the calculated applied forces/moments

5.3. Polymer Journal Bearing Testing

Polymer bearings are simplistic in nature, mostly produced from one material, they are relatively easy to produce in any topology, when compared to metal or alloy bearings. They have been proven to be corrosion resistant with low friction values, normally operating on a self-deposited thin hydrodynamic film of material which gradually wears the bearing down over time. These self-lubricating bearings can operate in both dry and wet conditions, dependant on load and velocity. Figure 5-3 indicates the build of the hydrodynamic film, indicating that for optimised operation a polymer journal bearing needs to operate under a minimum load. In this manner the life span of a polymer bearing can be assessed based on its wear rate whilst operating in conditions above its minimum load requirement.

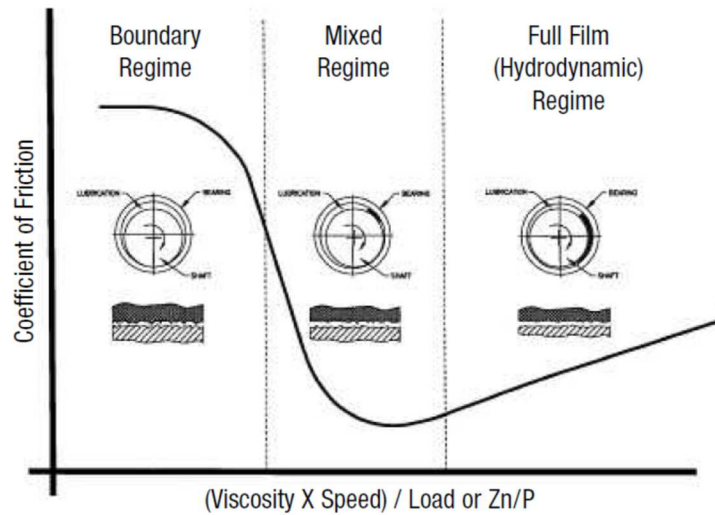


Figure 5-3. Stribeck curve illustrating the build-up of the hydrodynamic film on a journal bearing. Zn/P is the hydrodynamic parameter of the material [123]

A full study of self-lubricated bearings has been produced by Caraher in [119] and their operation in offshore renewable machines have been proposed by Meicke et al [220], YDong et al [221] and Nakanishi et al [222]. A selection of four polymer materials were selected for this study. In order to maintain anonymity, the manufacturers will not be named within this study. Instead the bearing samples will be referred to as bearing sample I, II, III and IV. Examples of the bearing samples machined and ready for testing are provided in Figure 5-4.

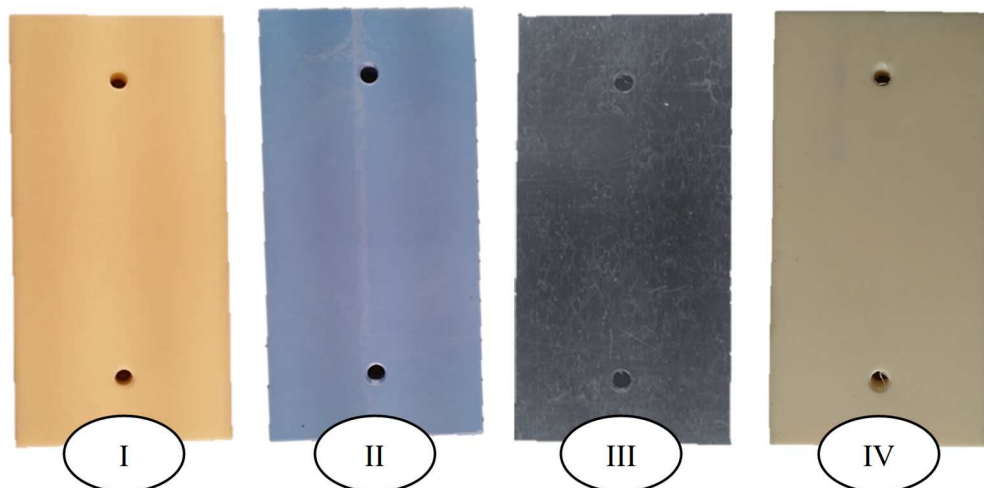


Figure 5-4. Bearing material samples with corresponding reference.

Details of the test samples physical properties are provided within Table 5-2.

	SAMPLE I	SAMPLE II	SAMPLE III	SAMPLE IV
Density (g/cm ³)	-	1.4	1.15	1.49
Water absorption wt%	1.3	0.034	2.8	1.3
UTS (MPa)	37.5	92	85	-
Hardness (Shore D)	-	83	83	74
Max temperature (°C)	107	110	95	90
Dry friction co-eff	0.1 - 0.2	~ 0.1	0.25	0.06 – 0.18
Wet friction co-eff	0.1 - 0.2	0.1 - 0.17	-	0.04

Table 5-2. Test samples physical properties

The test samples were machined into rectangular blocks, the dimensions of the pads are provided in Figure 5-6. For rigidity during testing the samples are bolted to an aluminium c shaped support clamp as demonstrated in Figure 5-5. In order to correctly identify specific bearing pads, the position of their installation was noted as A, B and C.

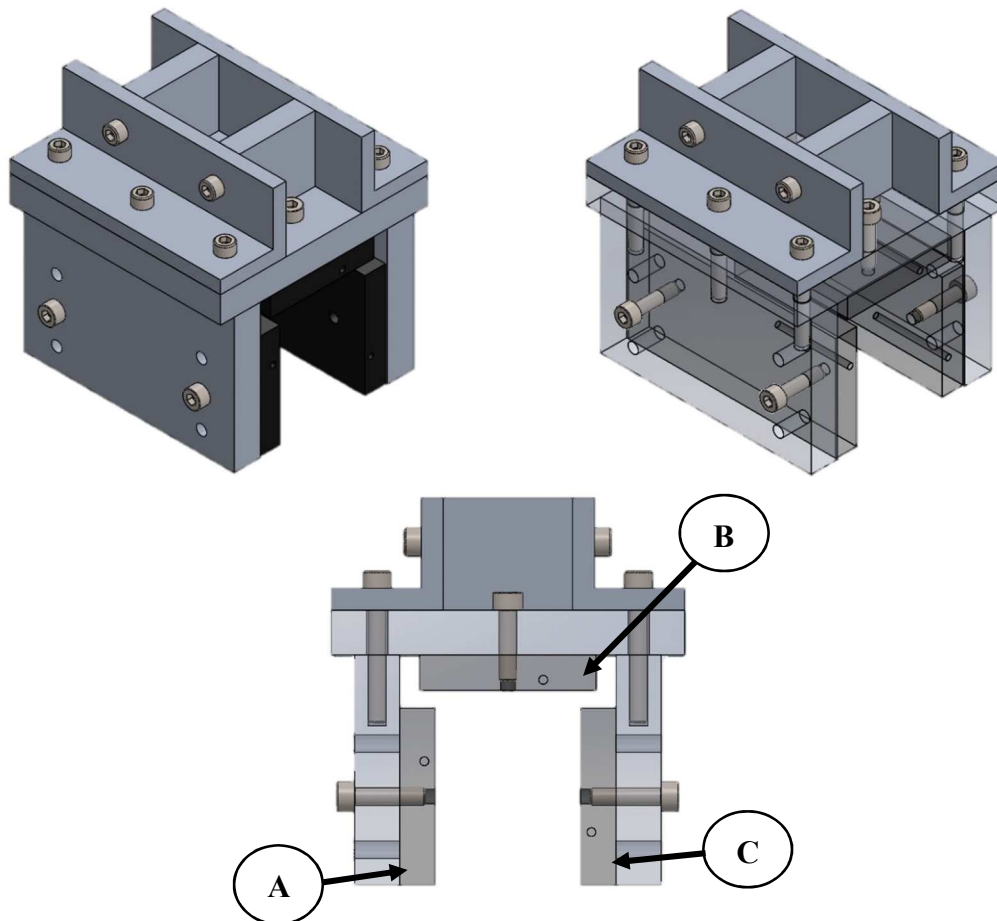


Figure 5-5. Linear bearing test rig c shaped supporting clamp with installed bearing samples. Arrows indicate order and placement of bearing sample pads

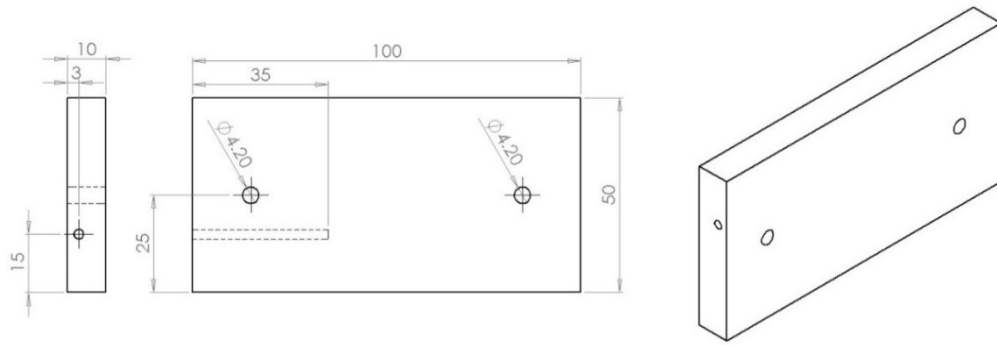


Figure 5-6. Bearing pad dimensions

5.3.1. Linear Test Rig Design

The bearing test rig and testing programme was developed with advice from a sub-sea bearing manufacturer. Standard bearing testing involves applying a point load, however it was felt that this was not appropriate, and the test procedure should mirror the actual application and operational conditions. Therefore, a reciprocating linear bearing test rig was designed for both dry and wet testing environments. The original test rig topology is presented in Figure 5-7, while the constructed test rig is provided in Figure 5-8. The overall design consists of a CDG1BN50-500 air piston capable of supplying a maximum of 0.7 ms^{-1} with a piston length of 0.5 m. The piston connects to a linear carriage supported by two sets of 30mm NSK ball bushings bearings and two hardened and ground steel guide rails. These components are installed on top of a stainless-steel tank with a removable lid. The construction of the test rig was completed by Fountain Design Ltd.

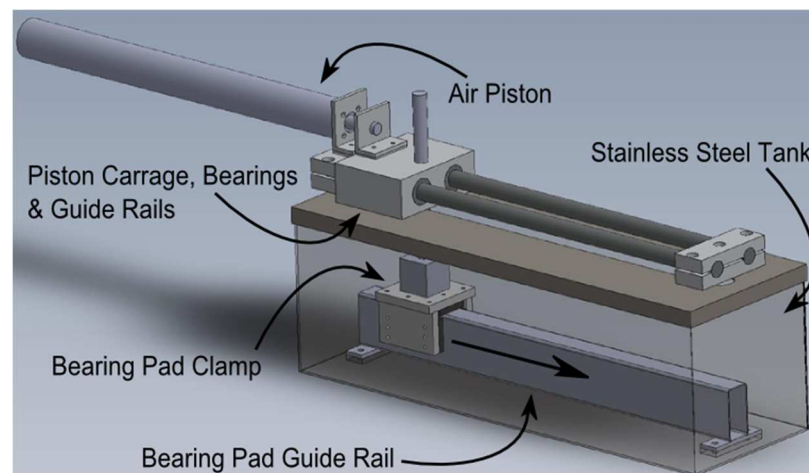


Figure 5-7. Simplified linear bearing test rig



Figure 5-8: Constructed linear bearing test rig. Left: Completed rig including actuators connected to the piston carriage. Right: The fabricated c-support with Type III test samples

The testing methodology for the bearing samples was to bolt each sample in to a c shaped support bracket which could be removed easily for bearing assessment and sample removal. The c-support is attached to the piston carriage which in turn drives the bearing sample back and forth on a stainless steel box section guide. A stroke is considered to be one cycle of the piston movement, equal to 1 m, each cycle is recorded on a counter thus providing the distance travelled in meters. In addition to the basic reciprocating operational design, compressed air actuators mounted on the piston carriage apply vertical and torsional loads to the c-support and in turn to the bearings. Further explanation of the bearing test rig construction is presented in Figure 5-9 and Table 5-3.

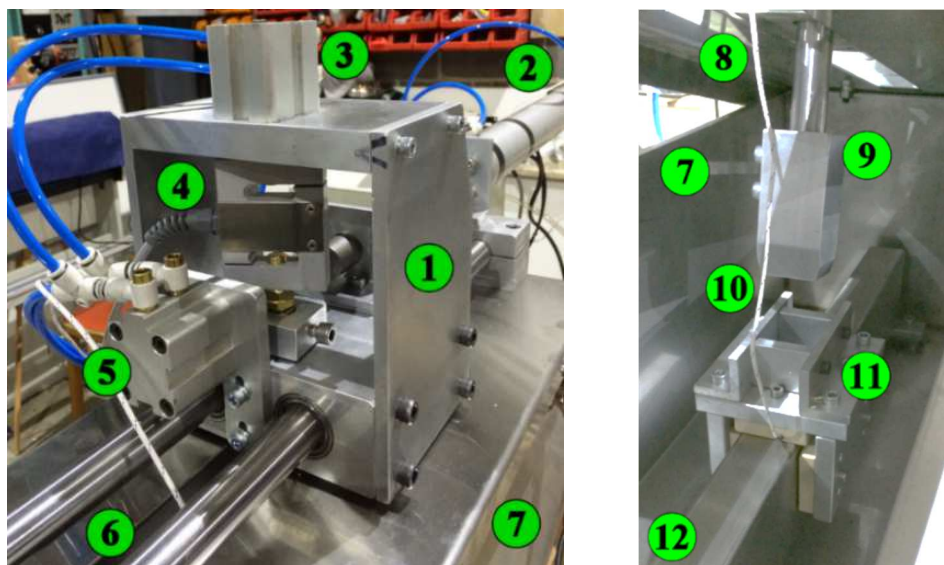


Figure 5-9. Critical bearing test rig components. Left: External. Right: Internal

- 1 Piston carriage
- 2 Piston
- 3 Vertical actuator
- 4 Load cell (rated 500 N)
- 5 Torsional actuator
- 6 Hardened steel guide (Dia 30mm)
- 7 Stainless steel tank
- 8 Removable tank lid
- 9 C-support connection
- 10 Thermocouple
- 11 C-support and bearing samples
- 12 Stainless steel box section guide rail

Table 5-3. Details of test rig design components

The application of loads and the speed of the test rig has been designed to emulate as close as possible the real life working conditions of the bearing material in a generator used in a wave device. Bearing pads A and C are expected to experience most of the torsional loading, while the bearing pad located in position B will experience the majority of the horizontal loading. The rig can apply up to 500 N of both vertical and torsional loading as well as a horizontal driving load of ~ 982 N and a maximum return load of ~ 800 N. However, these loads are dependent on the available pressure of the compressed air supply. Unfortunately, a private compressed air source could not be obtained so loads and reciprocating velocities fluctuated over the length of the tests.

5.3.2. Testing Procedure

During discussion with the bearing manufacturers it was decided that a surface pressure value of between 0.1 – 0.5 MPa for all samples would be achievable for these tests. Primarily operating on bearing pad in position B and whilst the surface pressure for pads in position A and C were maintained under maximum operational surface pressures. Reciprocating velocities were aimed to be maintain between $0.4 - 0.6 \text{ ms}^{-1}$, mimicking a normal sea state WEC operation [119]. Most WEC devices are expected to be subjected to 5000 hours of operation per year, with bearings travelling up to 8400 km [220]. Traditionally devices are designed to for 1 million cycles of operation [119]. However due to time restraints a distance of 200 km was achieved as the minimum distance of travel for all bearing pads, producing 2×10^5 cycles of the bearing along the guide. One sample achieved up to 500 km or 5×10^5 cycles in order to validate extrapolated data.

All bearings will be tested in both dry and salt water conditions for continuous periods. Before testing each sample will be weighed and imaged, if the bearing is being tested wet, the pads will be soaked in water over a week and weighed in order to define their saturated mass. Artificial salt water was produced using an aquarium salt mix recreating the salinity of the North Sea equal to 3.5 parts of salt to 1000 parts water, with a density of $\sim 1030 \text{ kg/m}^3$. Once clamped in place and installed into the test rig, a thermocouple will be installed within the top bearing pad to monitor the bearing pads operational temperature. During testing observations will be made every 50 -100 km, at which point the samples will be removed, briefly dried (if required) and weighed. Once complete the wear rate of the bearing pads (g/100km) will be calculated.

5.3.3. Mechanical Faults

The bearing test rig was constructed to run a simple reciprocating motion 24 hours a day 7 days a week. However, over time the rig suffered various faults, which cost testing time, but in some cases led to functional improvements of the testing design.

Over the course of 5 months, the compressed air supply failed a total of 8 times necessitating the replacement of two compressors and the installation of a large compressor capable of supplying 150 cubic litres of air at up to 14 bar. However due to an existing manufacturing fault which was exacerbated by a 24/7 testing schedule, the compressor failed after only 1 month of continuous supply.

In addition, it was discovered that the piston connection to the top carriage was too rigid, leading to the shearing of the L bracket connection, as shown in Figure 5-10. The L bracket was produced from two sections of aluminium bar welded together on the inside of the L joint. Off centre operational loads caused by inaccuracies during construction were exacerbated by the back and forth movement of the rig, eventually causing failure at the point of the weld. A new design was proposed which included a universal joint, a steel L bar section and a load cell to monitor the horizontal load and make it easier to evaluate friction coefficients. The proposed design is provided in Figure 5-11 while the fabricated and installed design is provided in Figure 5-12.



Figure 5-10. Damage to L bracket connecting piston to load carriage

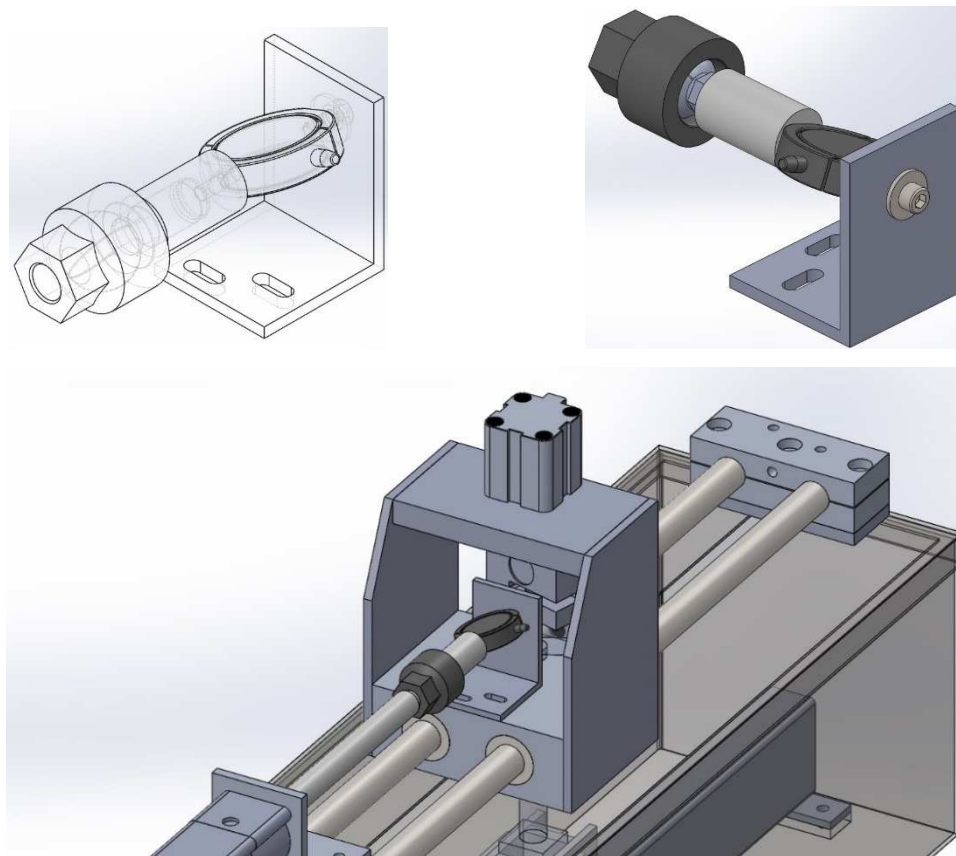


Figure 5-11. Proposed improved piston load carriage topology, including ball joint and load cell with reinforce L bracket connection

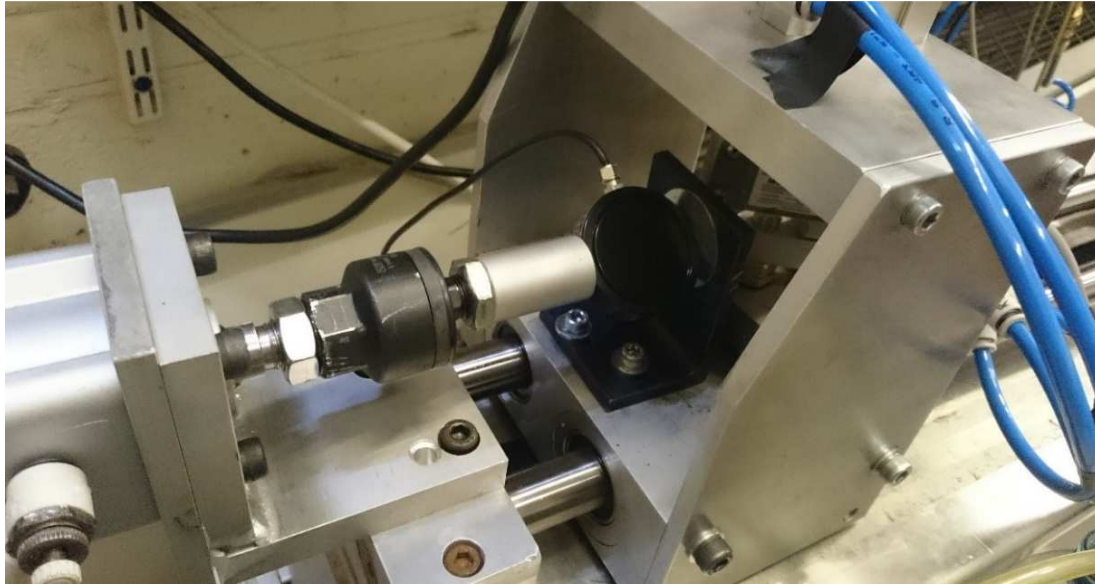
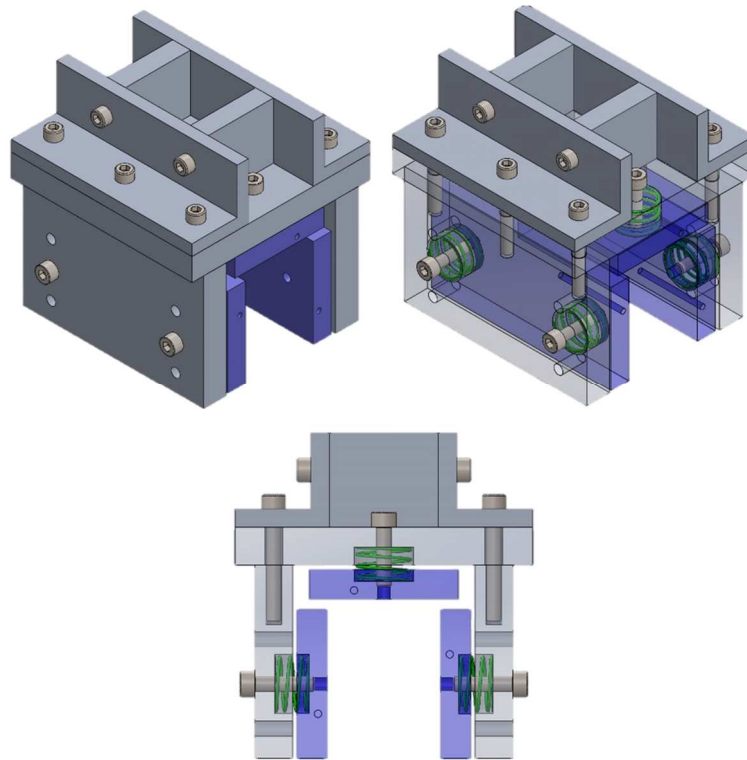


Figure 5-12. Installed improved piston load carriage topology, including ball joint and load cell with reinforce L bracket connection

During sea water testing the seals on the air piston disintegrated as did the ball bearing bushings for the piston carriage. As a result, the hardened steel guide rails were heavily scoured and the piston's ram was heavily damaged. To combat the effects of corrosion brushes were installed to minimise splash back. A new piston was installed with a reinforced aluminium support and silicon grease has been applied to the hardened steel guide rails in an attempt to reduce the risk of bearing disintegration further.

5.3.4. Bearing C-support Alterations

Initial results from dry tests showed that a slight rocking motion was present at the start and end of each cycle resulting in an uneven wear profile on the surface of the bearing pads. To counteract this movement, the bearing clamp and method of attaching the bearing samples has been modified by adding springs between the pad and the supporting aluminium clamp, ensuring as much surface contact between the bearing pads and the guide rail at all times.



*Figure 5-13. Improved linear bearing test rig c-support topology with sprung bearing pads.
Spring locations shown in green*

However, during initial tests with the new c-support it was discovered that the bolts maintaining the pads and springs in place were moving and coming into contact with the guide rail. This resulted in deep scouring of the stainless steel guide rail and heavy abrasion to the surface of the bearing pad, examples of which can be found in Figure 5-14. In order to counter act this problem, wire locking bolts were introduced to make sure there was no further movement in the bolts.



Figure 5-14. Left: Abrasion to bearing surface caused by metal shards from damaged guide rail. Right: Two damaged bearing guide rails

An additional side effect of installing a sprung bearing system is that the springs also added force in the normal direction to the samples surface contact. With a spring coefficient of 4.7 N/mm, and load length of 9.4 mm, two springs can add an extra 50 - 60 N of normal load to each bearing pad, at a compression of 2-3 mm depending on rocking motions. To validate this calculation a bearing pad was placed into a loading machine with the resulting force data provided in Figure 5-15. The plot includes the calculated data starting from the load length and generally shows good agreement between the experimental and calculated load. The majority of bearing samples were tested again with the new bearing clamp, unfortunately data from wet testing of Type I bearing sample was not completed due to time constraints.

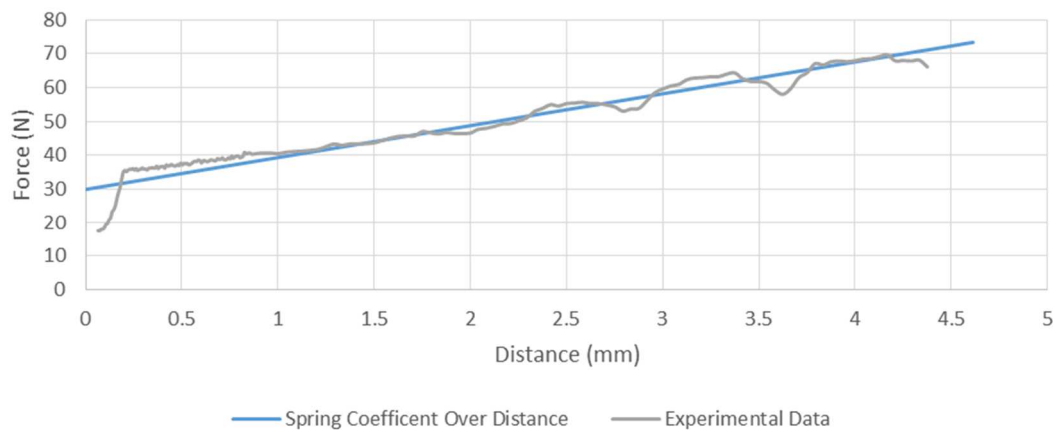


Figure 5-15. Spring coefficient vs experimental data

5.3.5. Loading Results

The addition of a load cell to the pneumatic piston of the bearing test rig has allowed the collection of load data perpendicular to the surface of bearing B. While the machine has 6-8 bar of air pressure it is operating at the optimum rate, 0.5 - 0.6 m/s with a vertical and torsional loads of between 200 – 500 N. For all bearing test pads both dry and wet load data was recorded, an example of bearing sample Type II total applied force of 588 N provided in Figure 5-16 and Figure 5-17 respectively.

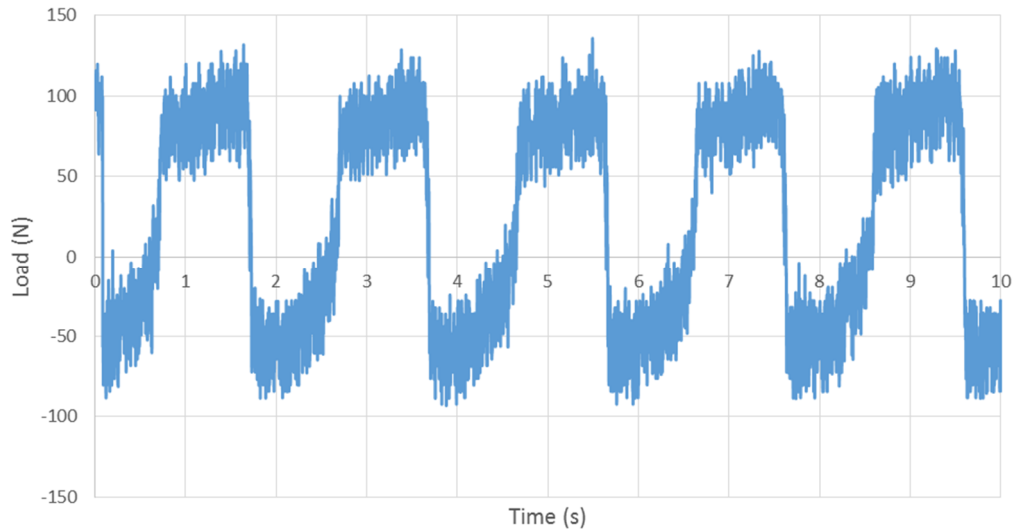


Figure 5-16. Friction force during 0.5 ms^{-1} operation

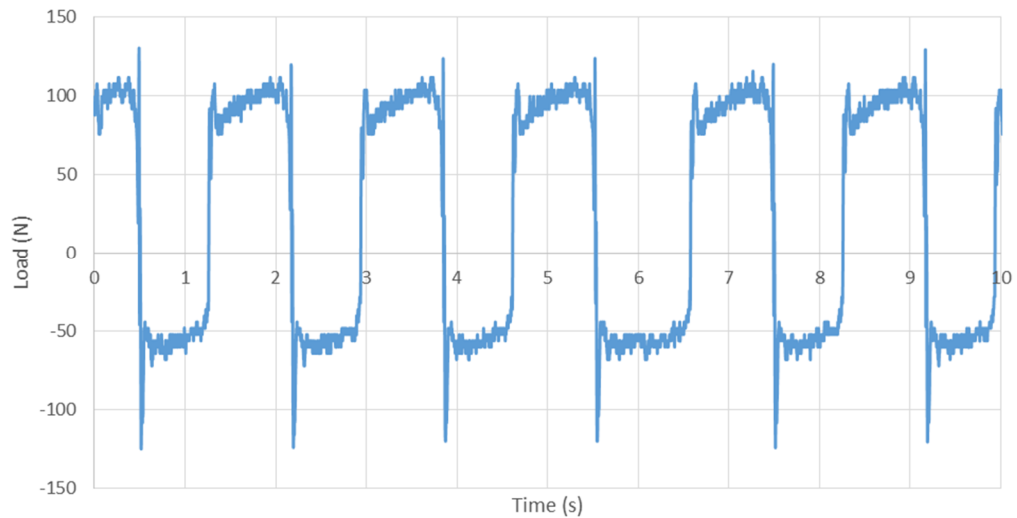


Figure 5-17. Friction force during 0.6 ms^{-1} operation

Results from the wave loading study indicate the maximum top stroke horizontal force would occur under a wave amplitude of 2.59 m and a wave period of 8.3 seconds. Therefore, the maximum applied load at the centre of the machine topology, based on ridged buoy connection to the PTO as provided in Figure 5-2, would be 22.8 kN at the top of stroke and 21.9 kN at the bottom of the stroke. However, waves of that severity would occur for 4% of operational time, therefore the bearing pads and structure of the machine would be fabricated to withstand operation during these intermittent high loads. During normal operation the machine would experience a top stroke load of 11.6 kN and a bottom stroke load of 10 kN. To maintain a surface pressure similar to the

pressure produced in this study, a total of 0.0116 m² of bearing surface would be required. Using this area it can be calculated that the maximum pressure the bearings would experience during dynamic operation would be 1.94 MPa, well within all materials operational surface pressures. In comparison the bearing pads installed in the test rig have an active surface area of between 0.003 – 0.005 mm². The bearings pad samples recorded maximum loading values as indicated in Table 5-4.

5.3.6. Bearing sample results

It was noted during dry testing that there was more wear visible on pads A and C for a smaller surface area, while pad B maintained a fairly uniform wear rate across it's surface. Before sprung bearing pad tests the surface contact on the bearings was significantly lower as showing Figure 5-18. Uneven surface wear was due to a rocking motion present on the bearing clamp angled on the outward stroke compared to the return stroke. This change in surface contact varied the pressure per unit area experience by the bearing. It has been calculated that, depending on the available compressed air pressure and surface contact area, the loading on each samples bearing pad B varied from 0.2 MPa to 2.5 MPa. The installation of the sprung bearing assembly allowed the distribution of loads across the bearing face resulting in surface wear as presented in Figure 1.9. The summary of the bearing tests are presented in Table 5-4 and Table 5-5.

	Type I		Type II			
	Dry		Dry		Wet	
	Sample I_A	Sample I_B	Sample II_A	Sample II_B	Sample II_A	Sample II_B
Original Mass	55.25	55.03	70.53	70.51	67.7	67.38
Max Operation Speed	0.4		0.6		0.6	
Distance Travelled km	218		501		590	
Max Temperature	115		51		15	
% mass lost	0.724	1.036	0.539	0.284	6.041	2.909
Wear rate (g/100 km)	0.183	0.263	0.059	0.031	0.566	0.272
Manufacturers Friction Co-eff	0.1 - 0.2		~0.1		0.1 - 0.17	
Calculated Friction Co-eff	0.5		0.15		0.17	

Table 5-4. S Summary of Type I and II experimental results

	Type III				Type IV			
	Dry		Wet		Dry		Wet	
	Sample III_A	Sample III_B	Sample III_A	Sample III_B	Sample IV_A	Sample IV_B	Sample IV_A	Sample IV_B
Original Mass	50.79	51.06	48.4	48.61	62.02	63.14	61.2	62.07
Max Operation Speed	0.5		0.45		0.6		0.6	
Distance Travelled km	210		204		205		215	
Max Temperature	80		17		55		18	
% mass lost	1.969	1.391	4.170	4.732	0.306	0.285	0.899	0.757
Wear rate (g/100 km)	0.518	0.366	1.129	1.282	0.082	0.077	0.231	0.195
Manufacturers Friction Co-eff	0.25		-		0.06 - 0.18		0.04	
Calculated Friction Co-eff	0.38		0.45		0.21		0.21	

Table 5-5. Summary of Type III and IV experimental results

Dry Tests

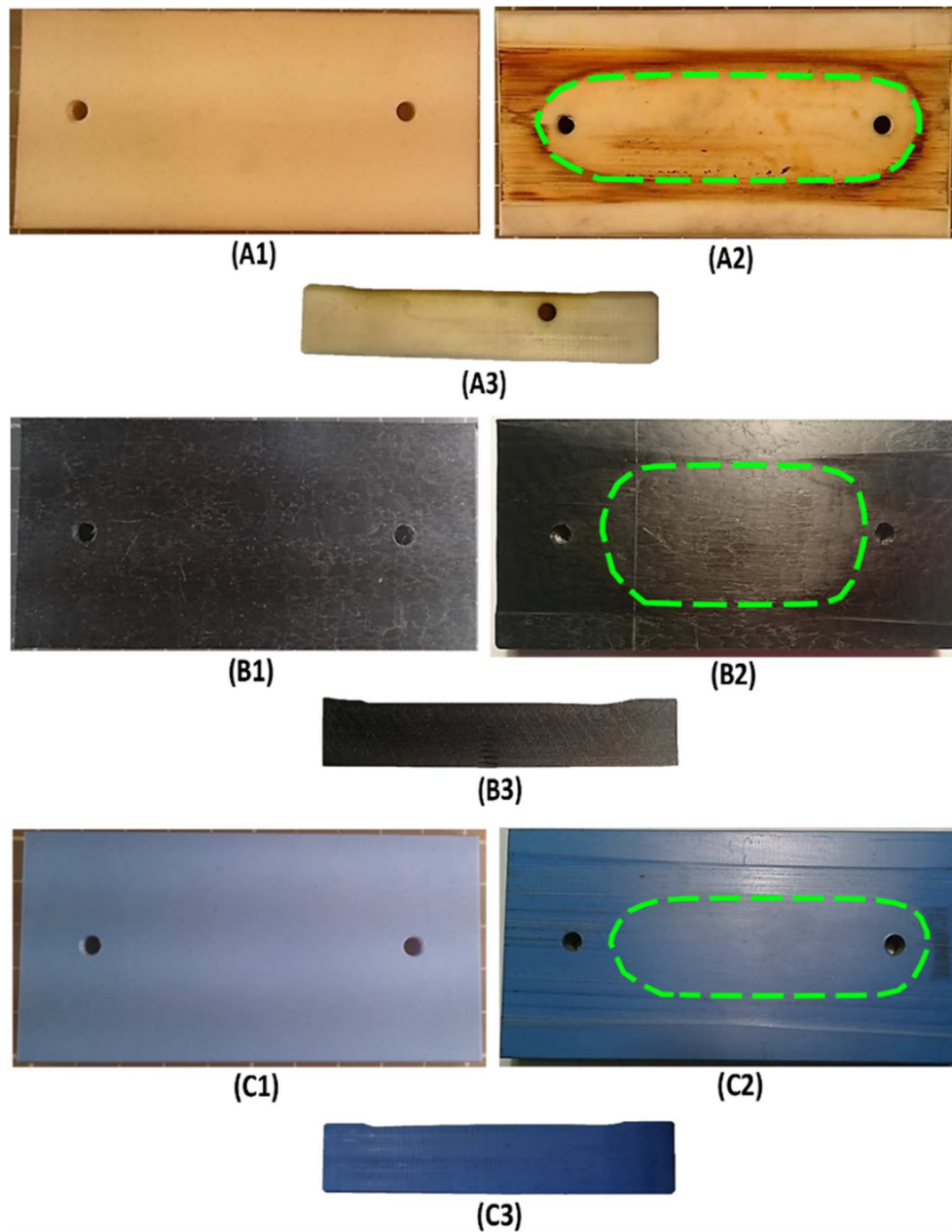


Figure 5-18. Bearing pad surface wear from initial tests before sprung bearing pads were employed. (A) Type I (B) Type II (C) Type III, (1) New pad; (2) Pad B surface wear; (3) Side view of pad B wear

The wear on the bearings for dry operation is graphed in Figure 5-19 while Figure 5-20, the extrapolated wear is provided up to 5000 km, equal to 5×10^6 cycles.

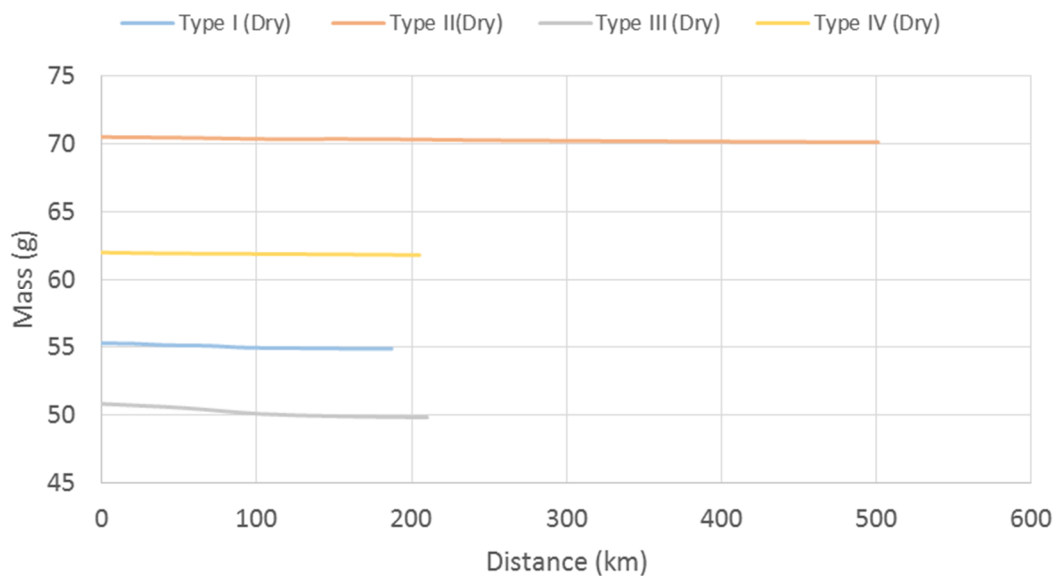


Figure 5-19. Distance vs mass lost for dry bearing operation

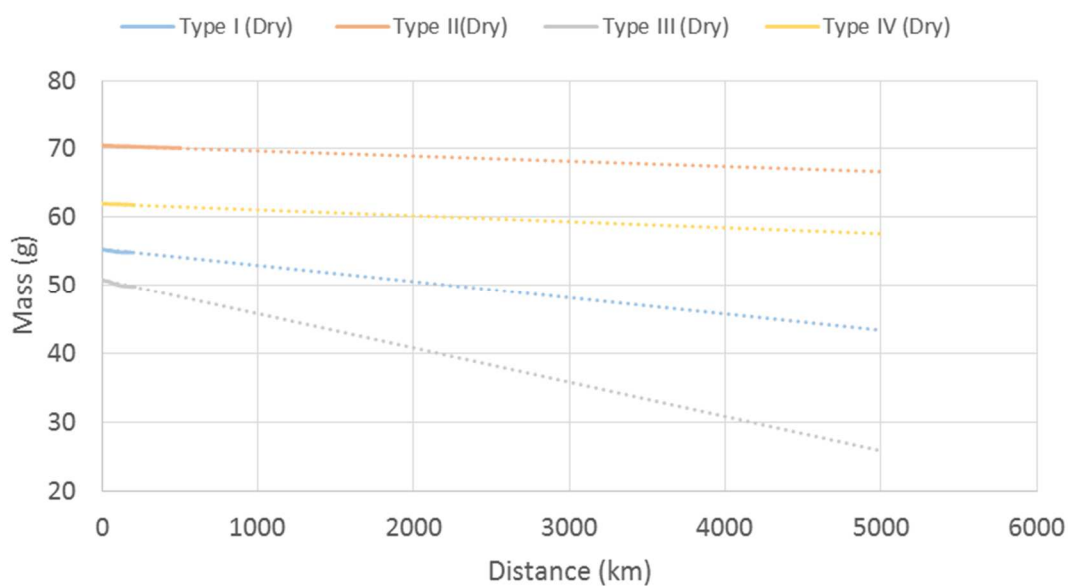


Figure 5-20. Extrapolated bearing data for dry tests indicating high wear rates with increased line gradient

Wet Tests

During wet testing, most pads experienced a higher rate of material loss. This led to a more uniform wear pattern on the surface of each sample, as highlighted Figure 5-21.

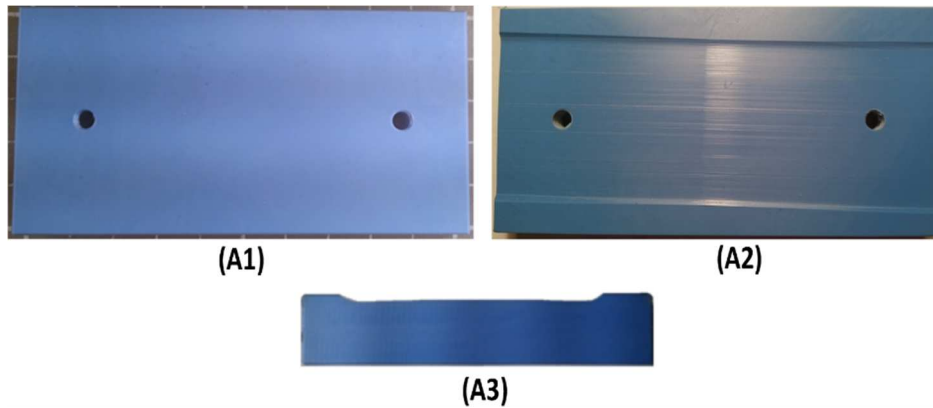


Figure 5-21. Type II. (A1) New Pad (A2) Pad B Surface Wear after 350km (A3) Side View of Pad B Surface Wear

Type II, III and IV bearing materials were tested wet. The results of loss of mass on the bearing samples during operation are shown in Figure 5-22 and extrapolated out to 5000 km in Figure 5-23. Type II bearing material did not perform as well in terms of wear rates, while type III performed with only slightly more wear than during the dry tests. Type IV retained more material during testing for the wet bearings. Once again even with this greater amount of wear the bearing material still exhibits a reasonable lifetime under the conditions of the test.

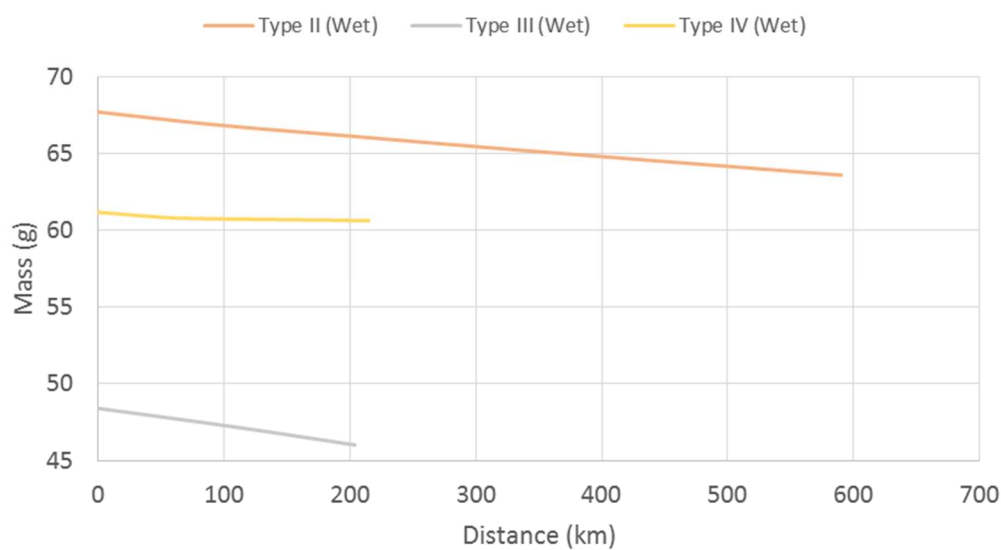


Figure 5-22. Distance vs mass lost for wet bearing operation

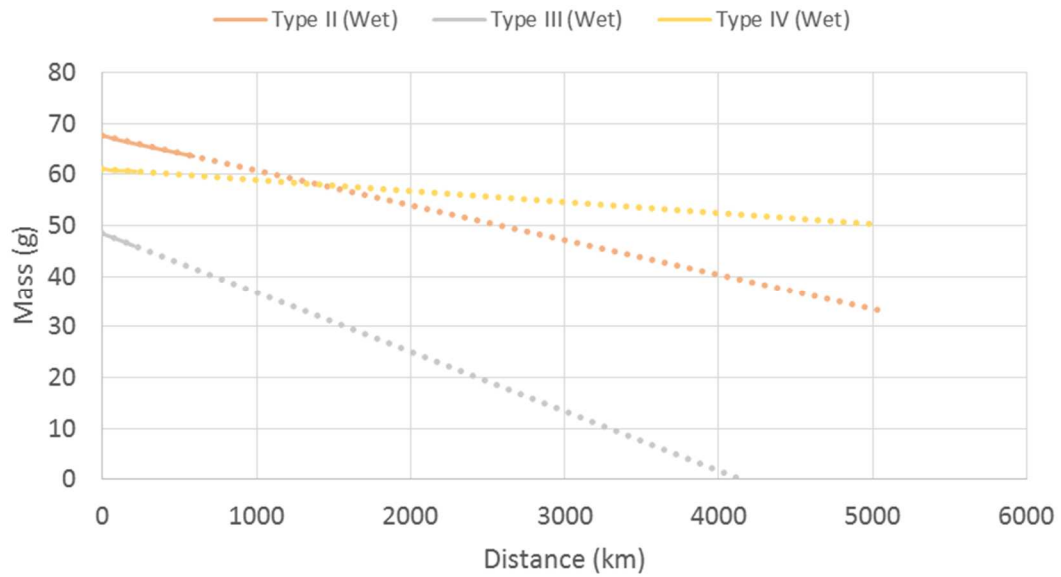


Figure 5-23. Extrapolated bearing data for wet tests indicating high wear rates with increased line gradient

The results of the bearing tests were used to calculate the average wear expected per 100 km. A summary of this data is provided in Figure 5-24.

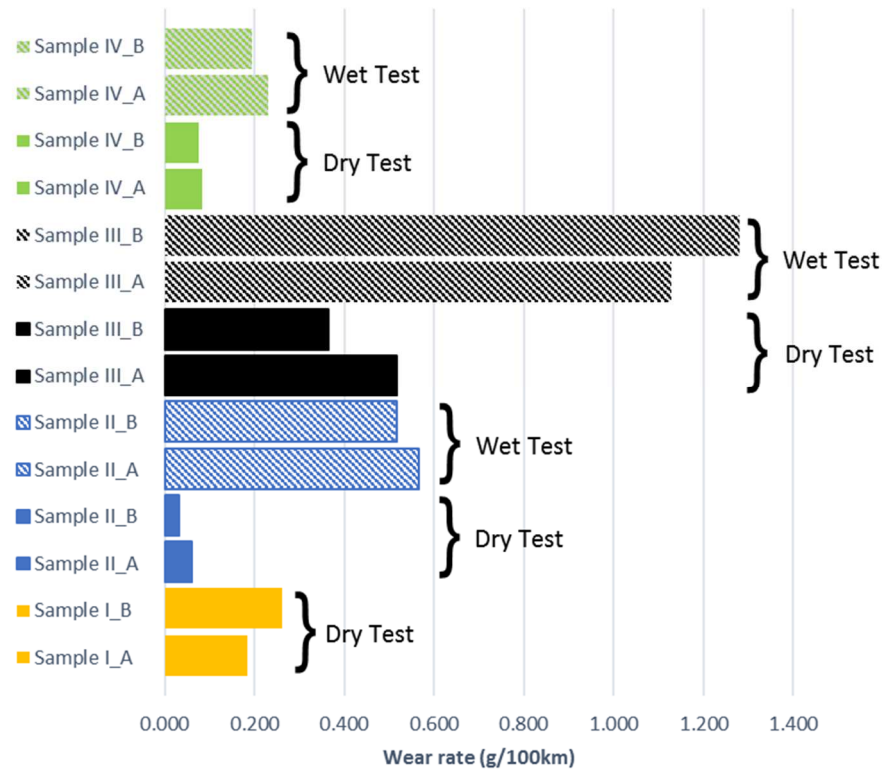


Figure 5-24. Wear rates over the samples during testing, solid for dry testing, and shaded for wet testing

5.3.7. Microscopy Imaging

Initially bearing samples were to be imaged using microscopy to view the changes in each sample's surface material, review site specific damage, wear patterns and pitting over the course of testing. However due to time restraints and difficulties in accessing suitable equipment, a full material study could not be complete. However, for completeness initial results for all bearing samples are presented here.

The Microscopy images provided in Figure 5-25, Figure 5-26 and Figure 5-27 were taken once before testing had commenced. Whilst the samples included in Figure 5-28, Figure 5-29, Figure 5-30 and Figure 5-31 record the surface wear and damage once testing had commenced. The samples were each cleaned with a non-corrosive degreasing agent and water. The samples were then dried and prepared for imaging. The microscopy camera allows observation of the wear in the bearing pad samples, including unusual wear effects for comparison of the wear processes over the range of sample materials.

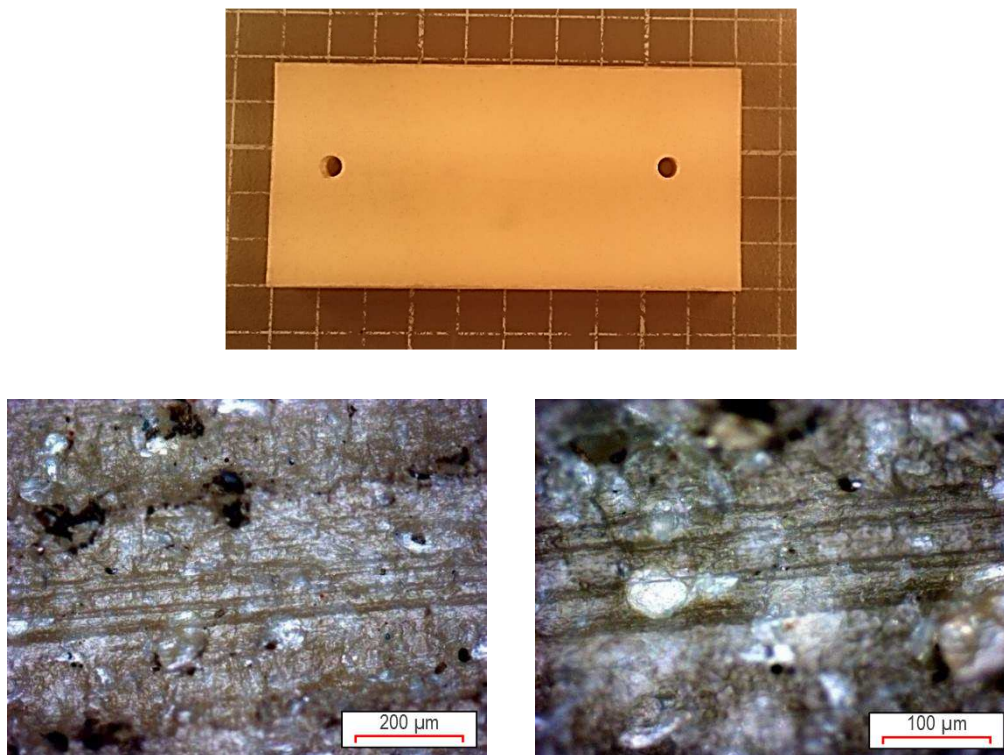


Figure 5-25. Sample I before testing. Top: Machined bearing pad. Bottom Left and Right: Irregular surface produced during machining

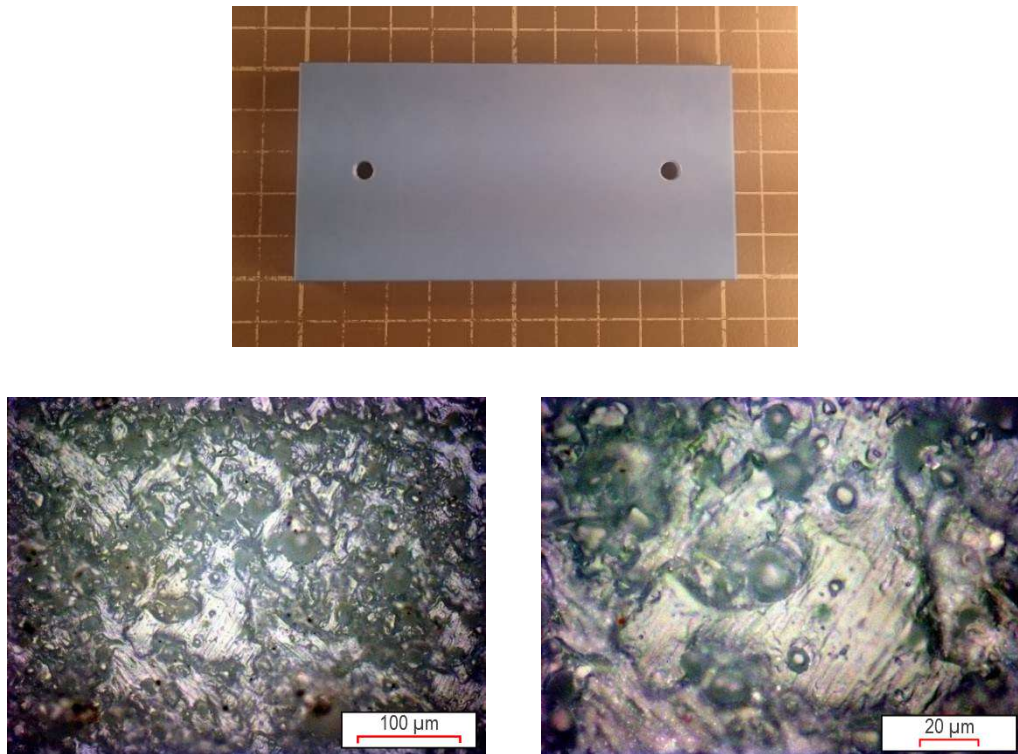


Figure 5-26. Sample II before testing. Top: Machined bearing pad. Bottom Left and Right: Surface images

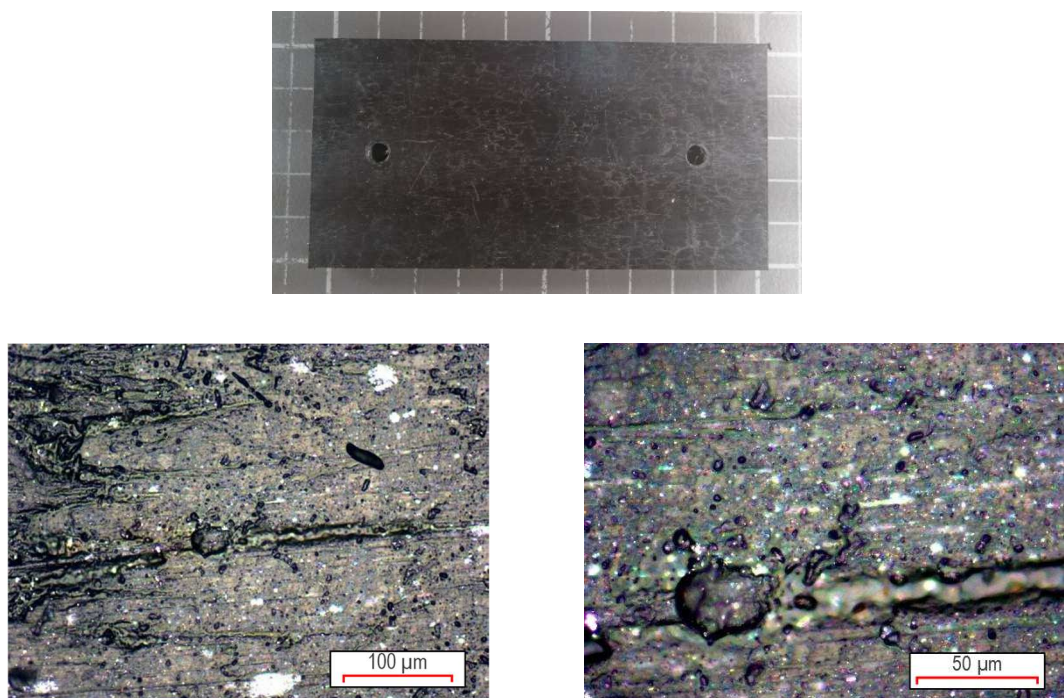


Figure 5-27. Sample III before testing. Top: machined bearing pad. Bottom Left and Right: Surface images

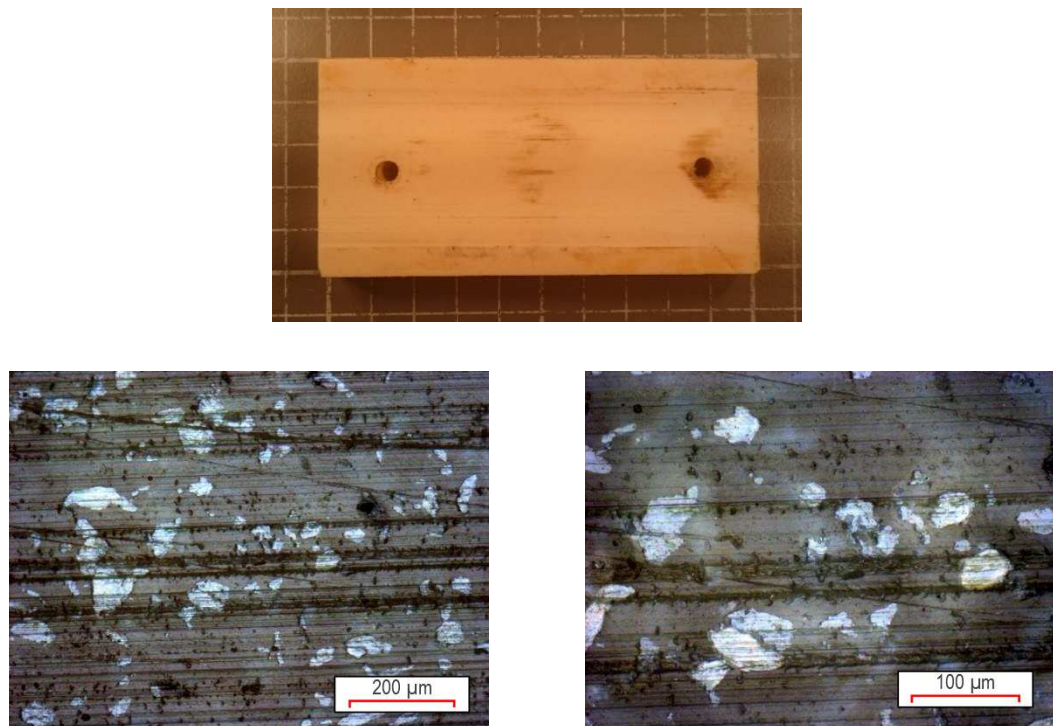


Figure 5-28. Sample IV after 50 km salt water testing. Top: Bearing pad showing wear. Bottom Left and Right. Break in wear from guide rail

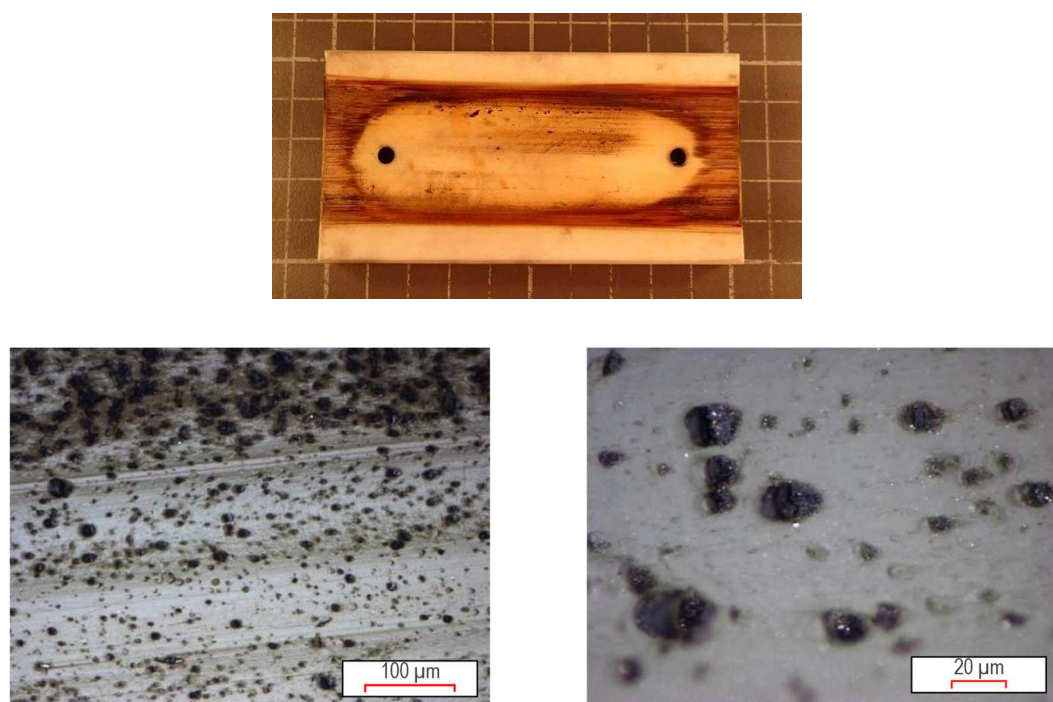


Figure 5-29. Microscopy of sample I after 150km dry testing. Top: Bearing pad showing wear. Bottom Left and Right: Imaging taken from scorched area

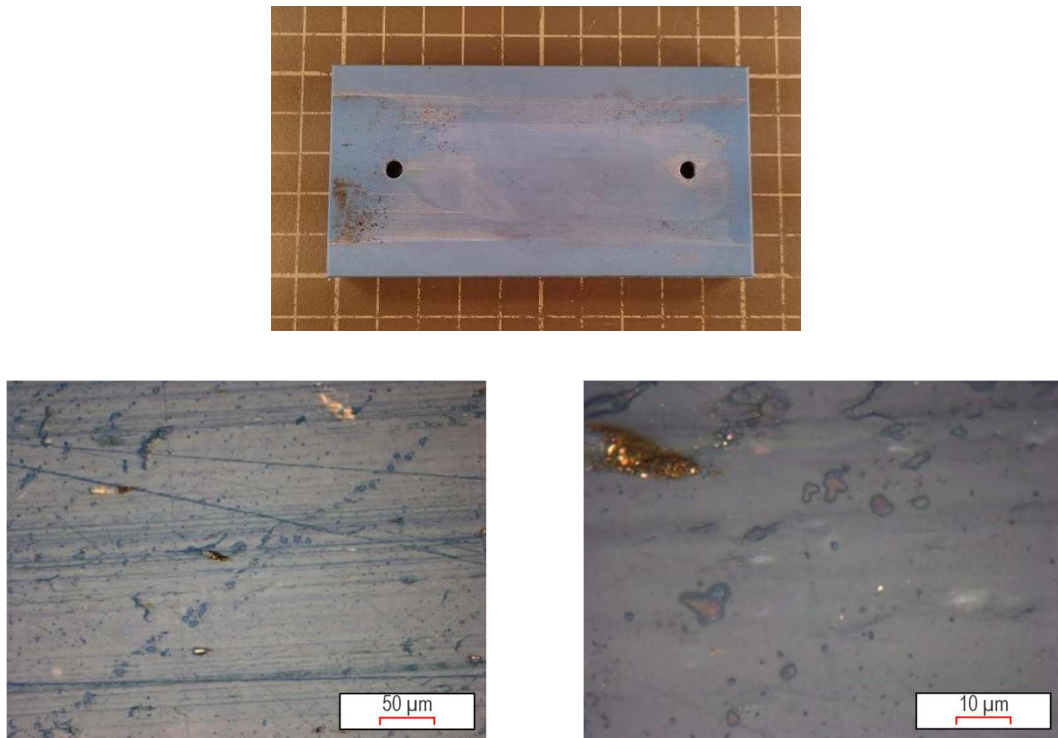


Figure 5-30. Microscopy of sample II after 150km. Bottom Left and Right: Indicating embedded particles

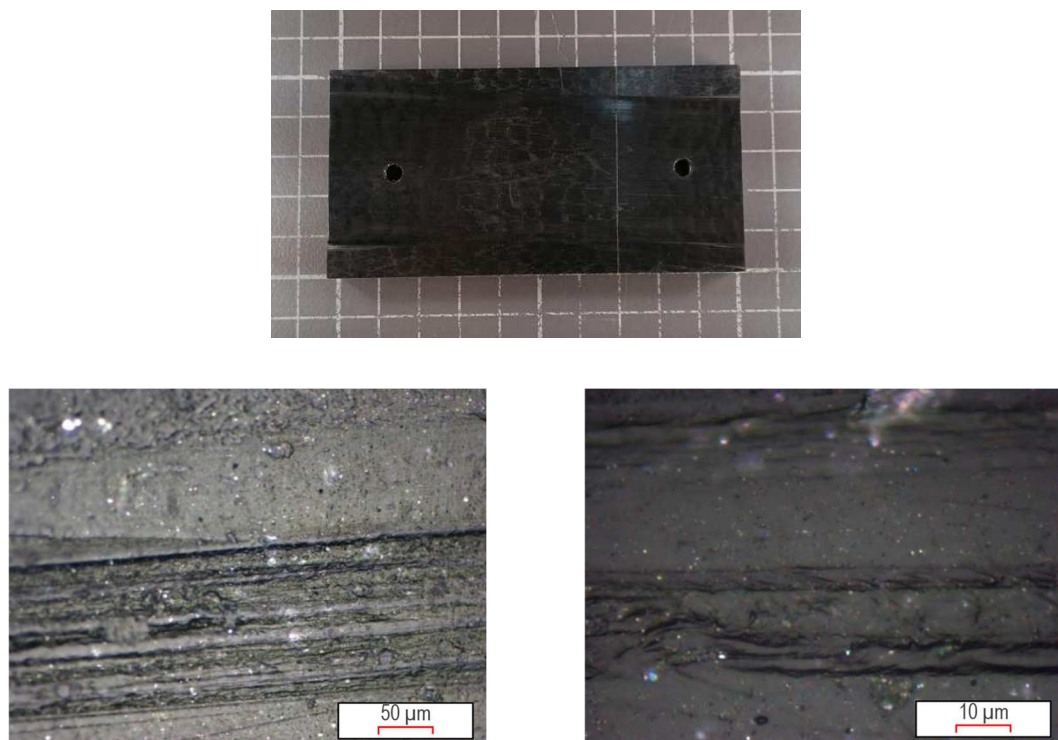


Figure 5-31. Microscopy of sample III after 150km. Bottom Left and Right: Indicating a scored surface

One of the most interesting images comes from Figure 5-29 which contains results from sample I. The first noticeable structure is the porous or sponge like texture of the materials surface. It is thought that, due to increasing friction during testing, the high temperatures experienced by the pads has altered their surface structure. The scorching marks are clearly visible without magnification. The second feature worth noting is that the porous surface has been filled with debris from the guide rail suggesting that mass data could be incorrect. Figure 5-30 contains images of sample material II, the surface of which has been worn very smooth. However metallic particles have been deposited on the samples surface, again potentially leading to false mass readings. Figure 5-31 contains images of sample III and indicates a worn surface with striations visible along its surface. The continuation of this study will be discussed in chapter 7.

5.4. Discussion

A linear bearing test rig has been successfully designed and built with the capability of applying loads during dry and fully flooded salt water testing. Four different polymer bearing materials have been used as test samples, undergoing extended wear testing up to 500 km in both dry and wet environments. Unfortunately, the force per unit area and the speed of the bearing test rig has varied due to irregular compressed air supply. Although this has hampered the collection of data, the testing period was sufficiently long enough for some design changes to be implemented to the test rig and the retesting of bearing samples to be completed.

The outcomes of the testing process have highlighted two important outcomes. Firstly, material wear rates during wet tests were generally significantly higher than those noted during dry testing. There are several explanations which could account for this difference:

1. The outside layers of the sample material may have been saturated by water leading to a more porous, softer contact surface when wet. This would lead to an increased rate of wear. All samples were weighed before and after being submerged within the salt water mix, although this was originally to enable accurate measurement of material loss, it also indicated that some samples held higher water content after saturation. Materials which experienced the highest

difference in wear between dry and wet operation also had the highest saturation levels.

2. The nature of linear operation compared to rotary operation would likely suggest that a fully formed hydrodynamic layer would be partially or fully lost at the end of each linear stroke. Therefore, if the surface of the bearing material was saturated and easier to wear, then material would be lost from the film layer at a quicker rate than that of the harder dry bearing sample.
3. Particulates of metal were less likely to become embedded within the bearing material during wet operation. Particles of metal were found embedded in the bearing samples surfaces more often during dry operation, with many wet samples showing smooth surfaces free of particle impregnation. The particles were the result of metal entering the chamber from wear experienced by the test rig assembly. Therefore, it may be possible that embedded material in the dry bearing samples gave inaccurate weighing results, leading to a greater inaccuracy between sample weights.

Secondly, when the dry and wet friction coefficients of each sample were calculated, as supplied in Table 5-4 and Table 5-5, it was noted that all samples (with one exception) had higher friction coefficients compared to the manufacturers data, Table 5-2. Although the coefficients would not necessarily impact the bearings operation negatively, this difference would suggest that the linear operation of these bearings is significantly different from rotary operation. However, discrepancies between the material data and testing could be explained by temperature differences, velocity differences, inaccurate load cell data and the start stop nature of linear testing.

Finally, when each bearings friction force was analysed, they were found to be very similar over the length of the stroke, with higher shock loads at the end of stroke and less loading on the outward stroke than the backward stroke, indicating that the pneumatic pistons load capabilities during the stroke changed. After extrapolation of the results to 5000 km of travel samples II and IV performed best, whilst also having the lowest calculated friction coefficients. If the machine is considered to complete one cycle a meter and a million cycles are expected within one year, then 5000 km approximates to 5 years of operation. The bearing samples of this size would be

expected to have survived that period of testing. Unlike mechanical bearings, polymer bearings have been shown to have a more predictable service life, with the ability to size the depth of bearing material depending on the life span required before maintenance. The bearing material could therefore be designed for a life span in excess of 5 years, however this would require some thought on how the bearing would be maintain in position as it lost surface material. Currently, many devices predict scheduled maintenance operations to occur at time intervals of 5 years, therefore modular bearing pads assemblies could be removed and replaced easily and at a much lower material cost than mechanical bearing assemblies. Finally, it can be postulated that polymer bearing materials would also be much lighter than their metal counterparts, allowing for easier transportation and a reduction in the overall mass of the device and power take off.

Chapter 6.

Flooded Direct Drive Machines

6.1. Introduction

It has been discussed in previous chapters that the offshore environment is detrimental to the operation of machines. Often the corrosive nature of the sea effects seals and whilst at times the inability to transfer heat away from the vital power take off components decreases machine efficiency. Chapter 4 noted various power take off methods and drive train loading, concluding that often utilising the simplest components can improve reliability and move technology forward. Thermal modelling completed in WES Stage 2 Cooling System Design Report, [223], indicates that a flooded airgap would provide a more efficient method of heat transfer within a PM machine topology.

Not all generator topologies suit a flooded airgap, however a low speed PM machine with adequate material protection has the potential of harnessing the heat transfer available within sea whilst removing seals, mechanical bearings and additional protective structures such as nacelles. Therefore, this chapter will investigate the benefits, in terms of cooling and generator efficiency, that marinisation can offer through physical testing. This chapter will discuss:

1. The construction of a miniature PM linear generator in order to assess the benefits of an open machine construction, primarily focusing on utilising surrounding water as a cooling agent for three coil topologies, comparing results with dry testing data.
2. The continuation of wet and dry tests carried out on a 5 kW C-GEN prototype generator.
3. A synopsis of methods for the protection for marinised machines.



Figure 6-1. Small linear machine stator topology

6.2. Miniature PM Linear Thermal Test Rig

A small linear PM machine was manufactured by Fountain Design Ltd, Figure 6-1. The topology consists of a double-sided castellated magnet stator bolted vertically into a stainless-steel tank with a viewing port, Figure 6-2. A pneumatic air piston was installed at the top of the tank, to which various translator designs were connected for reciprocating linear testing, Figure 6-3 indicates the topology of an epoxy potted translator. The production of a small rig allowed for a more economical method of testing various translator topologies before scaling up to a large machine design.

During stationary tests a constant DC current was supplied to the coils. Unfortunately, due to the size and specification of the installed neodymium iron boron magnets, the magnetic field produced was not large enough to create the required current within the coils during reciprocating operation, therefore it was decided that an external DC current source would supply the required current supply to the coils during dynamic testing.

Number of turns	130
Diameter of wire	0.75 mm
Active length	100 mm
Width	41 mm
Number of coils	3

Table 6-1. Specifications of smaller linear machine windings per translator sample



Figure 6-2. Left: Construction of small linear machine within a stainless steel tank. Right: Small linear machine flooded with artificial sea water

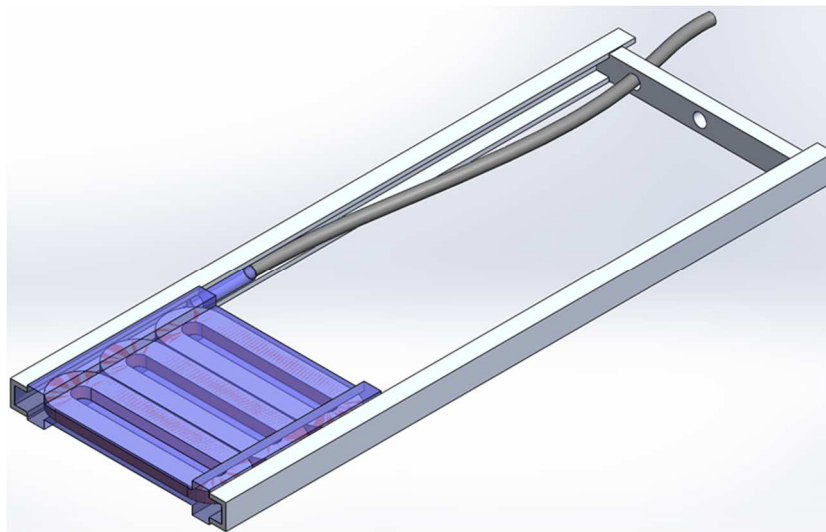


Figure 6-3. Three coil epoxy potted translator blade sample, CAD assembly

6.2.1. Test Programme

Sample copper windings contained within a translator structure for testing are presented in Figure 6-4. In order to investigate the benefits of a flooded air gap, three topologies of translator were considered, a simple enamelled coil translator, an epoxied coil translator with gaps and a fully epoxied translator. The topologies were chosen

based on the outcomes of a WES Cooling System Design Report, [223]. For all translators, three copper windings were installed, the specifications of which are provided in Table 6-1. The epoxy resin used within these tests is PC5308 blue epoxy, details of which can be found in Appendix B.



Figure 6-4. Test rig samples. Left to right: Epoxied coils with gaps, fully epoxied coils, enamelled coils

For each test a coil sample was inserted into the test rig and connected to a power supply, combined with a variable resistor in order to vary the excitation current, Figure 6-5. The coils would then be excited with a DC current supply in order to simulate expected operational loading. The resistance of the coils would be measured at regular intervals to assess increases in coil temperature while thermocouples were placed on the external face of the translator located in the centre of the second embedded coil. The pneumatic air piston was connected to a compressed air supply that allowed for a maximum velocity of 0.7 ms^{-1} during testing. However due to a fluctuating compressed air supply and increased forces created by the interaction of the PM magnetic field and the magnetic field produced by the excitation of the sample coils, velocities varied over the reciprocating tests depending on the compressed air supply and the excitation current. The average speed was recorded and noted for each test. For flooded testing an artificial sea water was used, as described in chapter 5, produced using an aquarium

salt mix recreating the salinity of the North Sea equal to 3.5 parts of salt to 1000 parts water, with a density of $\sim 1030 \text{ kg/m}^3$. In order to prevent damage to the coils, it was decided that testing would stop once the external temperature approached 90°C , therefore the experiments were stopped every 5 minutes in order to record the temperature and coil resistance data.

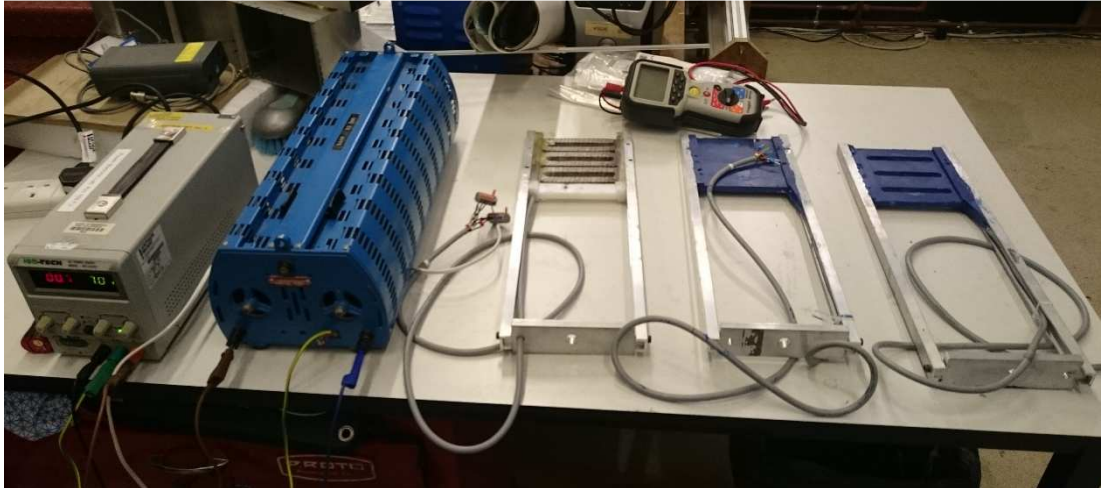


Figure 6-5. Testing equipment and samples. Left to right: Power source, variable resistor, sample coils and ammeter

Individual stationary dry and flooded tank tests were completed for DC currents ranging between 0.5 - 3 Amps per coil. The results of these tests were compared in order to provide data on heat transfer while stationary within an enclosed metal structure. Stationary to reciprocating flooded tests were complete for DC currents between 4 – 8 Amps, in order to provide data for increasing thermal transfer via a movement and induced turbulent flow.

6.2.2. Results Comparison

For the purposes of this section the maximum recorded current data for each experiment will be graphed to describe the most extreme temperature changes for easy comparison.

Stationary Test Results

The stationary test results are graphed to compare the effect of the air gap medium on the same coil topology.

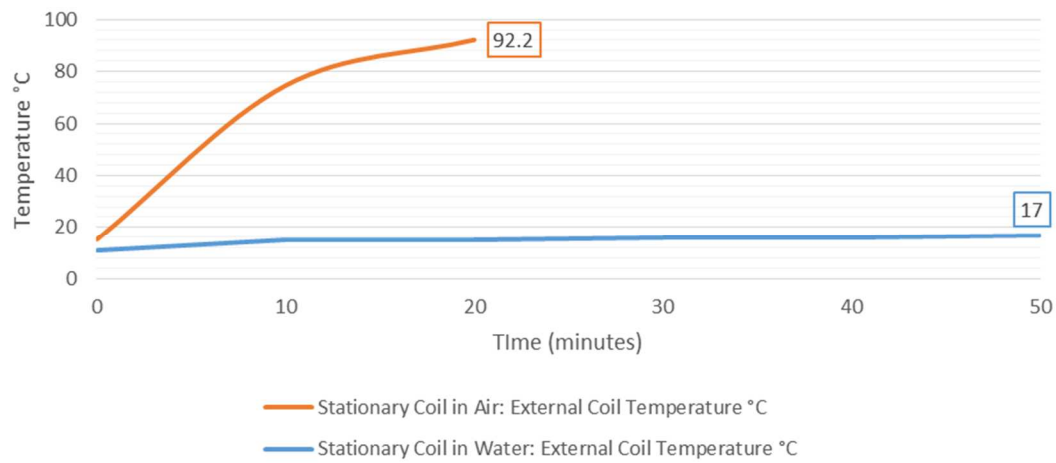


Figure 6-6. Enamelled coils, 3 A/coil. The final temperatures of the potted surfaces are highlighted

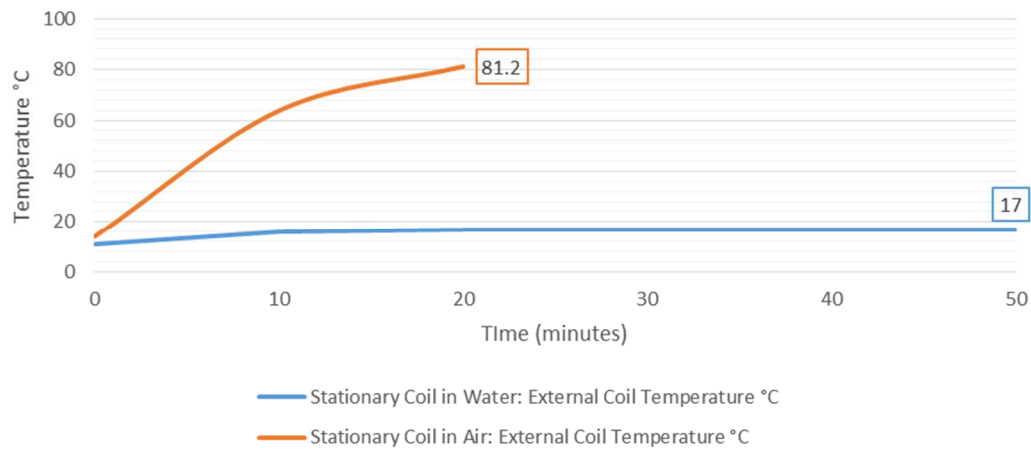


Figure 6-7. Epoxied coils with gaps, 3 A/coil. The final temperatures of the potted surfaces are highlighted

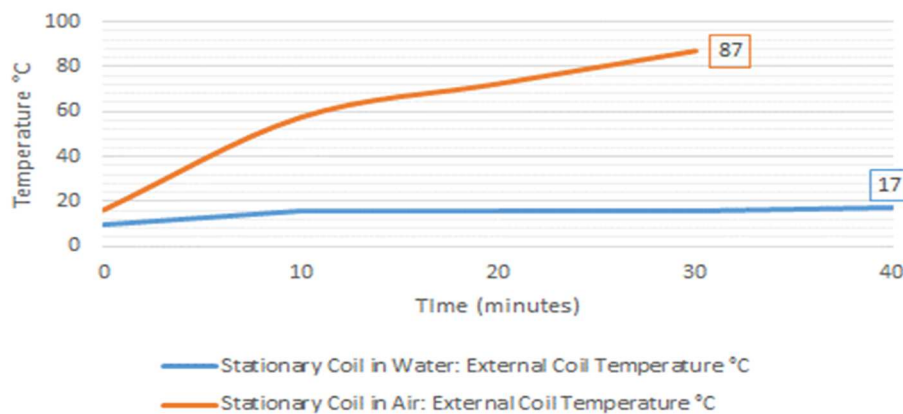


Figure 6-8. Epoxied coils, 3 A/coil. The final temperatures of the potted surfaces are highlighted

Figure 6-6, Figure 6-7, and Figure 6-8 show the temperature results for stationary translator dry and flooded testing with 3A DC current per coil. In each test the temperature was allowed to rise to close to an equilibrium value, and it can clearly be seen that operating in water has a significant thermal impact on the coils. All coil types perform similarly when stationary.

Stationary to reciprocating testing

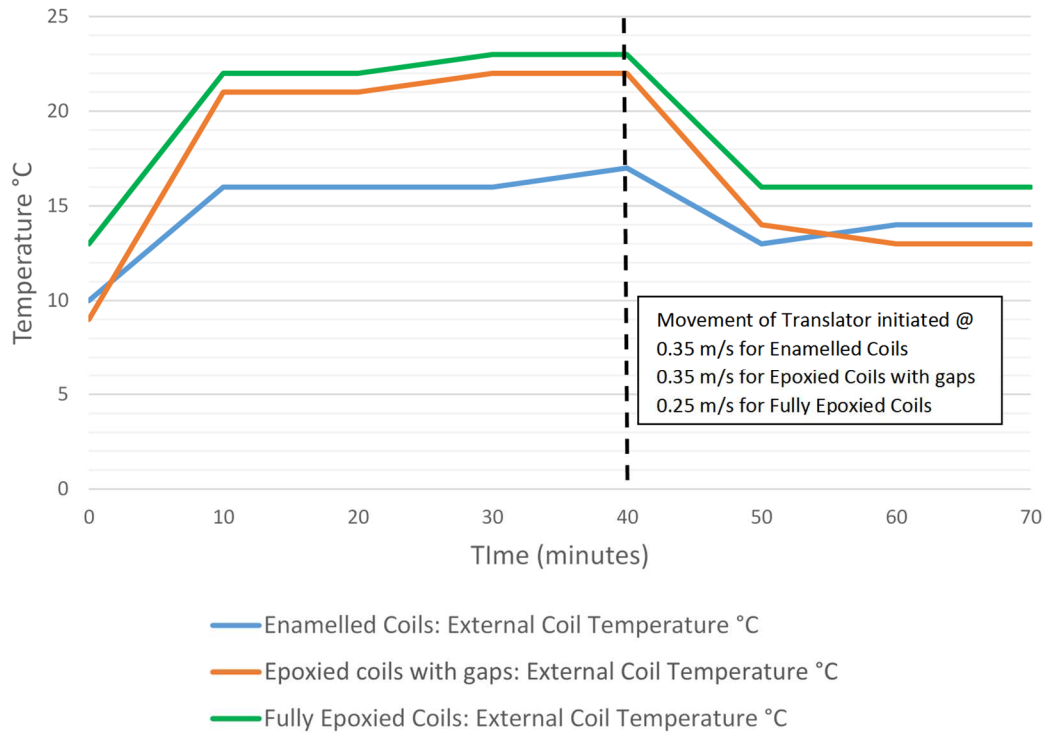


Figure 6-9. Movement with 4 Amps excitation per coil

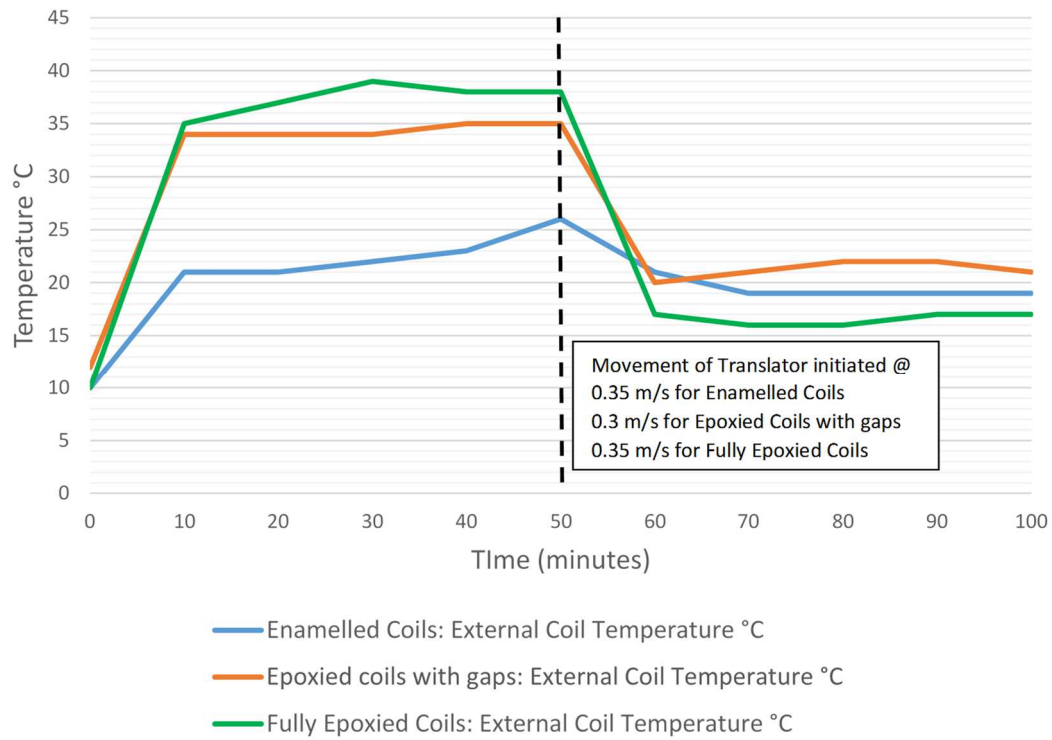


Figure 6-10. Movement with 6 Amps excitation per coil

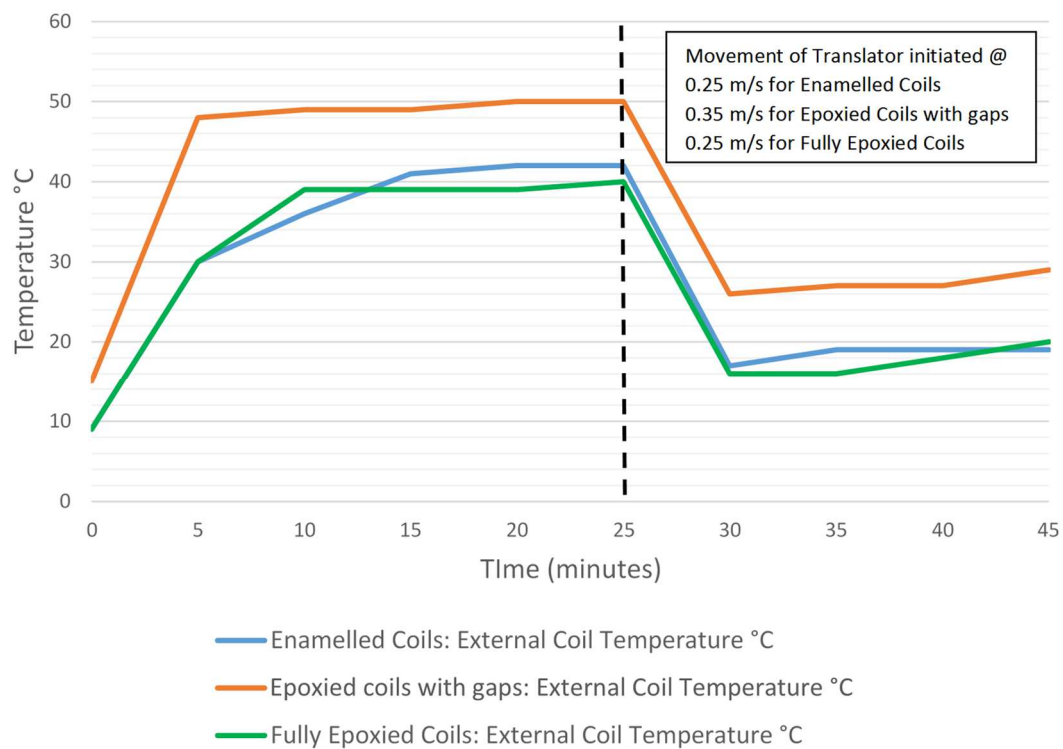


Figure 6-11. Movement with 8 Amps excitation per coil

Figure 6-9, Figure 6-10 and Figure 6-11 indicate cooling benefits when moving the translator on the winding temperature when operating wet. The dotted line shows the point at which movement was initiated. For all coil samples, the temperature reduces after the translator starts to move, and the decrease in temperature depends upon the velocity of the translator. The results in Figure 6-9, Figure 6-10 and Figure 6-11 indicate that the enamelled coils perform best when stationary and moving for all currents. The result for stationary contradicts the previous results for 3 Amps per coil. However, it is to be expected as there is less of a thermal barrier with no epoxy. In addition, the surface around the bare enamelled coils will be rougher than the epoxy potted coils, resulting in more turbulence.

Resistive and Thermal Data Comparison

The remaining graphed results provided in Figure 6-12, Figure 6-13 and Figure 6-14, compare the internal resistance of the coils and its corresponding external temperature in order to validate the temperature results. As temperature falls the resistance will also fall following a similar trend, and in all cases this is true, thus indicating that the external temperature readings provide adequate data to describe the internal change in temperature of the coils. Further results are included in Appendix E.

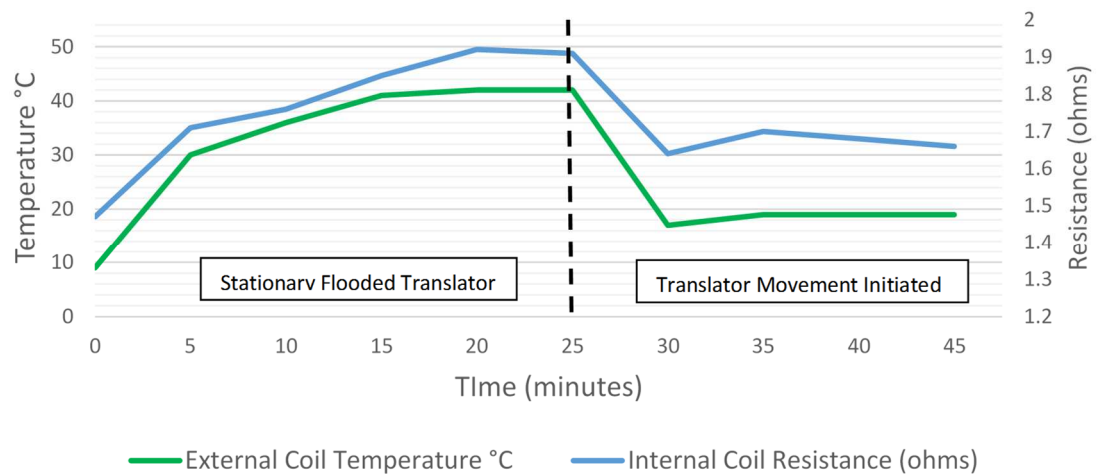


Figure 6-12. Enamelled coils submerged in water, 8 Amps per coil

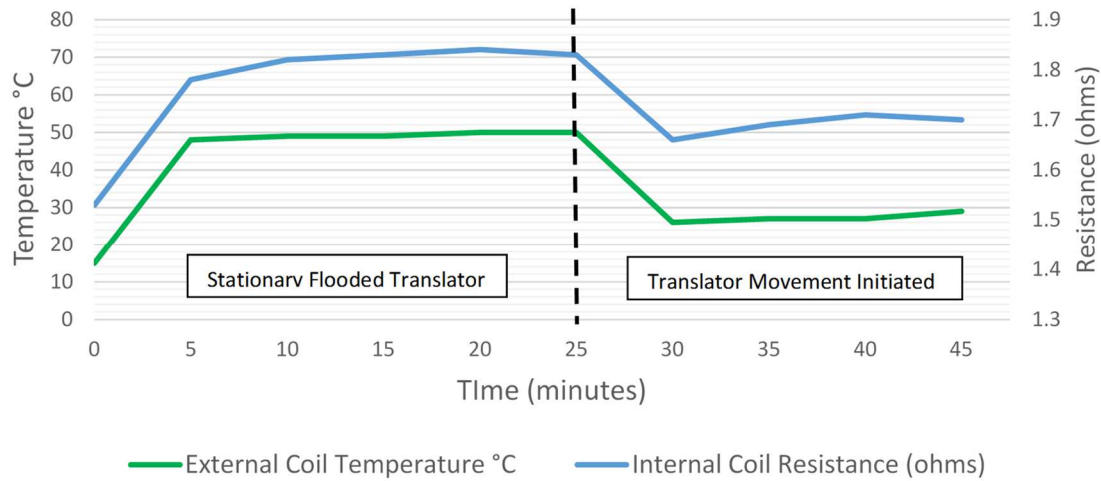


Figure 6-13. Epoxied coils with gaps submerged in water, 8 Amps per coil

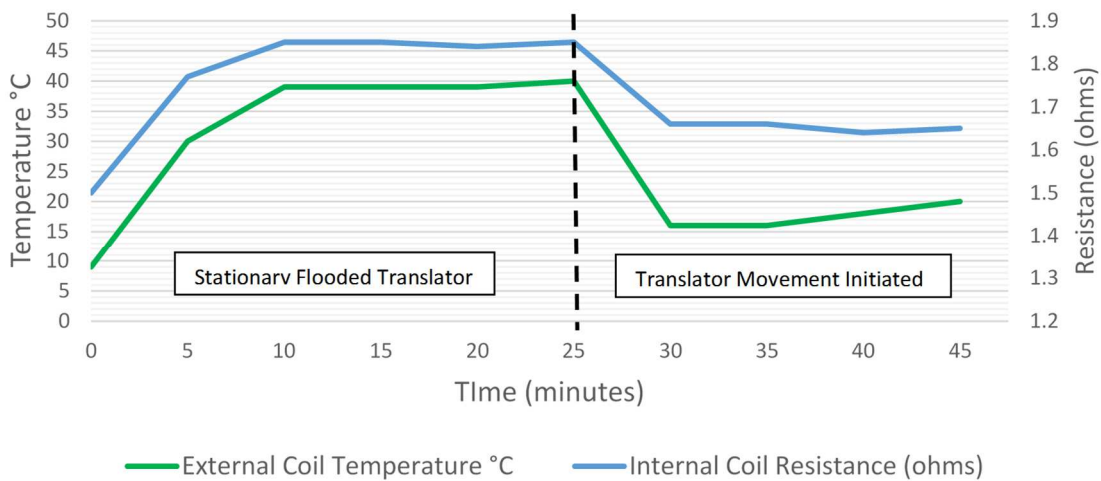


Figure 6-14. Epoxied coils submerged in water, 8 Amps per coil

6.2.3. Discussion

There were several limiting factors that curtailed the collection of data from the small linear prototype rig. Firstly, the installed compressed air supply fluctuated depending on the number of users within the building and ability of the compressor to maintain optimum operating temperatures. In order to reduce the chance of overheating the maximum operating pressure of the compressor was reduced. Therefore, the ability to operate the pneumatic ram at a constant speed fluctuated. In addition, the machine suffered from cogging forces as the excitation current of the translator coils was increased, increasing the load on the pneumatic ram and slowing down the experiments average speed. For excitation rates above 9 Amps in flooded conditions, the cogging

forces was too high for the pneumatic ram to overcome and thus this constraint capped the maximum current available. Finally, the small nature of the test rigs tank meant that the water used within the tests would be heated by the coils. Therefore, this curtailed the period of time that experiments could be run. The temperature of the water before and after was recorded for each experiment.

For all coil translator topologies, the experiments clearly demonstrate the benefit of running a fully flooded air gap in terms of thermal performance. With natural air cooled machines, a current density of 4 A/mm² is typical, but these results suggest that more than 18 A/mm² could be achieved for these coils with wire diameter of 0.75mm, at a current of 8A. As a result of this improved cooling the power density could be increased by about a factor of 5, which will reduce material costs per kg. However, increasing the power density of the machine could affect efficiency.

The results provided in this section helped in the designing of a 5 kW air cored translator for a C-GEN linear prototype.

6.3. 5 kW C-GEN Prototype Thermal Tests

Based on the results in the previous section a six coil translator was fabricated using a fully epoxied support structure. The results from the last section indicated that although the enamelled coil topology performed better, the epoxied topologies also provided a good thermal transfer. Therefore, in order to provide a more ridged, strengthened translator structure, the coils were installed fully epoxied. The 5 kW C-GEN linear prototype and the linear test rig were constructed by Fountain Design Ltd, Figure 6-15.

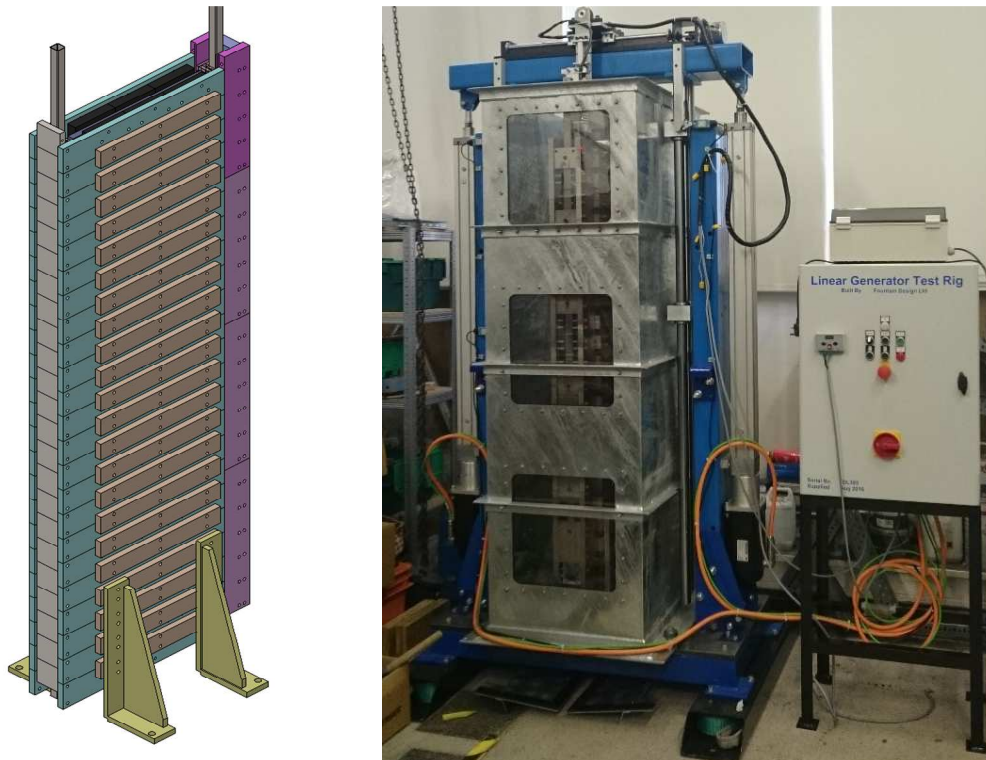


Figure 6-15. Left: 5 kW linear C-GEN prototype topology. Right: Linear test rig with C-GEN linear prototype installed within a water tank

The specifications of the linear generator are provided in Table 6-2. The prototype stator was fixed to the bottom of the water tank. The translators side supports were connected to a horizontal cross piece at the top of the test rig. In this manner the translator's movement can be fully controlled by the test rig.

Stroke Length (m)	1
Power Output Peak (kW)	5
Velocity Peak (ms^{-1})	1
Velocity Profile	Sinusoidal
Active coil length (m)	0.45
Number of coils	6
Wire diameter (mm)	1
Number of turns	590
Air gap (mm)	2

Table 6-2. Linear generator specifications

The design of the linear test rig includes two servo driven ball screw linear actuators, requiring a 3 phase 32 Amp power supply. The rig has an active stroke of 1m and the capability of variable speed operation up to a maximum of 1 ms^{-1} . A linear pull cord

transducer is used for position and speed feedback, while the servo drives are controlled using Workbench control software. The water tank has a capacity of ~ 960 litres with two viewing sides each containing three polycarbonate windows. Figure 6-16 provides a cut through section highlighting the main active components of the rig and generator.

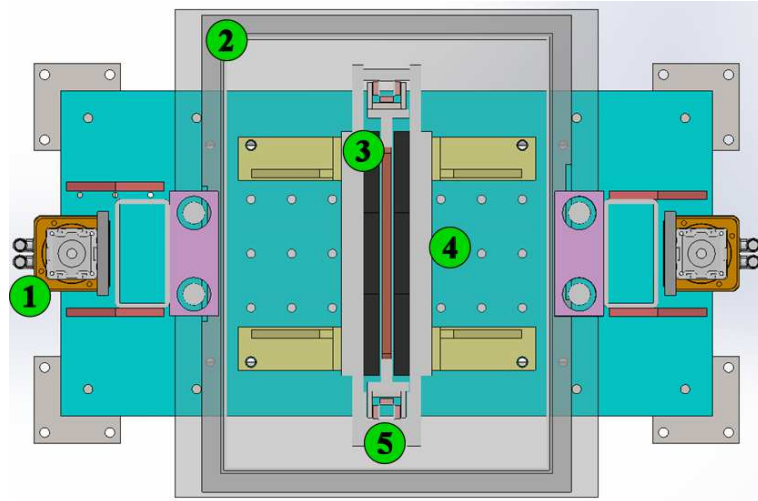


Figure 6-16. Cut through view from top indicating (1) linear actuators, (2) surrounding tank, (3) translator, (4) permanent magnets (black) and support structure (silver) and (5) linear journal bearing arrangement

Thermo-couples were installed within the epoxy resin at a position towards the middle of each coil in order to provide temperature data whilst two s-beam load cells are secured between the top of the translator assembly the linear actuators horizontal support beam, the load cells were rated to 5 kN. Before testing began the translator windings were connected in series with a star 3-phase connection, each phase monitored for voltage and current. During testing the linear drive system was programmed to create various velocity profiles, as shown in Figure 6-17.

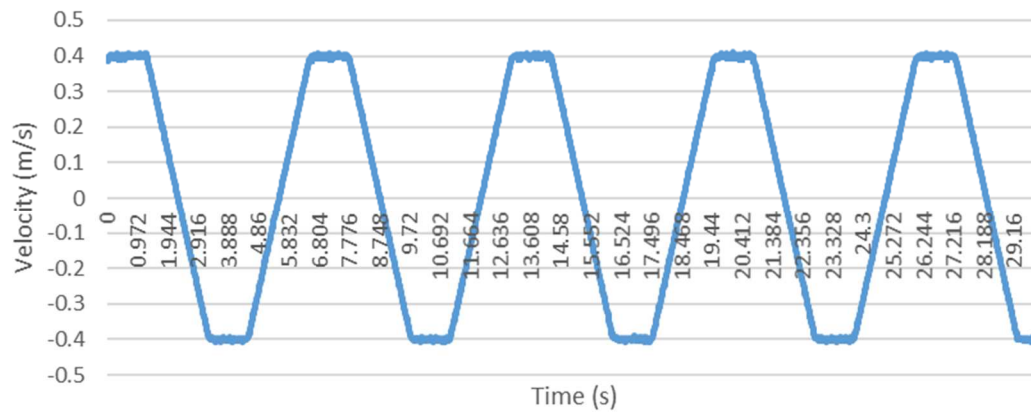


Figure 6-17. Translator velocity profile. Acceleration 0.4 ms^{-2} , max velocity 0.4 ms^{-1}

Due to the nature of the testing, a pure sinusoidal wave wasn't necessary, therefore a simple profile containing periods of constant acceleration and deceleration with a period of constant speed was designed. For the purposes of this section the maximum velocity of the profile will be referenced rather than the average speed of the velocity profile.

6.3.1. Test Programme

No load and Load Testing

The machine was tested under no load conditions in both dry and wet conditions, over a variety of speeds ranging from 0.3 ms^{-1} to 0.5 ms^{-1} . The voltage for each phase was recorded. Examples of both wet and dry no load tests are provided in Figure 6-18 and Figure 6-19.

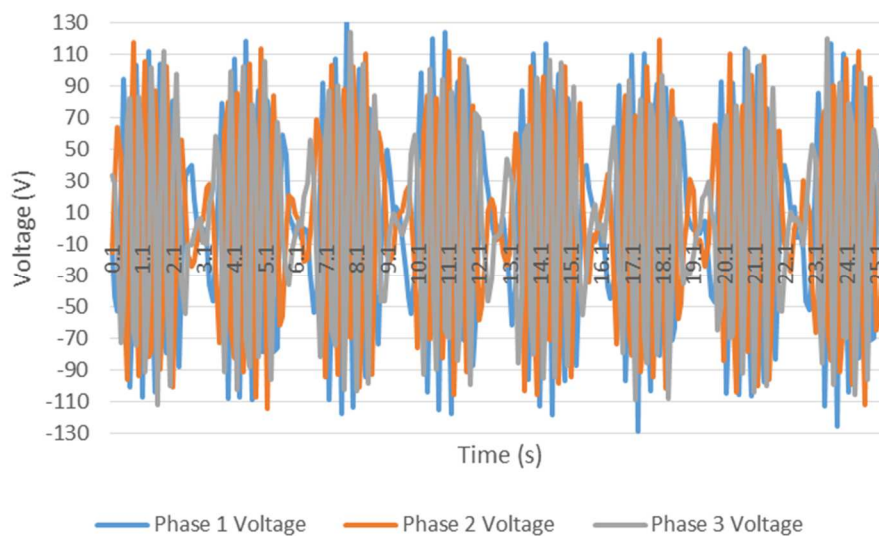


Figure 6-18. Dry no load voltage test results, maximum velocity 0.4 ms^{-1}

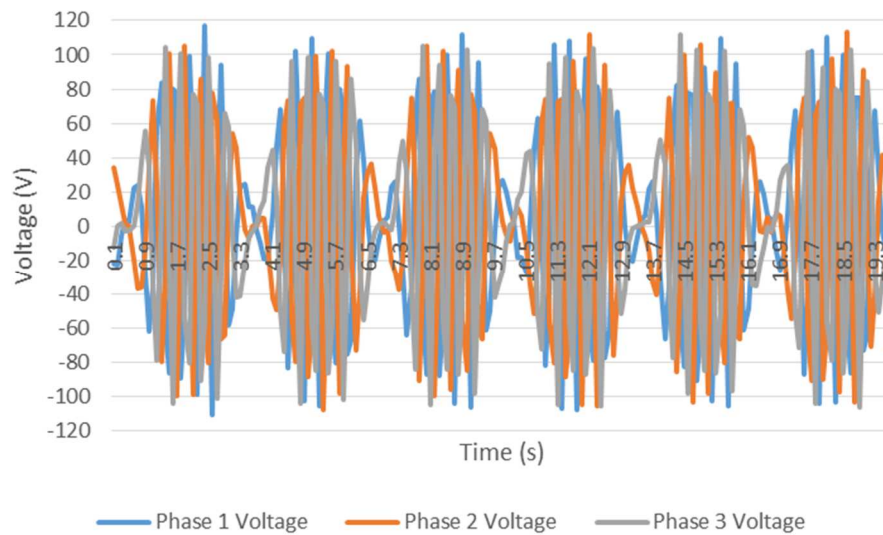


Figure 6-19. Flooded no load voltage test results, maximum velocity 0.4 ms^{-1}

The graphs indicate that under wet conditions the no load voltage is reduced. The most probable cause is increased drag effects, this issue can be offset by increasing the number of turns per coil.

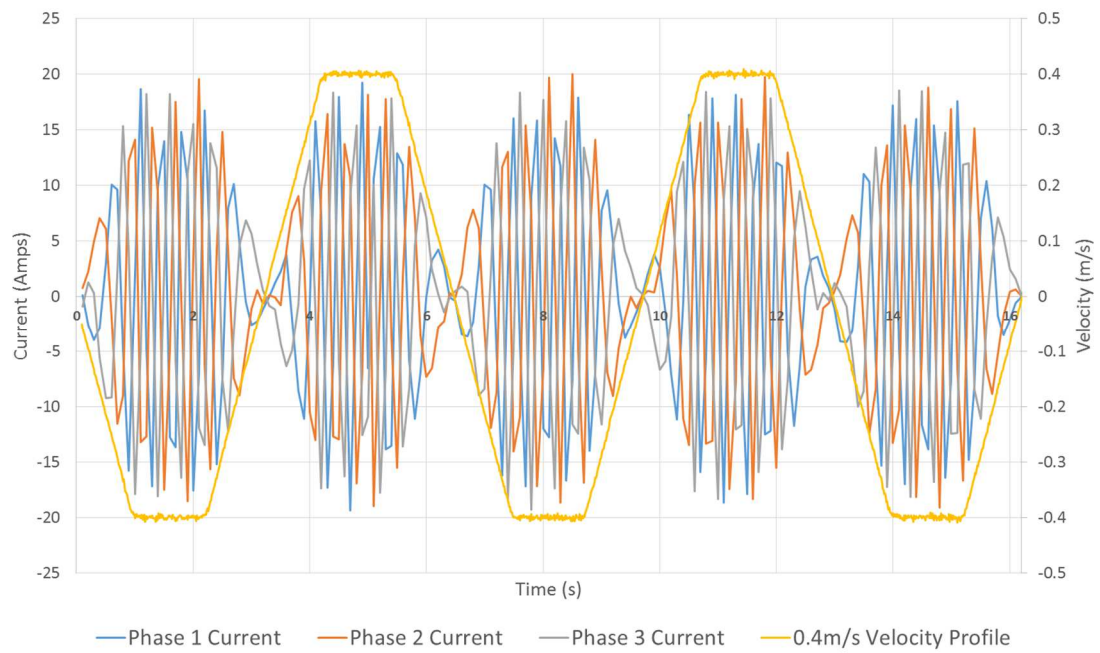


Figure 6-20. Three phase current output with related velocity profile with a 20 Amp load per phase and a maximum velocity of 0.4 ms^{-1}

For full load testing the machine was connected to a three phase resistive load and the current data was recorded for both flooded and dry test conditions as the machine was loaded up to 30 Amps per phase over a range of velocity profiles up to a maximum of 0.6 ms^{-1} . Figure 6-20 confirms that peak current is produced when the velocity is constant and at peak value. During loaded operation, peak power per phase and maximum machine power output were recorded, Figure 6-21. The slight difference in peak power for dry and wet operation can be explained by the addition of drag on the translator during wet operation. Additionally, temperature data from the coils was collected as well as data from the load cells, data was logged every 10 minutes, with a data set of at least 3 full translator strokes being captured. The peak load provided by the load cells during testing is provided in Table 6-3 whilst operation of the prototype in flooded conditions is shown in Figure 6-22.

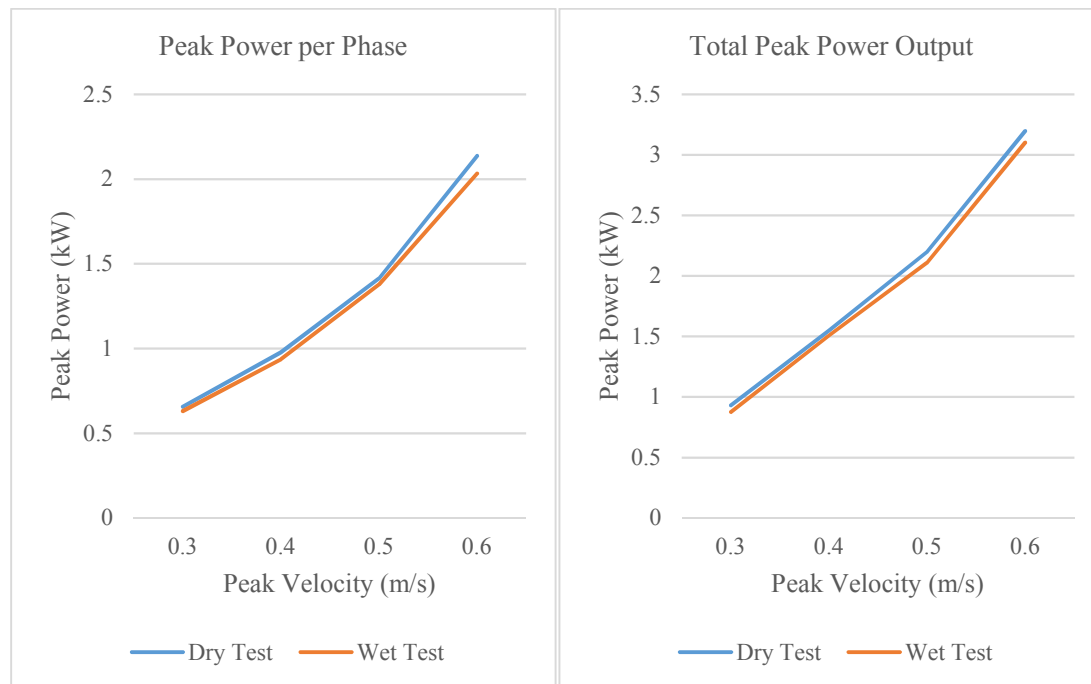


Figure 6-21. Peak power per phase and total peak power output of the machine, indicating the difference in wet to dry operation

Condition	No Load		Dry			Flooded			
Velocity (ms^{-1})	0.6	0.3	0.4	0.5	0.6	0.3	0.4	0.5	0.6
Peak Current (A)	NA	14.4	19.9	26.3	30.8	16.2	20.8	25.4	30.8
Peak Load (kN)	0.8	3.2	4	4.5	5.2	3	3.6	4	4.7

Table 6-3. Peak load data collected from the load cells during prototype testing



Figure 6-22. 5 kW linear C-GEN prototype installed and operating with a flooded airgap

6.3.2. Thermal Data Comparison

Dry testing provided a benchmark in order to demonstrate the benefits of fully flooded operation. Temperature profiles have been produced for both dry and wet operation under various loading conditions to show the difference between the two operation conditions. Temperature readings were logged every 10 minutes for all of the following figures.

The results below provide a sample of temperature data captured from a one of the centrally located coils within the translator. Coils towards the centre should experience the worst thermal loading due to heating from adjacent coils, however during testing

all coils experienced similar temperature increases within a margin $\sim 2^\circ\text{C}$. Figure 6-23, Figure 6-24 and Figure 6-25 provide temperature data at a maximum velocity of 0.3 ms^{-1} for peak current values of 12 Amps, 13.5 Amps and 15 Amps respectively.

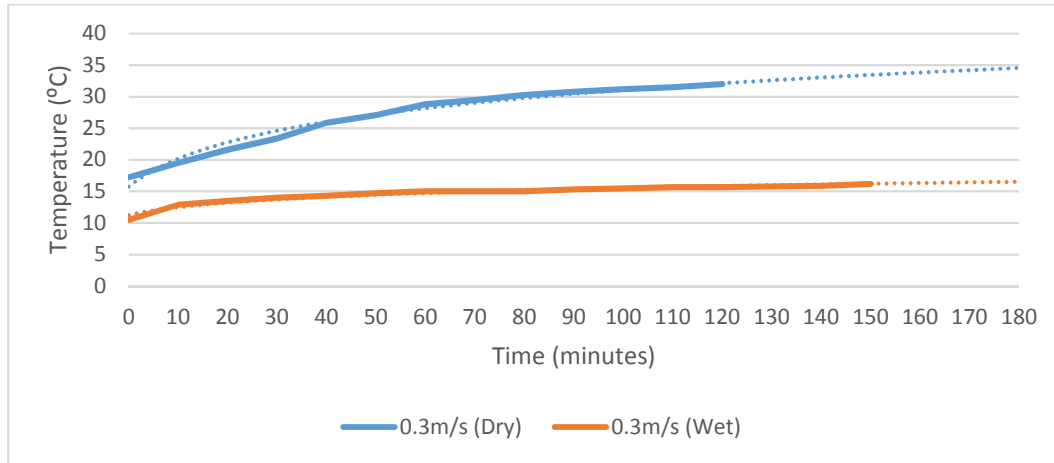


Figure 6-23. Coil temperature varying over time at a maximum velocity of 0.3 ms^{-1} and a peak current of 12 Amps per phase. Dotted lines indicate trend of graph

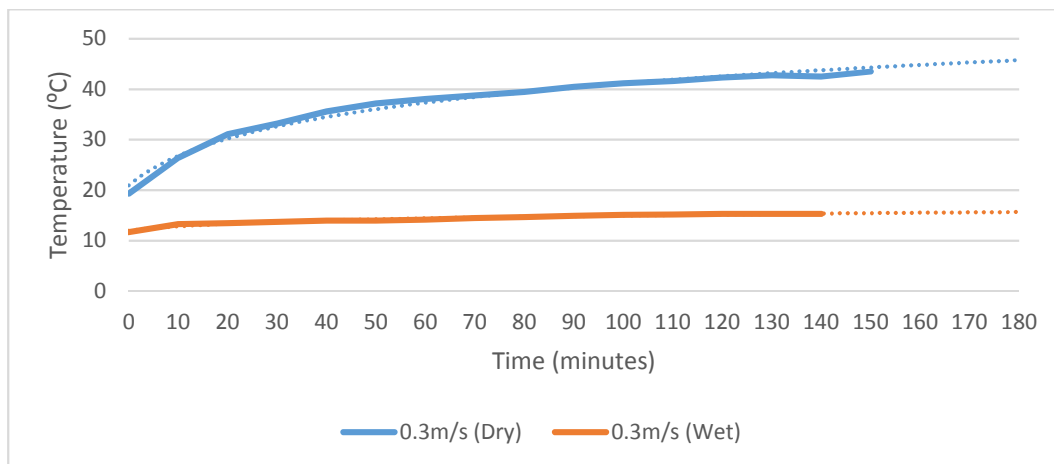


Figure 6-24. Coil temperature varying over time at a maximum velocity of 0.3 ms^{-1} and a peak current of 13.5 Amps per phase. Dotted lines indicate trend of graph

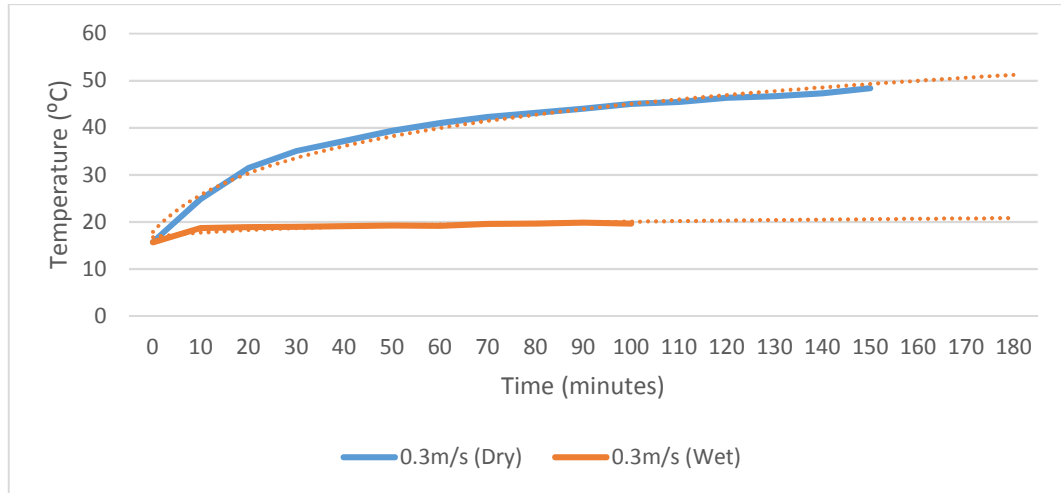


Figure 6-25. Coil temperature varying over time at a maximum velocity of 0.3 ms^{-1} and a peak current of 15 Amps per phase. Dotted lines indicate trend of graph

Figure 6-26, Figure 6-27 and Figure 6-28 present temperature data for a maximum translator velocity of 0.5 ms^{-1} for peak current values of 18 Amps, 22 Amps and 24.5 Amps respectively. For all translator speeds, fully flooded operation leads to a significant improvement in thermal performance.

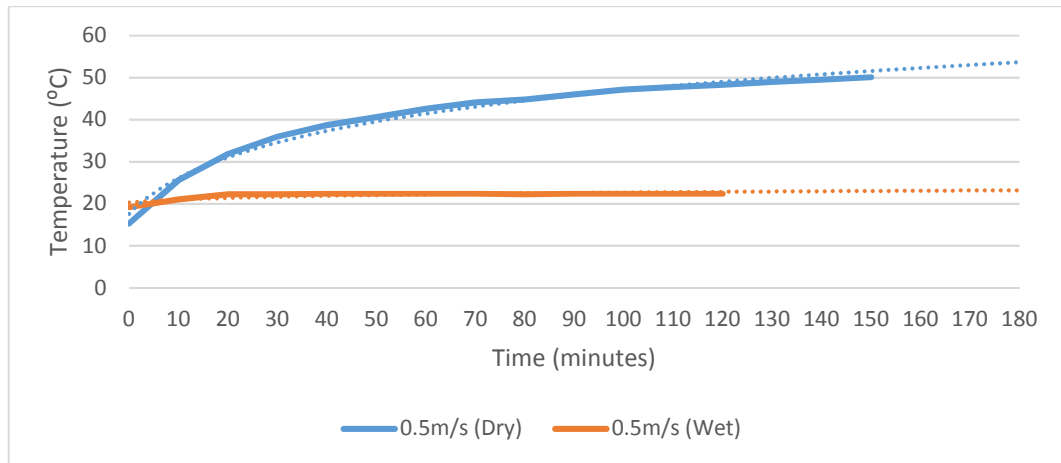


Figure 6-26. Coil temperature varying over time at a maximum velocity of 0.5 ms^{-1} and a peak current of 18 Amps per phase. Dotted lines indicate trend of graph

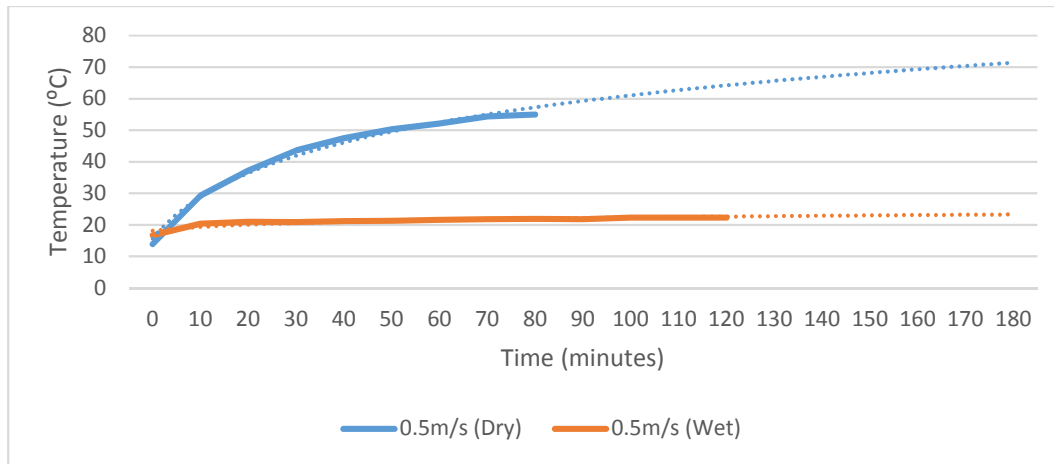


Figure 6-27. Coil temperature varying over time at a maximum velocity of 0.5 ms^{-1} and a peak current of 22 Amps per phase. Dotted lines indicate trend of graph

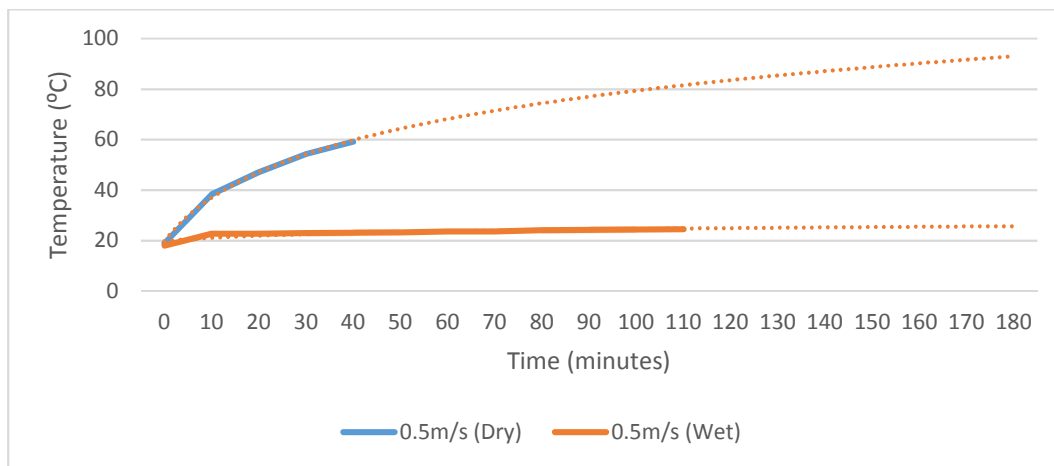


Figure 6-28. Coil temperature varying over time at a maximum velocity of 0.5 ms^{-1} and a peak current of 24.5 Amps per phase. Dotted lines indicate trend of graph

6.3.3. Discussion

Over the course of testing the internal resistance of the coils was maintained at safe levels. However, during dry testing under high resistive load, the increasing temperature trend of the coils was so extreme that testing was halted after temperatures approached 70°C . In addition, testing was halted when a relatively constant internal temperature had been reached.

There were two main factors that curtailed the logging of data from the 5 kW prototype and test rig. The first factor was that testing sessions had to be separated by long

periods of down time in order for the coils and translator structure to cool to ambient temperature, this was due to the size of the machine and the inability to provide adequate additional cooling. However, it should be noted that in flooded conditions, unlike the small prototype test rig, the 5 kW machine did not significantly alter the temperature of the surrounding water, therefore testing could continue for longer periods of time and the machine was able to cool quicker when flooded than when dry.

The second factor was the maximum velocity of testing that could be achieved. The value was capped at a maximum of 0.6 ms^{-1} , therefore the test rig could not operate at its maximum rated speed of 1 ms^{-1} , over a 1 m stroke. The reason for this was the large acceleration and deceleration loads that were required to maintain a short period of time at maximum velocity over a 1 m stroke. Once accelerations of 0.8 ms^{-2} were reached there was concern that the connecting structure between the translator and the test rig would fail. Therefore, results are unavailable for operation at rated speed and maximum loading.

The results from the 5kW linear test rig support the findings from the previous tests on the mini test rig, namely that fully flooded operation has a significant benefit on the thermal performance of the windings. The electrical loading can be increased significantly, which will lead to an increase in shear stress as discussed in Chapter 3. This would seem to imply that the physical size of the machine could be reduced, and thus reduce the mass of a direct drive system. However, losses are a function of the current squared, and so even though high currents can be achieved with good thermal performance, it will have a detrimental impact on efficiency.

In wave energy systems the device experiences a wide range of loads from part to full load all the way to extreme loads, as discussed in Chapter 2. Design of the PTO to cover all load ranges is not economically feasible, but the system has to survive extreme events. Results in this chapter demonstrate that significant current can flow in the machine whilst maintaining reasonable temperatures in the windings. It is therefore proposed, that rather than optimise for power density machines are designed for optimum efficiency, within reasonable economic constraints, and at normal current densities in the region of 5 A/mm^2 . Fully flooded operation will then allow the machine to absorb extreme events. For example, short circuit winding faults would not lead to

excessive winding temperature. The machine could be used to shed high loads during storm conditions through resistive loads. Under such conditions the machine would have to be disconnected from the power converter. Electric braking could also be used to limit motion of the wave device during extreme waves. Further work is required to investigate and verify such operation, but it is clear that the ability for the generator to absorb larger currents could contribute to survivability.

6.4. Marine Protection

The benefits of operating a PM machine with a flooded air gap have been explored in the previous section, however a barrier must be installed between the machines structural and active components, and the marine environment in order to avoid degradation from the corrosive effects of salt water medium.

For much of a generators structure, paints or plastic sprays can be used as protection, an overview of some relevant materials can be found in reviews by Eyres et al [224] and Yang et al [225]. However, interaction with marine organisms, commonly referred to as bio-fouling, can often undermine or remove simple paint and plastic protective layers. Paints that contain anti bio fouling properties have been developed, commonly containing biocides to stop the propagation of marine life on the structure. However, over time the concentration and potency of the biocides can wane. A review of common anti bio fouling paints can be found by Carteau et al in [226].

Cathodic protection is a technique by which the corrosion of a structure can be controlled by the introduction of an electric current flow to the metals surface. In the case of passive cathodic protection, an element is corroded, supplying a flow of electrons to the protected structure, such as the addition of zinc in the formation of galvanised steel. While for large structures, active cathodic protection can be used whereby a direct current can be introduced to replenish the structures electrons. In some cases bio fouling can be averted by the presence of the electrical current. However, the application of this type of protection to remote subsea structures in an accurate manner may be problematic [227].

The protection required by the magnets and coils is vital to the operation of the machine. It has been shown that epoxy can be used to coat the coils without detrimental

effects to thermal transfer, however bio fouling and prolonged operation submerged within seawater could lead to damage to the coil windings. Rare earth permanent magnets are specifically prone to the corrosive effects of salt water, experimental results are provided by Isotahdon et al [228], Kim et al [229] and Mao et al [230]. As salt is introduced to the surface of a PM it can infiltrate the magnets complex microstructure and oxidise the material rapidly. Magnets can be coated with various metallic, plastic, alloyed or ceramic coatings, the latter two being the least economical but generally supplying better protection [228]. For the C-GEN topology presented within this chapter the simplest protection method would be encasing the magnets in a stainless steel or nickel case. This would offer a strong, relatively thin protective boundary without impeding on the airgap length. Another option would be encase the magnets within an epoxy resin, however the thickness of the coating may need to be several times thicker than metallic encasement to form the same protection.

Chapter 7.

Conclusions and Discussion

The aim of this thesis is to examine issues facing developers and researchers when extracting energy from offshore renewable resources using direct drive generation systems and provide potential solutions and technological advancements in order to produce more reliable, low mass machines. To this end, the objectives of this thesis are split into three themes:

1. Present a literature review on offshore renewable energy sources, devices, power take off systems, and related sub-assemblies.
2. Introduce the structural development of claw pole transverse flux direct drive machines, specifically high temperature superconducting, HTS, topologies for multi megawatt offshore operations. Describe the design, build and testing of a linear claw pole transverse flux test rig; explain the alterations required to install a superconducting coil into the topology; and outline the structural requirements for the HTS design of a 30 kW prototype rotary machine and a proposed 10 MW rotary machine.
3. Investigate the benefits marinization offers to the operation and simplicity of the power take off systems for offshore energy devices. Specifically, this involved investigation of polymer surface contact bearings and flooded airgaps through physical testing of various materials and machine topologies.

The steps taken to complete this work are outlined in the next section.

7.1. Approach

The offshore environment is an energy rich resource which requires both devices and power take off systems to be robust, low maintenance, efficient and reliable. For these power generation systems to be advanced for offshore wind, wave and tidal energy harvesting, technological advancements must be explored, and the simplification of the energy convertor must be encouraged. This thesis proposes three design

advancements, novel machine construction, polymer bearing installation and flooded airgap machine operation, and creates the physical platform for them to be tested. The first design advancement utilises an HTS machine topology and structure to produce 10+ MW generators with mass lower than similarly rated conventional direct drive machines. The second design advancement is the installation of simplified polymer bearings within the direct drive system; with higher marine survivability characteristics, better life time predictability, and lower costs than conventional and complex bearing systems. The third and final design advancement proposes flooding a generation system airgap for subsea applications thereby improving heat transfer characteristics, and so increasing the resilience of the generating system.

This thesis starts with chapters 1 to 3 illustrating the potential of offshore renewable energy, detailing the vast energy present within all offshore resources; a history of wind, wave and tidal energy extraction systems was presented and different methods for power take off methods were discussed. Next various types of electrical generation machines were reviewed with a focus on direct drive electrical generator topologies and sub-assemblies. The application of superconducting materials into electric machines was investigated, concluding that the technology has the potential to increase power output while decreasing generator size and mass. Multiple superconducting, SC, machine projects were outlined to indicate the maturity of the technology and the direction of current research. The operational loads experienced by direct drive systems were explained to form a complete picture of the design process behind the construction of direct drive power take off systems. Finally, two case studies were outlined, the C-Gen technology and a proposed transverse flux HTS generator. These case studies were explored at some length, as they would be referred to throughout the thesis.

Several techniques were employed to investigate the structural design of the transverse flux generator in chapter 4. First, to provide validation of Keysan's original transverse flux claw pole machine design, a linear machine prototype was designed, constructed and tested. The results from this first stage of testing were then used to improve the simulation models and to redesign the prototype for future testing with an HTS coil. Knowledge gained through this redesign was used to model a 30 kW HTS claw pole

structural topology for future build and testing. Finally, the optimisation of a 10 MW scale HTS machine is presented for offshore shore wind energy extraction.

In chapter 5 a linear bearing test rig was designed and built to investigate the premise that mechanical bearings could be removed from the power take off subassembly and replaced with a simpler and cheaper alternative. Since polymer bearings are currently primarily used within rotary applications such as ship propulsion, it was decided that the less researched linear application of these materials would be reviewed. Various samples of polymer bearing materials were operated and tested within the linear rig. Over the course of operation, the test rig was altered to allow improved operation and better cataloguing of sample results. The test results were compared against an analytical force model of a heaving wave buoy, which indicated that polymer bearing materials can be a suitable alternative to conventional bearing systems for both wet and dry operation.

In chapter 6 the C-Gen case study was employed to investigate the thermal ramifications of introducing a flooded airgap into the machine's topology. A small 3 coil linear prototype was designed, built and operated to study the thermal effects different coil potting materials and topologies had on the operation of the machine with either a dry and wet airgap. A substantially larger 5 kW C-Gen 6 coil linear generator topology was then designed, built and operated to confirm the results catalogued from the previous test. Testing confirmed that operation with a flooded airgap significantly improved the operation of the coil windings within the generators. For completeness, a brief discussion on the marinization of generator components for flooded airgap operation was provided.

7.2. Discussion

Every model is, by its nature, an approximation and, in the case of this thesis, each simulated model has been physically tested in order to provide corroborative data or to help improve the design process and advance direct drive machine knowledge. This thesis proposed the advancement of direct drive generators for offshore renewable energy production via the simplification of bearing assemblies; reduction of seals and secondary cooling systems through the flooding of the generator airgap; and the

implementation of novel materials such as superconducting coils to produce smaller and lighter generator systems. As illustrated in the previous section, a number of test rig topologies and a linear generator prototype were employed to explore these mission statements. The design and operation of the test rigs has been explained and alterations detailed. The data collected from linear bearing tests is vital to validate their operation in a linear generation device, while the operation of a flooded machine validated previous simulation results. The construction and testing of a linear generator prototype provided information for the creation of a 30 kW prototype design. The proposed optimised 10 MW HTS machine utilises materials found within the construction industry as well as providing data on the design of a novel machine structure. Although including a technology as complex as a superconducting machine within this thesis may seem counter intuitive, it is justified by the reduction in mass and improved robustness offered by this technology. The author is confident that the aims of this investigation have been met.

7.3. Contribution to Knowledge

The information contained within this thesis has contributed to several publications and the advancement of several projects including the installation of the Applied Superconducting Laboratory within the University of Edinburgh, the validation of data from a Wave Energy Scotland Stage II project, and the construction and continued data production on Keysan's transverse flux claw pole HTS generator topology. The most significant contributions may be summarised as:

1. The design and build of a novel linear generator prototype has been presented and description of its alteration for superconducting operation has been detailed, incorporating collaborative work with past PhD and MEng students.
2. A novel 30 kW direct drive transverse flux generator structural design has been presented for future production.
3. A novel 10 MW direct drive transverse flux generator structure and related optimisation process has been provided, indicating the reduction in mass and superconducting material achievable with its design.
4. A linear bearing test rigs design and build has been detailed and bearing test samples have had their results compared to their rotary operational properties.

The differences in the results have been discussed and suitability for linear machine marine applications have been proven.

5. The data collected from the coils and associated potting agents during operation within a flooded airgap has validated previous simulation results.

7.4. Recommendations for Future Work

The work contained within this thesis introduces many interesting elements that could lead to further investigation. These have been categorised as follows:

- Recommendations for further work on the HTS transverse flux claw pole machines.
 - Testing of the linear HTS claw pole machine within the vacuum chamber of the new Applied Superconducting Laboratory at the University of Edinburgh
 - Construction and testing of the 30 kW machine to gain further knowledge of the structural implications of SC generation.
 - Construction of an integrated cryostat for the 30 kW prototype and an investigation into the installation of cryostats in the offshore environment
- Recommendations for further investigation into linear polymer bearing testing and applications.
 - Alteration of the bearing test rig, as shown in Figure 7-1, in order to improve its operation and loading of bearing samples. In addition, the design of a larger electric actuator bearing test rig, to simulate higher loading.
 - Continued bearing testing will be continued in order to validate the predicted life time of the samples tested.
 - Testing bearings within a particulate rich water environment is required in order to assess their operation in real world conditions.
 - The bearing samples will be installed within the 5 kW linear C-GEN machine in order to access load and wear conditions within a working machine. The linear generator will be altered to include a linear motor

which will apply horizontal loading to simulate the action of wave loading. The design of the loading device is presented in Figure 7-2.

- Recommendations for further testing into the marinization of the C-Gen generator, specifically the operation with a flooded airgap.
- The material properties of the potting agent used for the coils should be further investigated to investigate degradation during operation within the offshore environment.
- Potting methods and potting materials should be investigated in order to simplify fabrication and manufacturing techniques.

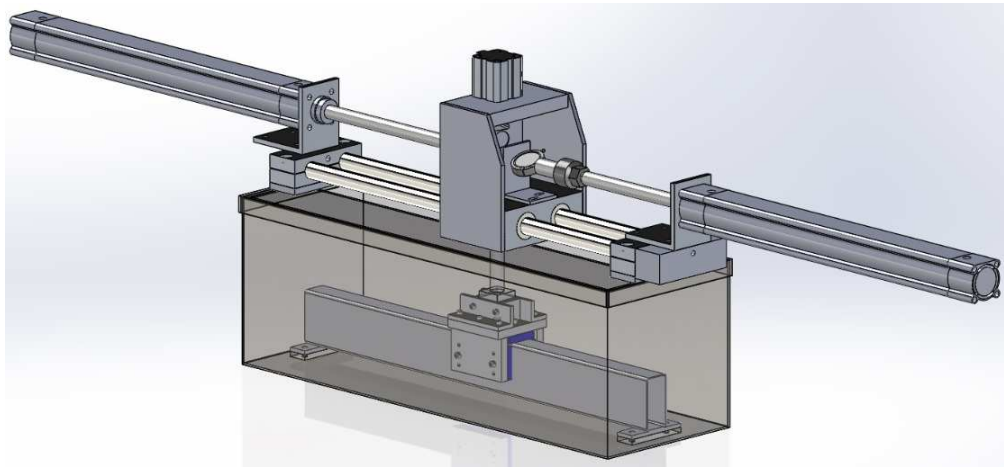


Figure 7-1. The alteration of the bearing test rig to include a second compressed air actuator in order to improve bearing testing and machine performance

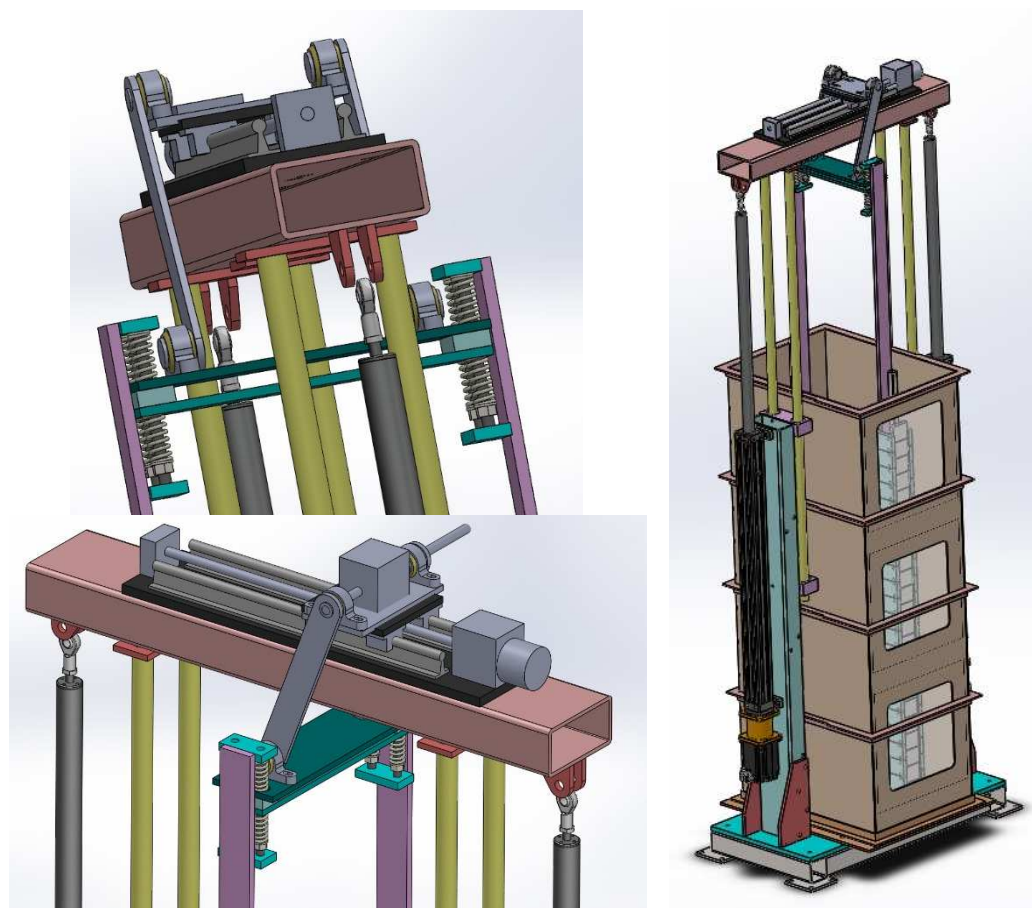


Figure 7-2. Addition of a stepper motor to the 5 kW test rig in order to simulate wave loads as calculated in chapter 5

Appendix A

Geared and Direct Drive Sub System Failures

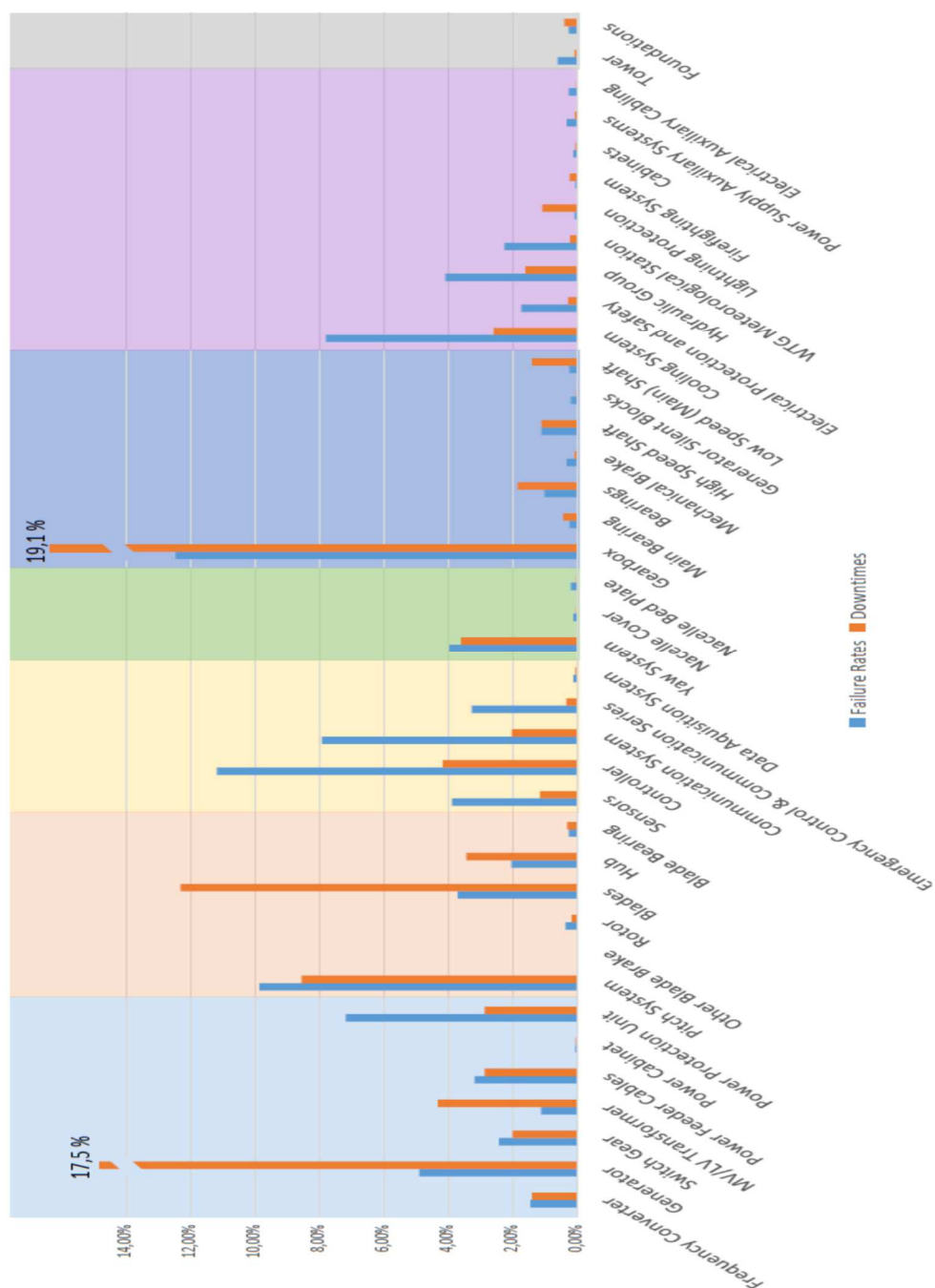


Figure A- 1. Normalised failure rates and downtimes for geared generators $\geq 1\text{MW}$ wind turbines [88]

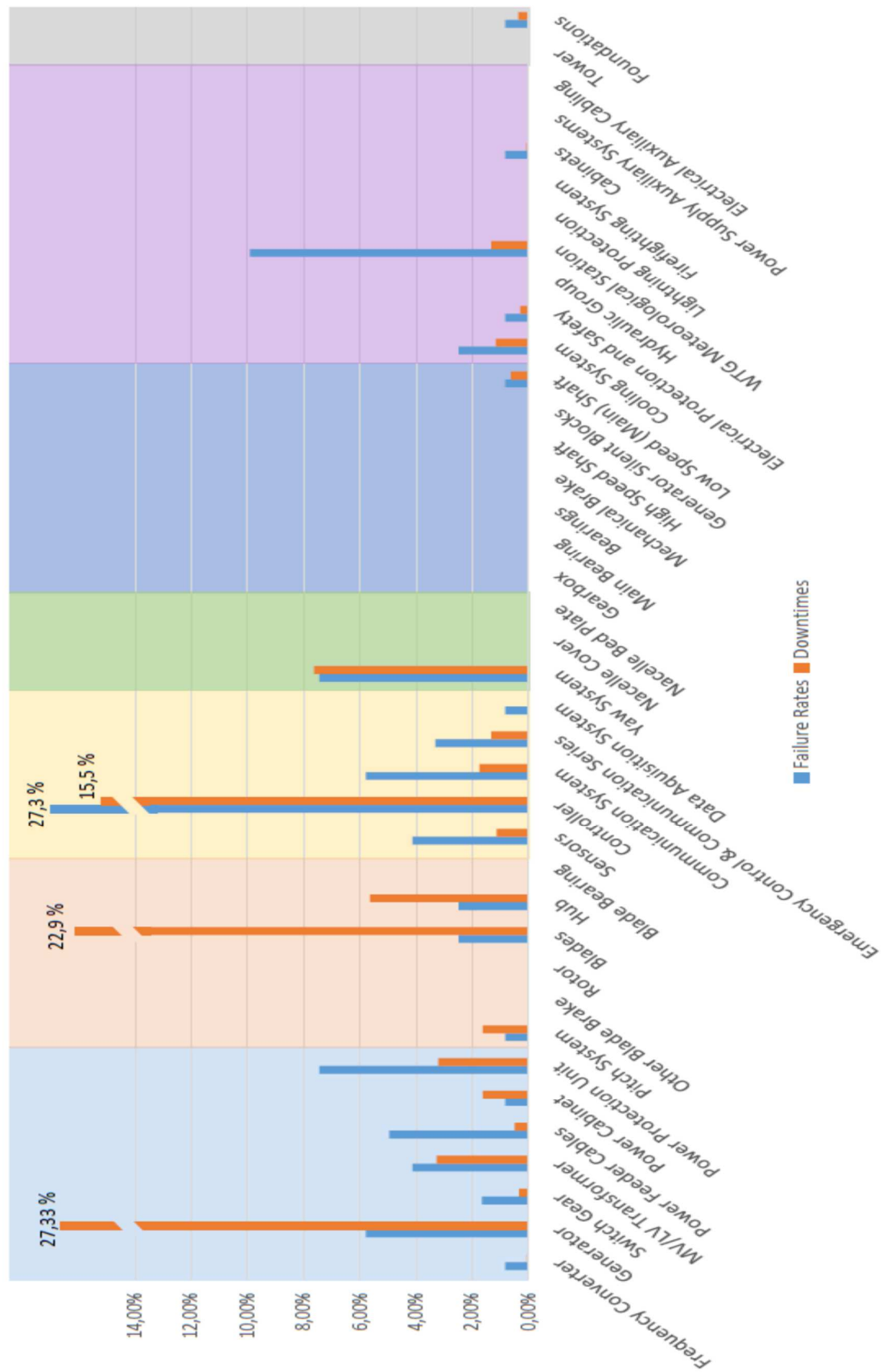


Figure A- 2. Normalised Failure Rates and Downtimes for Direct Drive Wind Turbines [88]

Appendix B

Data Sheet Blue PC5308 Epoxy Resin



PC 5308 RESIN / PC 5308 HARDENER EPOXIDE RESIN SYSTEM

DESCRIPTION- PC 5308 Resin / PC 5308 Hardener is a room temperature cured two component rigid epoxy resin system.

APPLICATION- PC 5308 Resin / PC 5308 Hardener is used in the potting and encapsulation of electronic and electrical components and sub assemblies. Pigmented blue the product was designed for excellent thermal conductivity values. It is currently used in a number of applications requiring excellent heat dissipation. These include linear motors where the product is used as a casting material.

PROCESSING METHODS- PC 5308 Resin / PC 5308 Hardener can be hand mixed or for the best results mixed through automated dispensing equipment. Please note that due to the high viscosity of the Resin component flow is limited and abrasive and any equipment should be assessed in terms of longevity. It is also suitable for vacuum casting operation. Cure may be accelerated by baking at 50°C – 90°C. Usable life 500gram @ room temperature 1hr. Further information on suitable equipment and methods is available on request.

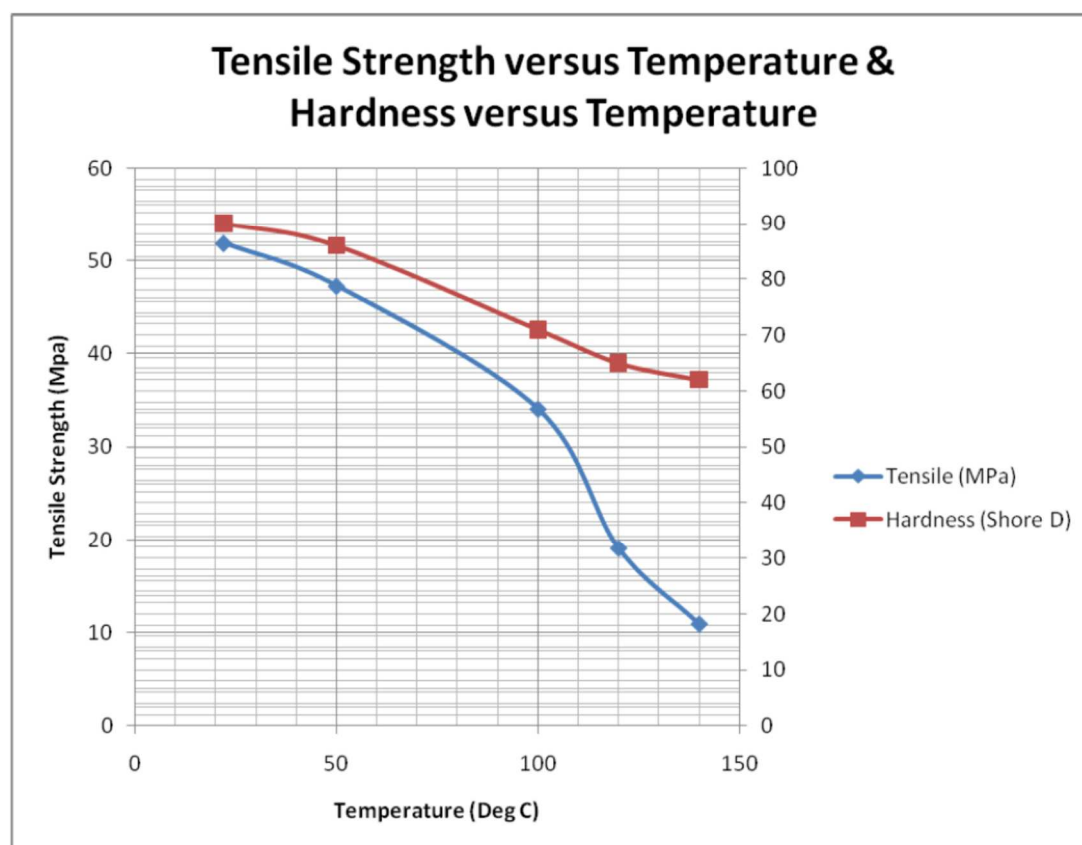
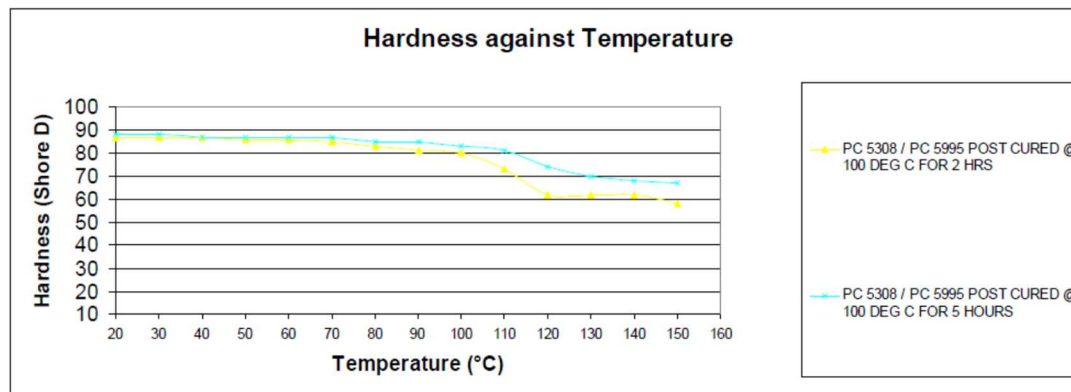
PROPERTIES- Room temperature cured, long working life, high gloss finish, excellent thermal conductivity, rigid, excellent moisture resistance, excellent adhesion to most substrates.

CURED PROPERTIES

Shore D Hardness (DIN 53505)	85 - 90
Elongation at break %	approx. 1-2
Thermal Conductivity	> 1 W/mk
Dielectric Strength (DIN 53481)	>20 Kv/mm
Dielectric Constant (DIN 53483)	5.5
Coefficient of Expansion (ASTM D696-70)	50 – 60 X 10 ⁶ linear/° C
Volume resistivity (BS2782)	>12log ₁₀ ohm cm

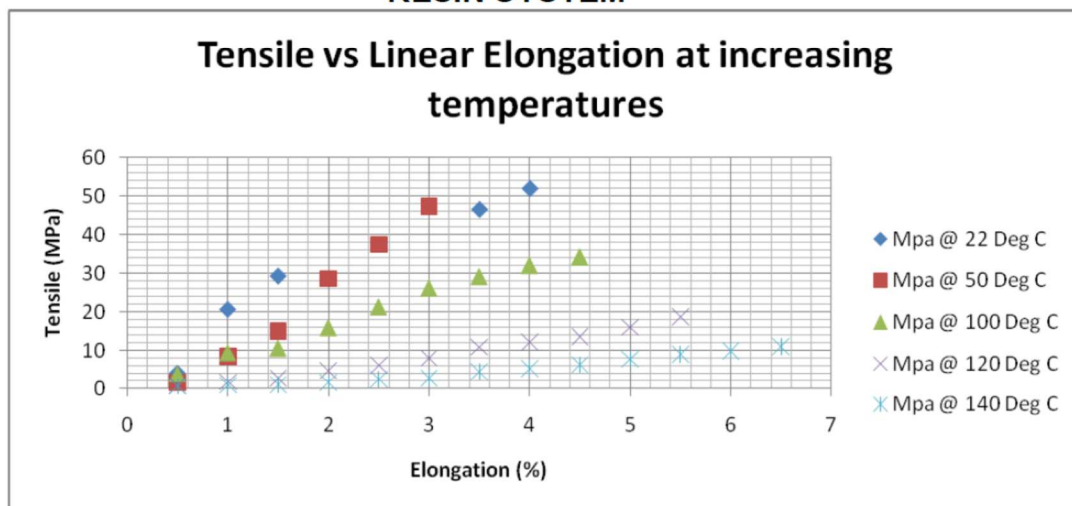


PC 5308 RESIN / PC 5308 HARDENER EPOXIDE RESIN SYSTEM





**PC 5308 RESIN / PC 5308 HARDENER EPOXIDE
RESIN SYSTEM**



Speed 100mm/min. Samples cured at 90 Deg C for 4 hours

For improved Hardness against Temperature see separate publication - PC 5308 RESIN with PC 5995 HARDENER.

Disclaimer: WHILE THE INFORMATION AND RECOMMENDATIONS IN THIS PUBLICATION ARE TO THE BEST OF OUR KNOWLEDGE, INFORMATION AND BELIEF ACCURATE AT THE TIME OF THE PUBLICATION, NO GUARANTEE, WARRANTY, OR REPRESENTATION IS MADE, INTENDED, OR IMPLIED AS TO THE CORRECTNESS OR SUFFICIENCY OF ANY INFORMATION, OR AS TO THE SUITABILITY OF ANY CHEMICAL COMPOUNDS FOR ANY PARTICULAR USE, OR THAT ANY CHEMICAL COMPOUNDS OR USE THEREOF ARE NOT SUBJECT TO A CLAIM BY A THIRD PARTY FOR INFRINGEMENT OF ANY PATENT OR OTHER INTELLECTUAL PROPERTY RIGHT. EACH USER SHOULD CONDUCT A SUFFICIENT INVESTIGATION TO ESTABLISH THE SUITABILITY OF ANY PRODUCT FOR ITS INTENDED USE.

GREENFIELD POLYMERS LIMITED

MYLESTONE HOUSE, SOWERBY NEW ROAD, SOWERBY BRIDGE, WEST YORKS. HX6 1AA.

www.greenfieldpolymers.com

TEL: 01422 835835

FAX: 01422 839439

Appendix C

Matlab Source Code for Calculation of Force and Moments about Heaving Buoy

% Gravitational acceleration, g [$\text{m}/(\text{s}^2)$]:

$g = 9.806;$

% Water density, ρ [$\text{kg}/(\text{m}^3)$]:

$\rho = 1030;$

% YOU CAN CHANGE THIS - Water depth, h [m]:

$h = 25;$

% Wave amplitude, a [m];

$a = 0.76;$

% Wave period, T [s];

$T = 5.2;$

% Radius of buoy, r [m]:

$r = 1.5;$

% The vertical coordinate z is measured upwards from the undisturbed

% free-surface. So $z = -h$ is the z coordinate of the flat seabed.

% z coordinate of the top of the buoy, z_t [m] (top stroke -3, bottom stroke -4):

$z_t = -3;$

% z coordinate of the bottom of the buoy, z_b [m] (top stroke -5, bottom stroke -6):

z_b = -5;

% The inertia coefficient, C_m:

C_m = 1.3;

% The drag coefficient, C_d:

C_d = 0.6;

% z coordinate of point directly below the buoy and

% about which the moment is measured, z_m [m] (top stroke -18, bottom stroke -19):

z_m = -18;

% Number of equal horizontal sections that the buoy

% is divided into, N:

Nz = 50;

% Number of equal time intervals that a wave period

% is divided into, Nt:

Nt = 100;

% Calculating the angular frequency, omega, from the period T:

omega = 2*pi/T;

% Calculating the deep-water wavenumber, k_0, which will be used as an

% initial guess for the actual (finite-depth) wavenumber, k:

k_0 = omega^2/g;

% Calculating the wavenumber, k = 2*pi/lambda (where lambda is the

% wavelength), from omega, using the dispersion relation:

% $\omega^2 = g*k*\tanh(k*h)$:

k = fsolve(@(k)g*k*tanh(k*h)-omega^2,k_0);

% Recalculating T to check that we have found the right k:

T_check = 2*pi/sqrt(g*k*tanh(k*h));

% Calculating the wavelength:

lambda = 2*pi/k;

% Calculating the height of each horizontal section of the cylindrical

% buoy, delta_z [m]:

delta_z = (z_t-z_b)/Nz;

% Calculating the frontal area of each horizontal section of the

% cylindrical buoy, i.e. the cross-sectional area perpendicular to the flow

% direction, delta_A [m²]:

delta_A = 2*r*delta_z;

% Calculating the volume of each horizontal section of the cylindrical

% buoy, delta_v [m³]:

delta_V = delta_z*pi*(r^2);

% Calculating vector of z coordinates of the midpoints of each horizontal

% section of the cylindrical buoy, z [m]:

z = linspace(z_b+(delta_z/2),z_t-(delta_z/2),Nz);

% Calculating the vector of times that divides the wave period into Nt

% equal intervals:

t = linspace(0,T,Nt+1);

% Initialising the vectors which will contain, respectively, the inertia

% force, drag force, total force, inertia moment, drag moment and total

% moment, acting on the buoy at each of the times within the vector t:

F_inertia = zeros(1,Nt+1);

F_drag = zeros(1,Nt+1);

F_total = zeros(1,Nt+1);

M_inertia = zeros(1,Nt+1);

M_drag = zeros(1,Nt+1);

M_total = zeros(1,Nt+1);

% Loop for the different times:

sinh_kh = sinh(k*h);

for n1 = 1:Nt+1

 % Calculating the horizontal fluid particle velocity at each of the z

 % coordinates. This comes from linear wave theory for finite-depth

 % water (see page 27 of [1]):

 u = omega*a*(cosh(k*(z+h))/sinh_kh)*sin(omega*t(n1));

 % Calculating the horizontal fluid particle acceleration at each of the

 % z coordinates. This comes from linear wave theory for finite-depth

 % water (see page 27 of [1]):

```
u_dot = (omega^2)*a*(cosh(k*(z+h))/sinh_kh)*cos(omega*t(n1));
```

```
% Calculating the inertia force on each horizontal section of the
```

```
% cylindrical buoy:
```

```
delta_F_inertia = rho*C_m*delta_V*u_dot;
```

```
% Calculating the drag force on each horizontal section of the
```

```
% cylindrical buoy:
```

```
delta_F_drag = 0.5*rho*C_d*delta_A*(u.*abs(u));
```

```
% Calculating the inertia moment on each horizontal section of the
```

```
% cylindrical buoy:
```

```
delta_M_inertia = delta_F_inertia.*(z-z_m);
```

```
% Calculating the drag moment on each horizontal section of the
```

```
% cylindrical buoy:
```

```
delta_M_drag = delta_F_drag.*(z-z_m);
```

```
% Calculating the total inertia force on the bouy at time t(n1):
```

```
F_inertia(n1) = sum(delta_F_inertia);
```

```
% Calculating the total drag force on the bouy at time t(n1):
```

```
F_drag(n1) = sum(delta_F_drag);
```

```
% Calculating the total force on the bouy at time t(n1):
```

```
F_total(n1) = F_inertia(n1)+F_drag(n1);
```

```
% Calculating the total inertia moment on the bouy at time t(n1):
```

```
M_inertia(n1) = sum(delta_M_inertia);
```

```
% Calculating the total drag moment on the bouy at time t(n1):

M_drag(n1) = sum(delta_M_drag);

% Calculating the total moment on the bouy at time t(n1):

M_total(n1) = M_inertia(n1)+M_drag(n1);

end

% Calculating the maximum absolute force:

max_F = max(abs(F_total));

% Calculating the maximum absolute moment:

max_M = max(abs(M_total));

% Plotting the force results:

figure(1)

plot(t,F_inertia,'b',t,F_drag,'r',t,F_total,'k');

title('Horizontal Force on Cylinder');

xlabel('Time [s]');

ylabel('Force [N]');

legend('Inertia Force','Drag Force','Total Force','Location','SouthWest');

text(0.7*T,-max_F+0.1*max_F, ...

     ['max(|Total Force|) = ' char(10) num2str(max_F) ' N']);

% Plotting the moment results:

figure(2)

plot(t,M_inertia,'b',t,M_drag,'r',t,M_total,'k');
```

```
title('Moment about Point on Cylinder Centre Line with  $z = z_m$ ');  
  
xlabel('Time [s]');  
  
ylabel('Moment [Nm]');  
  
legend('Inertia Moment','Drag Moment','Total Moment','Location','SouthWest');  
  
text(0.7*T,-max_M+0.1*max_M, ...  
  
      ['max(|Total Moment|) = ' char(10) num2str(max_M) ' Nm']);
```

Appendix D

Wave Study Graphical Data of Horizontal Force and Moments about Heaving Buoy

Wave Loading Case 1 Bottom of stroke. $A = 0.76 \text{ m}$

$T = 5.20 \text{ s}$

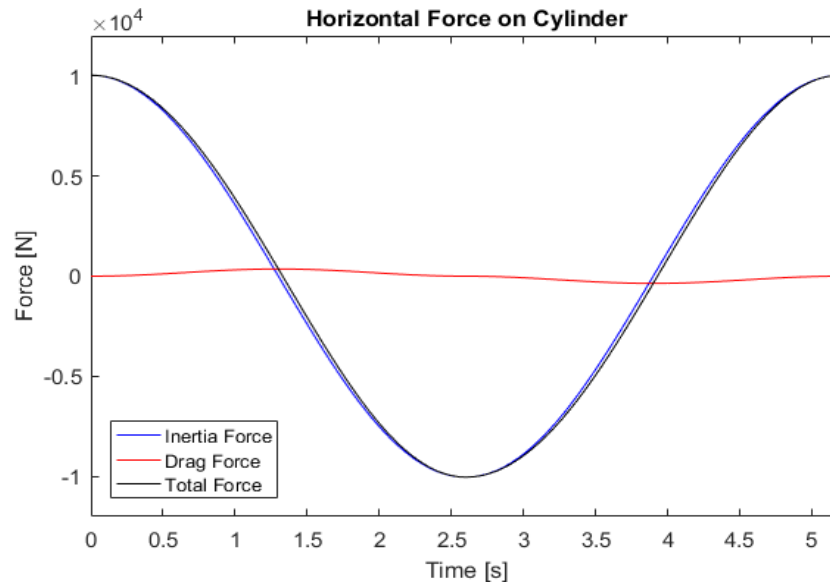


Figure D-1. Horizontal forces at bottom of stroke, wave loading case 1

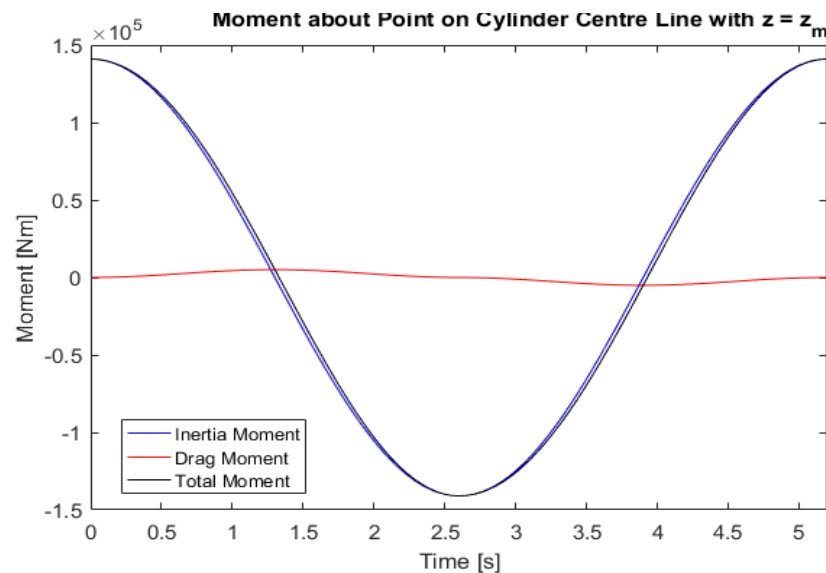


Figure D-2. Momentum about z_m at bottom of stroke, wave loading stroke case 1

Wave Loading Case 1: Top of stroke. $A = 0.76$ m $T = 5.20$ s

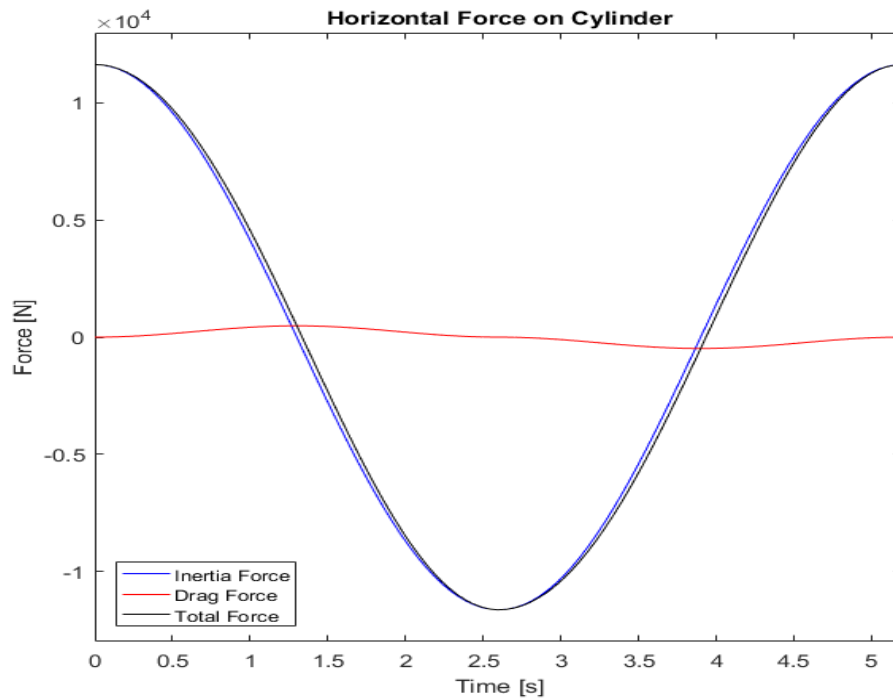


Figure D-3. Horizontal forces at top of stroke, wave loading data case 1

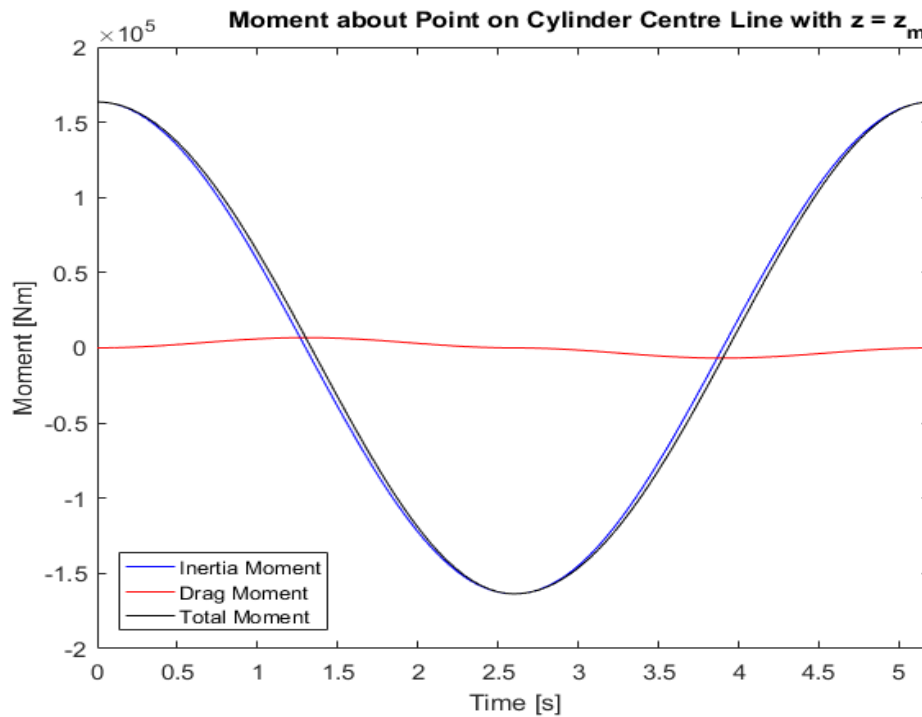


Figure D-4. Momentum about z_m at top of stroke, wave loading data case 1

Wave Loading Case 2: Bottom of stroke. $A = 0.86$ m $T = 6.80$ s

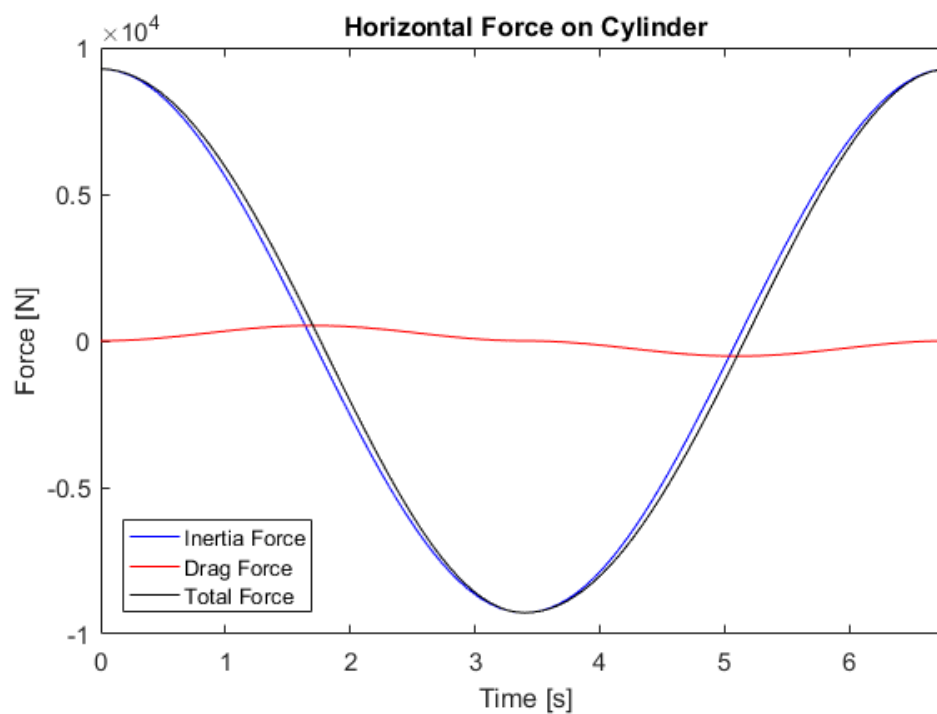


Figure D-5. Horizontal forces at bottom of stroke, wave loading data case 2

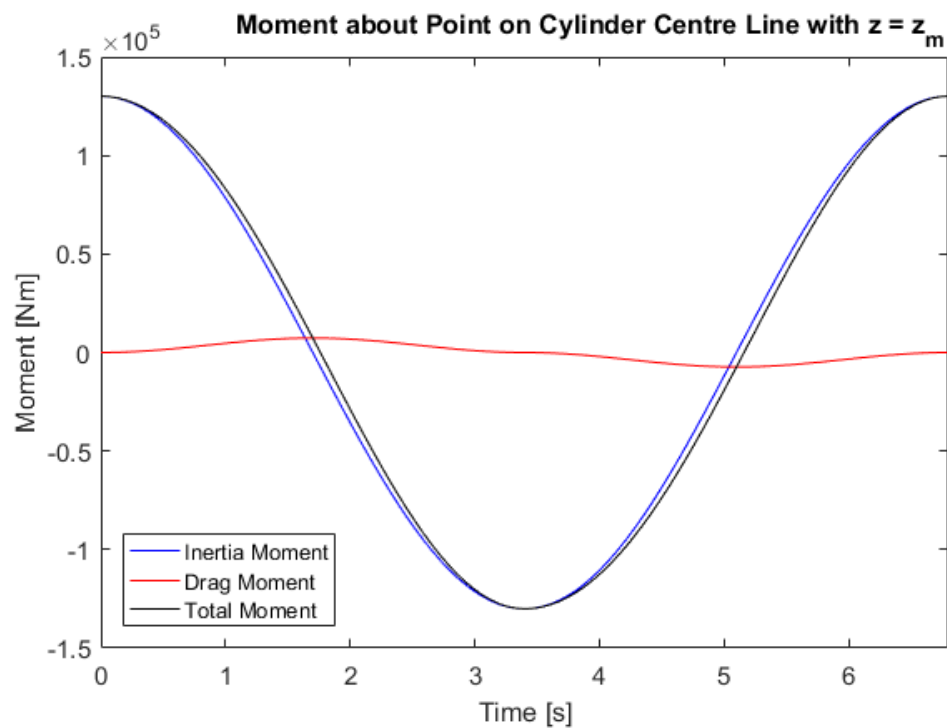


Figure D-6. Momentum about z_m at bottom of stroke, wave loading data case 2

Wave Loading Case 2: Top of stroke. $A = 0.86 \text{ m}$ $T = 6.80 \text{ s}$

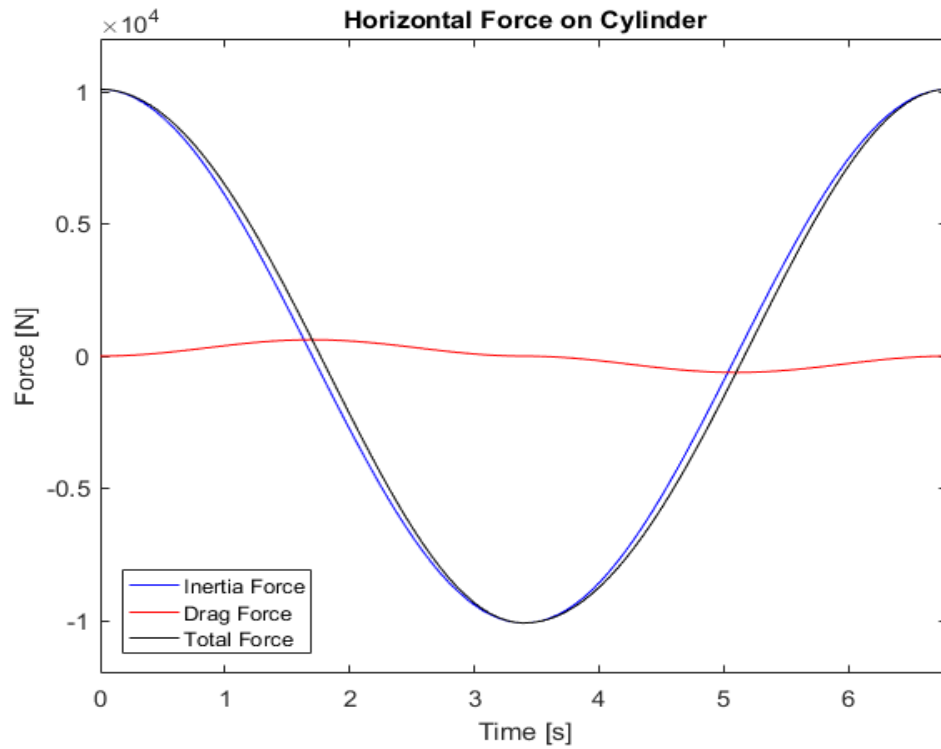


Figure D-7. Horizontal forces at top of stroke, wave loading data case 2

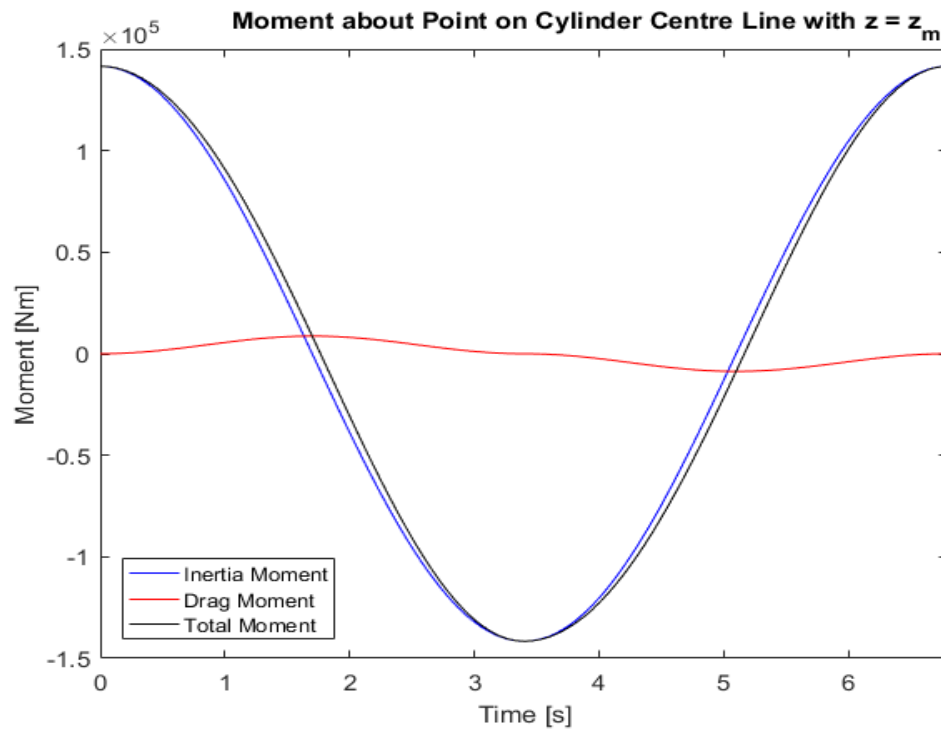


Figure D-8. Momentum about z_m at top of stroke, wave loading data case 2

Wave Loading Case 3: Bottom of stroke. $A = 1.55 \text{ m}$ $T = 6.40 \text{ s}$

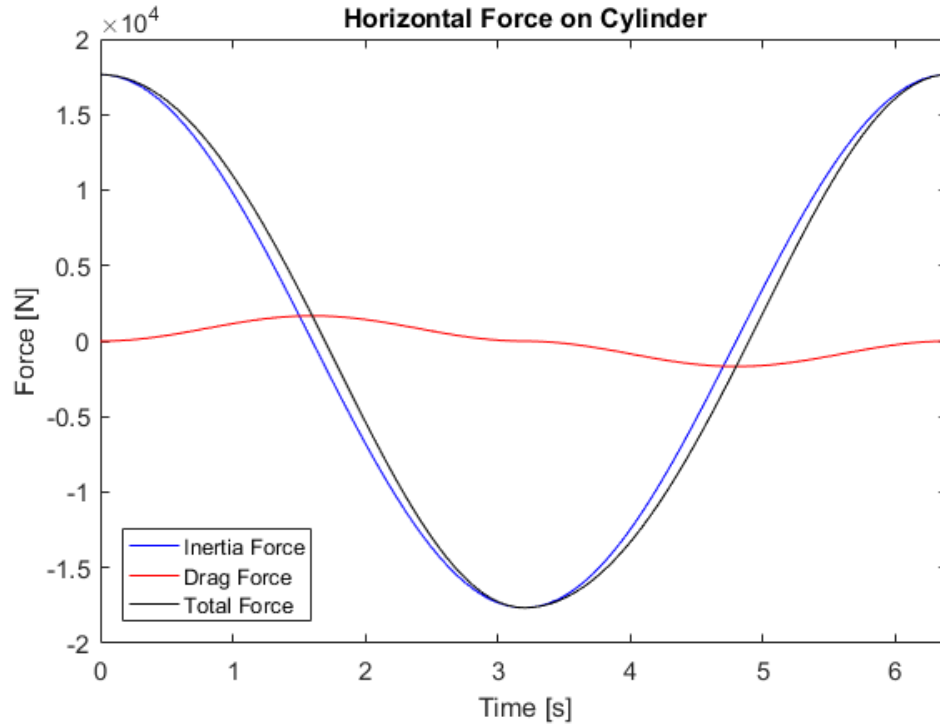


Figure D-9. Horizontal forces at bottom of stroke, wave loading data case 3

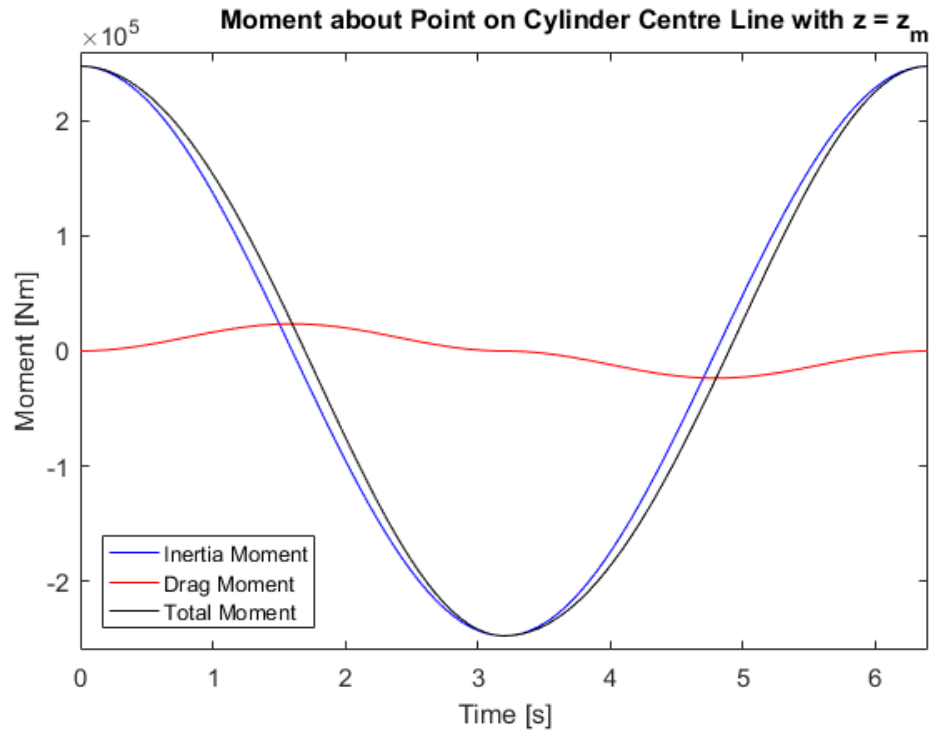


Figure D-10. Momentum about z_m at bottom of stroke, wave loading data case 3

Wave Loading Case 3: Top of stroke. $A = 1.55 \text{ m}$ $T = 6.40 \text{ s}$

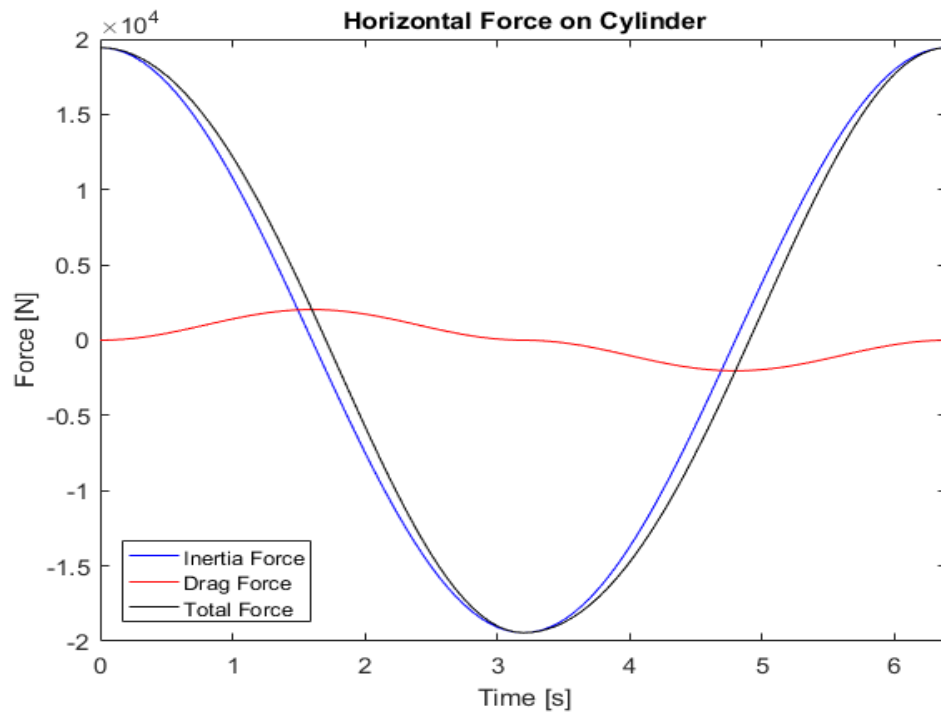


Figure D-11. Horizontal force at top of stroke, wave loading data case 3

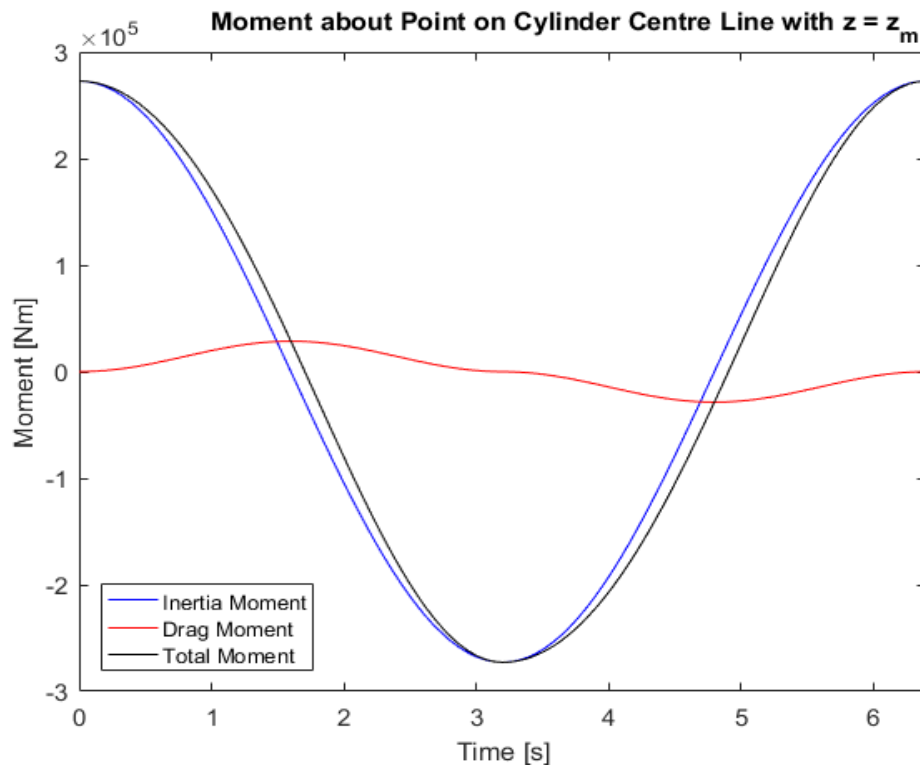


Figure D-12. Momentum about z_m at top of stroke, wave loading data case 3

Wave Loading Case 4: Bottom of stroke. $A = 1.83$ m $T = 7.70$ s

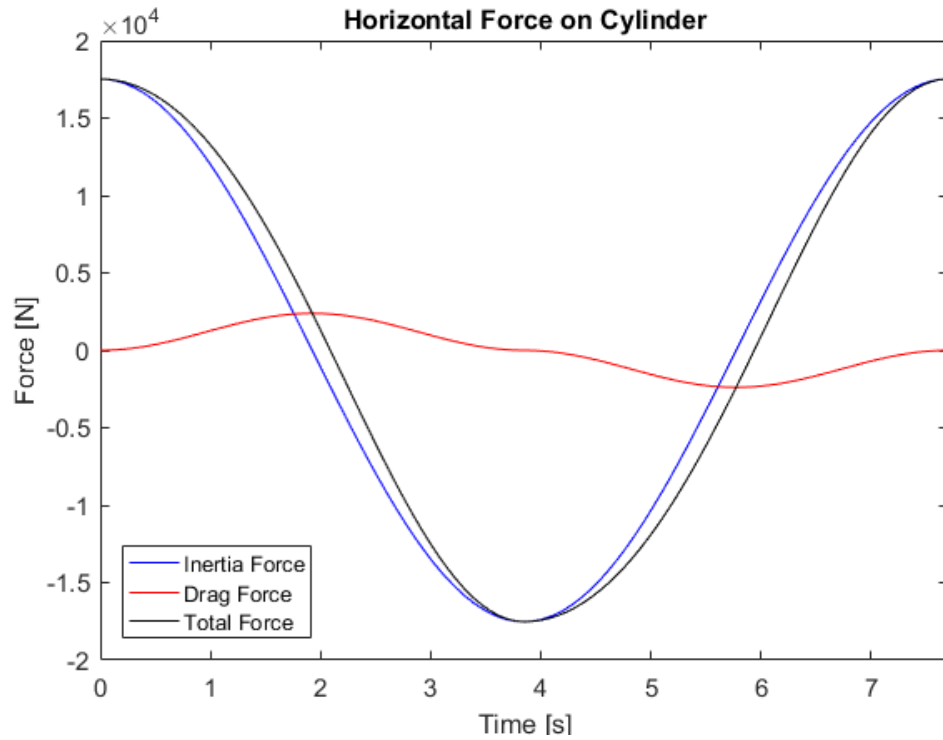


Figure D-13. Horizontal forces at bottom of stroke, wave loading data case 4

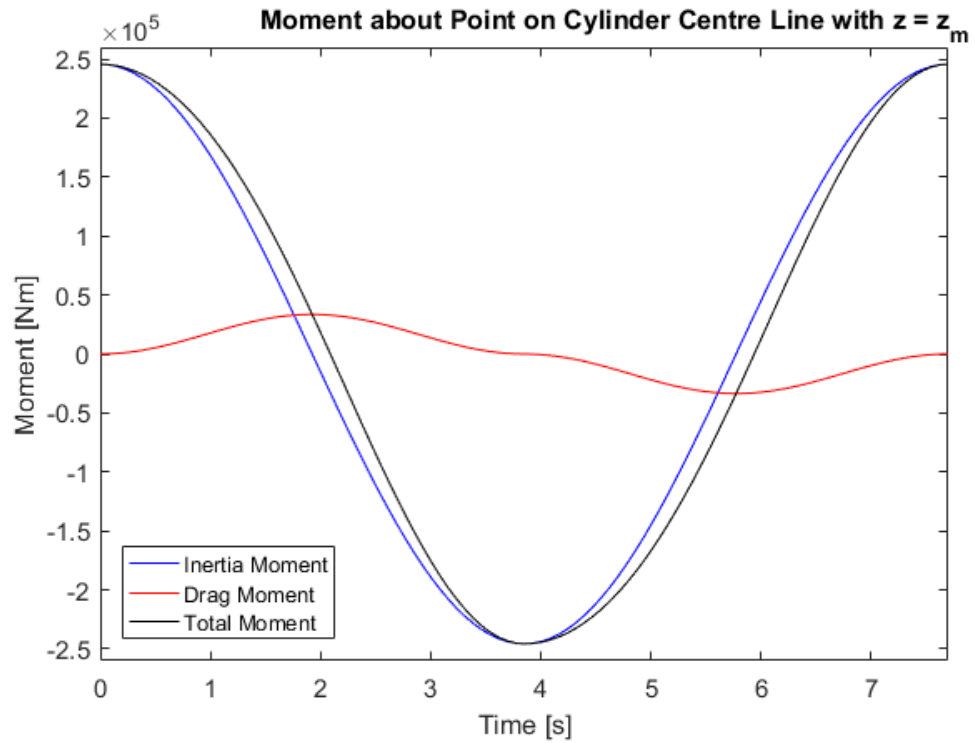


Figure D-14. Momentum about z_m at bottom of stroke, wave loading data case 4

Wave Loading Case 4: Top of stroke. $A = 1.83 \text{ m}$ $T = 7.70 \text{ s}$

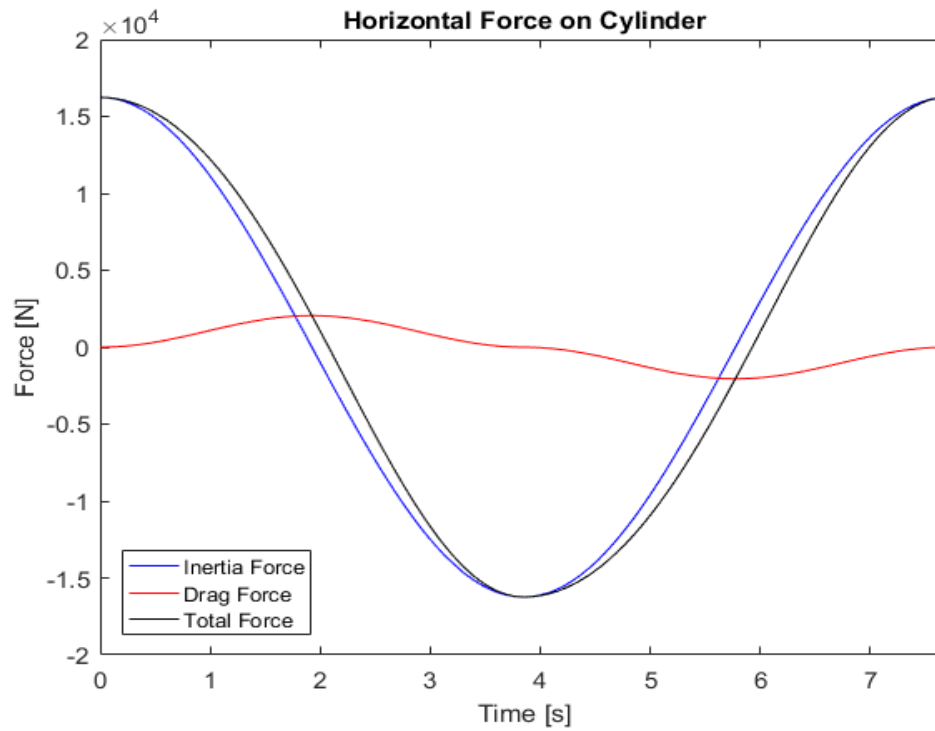


Figure D-15. Horizontal force at top of stroke, wave loading data case 4

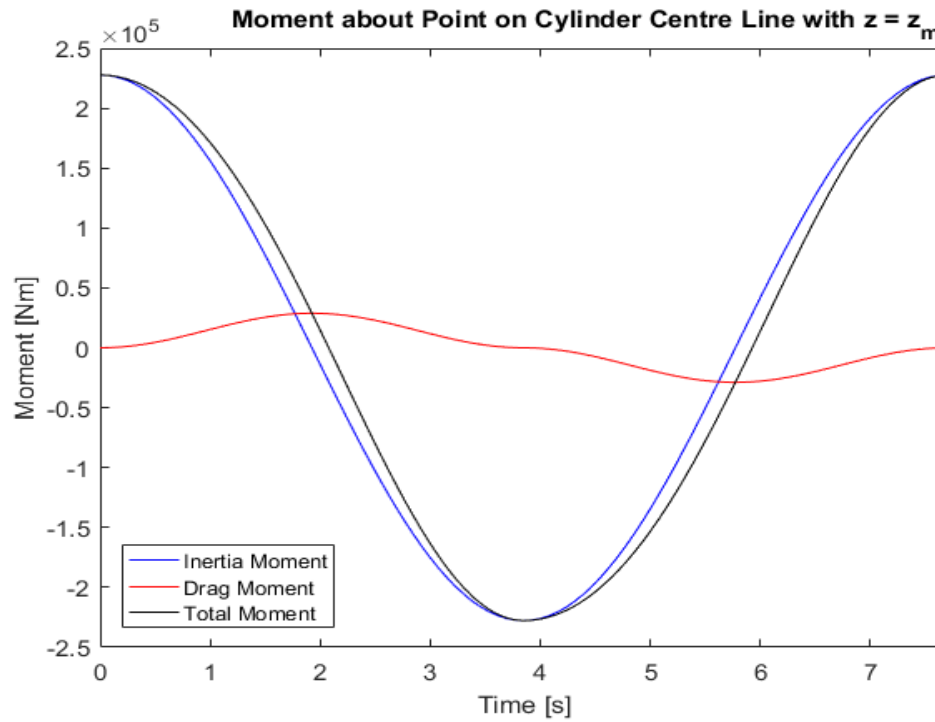


Figure D-16. Momentum about z_m at bottom of stroke, wave loading data case 4

Wave Loading Case 5: Bottom of stroke. $A = 2.59$ m $T = 8.30$ s

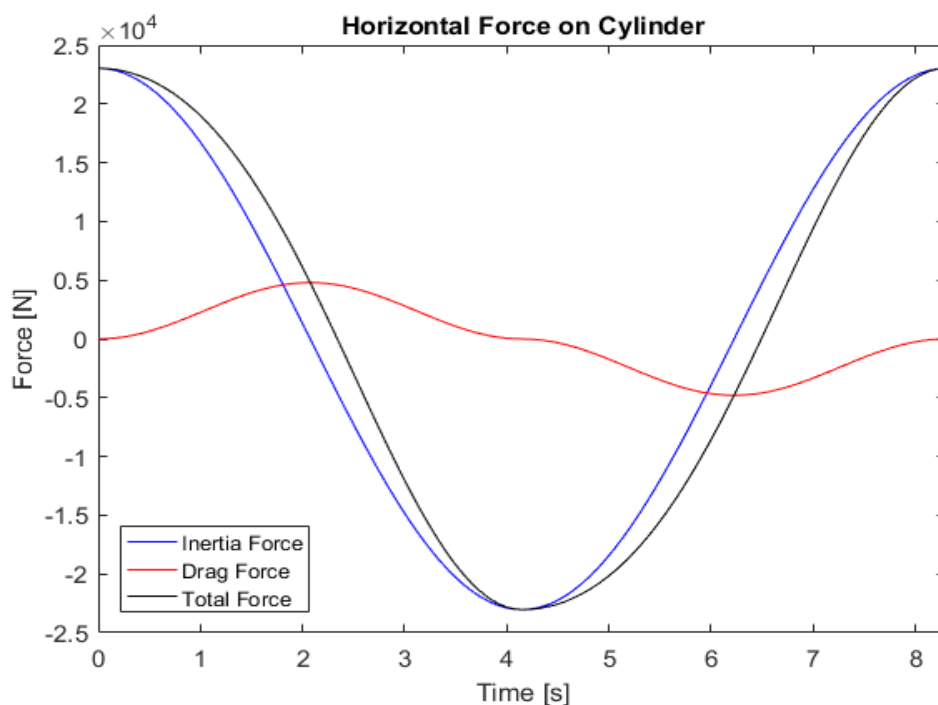


Figure D-17. Horizontal forces at bottom of stroke, wave loading data case 5

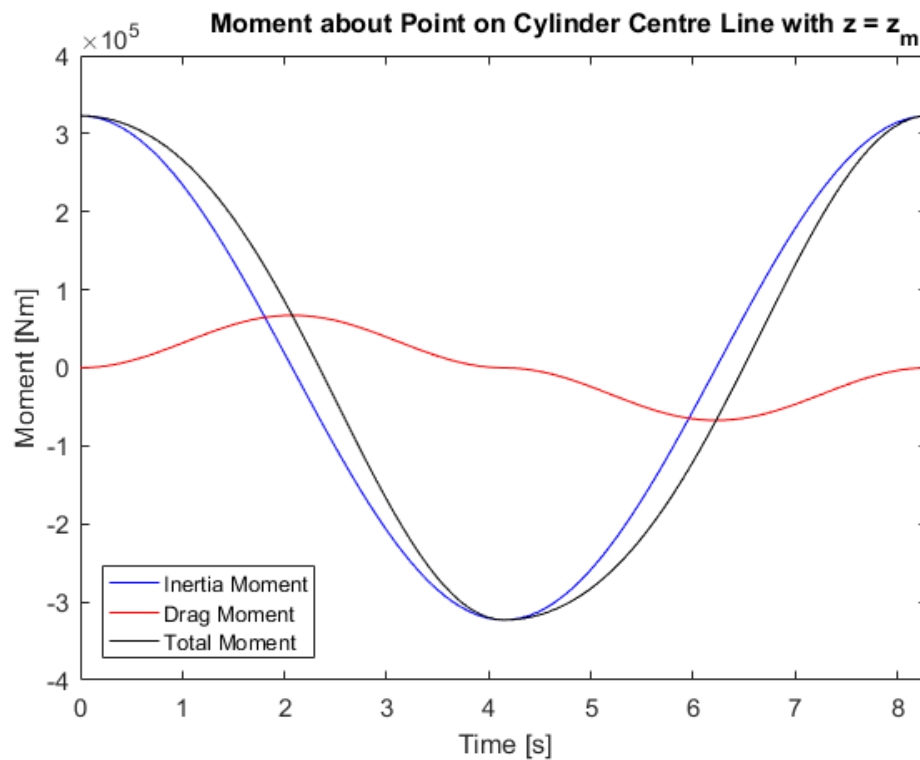


Figure D-18. Momentum about z_m at bottom of stroke, wave loading data case 5

Wave Loading Case 5: Top of stroke. $A = 2.59 \text{ m}$ $T = 8.30 \text{ s}$

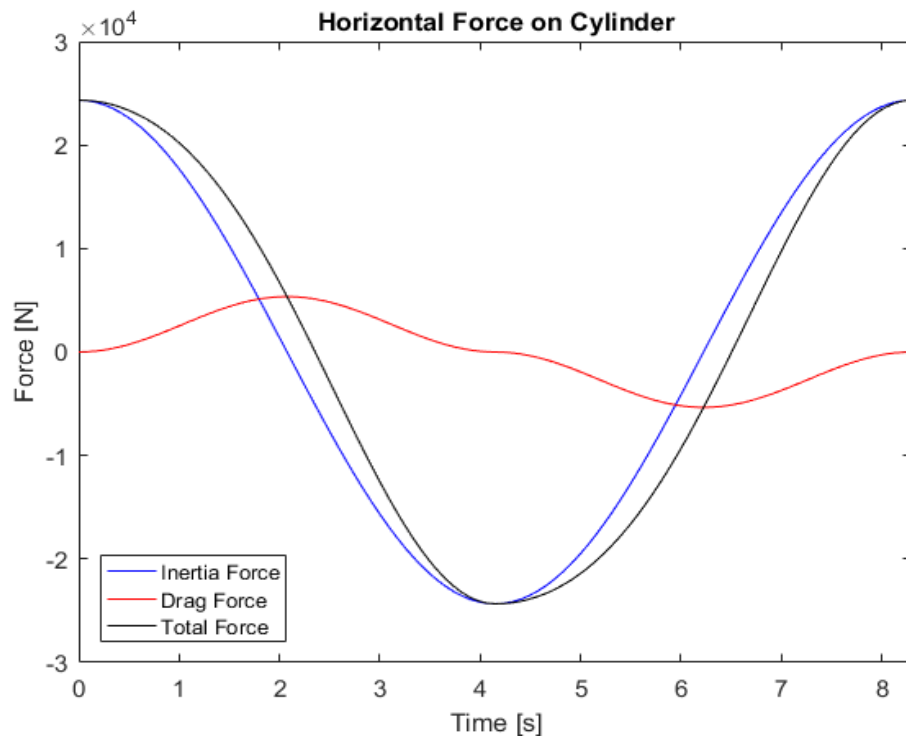


Figure D-19. Horizontal force at top of stroke, wave loading data case 5

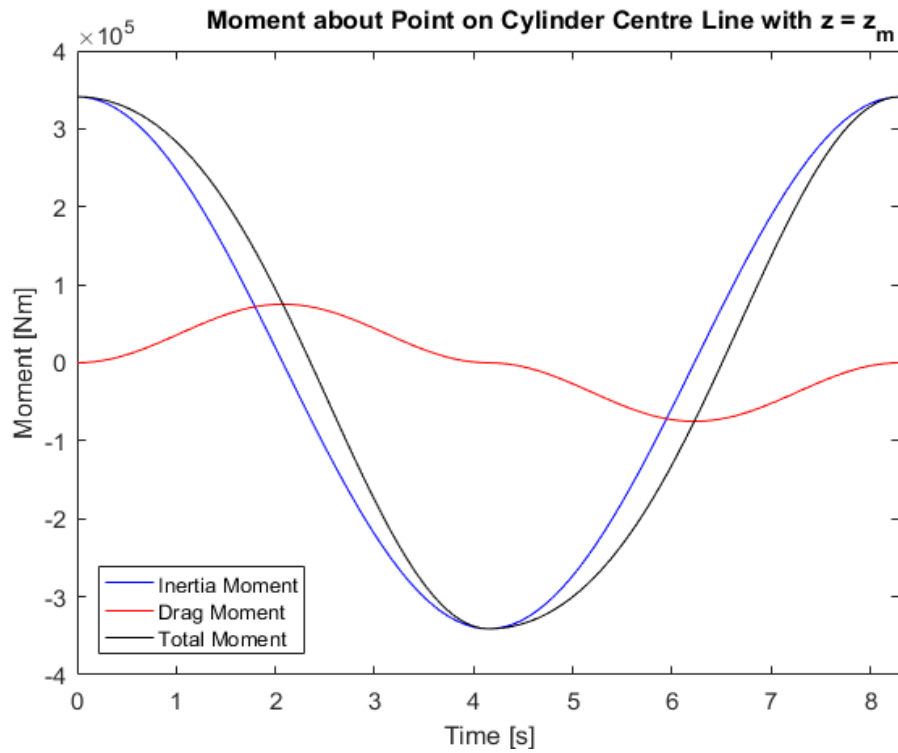


Figure D-20. Momentum about z_m at top of stroke, wave loading data case 5

Wave Loading Case 6: Bottom of stroke. $A = 2.85$ m $T = 9.60$ s

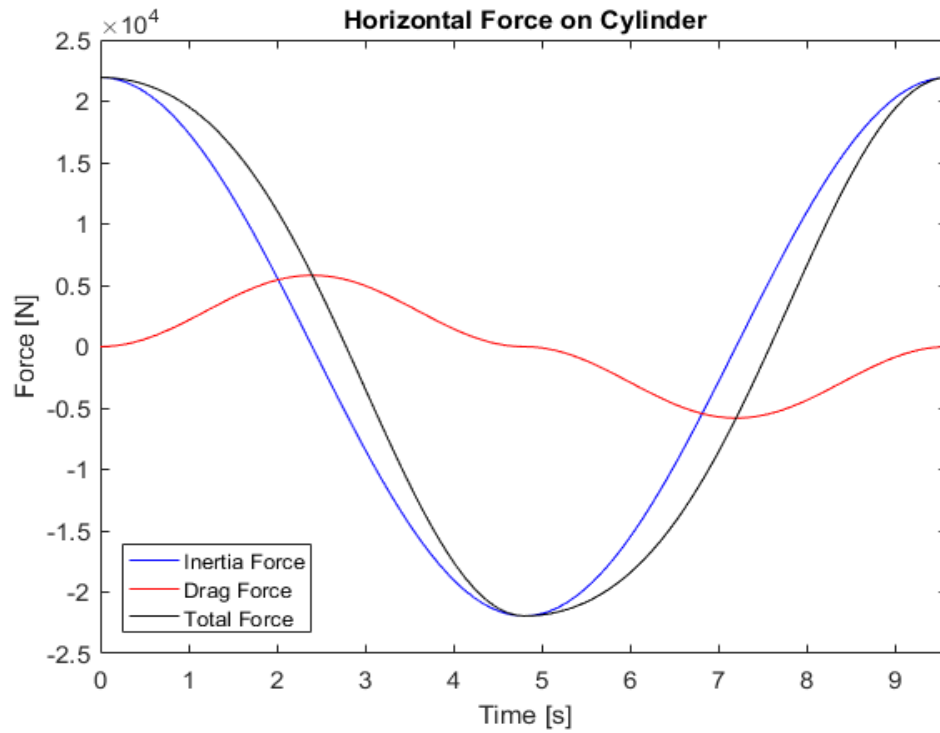


Figure D-21. Horizontal forces at bottom of stroke, wave loading data case 6

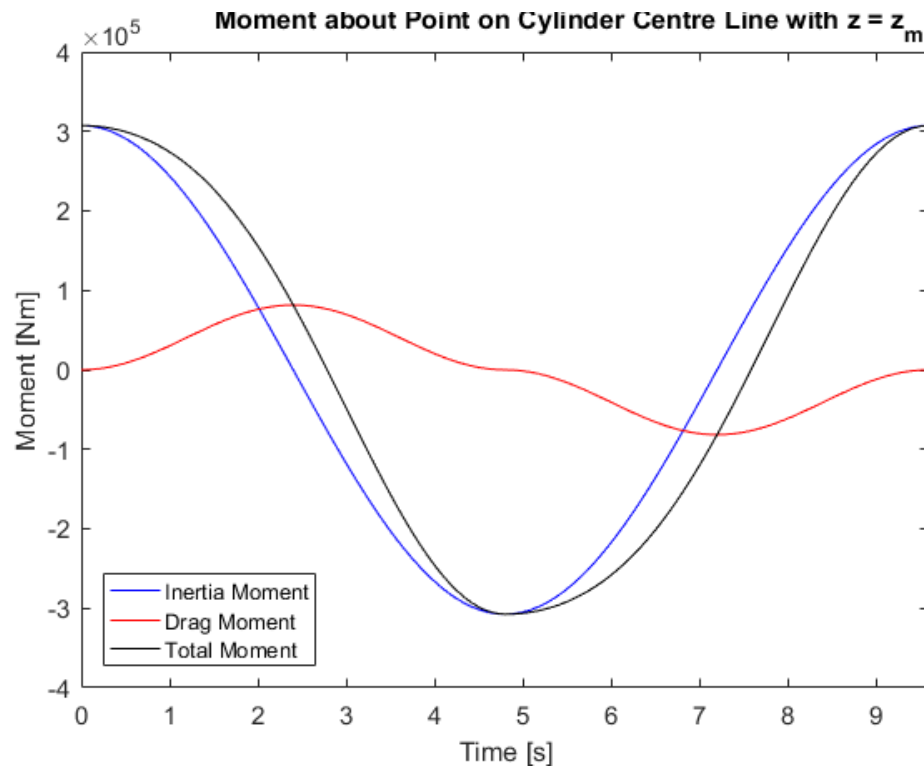


Figure D-22. Momentum about z_m at bottom of stroke, wave loading data case 6

Wave Loading Case 6: Top of stroke. $A = 2.85 \text{ m}$ $T = 9.60 \text{ s}$

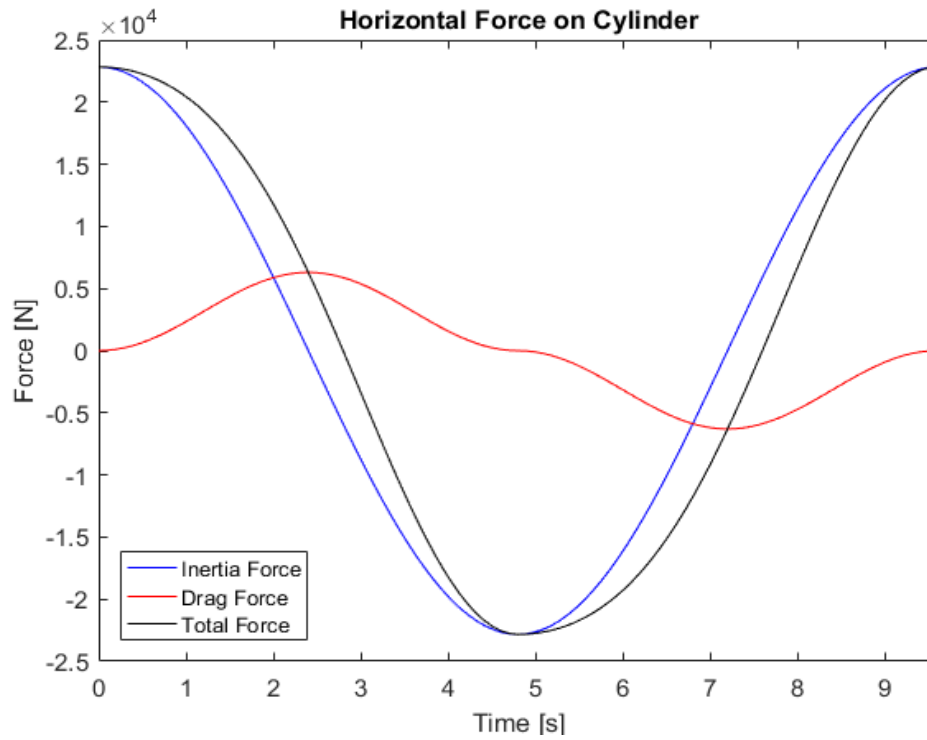


Figure D-23. Horizontal force at top of stroke, wave loading data case 6

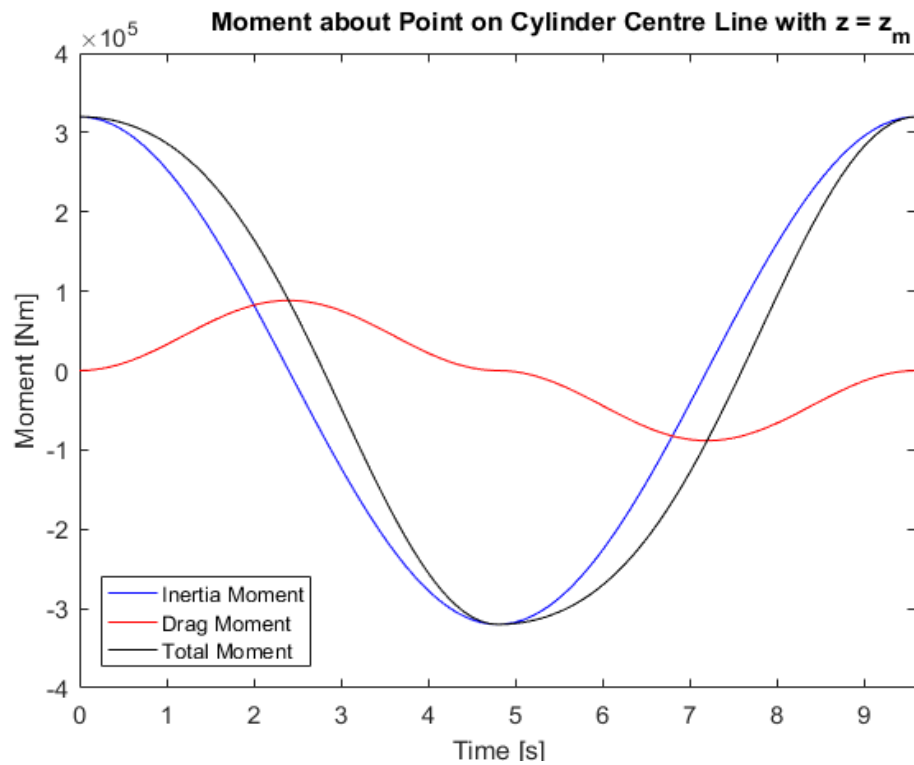


Figure D-24. Momentum about z_m at top of stroke, wave loading data case 6

Appendix E

Additional Coil Experimental Data for Water-Cooled Coil Testing

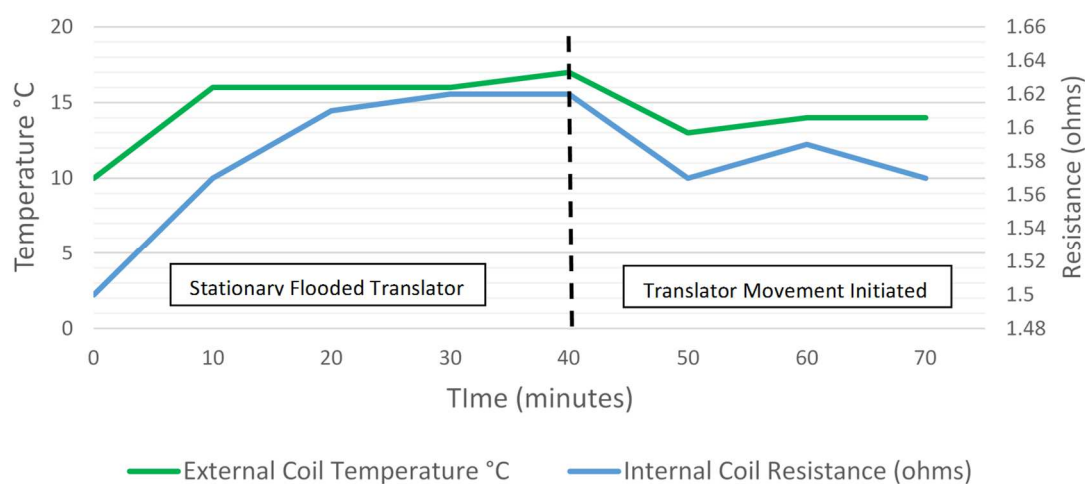


Figure E-1. Enamelled coil translator, submerged in water, 4A per coil

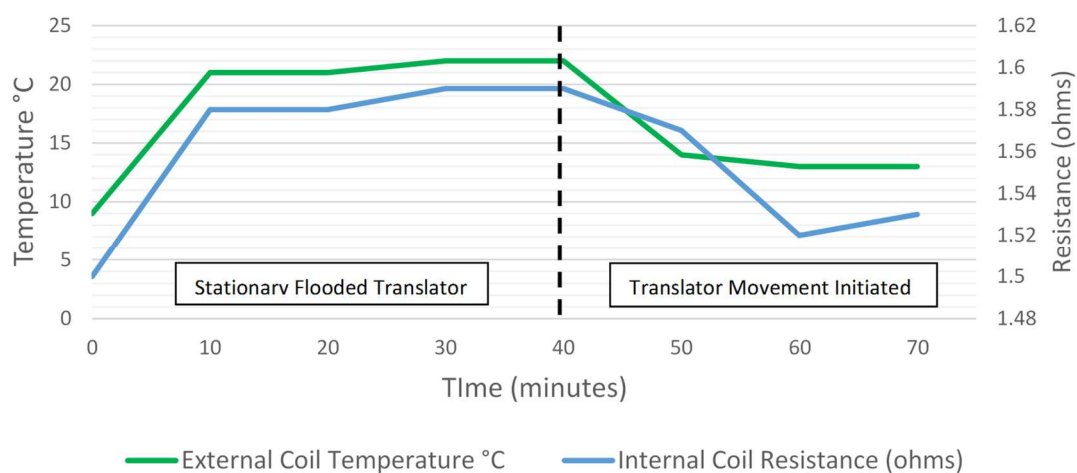


Figure E-2. Epoxy potted coil translator with gaps, submerged in water, 4A per coil

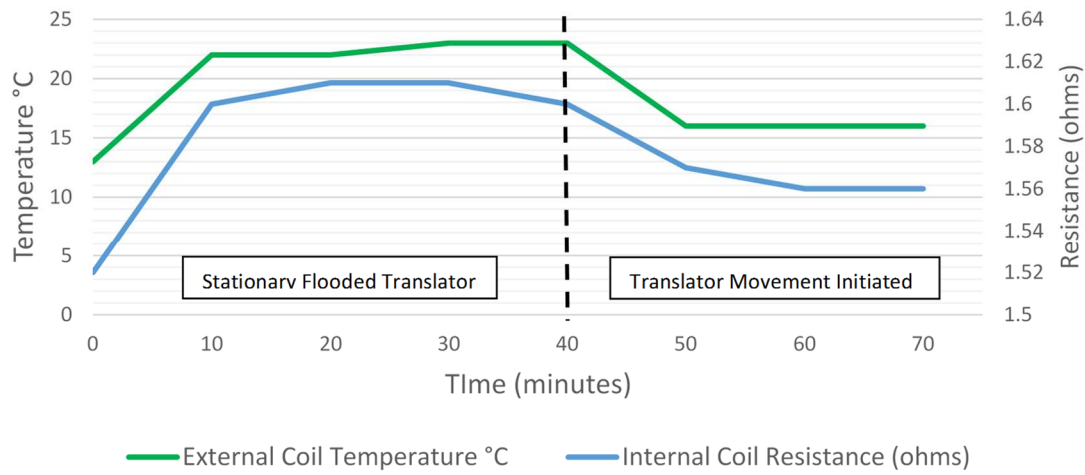


Figure E-3. Epoxy potted coil translator, submerged in water, 4A per coil

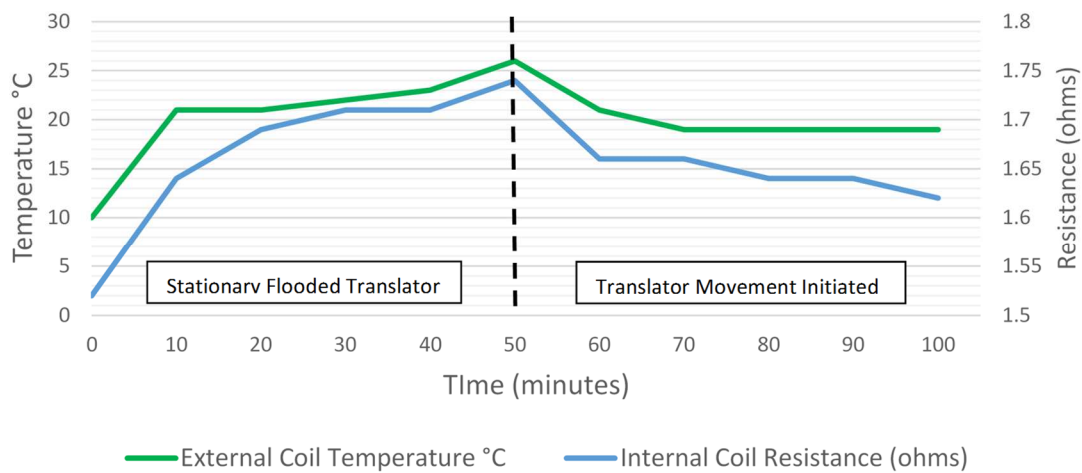


Figure E-4. Enamelled coil translator, submerged in water, 6A per coil

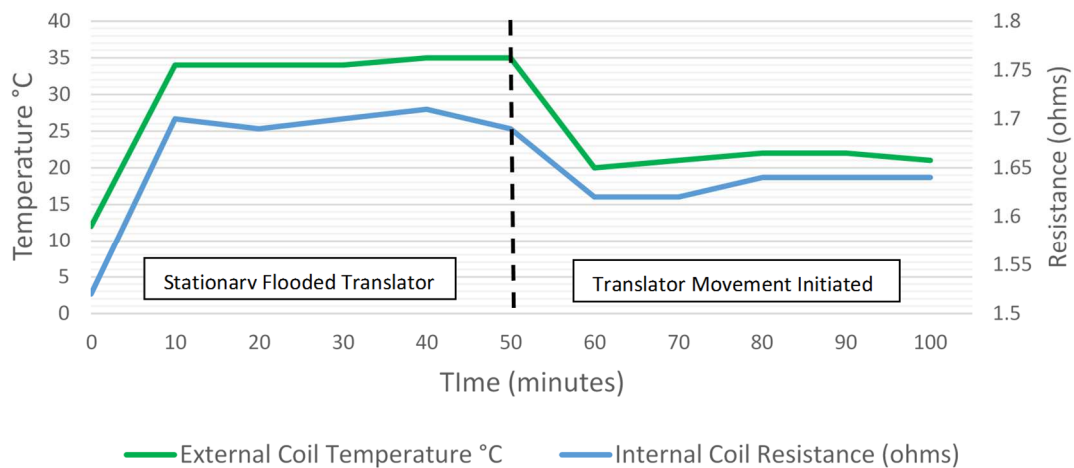


Figure E-5. Epoxy potted coil translator with gaps, submerged in water, 6A per coil

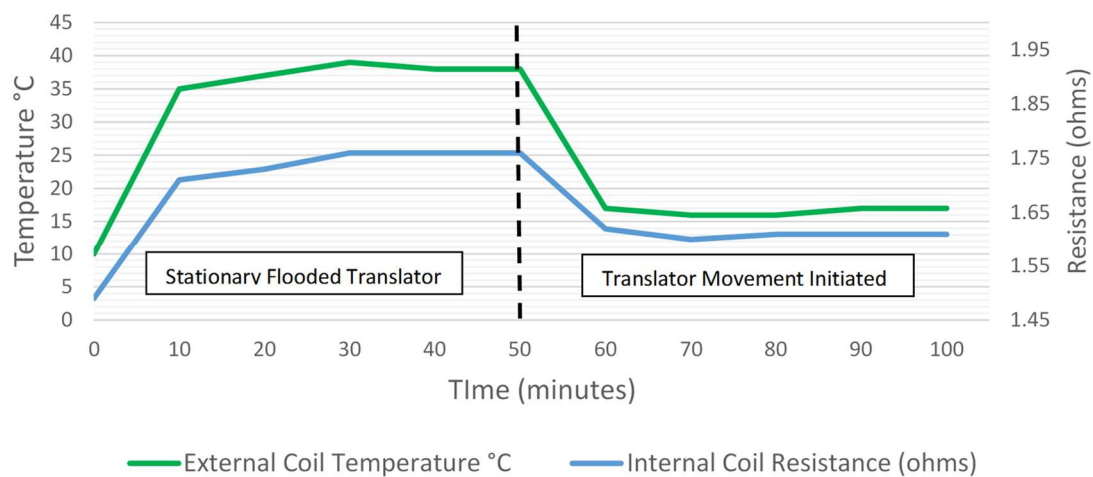


Figure E-6. Epoxy potted coil translator, submerged in water, 6A per coil

References

- [1] bp Global, “Statistical Review of World Energy 2016.” [Online]. Available: <http://www.bp.com/en/global/corporate/energy-economics/statistical-review-of-world-energy.html>. [Accessed: 08-Dec-2016].
- [2] United Nations, “The World at Six Billion,” 1999. [Online]. Available: <http://www.un.org/esa/population/publications/sixbillion/sixbilpart1.pdf>. [Accessed: 30-Jun-2017].
- [3] U.S. Energy Information Administration, “International Energy Outlook 2016: With Projections to 2040,” 2016.
- [4] World Energy Council, “World Energy Resources 2016,” 2016. [Online]. Available: <https://www.worldenergy.org/wp-content/uploads/2016/10/World-Energy-Resources-Full-report-2016.10.03.pdf>. [Accessed: 30-Jun-2018].
- [5] T. J. Price, “James Blyth - Britain’s first modern wind power engineer,” *Wind Eng.*, vol. 29, no. 3, pp. 191–200, 2005.
- [6] J. K. Kaldellis and D. Zafirakis, “The wind energy (r)evolution: A short review of a long history,” *Renew. Energy*, vol. 36, no. 7, pp. 1887–1901, 2011.
- [7] “Vísindavefurinn: Hvenær var vindorka fyrst virkjuð?” [Online]. Available: <https://www.visindavefur.is/svar.php?id=30268>. [Accessed: 31-Jul-2017].
- [8] T. C. Corke and R. C. Nelson, *Wind Energy Design*, 1st Edition. CRC Press, 2018.
- [9] D. A. Rivkin, K. Toomey, and L. Silk, *Wind Turbine Technology and Design*. Jones & Bartlett Learning, 2013.
- [10] N. I. Meyer, “Danish wind power development,” *Energy Sustain. Dev.*, vol. 2, no. 1, pp. 18–25, May 1995.
- [11] “WIND-WORKS: Smith-Putnam Industrial Photos.” [Online]. Available: <http://www.wind-works.org/cms/index.php?id=223>. [Accessed: 31-Jul-2017].

- [12] T. Ackermann and L. Söder, “An overview of wind energy-status 2002,” *Renew. Sustain. Energy Rev.*, vol. 6, pp. 67–128, 2002.
- [13] P. Breeze, “An Introduction to Wind Power,” in *Wind Power Generation*, Elsevier, 2016, pp. 1–8.
- [14] Y. Kumar, J. Ringenberg, S. S. Depuru, V. K. Devabhaktuni, J. W. Lee, E. Nikolaidis, B. Andersen, and A. Afjeh, “Wind energy: Trends and enabling technologies,” *Renew. Sustain. Energy Rev.*, vol. 53, pp. 209–224, 2016.
- [15] M. R. Islam, S. Mekhilef, and R. Saidur, “Progress and recent trends of wind energy technology,” *Renew. Sustain. Energy Rev.*, vol. 21, pp. 456–468, 2013.
- [16] R. Lacal-Arántegui, “Materials use in electricity generators in wind turbines – state-of-the-art and future specifications,” *J. Clean. Prod.*, vol. 87, pp. 275–283, Sep. 2014.
- [17] GWEC, “Global Wind Statistics 2016,” 2017. [Online]. Available: http://www.gwec.net/wp-content/uploads/vip/GWEC_PRstats2016_EN_WEB.pdf. [Accessed: 06-Mar-2017].
- [18] Vestas Wind Systems, “Vestas V66 – 1.75 MW & V66 – 2.0 MW,” p. 5, 2000.
- [19] Wind Energy Market Intelligence, “Enercon E-112/4500,” 2017. [Online]. Available: <http://www.thewindpower.net/scripts/fpdf181/turbine.php?id=462>. [Accessed: 07-Mar-2017].
- [20] REpower Systems SE, “REpower 5MW Wind Turbine Product Brochure.” [Online]. Available: http://www.renugen.co.uk/content/large_wind_turbine_brochures/large_wind_turbine_brochures/repower_5m.pdf. [Accessed: 07-Mar-2017].
- [21] Siemens AG, “Think inside the box: The new SWT-8.0-154,” 2016. [Online]. Available: <http://www.siemens.com/content/dam/internet/siemens-com/global/market-specific-solutions/wind/brochures/siemens-wind-power-offshore-swt-8.0-154-productflyer-web-doublepages.pdf>. [Accessed: 07-Mar-2017].

- [22] Technical University of Denmark, “Danish wind turbine sets new record - DTU Wind Energy,” 2017. [Online]. Available: [http://www.dtu.dk/english/news/dtuavis/nyhed?id=B18A67D1-8911-4460-8499-D9C2AAEB0B3F&utm_device=web&utm_source=RelatedNews&utm_campaign=V](http://www.dtu.dk/english/news/dtuavis/nyhed?id=B18A67D1-8911-4460-8499-D9C2AAEB0B3F&utm_device=web&utm_source=RelatedNews&utm_campaign=Voltage-Sourced-Converter-project-is-finished)oltage-Sourced-Converter-project-is-finished. [Accessed: 07-Mar-2017].
- [23] Wind Energy Market Intelligence, “Adwen AD 8-180,” 2017. [Online]. Available: <http://www.thewindpower.net/scripts/fpdf181/turbine.php?id=1050>. [Accessed: 07-Mar-2017].
- [24] R. Wiser, M. Hand, J. Seel, and B. Paulos, “Reducing Wind Energy Costs through Increased Turbine Size: Is the Sky the Limit?,” *Berkeley Lab*, 2016. [Online]. Available: https://emp.lbl.gov/sites/all/files/scaling_turbines_1.pdf. [Accessed: 07-Mar-2017].
- [25] Siemens plc, “Siemens United Kingdom,” 2017. [Online]. Available: <http://www.siemens.co.uk/en/>. [Accessed: 07-Mar-2017].
- [26] WindEurope, H. Andrew, A. Mbistrova, I. Pineda, and P. Tardie, “The European offshore wind industry Wind - Key trends and statistics 2016,” Wind Europe, 2017.
- [27] P. E. Morthorst and L. Kitzing, “2 – Economics of building and operating offshore wind farms,” in *Offshore Wind Farms*, 2016, pp. 9–27.
- [28] R. Swart, C. Coppens, H. Gordjin, M. Piek, P. Ruysenaars, J. J. Schrande, M. Hoogwijk, M. Papalexandrou, and J. Horalek, *Europe’s onshore and offshore wind energy potential - An assessment of environmental and economic constraints*, vol. 6, no. 6. European Environment Agency, 2009.
- [29] “World’s First Offshore Wind Farm Passes into History | Offshore Wind.” [Online]. Available: <http://www.offshorewind.biz/2017/03/15/worlds-first-offshore-wind-farm-passes-into-history/>. [Accessed: 17-Apr-2017].
- [30] R. McKenna, P. Ostman v.d. Leye, and W. Fichtner, “Key challenges and prospects for large wind turbines,” *Renew. Sustain. Energy Rev.*, vol. 53, pp. 1212–1221, 2016.
- [31] H. Polinder, J. A. Ferreira, B. B. Jensen, A. B. Abrahamsen, K. Atallah, and R. A. McMahon, “Trends in Wind Turbine Generator Systems,” *IEEE J. Emerg. Sel. Top. Power Electron.*, vol. 1, no. 3, pp. 174–185, Sep. 2013.

- [32] E. I. Konstantinidis and P. N. Botsaris, “Wind turbines: current status, obstacles, trends and technologies,” *IOP Conf. Ser. Mater. Sci. Eng.*, vol. 161, p. 012079, Nov. 2016.
- [33] Tide Mill Institute, “Definition of a Tide Mill.” [Online]. Available: <http://www.tidemillinstitute.org/33.html>. [Accessed: 19-Apr-2017].
- [34] T. J. Hammons, “Tidal power,” *Proc. IEEE*, vol. 81, no. 3, pp. 419–433, Mar. 1993.
- [35] I.G. Bryden & R.M. Taylor & T.W. Thorpe, “2010 Survey of Energy Resources.” World Energy Council, p. 618, 2010.
- [36] R. Pelc and R. M. Fujita, “Renewable energy from the ocean,” *Mar. Policy, Elsevier Sci. Ltd*, vol. 26, pp. 471–479, 2002.
- [37] “The first known wave energy patent (1799) - WavePowerLab.” [Online]. Available: <http://wavepowerlab.weebly.com/blog/the-first-known-patent-1799>. [Accessed: 20-Apr-2017].
- [38] S. Lindroth and M. Leijon, “Offshore wave power measurements—A review,” *Renew. Sustain. Energy Rev.*, vol. 15, no. 9, pp. 4274–4285, 2011.
- [39] M. A. U. Amir, R. M. Sharip, M. A. Muzanni, and H. A. Anuar, “Wave energy convertors (WEC): A review of the technology and power generation,” 2016, p. 16.
- [40] J. Cordonnier, F. Gorintin, A. De Cagny, A. H. Clément, and A. Babarit, “SEAREV: Case study of the development of a wave energy converter,” *Renew. Energy*, vol. 80, pp. 40–52, 2015.
- [41] J. Wolfram, “On Assessing the Reliability and Availability of Marine Energy Converters: The Problems of a New Technology,” *Proc. Inst. Mech. Eng. Part O J. Risk Reliab.*, vol. 220, no. 1, pp. 55–68, Jan. 2006.
- [42] A. Uihlein and D. Magagna, “Wave and tidal current energy – A review of the current state of research beyond technology,” *Renew. Sustain. Energy Rev.*, vol. 58, pp. 1070–1081, 2016.

- [43] J. Widén, N. Carpman, V. Castellucci, D. Lingfors, J. Olauson, F. Remouit, M. Bergkvist, M. Grabbe, and R. Waters, “Variability assessment and forecasting of renewables: A review for solar, wind, wave and tidal resources,” *Renew. Sustain. Energy Rev.*, vol. 44, pp. 356–375, 2015.
- [44] P. Breeze, “The Anatomy of a Wind Turbine,” in *Wind Power Generation*, Elsevier, 2016, pp. 19–27.
- [45] P. Breeze, “Offshore Wind,” in *Wind Power Generation*, Elsevier, 2016, pp. 75–84.
- [46] NHD-INFO, H. Pettersen, and Statoil, “Sheringham Shoal Wind Farm 2012,” 2012. [Online]. Available: <https://www.flickr.com/photos/nhd-info/8033151828/>. [Accessed: 20-Jun-2017].
- [47] P. Greaves, “Design of offshore wind turbine blades,” in *Offshore Wind Farms*, Elsevier, 2016, pp. 105–135.
- [48] Nenuphar Wind and Kirt.Thompson, “Nenuphar Wind. Floating Offshore Wind Power.,” 2017. [Online]. Available: <http://www.nenuphar-wind.com/en/actualites.html>. [Accessed: 01-Jun-2017].
- [49] W. Haans, L. Blonk, E. Echavarria, and P. G. Gardner for Garrad Hassan, “Offshore wind turbine market developments in The Netherlands,” 2015.
- [50] S. Marcacci, “Offshore Wind Industry Will Become €130 Billion Annual Market By 2020,” 2013. [Online]. Available: <https://cleantechnica.com/2013/05/08/offshore-wind-industry-will-become-e130-billion-annual-market-by-2020/>. [Accessed: 20-Apr-2017].
- [51] Suprapower, “Report on the test results of an MgB2 coil for a 10MW wind generator,” 2015. [Online]. Available: <http://www.suprapower-fp7.eu/docs.php?pag=3>.
- [52] DTU, “Superconducting generator for large wind turbines - DTU Orbit.” [Online]. Available: [http://orbit.dtu.dk/en/projects/superconducting-generator-for-large-wind-turbines\(ba77a1d8-8190-4cdc-85fc-8efd51746a84\).html](http://orbit.dtu.dk/en/projects/superconducting-generator-for-large-wind-turbines(ba77a1d8-8190-4cdc-85fc-8efd51746a84).html). [Accessed: 08-Jul-2017].
- [53] EcoSwing Consortium, “EcoSwing.” [Online]. Available: <https://ecoswing.eu/project>. [Accessed: 09-Jul-2017].

- [54] Sandia National Laboratories; “News Releases : Enormous blades could lead to more offshore energy in U.S.” [Online]. Available: https://share-ng.sandia.gov/news/resources/news_releases/big_blades/#.WXN8oITys-V. [Accessed: 22-Jul-2017].
- [55] M. Ma, “THE 10 BIGGEST TURBINES IN THE WORLD,” *Pulse, LinkedIn*. [Online]. Available: <https://www.linkedin.com/pulse/10-biggest-turbines-world-michael-ma>. [Accessed: 22-Jul-2017].
- [56] P. Breeze, “The Wind Energy Resource,” in *Wind Power Generation*, Elsevier, 2016, pp. 9–17.
- [57] R. Gobato, A. Gobato, and D. F. G. Fedrigo, “Study Pelamis system to capture energy of ocean wave,” p. 31, Aug. 2015.
- [58] A.M Cornett, “A Global Wave Energy Resource Assessment,” *Sea Technol.*, vol. 50, no. 4, p. 10, 2008.
- [59] Polly Hunter, “If the wind blows hard enough (speed) and long enough (duration) over a long enough area (fetch), waves become fully developed. - Power Point Presentation.” [Online]. Available: <http://slideplayer.com/slide/9852935/>. [Accessed: 22-Jul-2017].
- [60] M. J. Tucker and E. G. Pitt, *Waves in Ocean Engineering, Volume 5*. Elsevier Science, 2001.
- [61] B. Drew, A. R. Plummer, and M. N. Sahinkaya, “A review of wave energy converter technology,” *Proc. Inst. Mech. Eng. Part A J. Power Energy*, vol. 223, no. 8, pp. 887–902, Dec. 2009.
- [62] K. Gunn and C. Stock-Williams, “Quantifying the global wave power resource,” *Renew. Energy*, vol. 44, pp. 296–304, 2012.
- [63] Ingvald Straume, “Global wave power estimates.” [Online]. Available: <https://commons.wikimedia.org/w/index.php?curid=31768763>. [Accessed: 25-Feb-2017].
- [64] D. V. Evans, “A theory for wave-power absorption by oscillating bodies,” *J. Fluid Mech.*, vol. 77, no. 01, p. 1, Sep. 1976.

- [65] G. Lavidas, V. Venugopal, and D. Friedrich, "Wave energy extraction in Scotland through an improved nearshore wave atlas," *Int. J. Mar. Energy*, vol. 17, pp. 64–83, 2017.
- [66] S. P. Neill, M. R. Hashemi, and M. J. Lewis, "Tidal energy leasing and tidal phasing," *Renew. Energy*, vol. 85, pp. 580–587, Jan. 2016.
- [67] H. Polinder and M. Scuotto, "Wave energy converters and their impact on power systems," in *2005 International Conference on Future Power Systems*, 2005, vol. 5, no. 4, p. 9 pp.-9.
- [68] J. Twidell and T. Weir, *Renewable Energy Resources*, Second Edition. Taylor & Francis, 2006.
- [69] European Marine Energy Centre, "Wave developers," 2017. [Online]. Available: <http://www.emec.org.uk/marine-energy/wave-developers/>. [Accessed: 25-Feb-2017].
- [70] N. Khan, A. Kalair, N. Abas, and A. Haider, "Review of ocean tidal, wave and thermal energy technologies," *Renew. Sustain. Energy Rev.*, vol. 72, pp. 590–604, 2017.
- [71] Seabased, "Gallery." [Online]. Available: <http://www.seabased.com/en/newsroom/gallery/category/2-park>. [Accessed: 31-Jul-2017].
- [72] K. Koca, A. Kortenhaus, H. Oumeraci, B. Zanuttigh, and E. Angelelli, "Recent Advances in the Development of Wave Energy Converters," in *The 10th European Wave and Tidal Energy Conference, Aalborg, Denmark*, 2013, p. 7.
- [73] N. Owano, "Oceanlinx celebrates wave-power unit launch in Australia." [Online]. Available: <https://phys.org/news/2013-11-oceanlinx-celebrates-wave-power-australia.html>. [Accessed: 31-Jul-2017].
- [74] "Aquamarine launches Oyster wave machine that could power 1400 homes by 2011." [Online]. Available: <http://drprem.com/green/aquamarine-launches-oyster-wave-machine-that-could-power-1400-homes-by-2011>. [Accessed: 31-Jul-2017].
- [75] "Wave Dragon." [Online]. Available: <http://www.wavedragon.net/>. [Accessed: 31-Jul-2017].

- [76] Power Engineering International, “AWS and Trident Energy collaborate on new innovative wave energy device.” [Online]. Available: <http://www.powerengineeringint.com/articles/2016/10/aws-and-trident-energy-collaborate-on-new-innovative-wave-energy-device.html>. [Accessed: 31-Jul-2017].
- [77] Tidal Energy Today, “Penguin wave energy converter completes third test season.” [Online]. Available: <http://tidalenergytoday.com/2014/12/10/penguin-wave-energy-converter-completes-third-test-season/>. [Accessed: 31-Jul-2017].
- [78] Atlantis Resources, “Estimate of global potential tidal resources | Tidal Energy Today.” [Online]. Available: <http://tidalenergytoday.com/2015/02/17/estimate-of-global-potential-tidal-resources/>. [Accessed: 25-Feb-2017].
- [79] European Marine Energy Centre, “Tidal developers,” 2017. [Online]. Available: <http://www.emec.org.uk/marine-energy/tidal-developers/>. [Accessed: 25-Feb-2017].
- [80] University of Strathclyde, “Tidal Energy - Tidal Stream Energy.” [Online]. Available: http://www.esru.strath.ac.uk/EandE/Web_sites/10-11/Tidal/tidal.html. [Accessed: 31-Jul-2017].
- [81] “Hydrovolts: The Hydrovolts Turbine.” [Online]. Available: <http://hydrovolts.blogspot.co.uk/2009/04/hydrovolts-turbine.html>. [Accessed: 31-Jul-2017].
- [82] “OpenHydro.” [Online]. Available: <http://www.openhydro.com/>. [Accessed: 23-Jul-2017].
- [83] JupiterHydro, “A Bit Of History On Jupiter’s Technology.” [Online]. Available: <http://www.jupiterhydro.com/technology>. [Accessed: 31-Jul-2017].
- [84] “Underwater kites: a new generation of tidal power.” [Online]. Available: <http://www.futuretimeline.net/blog/2013/12/3.htm#.WX-SvYTys-U>. [Accessed: 31-Jul-2017].
- [85] A. Kurniawan, E. Pedersen, and T. Moan, “Bond graph modelling of a wave energy conversion system with hydraulic power take-off,” *Renew. Energy*, vol. 38, no. 1, pp. 234–244, Feb. 2012.

- [86] S. Yagi and N. Ninoyu, "Technical Trends in Wind Turbine Bearings," *NTN Technical Review* No.76, 2008. [Online]. Available: http://www.ntn.co.jp/english/products/review/pdf/NTN_TR76_en_p113_120.pdf. [Accessed: 25-Jun-2018].
- [87] P. Takoutsing, R. Wamkeue, M. Ouhrouche, F. Slaoui-Hasnaoui, T. Tameghe, and G. Ekemb, "Wind Turbine Condition Monitoring: State-of-the-Art Review, New Trends, and Future Challenges," *Energies*, vol. 7, no. 4, pp. 2595–2630, Apr. 2014.
- [88] M. D. Reder, E. Gonzalez, and J. J. Melero, "Wind Turbine Failures - Tackling current Problems in Failure Data Analysis," *J. Phys. Conf. Ser.*, vol. 753, p. 072027, Sep. 2016.
- [89] J. M. Pinar Pérez, F. P. García Márquez, A. Tobias, and M. Papaelias, "Wind turbine reliability analysis," *Renew. Sustain. Energy Rev.*, vol. 23, pp. 463–472, 2013.
- [90] J. Carroll, A. McDonald, and D. McMillan, "Failure rate, repair time and unscheduled O&M cost analysis of offshore wind turbines," *Wind Energy*, vol. 19, no. 6, pp. 1107–1119, Jun. 2016.
- [91] J. Igba, K. Alemzadeh, C. Durugbo, and K. Henningsen, "Performance assessment of wind turbine gearboxes using in-service data: Current approaches and future trends," *Renew. Sustain. Energy Rev.*, vol. 50, pp. 144–159, 2015.
- [92] A. Têtu, "Power Take-Off Systems for WECs," Springer International Publishing, 2017, pp. 203–220.
- [93] A. M. Ragheb and M. Ragheb, "Wind Turbine Gearbox Technologies," in *Fundamental and Advanced Topics in Wind Power*, R. Carriveau, Ed. Rijeka: InTech, 2011.
- [94] B. Maples, M. Hand, and W. Musial, "Comparative Assessment of Direct Drive High Temperature Superconducting Generators in Multi-Megawatt Class Wind Turbines," 2010.
- [95] A. Zavvos, "Structural Optimisation of Permanent Magnet Direct Drive Generators for 5MW Wind Turbines," University of Edinburgh. Thesis available: <https://www.era.lib.ed.ac.uk/handle/1842/8299>, 2013.

- [96] R. Budny, “Why Wind Turbine Gearboxes Fail, How Failures Can Be Prevented,” *LinkedIn*. [Online]. Available: <https://www.linkedin.com/pulse/why-wind-turbine-gearboxes-fail-how-failures-can-prevented-rob-budny>. [Accessed: 09-Jul-2017].
- [97] A. Ragheb and M. Ragheb, “Wind turbine gearbox technologies,” in *2010 1st International Nuclear & Renewable Energy Conference (INREC)*, 2010, pp. 1–8.
- [98] R. Scott Semken, M. Polikarpova, P. R  ytt  , J. Alexandrova, J. Pyrh  nen, J. Nerg, A. Mikkola, and J. Backman, “Direct-drive permanent magnet generators for high-power wind turbines: benefits and limiting factors,” *IET Renew. Power Gener.*, vol. 6, no. 1, p. 1, 2012.
- [99] Tobias Schulze, “Powerful analysis of wind turbine gearboxes - Power Transmission World.” [Online]. Available: <http://www.powertransmissionworld.com/powerful-analysis-of-wind-turbine-gearboxes/>. [Accessed: 21-Jul-2017].
- [100] J. Peel, “Worlds largest wind turbine gearbox as part of a an Integrated Drive System,” 2016. [Online]. Available: <https://www.linkedin.com/pulse/worlds-largest-wind-turbine-gearbox-part-siemens-fully-jason-peel>. [Accessed: 25-Mar-2017].
- [101] S. Funke, “The world’s biggest wind turbine gearbox | Offshore Wind Industry,” 2016. [Online]. Available: <http://www.offshorewindindustry.com/news/worlds-biggest-wind-turbine-gearbox>. [Accessed: 16-Apr-2017].
- [102] E. F. Aune, H. Lind, and G. Muller, “A reflection on the use of A3 architecture overview in designing Wave Energy Converters,” in *2016 11th System of Systems Engineering Conference (SoSE)*, 2016, pp. 1–6.
- [103] CorPower Ocean, “The CorPower Wave Energy Converter,” 2012. [Online]. Available: <http://www.corpowerocean.com/corpower-technology/corpower-wave-energy-converter/>. [Accessed: 27-Jun-2017].
- [104] J. Gaspar, M. Calvario, M. Kamarlouei, and C. Guedes Soares, “Power take-off concept for wave energy converters based on oil-hydraulic transformer units,” *Renew. Energy*, vol. 86, pp. 1232–1246, Feb. 2016.
- [105] R. Yemm, D. Pizer, C. Retzler, and R. Henderson, “Pelamis: experience from concept to connection,” *Philos. Trans. R. Soc. A Math. Phys. Eng. Sci.*, 2012.

- [106] Y. Lin, J. Bao, H. Liu, W. Li, L. Tu, and D. Zhang, “Review of hydraulic transmission technologies for wave power generation,” *Renew. Sustain. Energy Rev.*, vol. 50, pp. 194–203, Oct. 2015.
- [107] N. F. B. Diepeveen Duwind, “Design Considerations for a Wind - Powered Seawater Pump,” in *European Offshore Wind Conference Proceedings*, 2009.
- [108] Y. Zhang, X. Kong, L. Hao, and C. Ai, “Controls of Hydraulic Wind Turbine,” *MATEC Web Conf.*, vol. 40, p. 08002, Jan. 2016.
- [109] B. Skaare, B. Hörnsten, and F. G. Nielsen, “Energy Considerations for Wind Turbines with Hydraulic Transmission Systems,” in *Offshore Wind, EWE Proc.*, 2011.
- [110] P. Silva, A. Giuffrida, N. Fergnani, E. Macchi, M. Cantù, R. Suffredini, M. Schiavetti, and G. Gigliucci, “Performance prediction of a multi-MW wind turbine adopting an advanced hydrostatic transmission,” *Energy*, vol. 64, pp. 450–461, 2014.
- [111] “UK: MHI Testing Digital Hydraulic Drive Train for OW Turbines | Offshore Wind.” [Online]. Available: <http://www.offshorewind.biz/2015/02/05/uk-mhi-testing-digital-hydraulic-drive-train-for-ow-turbines/>. [Accessed: 19-Jul-2017].
- [112] ENERCON, “Brochure Technology & Services,” 2016. [Online]. Available: https://www.enercon.de/fileadmin/Redakteur/.../ENERCON_TuS_en_06_2015.pdf. [Accessed: 26-May-2018].
- [113] Tocardo Tidal Power, “Offshore Solutions.” [Online]. Available: <http://www.tocardo.com/solutions/offshore/>. [Accessed: 31-Jul-2017].
- [114] Alstom, “Press Release Alstom - Co-operation with Belwind.” [Online]. Available: <http://www.alstom.com/press-centre/2011/3/2011-03-15-Cooperation-with-Belwind/>. [Accessed: 23-Jul-2017].
- [115] M. Prado and H. Polinder, “9 – Case study of the Archimedes Wave Swing (AWS) direct drive wave energy pilot plant,” in *Electrical Drives for Direct Drive Renewable Energy Systems*, 2013, pp. 195–218.
- [116] “TiPA-H2020 Project | Tidal Turbine.” [Online]. Available: <http://www.tipa-h2020.eu/tipa-project/>. [Accessed: 31-Jul-2017].

- [117] N. Hodgins, A. S. McDonald, J. Shek, O. Keysan, and M. A. Mueller, "Current and Future Developments of the C-GEN Lightweight Direct Drive Generator for Wave & Tidal Energy," in *Proceedings of the 8th European Wave and Tidal Energy Conference*, 2009.
- [118] M. Whittle, "Wind Turbine Generator Reliability: An Exploration of the Root Causes of Generator Bearing Failures," Durham University. Available at Durham E-Theses Online: <http://etheses.dur.ac.uk/9422/>, 2013.
- [119] S. Caraher, "Bearing options, including design and testing, for direct drive linear generators in wave energy converters," University of Edinburgh. Thesis available: <https://www.era.lib.ed.ac.uk/handle/1842/5740>, 2011.
- [120] C. Bianchini, F. Immovilli, M. Cocconcelli, R. Rubini, and A. Bellini, "Fault Detection of Linear Bearings in Brushless AC Linear Motors by Vibration Analysis," *IEEE Trans. Ind. Electron.*, vol. 58, no. 5, pp. 1684–1694, May 2011.
- [121] G. Shrestha, H. Polinder, D.-J. Bang, and J. A. Ferreira, "Structural Flexibility: A Solution for Weight Reduction of Large Direct-Drive Wind-Turbine Generators," *IEEE Trans. Energy Convers.*, vol. 25, no. 3, pp. 732–740, 2010.
- [122] D. H. N. Dias, E. S. Motta, G. G. Sotelo, R. de Andrade, R. M. Stephan, L. Kuehn, O. de Haas, and L. Schultz, "Simulations and Tests of Superconducting Linear Bearings for a MAGLEV Prototype," *IEEE Trans. Appl. Supercond.*, vol. 19, no. 3, pp. 2120–2123, Jun. 2009.
- [123] Thordon Bearings, "Engineering Manual Version E2006.1." [Online]. Available: http://thordonbearings.com/system/documents/documents/32/original/Engineering_Manual.pdf?1278591800. [Accessed: 24-Jun-2018].
- [124] M. Gustavo and P. Enrique, "Modelling and Control Design of Pitch-Controlled Variable Speed Wind Turbines," in *Wind Turbines*, InTech, 2011.
- [125] Y. Feng, P. J. Tavner, and H. Long, "Early experiences with UK round 1 offshore wind farms," *Proc. Inst. Civ. Eng. - Energy*, vol. 163, no. 4, pp. 167–181, Nov. 2010.
- [126] "AMSC." [Online]. Available: http://www.amscom.com/solutions-products/marine_solutions.html. [Accessed: 01-Aug-2017].

- [127] S. S. Kalsi, B. B. Gamble, G. Snitchler, and S. O. Ige, "The status of HTS ship propulsion motor developments," in *2006 IEEE Power Engineering Society General Meeting*, 2006, p. 5 pp.
- [128] AMSC, "AMSC and Northrop Grumman Announce Successful Load Testing of 36.5 Megawatt Superconductor Ship Propulsion Motor (NASDAQ:AMSC)." [Online]. Available: <http://ir.amsc.com/releasedetail.cfm?ReleaseID=642770>. [Accessed: 01-Aug-2017].
- [129] K. Mostafa, "Direct Drive Wind Turbines: The Effect of Unbalanced Magnetic Pull on Permanent Magnet Generators and Bearing Arrangements," University of Edinburgh. Thesis available: <https://www.era.lib.ed.ac.uk/handle/1842/31360>, 2017.
- [130] W. Wu, V. S. Ramsden, T. Crawford, and G. Hill, "A low speed, high-torque, direct-drive permanent magnet generator for wind turbines," *Industry Applications Conference, 2000. Conference Record of the 2000 IEEE*, vol. 1. pp. 147–154 vol.1, 2000.
- [131] T. Heikkilä, "Permanent Magnet Synchronous Motor for Industrial Inverter Applications - Analysis and Design," Lappeenranta University of Technology, Finland, 2002.
- [132] A. Parviainen, "Design of Axial-Flux Permanent-Magnet Low-Speed Machines and Performance Comparison between Radial-Flux and Axial-Flux Machines," Ph.D Thesis, Lappeenranta University of Technology, Lappeenranta, Finland, 2005.
- [133] Y. Chen, P. Pillay, and A. Khan, "PM wind generator topologies," *Industry Applications, IEEE Transactions on*, vol. 41, no. 6. pp. 1619–1626, 2005.
- [134] Y. Chen and P. Pillay, "Axial-flux PM wind generator with a soft magnetic composite core," *Industry Applications Conference, 2005. Fourtieth IAS Annual Meeting. Conference Record of the 2005*, vol. 1. p. 231–237 Vol. 1, 2005.
- [135] C. Boccaletti, S. Elia, and E. Nistico, "Deterministic and stochastic optimisation algorithms in conventional design of axial flux PM machines," *Power Electronics, Electrical Drives, Automation and Motion, 2006. SPEEDAM 2006. International Symposium on*. pp. 111–115, 2006.

- [136] “Boulder Wind Power Testing.” [Online]. Available: <http://www.boulderwindpower.com/testing/>. [Accessed: 01-Aug-2017].
- [137] E. Spooner, “Lightweight, ironless-stator, PM generators for direct-drive wind turbines,” in *Second IEE International Conference on Power Electronics, Machines and Drives*, 2004, vol. 2004, pp. v1-29-v1-29.
- [138] H. Weh, H. Hoffman, and J. Landrath, “New Permanent Magnet Excited Synchronous Machine with High Efficiency at Low Speeds,” in *Int. Conf. Elec. Machines*, 1988, p. pp 35-40.
- [139] D. Bang and H. Polinder, “Review of generator systems for direct-drive wind turbines,” *Eur. Wind Energy ...*, pp. 1–11, 2008.
- [140] H. Polinder, G. Shrestha, J. A. Ferreira, D. J. Bang, H. Polinder, G. Shresth, and J. A. Ferreira, “Comparative design of radial and transverse flux PM generators for direct-drive wind turbines,” *2008 18th Int. Conf. Electr. Mach.*, pp. 1–6, Sep. 2008.
- [141] M. R. J. Dubois, “Optimized Permanent Magnet Generator Topologies for Direct-Drive Wind Turbines,” Technische Universiteit Delft, 2004.
- [142] A. S. McDonald, “Structural analysis of low speed, high torque electrical generators for direct drive renewable energy converters,” University of Edinburgh. Thesis available: <https://www.era.lib.ed.ac.uk/handle/1842/12608>, 2008.
- [143] D. Bang, “Design of Transverse Flux Permanent Magnet Machines for Large Direct-Drive Wind Turbines,” Technische Universiteit Delft. Thesis available: <https://repository.tudelft.nl/.../uuid%3Ac6867c53-fc10-468d-b6d7-082b7a052f4b>, 2010.
- [144] L. Sethuraman, “Hydrodynamics and drive-train dynamics of a direct-drive floating wind turbine,” University of Edinburgh. Thesis available: <https://www.era.lib.ed.ac.uk/handle/1842/9701>, 2014.
- [145] Y. G. Guo, J. G. Zhu, and V. S. Ramsden, “Calculation of Cogging Torque in Claw Pole Permanent Magnet Motors,” in *Proceeding of Australasian Universities Power Engineering Conference*, pp. 343–347.

- [146] D. Zarko, D. Ban, and T. A. Lipo, “Analytical Solution for Cogging Torque in Surface Permanent-Magnet Motors Using Conformal Mapping,” *IEEE Trans. Magn.*, vol. 44, no. 1, pp. 52–65, Jan. 2008.
- [147] E. Buckingham, “The Theory of the Hampson Liquefier,” *Bull. Bur. Stand.*, vol. 6, no. S123, pp. 125–147, 1909.
- [148] D. van Delft and P. Kes, “The discovery of Superconductivity,” *Physics Today*. American Institute of Physics, pp. 38–42, 2010.
- [149] D. van Delft, “History and significance of the discovery of superconductivity by Kamerlingh Onnes in 1911,” *Phys. C Supercond.*, vol. 479, pp. 30–35, 2012.
- [150] “Heike Kamerlingh Onnes - Facts,” *Nobel Media AB*, 2014. [Online]. Available: https://www.nobelprize.org/nobel_prizes/physics/laureates/1913/annes-facts.html. [Accessed: 08-Mar-2017].
- [151] P. J. Ray, “Master’s thesis: Structural investigation of $\text{La}_{2-x}\text{Sr}_x\text{CuO}_{4+y}$ - Following staging as a function of temperature,” University of Copenhagen, 2016.
- [152] Open University, “The critical temperature T_c of various superconductors plotted against their discovery date. - OpenLearn.” [Online]. Available: http://www.open.edu/openlearn/ocw/mod/oucontent/view.php?id=2685&extra=thumbnail_idp2967152#. [Accessed: 01-Jul-2017].
- [153] H. K. Moudgil, *Textbook of Physical Chemistry*, 2nd Edition. Prentice-Hall of India Pvt.Ltd, 2014.
- [154] G. W. Webb, F. Marsiglio, and J. E. Hirsch, “Superconductivity in the elements, alloys and simple compounds,” *Phys. C Supercond. its Appl.*, vol. 514, pp. 17–27, Jul. 2015.
- [155] Ankara University, “History of Superconductors | Center of Excellence for Superconductivity Research.” [Online]. Available: <http://cesur.en.ankara.edu.tr/history-of-superconductors/>. [Accessed: 02-Jul-2017].
- [156] C. M. Rey and A. P. Malozemoff, “Fundamentals of superconductivity,” in *Superconductors in the Power Grid*, Elsevier, 2015, pp. 29–73.

- [157] J. W. Bray, "Superconducting Applications: Present and Future," *J. Supercond. Nov. Magn.*, vol. 21, no. 6, pp. 335–341, Oct. 2008.
- [158] A. Mourachkine, *Room-temperature Superconductivity*. Cambridge International Science Pub., 2004.
- [159] Brookhaven National Laboratory, "Room-temp superconductors could be possible," 2016. [Online]. Available: <https://phys.org/news/2016-09-room-temp-superconductors.html>. [Accessed: 30-Jun-2017].
- [160] J. R. Bumby, *Superconducting rotating electrical machines*. Clarendon Press - Oxford, 1983.
- [161] C. P. Poole, J. F. Zasadzinski, R. K. Zasadzinski, and P. B. Allen, "Characteristic parameters," in *Handbook of Superconductivity*, Elsevier, 2000, pp. 433–489.
- [162] A. C. Rose-Innes, *Introduction to Superconductivity*, 2nd ed. Elsevier, 2012.
- [163] C. P. Poole, "Introduction," in *Handbook of Superconductivity*, Elsevier, 2000, pp. 1–27.
- [164] O. Keysan, "Superconducting Generators for Large Offshore Wind Turbines," University of Edinburgh. Thesis available: <https://www.era.lib.ed.ac.uk/handle/1842/8841>, 2014.
- [165] S. Samoilenov, A. Molodyk, S. Lee, V. Petrykin, V. Kalitka, I. Martynova, A. Makarevich, A. Markelov, M. Moyzykh, and A. Blednov, "Customised 2G HTS wire for applications," *Supercond. Sci. Technol.*, vol. 29, no. 2, p. 024001, Feb. 2016.
- [166] J. W. Bray, "Superconductors in Applications; Some Practical Aspects," *IEEE Trans. Appl. Supercond.*, vol. 19, no. 3, pp. 2533–2539, Jun. 2009.
- [167] V. Selvamanickam, "2 – High temperature superconductor (HTS) wires and tapes," in *High Temperature Superconductors (HTS) for Energy Applications*, 2012, pp. 34–68.
- [168] Y. Wang, *Fundamental Elements of Applied Superconductivity in Electrical Engineering*, Har/Psc. Singapore: Wiley, 2014.

- [169] J. Fraunhofer, J. Grundmann, G. Klaus, and W. Nick, “Basic concepts, status, opportunities, and challenges of electrical machines utilizing high-temperature superconducting (HTS) windings,” *J. Phys. Conf. Ser.*, vol. 97, no. 1, p. 012189, 2008.
- [170] V. Selvamanickam, “Recent Advances in High Temperature Superconductors and Potential Applications,” *FermiLab*, 2014.
- [171] D. Christen, “Superconductors: Current limits to wire technology,” *Nature*, vol. 392, no. 6679, pp. 862–863, Apr. 1998.
- [172] B. A. Albiss and I. M. Obaidat, “Applications of YBCO-coated conductors: a focus on the chemical solution deposition method,” *J. Mater. Chem.*, vol. 20, no. 10, pp. 1836–1845, Feb. 2010.
- [173] S. S. Kalsi, “Superconducting Wind Turbine Generator Employing MgB₂ Windings Both on Rotor and Stator,” *IEEE Trans. Appl. Supercond.*, vol. 24, no. 1, pp. 47–53, 2014.
- [174] W. Li and S.-X. Dou, “High Critical Current Density MgB₂,” in *Superconductors - New Developments*, InTech, 2015.
- [175] K. Konstantopoulou, A. Ballarino, A. Gharib, A. Stimac, M. G. Gonzalez, A. T. P. Fontenla, and M. Sugano, “Electro-mechanical characterization of MgB₂ wires for the Superconducting Link Project at CERN,” *Supercond. Sci. Technol.*, vol. 29, no. 8, p. 084005, Aug. 2016.
- [176] Q. Wang, “Fabrication and superconducting properties of MgB₂/Nb/Cu wires with chemical doping by using Powder-In-Tube (PIT) method,” Université Joseph-Fourier - Grenoble I, 2014.
- [177] R. Radebaugh, “Cryocoolers: the state of the art and recent developments,” *J. Phys. Condens. Matter*, vol. 21, no. 16, p. 164219, 2009.
- [178] B. Sundén, J. Fu, B. Sundén, and J. Fu, “Chapter 5 – Cryogenics,” in *Heat Transfer in Aerospace Applications*, 2017, pp. 71–88.

- [179] Y. Yang, S. Duan, Y. Ren, Y. Jiang, L. Feng, X. Zhang, H. Chai, M. Kuang, J. Wu, X. Yang, and Y. Zhao, "Design and Development of a Cryogen-Free Superconducting Prototype Generator With YBCO Field Windings," *IEEE Trans. Appl. Supercond.*, vol. 26, no. 4, pp. 1–5, Jun. 2016.
- [180] H. Ohsaki, Y. Terao, and M. Sekino, "Wind turbine generators using superconducting coils and bulks," *J. Phys. Conf. Ser.*, vol. 234, no. 3, p. 032043, 2010.
- [181] N. Mijatovic, B. B. Jensen, C. Træholta, A. B. Abrahamsen, V. M. R. Zermeno, and N. F. Pedersen, "An HTS Machine Laboratory Prototype," *Phys. Procedia*, vol. 36, pp. 771–776, 2012.
- [182] J. Wang, R. Qu, Y. Tang, Y. Liu, B. Zhang, J. He, Z. Zhu, H. Fang, and L. Su, "Design of a Superconducting Synchronous Generator With LTS Field Windings for 12 MW Offshore Direct-Drive Wind Turbines," *IEEE Trans. Ind. Electron.*, vol. 63, no. 3, pp. 1618–1628, Mar. 2016.
- [183] M. Ainslie, M. Izumi, and M. Miki, "Recent advances in superconducting rotating machines: an introduction to the 'Focus on Superconducting Rotating Machines,'" *Supercond. Sci. Technol.*, vol. 29, no. 6, p. 060303, Jun. 2016.
- [184] G. Snitchler, B. Gamble, and S. S. Kalsi, "The Performance of a 5 MW High Temperature Superconductor Ship Propulsion Motor," *IEEE Trans. Applied Supercond.*, vol. 15, no. 2, pp. 2206–2209, Jun. 2005.
- [185] R. H. Qu, "Keynote talk — Design of large electrical machines," in *2013 IEEE International Conference on Applied Superconductivity and Electromagnetic Devices*, 2013, pp. 536–536.
- [186] M. Lesser, R. Gmbh, J. Müller, and Z. P. Gmbh, "Superconductor Technology – Generating the Future of Offshore Wind Power," no. May 2009, pp. 1–10, 2010.
- [187] B. B. Jensen, N. Mijatovic, and A. B. Abrahamsen, "Development of superconducting wind turbine generators," *J. Renew. Sustain. Energy*, vol. 5, no. 2, p. 13, Mar. 2013.
- [188] J. Lloberas, A. Sumper, M. Sanmarti, and X. Granados, "A review of high temperature superconductors for offshore wind power synchronous generators," *Renew. Sustain. Energy Rev.*, vol. 38, pp. 404–414, Oct. 2014.

- [189] R. Qu, Y. Liu, J. Wang, Ronghai Qu, Yingzhen Liu, Jin Wang, R. Qu, Y. Liu, and J. Wang, "Review of superconducting generator topologies for direct-drive wind turbines," *IEEE Trans. Appl. Supercond.*, vol. 23, no. 3, pp. 5201108–5201108, Jun. 2013.
- [190] G. Sarmiento, J. M. Merino, J. Garcia-Tejedor, P. Ibañez, and S. Apiñaniz, "Direct-action superconducting synchronous generator for a wind turbine," PCT/ES2009/070639, 2012.
- [191] J. Sun, S. Sanz, and H. Neumann, "Conceptual design and thermal analysis of a modular cryostat for one single coil of a 10 MW offshore superconducting wind turbine," *IOP Conf. Ser. Mater. Sci. Eng.*, vol. 101, no. 1, p. 012088, Dec. 2015.
- [192] J. Sun, R. Ramalingam, S. Sanz, and H. Neumann, "Preliminary test of the prototype modular cryostat for a 10 MW offshore superconducting wind turbine," *IOP Conf. Ser. Mater. Sci. Eng.*, vol. 171, no. 1, p. 012121, Feb. 2017.
- [193] I. Marino, A. Pujana, G. Sarmiento, S. Sanz, J. M. Merino, M. Tropeano, J. Sun, and T. Canosa, "Lightweight MgB₂ superconducting 10 MW wind generator," *Supercond. Sci. Technol.*, vol. 29, no. 2, p. 024005, Feb. 2016.
- [194] Suprapower, "First modular cryostat," *Suprapower Report*, 2015. [Online]. Available: <http://www.suprapower-fp7.eu/docs.php?pag=3>. [Accessed: 24-Apr-2017].
- [195] Suprapower, "Superconducting light generator for large offshore wind turbines." [Online]. Available: <http://www.suprapower-fp7.eu/summary.php#prettyPhoto>. [Accessed: 08-Jul-2017].
- [196] X. Song, N. Mijatovic, J. Kellers, C. Buhrer, A. V. Rebsdorf, J. Hansen, M. Christensen, J. Krause, J. Wiezoreck, H. Putz, and J. Holboll, "A Full-Size High-Temperature Superconducting Coil Employed in a Wind Turbine Generator Setup," *IEEE Trans. Appl. Supercond.*, vol. 27, no. 4, pp. 1–5, Jun. 2017.
- [197] EWEA, "Upwind." [Online]. Available: <http://www.ewea.org/our-activities/eu-funded-projects/completed-projects/upwind/>. [Accessed: 09-Jul-2017].
- [198] H. Polinder and A. B. Abrahamsen, "Superconducting Generators in INNWIND.EU," 2017.

- [199] A. Thomas and Z. Azar, "Summary Report for Work Package 3.1.2 - Investigation of Super-Conducting Direct Drive Generators."
- [200] D. Liu, H. Polinder, A. B. Abrahamsen, X. Wang, and J. A. Ferreira, "Comparison of Superconducting Generators and Permanent Magnet Generators for 10-MW Direct-Drive Wind Turbines," in *Electrical Machines and Systems (ICEMS), 2016 19th International Conference on*, 2016, p. 6.
- [201] D. Liu, H. Polinder, X. Wang, and J. A. Ferreira, "Evaluating the cost of energy of a 10 MW direct-drive wind turbine with superconducting generators," in *2016 XXII International Conference on Electrical Machines (ICEM)*, 2016, pp. 318–324.
- [202] M. Bauer, "Introducing EcoSwing," SUPRAPOWER workshop, Bilbao, 2017.
- [203] Y. R. Chen and T. Coombs, "Design Methodology of HTS Bulk Machine for Direct-Driven Wind Generation," *IEEE Trans. Appl. Supercond.*, vol. 22, no. 3, pp. 5201804–5201804, Jun. 2012.
- [204] C. Liu, K. T. Chau, S. Member, J. Zhong, W. Li, and F. Li, "Quantitative Comparison of Double-Stator Permanent Magnet Vernier Machines With and Without HTS Bulks," vol. 22, no. 3, 2012.
- [205] T. A. Coombs, "Trial Test of a Bulk-Type Fully HTS Synchronous Motor," *IEEE Trans. Appl. Supercond.*, vol. 24, no. 3, pp. 1–5, 2014.
- [206] S. F. Jia, R. H. Qu, J. Li, H. Y. Fang, D. W. Li, and J. X. Hu, "Design and analysis of a novel vernier reluctance fully superconducting synchronous generator with LTS windings for wind power generation," 2016, pp. 462–463.
- [207] D. Kostopoulos, D. Liu, G. Genani, and H. Polinder, "Feasibility Study of a 10 MW MgB2 Fully Superconducting Generator for Offshore Wind Turbines," in *EWEA Offshore Conference*, 2013.
- [208] Y. Terao, M. Sekino, and H. Ohsaki, "Electromagnetic Design of 10 MW Class Fully Superconducting Wind Turbine Generators," *IEEE Trans. Appl. Supercond.*, vol. 22, no. 3, pp. 5201904–5201904, Jun. 2012.

- [209] O. Keysan and M. A. Mueller, “A Transverse Flux High-Temperature Superconducting Generator Topology for Large Direct Drive Wind Turbines,” *Phys. Procedia*, vol. 36, pp. 759–764, 2012.
- [210] O. Keysan, A. S. McDonald, M. A. Mueller, R. Doherty, and M. Hamilton, “C-GEN, a lightweight direct drive generator for marine energy converters,” in *5th IET International Conference on Power Electronics, Machines and Drives (PEMD 2010)*, 2010, pp. 1–6.
- [211] Fountain Design Ltd, “Fountain Design Ltd. Development Engineers.” [Online]. Available: <http://www.fountaindesign.co.uk/index.html>. [Accessed: 24-Jul-2017].
- [212] N. Hodgins, O. Keysan, A. S. McDonald, and M. A. Mueller, “Design and Testing of a Linear Generator for Wave Energy Applications,” *IEEE Trans. Ind. Electron.*, no. c, pp. 1–10, 2011.
- [213] Macalloy, “Post Tensioning System,” *Post Tensioning System Brochure*, 2011. [Online]. Available: www.macalloy.com/brochures/post-tensioning. [Accessed: 25-May-2015].
- [214] P. Radyjowski, O. Keysan, J. Burchell, and M. Mueller, “Development of a superconducting claw-pole linear test-rig,” *Supercond. Sci. Technol.*, vol. 29, no. 4, p. 044002, Apr. 2016.
- [215] S. Ganz, “Soft magnetic CoFe alloys for electric motors and generators,” 2009. [Online]. Available: www.prizz.fi/sites/default/files/tiedostot/linkki2ID432.pdf.
- [216] Thordon Bearings, “Thordon Bearings.” [Online]. Available: <http://thordonbearings.com/>. [Accessed: 28-Jul-2017].
- [217] SKF Brochure, “Nautilus bearing arrangement solution from SKF,” *SKF Report*, 2010. [Online]. Available: <http://www.skf.com/medialibrary/asset/0901d19680059bbf>. [Accessed: 20-Feb-2017].
- [218] R. Waters and Edita Västra Aros), *Energy from ocean waves : full scale experimental verification of a wave energy converter*. Acta Universitatis Upsaliensis, 2008.
- [219] O. M. Faltinsen, *Sea Loads on Ships and Offshore Structures*. Cambridge University Press, 1990.

- [220] S. Meicke and R. Paasch, “Seawater lubricated polymer journal bearings for use in wave energy converters,” 2012.
- [221] Y. Dong, W. Zhu, X. Zhang, and J. Guo, “Design of Special Plastic Bearings and Their Application in Renewable Energy Conversion System,” *Open Mater. Sci. J.*, vol. 9, no. 1, pp. 203–209, Nov. 2015.
- [222] Y. Nakanishi, K. Shimazu, Y. Matsumoto, S. Kai, Y. Oka, and H. Higaki, “Eco-friendly bearing for tidal power generation,” in *2012 International Conference on Renewable Energy Research and Applications (ICRERA)*, 2012, pp. 1–5.
- [223] University of Edinburgh, “C-GEN Direct Drive PTO Stage 2 - Public Report - University of Edinburgh,” 2017.
- [224] D. J. Eyres and D. J. Eyres, “27 – Corrosion control and anti-fouling systems,” in *Ship Construction*, 2007, pp. 309–325.
- [225] W. J. Yang, K.-G. Neoh, E.-T. Kang, S. L.-M. Teo, and D. Rittschof, “Polymer brush coatings for combating marine biofouling,” *Prog. Polym. Sci.*, vol. 39, no. 5, pp. 1017–1042, 2014.
- [226] D. Carteau, K. Vallée-Réhel, I. Linossier, F. Quiniou, R. Davy, C. Compère, M. Delbury, and F. Faÿ, “Development of environmentally friendly antifouling paints using biodegradable polymer and lower toxic substances,” *Prog. Org. Coatings*, vol. 77, no. 2, pp. 485–493, 2014.
- [227] O. Rodríguez Peralta, “Corrosion and Cathodic Protection Problems,” in *3rd International Conference on Ocean Energy*, 2010.
- [228] E. Isotahdon, E. Huttunen-Saarivirta, V.-T. Kuokkala, M. Paju, and L. Frisk, “Corrosion protection provided by electrolytic nickel and tin coatings for Nd-Fe-B magnets,” *J. Alloys Compd.*, vol. 585, pp. 203–213, Feb. 2014.
- [229] A. S. Kim, “Permanent Magnets: Corrosion Properties,” in *Encyclopedia of Materials: Science and Technology*, 2001, pp. 6812–6815.
- [230] X. MA, F. Fang, J. Jiang, and R. Tan, “Effect of rare earths on corrosion resistance of Cu-30Ni alloys in simulated seawater,” *J. Rare Earths*, vol. 27, no. 6, pp. 1037–1041, Dec. 2009.

The End.